



Report on seismic modelling

D 5.5

Report on seismic modelling

D5.5

Flavio Poletto, Biancamaria Farina, José M. Carcione, Gualtiero Böhm, Dimitrios Mendrinou, Philippe Jousset, Giorgia Pinna, Erika Barison

Work package 5 – Task 2.4

2019.05.27

Website: <http://www.gemex-h2020.eu>



The GEMex project is supported by the European Union's Horizon 2020 programme for Research and Innovation under grant agreement No 727550

Table of Contents¹

List of figures	4
List of tables	7
Executive summary	9
1 Introduction	10
1.1 <i>Objective of the task</i>	10
1.2 <i>Limitations of the report</i>	10
1.3 <i>Structure of the report</i>	11
1.3.1 Full-waveform modelling	11
1.3.2 Sensitivity analysis	11
1.3.3 Model parameters	11
1.3.4 Elastic characterization of geothermal system	11
1.3.5 Characterization of geothermal systems including temperature	11
1.3.6 Conclusions	12
1.3.7 List of Annexes	12
1.3.8 References	12
2 Full wave-form modelling (OGS)	13
2.1 <i>Numerical simulation approach and method</i>	13
2.1.1 Background theory for poro-viscoelastic media (OGS)	13
2.1.2 Model description	14
2.1.3 The Burgers mechanical model	14
2.1.4 Temperature dependence by Arrhenius equation	16
2.1.5 Equations of motion	16
2.1.6 Pressure dependence	16
2.1.7 Summary of rock properties and temperature properties	17
3 Sensitivity analysis	18
3.1 <i>Sensitivity analysis of seismic properties in geothermal fields</i>	18
3.2 <i>Examples of seismic results with full waveform simulation</i>	23
4 Model parameters	24
4.1 <i>Benchmarking</i>	24
4.1.1 Initial benchmarking model (OGS)	24
4.1.2 Benchmarking by comparison of modelling approaches	29
4.1.3 Contribution P. Jousset (GFZ) to D 5.5 – Benchmarking numerical method	29
5 Elastic characterization of geothermal system	30
5.1 <i>Elastic simulation of Los Humeros active seismic-lines response</i>	30

¹ The content of this report reflects only the authors' view. The Innovation and Networks Executive Agency (INEA) is not responsible for any use that may be made of the information it contains.

5.2	<i>Comparison of modelling with active Los Humeros seismic data results</i>	30
6	Characterization of geothermal systems including temperature	34
6.1	<i>Analysis of seismic wavefields in conductive and convective geothermal systems</i>	34
6.2	<i>Poro-viscoelastic modelling of seismic wavefields including temperature, with simulation of Los-Humeros wavefields</i>	36
6.3	<i>Poro-viscoelastic modelling of seismic wavefields including temperature, with simulation of Acoculco wavefields</i>	41
6.3.1	Introduction	41
6.3.2	Lithological and seismic model	41
6.3.3	Thermodynamic parameters	42
6.3.4	Poro-viscoelastic simulation with temperature and benchmarking examples	42
6.3.5	Contribution P. Jousset (GFZ) to D5.5 – Benchmarking simulation	53
7	Conclusion	60
7.1	<i>Main results achieved – milestones of the task</i>	60
7.2	<i>Scientific knowledge increased</i>	61
7.3	<i>Future project work and links with other WPs</i>	61
7.3.1	Constraints	61
7.3.2	Data integration	61
8	List of Annexes	62
9	References	63

List of figures

Figure 1:	Octahedral stress σ_o as a function of strain. The rock starts to yield when σ_o exceeds the elastic limit σ_{oe} . Steady-state flow occurs when σ_o is between σ_{oe} and σ_{op} (modified after Carcione et al. 2014).....	14
Figure 2:	Burgers mechanical model for shear deformation (Carcione 2014). σ , ϵ , μ and η represent stress, strain, shear modulus and viscosity, respectively. The seismic relaxation is described by η_1 and the plastic flow by η	14
Figure 3:	Plot of (a) P-wave velocity VP , calculated with and without porosity, and pressure effects for the bulk and shear moduli. In the curve with porosity we observe the fluid Gassmann effect, while the curve without porosity is flat in the Gassmann zone. (b) S-wave velocity VS , calculated with and without porosity, and pressure effects for the bulk modulus. The curves with and without porosity and both without pressure are superimposed.	21
Figure 4:	(a) P-wave modulus EP curves, calculated with and without porosity, and pressure effects for the bulk and shear moduli. The curves without pressure are parallel, hence they present the same sensitivity to temperature variation. (b) S-wave modulus ES curves, calculated with and without porosity, and pressure effects for the bulk and shear moduli.....	22
Figure 5:	From OGS Contributions to WP 5.2 Seismic Imaging, Potsdam, January 2017.....	23
Figure 6:	Open view of the 3D cube velocity model. Digitized grid version of the local model of Los Humeros (provided by OGS) using the geological model of WP3 (Calcagno et al., 2018).	25
Figure 7:	3D view of the geological interfaces of Acoculco regional model (Calcagno et al., 2018).....	27

Figure 8: Section extracted from the GeoModeller model, with geological interpretation and estimated provisional-initial seismic P-velocity.	28
Figure 9: Open view of the 3D cube velocity model. Digitized grid version of the local model Acoculco (provided by OGS) using the geological model of WP3 (Calcagno et al., 2018).	28
Figure 10: Comparison of a) synthetic, b) synthetic with ‘pattern simulation’ mixing and c) real shots of line L5.	32
Figure 11: Comparison of a) full-waveform synthetic and b) real common mid points (CMP) of line L4. These data are used for PSDM with the same migration velocity model.	32
Figure 12: Comparison of a) full-waveform synthetic PSDM and b) real PSDM of line L5.	33
Figure 13: Comparison of a) synthetic PSDM and b) real PSDM of line L5, superimposed to the velocity model and interpretation.	33
Figure 14: Fluid properties as it ascends from deep heat source to the wellhead plotted in the Mollier pressure-enthalpy diagram of pure water: examples of a liquid dominated hydrothermal system (left red line), of a convectively heated vapor dominated hydrothermal system (right red line) and of a conductively heated vapor dominated hydrothermal system (dark red line). Main assumptions are isenthalpic upwards fluid flow, as well as hydrostatic pressure for the liquid dominated system and vapor-static pressure for the deep part of the vapor dominated system.	35
Figure 15: a) Pressure and (b) temperature profiles for a superhot geothermal reservoir with convective (blue) and conductive (red) mechanism in the deeper part.	35
Figure 16: New definition of melting-rate point based on seismic curves (after Poletto et al., 2019).	38
Figure 17: Estimation of melting points at depth (for selected signal frequency 10 Hz) according to the velocity-inflexion point definition (case z, 2, 2, 2 in Poletto et al. 2019).	38
Figure 18: Input P-velocity model of the rock frame used for synthetic simulation. The yellow lines indicate the VSP and the surface profiles, the red star denotes source.	39
Figure 19: Modeled VSP acquired assuming a source at depth. a) In the absence of melting, b) with melting, and c) difference. We observe a clear variation of the synthetic signal in the melting zone. However also the reflection predicting the interface of the melting formation from shallower depths changes its magnitude, as shown by the upgoing events in panel (c) (Poletto et al., 2019).	40
Figure 20: Signal of the surface seismic line acquired a) in the model with superhot chimney, b) in the model without superhot chimney, and c) difference of the results (a) and (b).	40
Figure 21: 2D section of Acoculco extracted from the GeoModeller 3D regional model, with geological interpretation and estimated provisional-initial seismic P-velocity. The depth, calculated with respect the top of the wells is reported in blue on the left side of the model. The lithologies of EAC1 and EAC2 wells are superimposed.	44
Figure 22 Models used for the Acoculco initial simulation (calculated using the local scheme of Figure 8). Two different Arrhenius parameters are used in the simulation.	45
Figure 23: Compressional velocity model of Acoculco used to simulate the wave propagation. The red line represents the position of a vertical recording line, below well EAC1. The red stars represent the position of three surficial sources.	45

Figure 24: Acoculco section with the 1D temperature profile (see Figure 22) superimposed.....	45
Figure 25: Zero-offset VSP (vertical Z receiver component) acquired with the source at the position of well EAC1. a) Benchmarking elastic model. Poro-viscoelastic model including temperature obtained when the lithological unit U4 (Table 10) is characterized: b) by Arrhenius set AC1 (no melting); c) by Arrhenius set AC2. In (c) the melting effects appears at about 4.5 km depth (from well ground level), where the temperature exceeds 700 °C and the profile enters the transition from the brittle to ductile rock behaviour. Note in Figure 24 that this zone is not characterized by geological changes, but only by temperature variations.	46
Figure 26: Offset VSP (vertical Z receiver component) acquired with the source at 4000 m lateral position from EAC1 well head. a) Shows the benchmarking elastic model. B) and c) show the poro-viscoelastic models including temperature obtained when the lithological unit U4 (Table 10) is characterized: b) by Arrhenius set AC1 (no melting); c) by Arrhenius set AC2. In (c) the melting effects appears at about 4.5 km depth (from well ground level), where the temperature exceeds 700 °C and the profile enters the transition from the brittle to ductile rock behaviour. Note in Figure 24 that this zone is not characterized by geological changes, but only by temperature variations.	46
Figure 27: Offset VSP (horizontal X receiver component) acquired with the source at 4000 m lateral position from EAC1 well head. a) Shows the benchmarking elastic model. B) and c) show the poro-viscoelastic models including temperature obtained when the lithological unit U4 (Table 10) is characterized: b) by Arrhenius set AC1 (no melting); c) by Arrhenius set AC2. In (c) the melting effects appears at about 4.5 km depth (from well ground level), where the temperature exceeds 700 °C and the profile enters the transition from the brittle to ductile rock behaviour. Note in Figure 24 that this zone is not characterized by geological changes, but only by temperature variations.	47
Figure 28: Zero-offset VSP (vertical Z receiver component) acquired with the source at the position of well EAC1. Poro-viscoelastic model including temperature, obtained when the lithological unit U4 (Table 10) is characterized: a) by the Arrhenius set AC1 (no melting); b) by Arrhenius set AC2 with melting effects at large depths. c) Difference between the signals in (a) and (b).	47
Figure 29: Offset VSP (vertical Z receiver component) acquired with the source at lateral position 4000 m from well EAC1. Poro-viscoelastic model including temperature, obtained when the lithological unit U4 (Table 10) is characterized: a) by the Arrhenius set AC1 (no melting); b) by Arrhenius set AC2 with melting effects at large depths. c) Difference between the signals in (a) and (b).	48
Figure 30: Offset VSP (horizontal X receiver component) acquired with the source at lateral position 4000 m from well EAC1. Poro-viscoelastic model including temperature, obtained when the lithological unit U4 (Table 10) is characterized: a) by the Arrhenius set AC1 (no melting); b) by Arrhenius set AC2 with melting effects at large depths. c) Difference between the signals in (a) and (b).	48
Figure 31: Successive snapshots of the amplitude of the 2D wavefield (vertical particle velocity component) propagating in the model using Arrhenius set AC1 for unit U4. With these thermal properties melting is not expected in the model zone.	49
Figure 32: Successive snapshots of the amplitude of the 2D wavefield (vertical particle velocity component) propagating in the model using Arrhenius set AC2 for unit U4. With these thermal properties melting occurs in the deeper model zone, and some differences can be interpreted with respect to Figure 31. These effects can be observed in the plot of the differences in Figure 33.	50
Figure 33: Snapshot at 1.8 s of the amplitude of the 2D wavefield (vertical particle velocity component) propagating in the model using for unit U4 Arrhenius set AC1 (a), AC2 (b) and their difference (c).	51

Figure 34: Simulation of signals acquired by a surface seismic line of vertical receivers and the source at the position of well EAC1. Poro-viscoelastic model including temperature, obtained when the lithological unit U4 (Table 10) is characterized: a) by the Arrhenius set AC1 (no melting); b) by Arrhenius set AC2 with melting effects at large depths and recording times.	52
Figure 35: Detail of Figure 34. Simulation of signals acquired by a surface seismic line of vertical receivers acquired with the source at the position of well EAC1. Poro-viscoelastic model including temperature, obtained when the lithological unit U4 (Table 10) is characterized: a) by the Arrhenius set AC1 (no melting); b) by Arrhenius set AC2 with melting effects at large depths. c) Difference between the signals in (a) and (b). The panel (c) is normalized to evidence low amplitude variations in the reflection signals.	52
Figure 36: Interfaces created by OGS. See Figure 22 (OGS report).	53
Figure 37: Extended interfaces. The initial interfaces are extended by 3 km on each side assuming a constant depth in the extended area. Illustration of this process on the topography interface. The initial interface is represented in red. The extended is represented in blue.	53
Figure 38: Extended interfaces. The initial interfaces are extended by 3 km on each side assuming a constant depth in the extended area. Illustration of this process on the topography interfaces. All interfaces are extended.	54
Figure 39: P-wave velocity models. a) initial model (same as in Figure 24). b) Extended model.....	55
Figure 40: Extended models for a) S-wave and b) density.	55
Figure 41: Curved grid in the (x, z) system and rectangular grid in the (ζ , η) system.	56
Figure 42: Stretching of the interfaces with respect to the topography. Fine lines are the original position of the interfaces, and in bold are the stretched positions. Note then the flat topography. The inverse transformation in the code will replace the interfaces at their true position and the topography will be taken into account without possible numerical instabilities due to stair case topography.	56
Figure 43: Successive snapshots of the amplitude of the 2D wavefield propagating in the model. Note that we can recognise the layers of the model by the wave reflections. The source appears at 12.6 km, however it is at the same location as for the OGS models there is a 3 km absorbing boundary on each side. Green color means no energy. Red color mark the locations where energy is larger.	57
Figure 44: Zero offset VSP (vertical component) as modelled at the position of the well EAC1. The horizontal axis is depth, and ranges between 0 and 7 km. The vertical time scale ranges between 0 and 2.5 s.....	58
Figure 45: Vertical component are recorded by a virtual streamer placed all along the topography. The vertical time scale ranges between 0 and 5 s. The horizontal axis is horizontal distance.....	58
Figure 46: Vertical component records for a vertical source located at an offset of 4310 m. a) at the virtual VSP location (well EAC1). b) by receivers at the surface. The vertical axis is time and ranges from 0 to 2.5 s in (a) and from 0 to 5 s in (b). In a) the horizontal scale is depth from 0 to 7 km. In b) the horizontal scale is the horizontal distance in the model.....	59

List of tables

Table 1: Rock and fluid parameters.....	17
---	----

Table 2: Arrhenius parameters.....	17
Table 3: Physical parameters	18
Table 4: Parameters of Los Humeros regional model	25
Table 5: Parameters of Los Humeros local model.....	25
Table 6: Parameters of FILE: Acoculco_reg_100x100x100_XYZ.vox	26
Table 7: Parameters of FILE: Acoculco_reg_200x200x50_XYZ.vox	26
Table 8: Model input parameters.....	30
Table 9: Seismic and Arrhenius parameters used for the model of Los Humeros.	39
Table 10: Seismic and thermodynamic parameters used to model the West-East section represented in Figure 21.	44
Table 11: List of Milestones	60
Table 12: List of Deliverables.....	61

Executive summary

Los Humeros and Acoculco are the two target Mexican geothermal fields of the collaboration study in the GEMex project. These fields represent important examples of superhot and enhanced geothermal systems (EGS) in the Trans-Mexican volcanic belt. Imaging of the deep structures of these study sites is reported in D5.3 in the framework of Task 5.2.

In the present report we summarize the study and the results obtained by innovative approach to simulate the seismic wavefields and to model their properties including temperature in these hot and superhot geothermal systems.

The study covers analytical aspects and full waveform signal simulation in poro-viscoelastic formation including possible melting conditions in the proximity of the brittle-ductile transition (BDT) characterized by rock thermodynamic Arrhenius parameters and temperature, as well as pressure and fluid-phase properties, including possible supercritical conditions, and different hydrothermal mechanisms, by convective and conductive heat transport.

Important inputs come from other work packages of the project, in particular the geological results of WP3 (Calcagno et al., 2018), from results of WP5.2 reported in D5.3, and has relevant links for data integration in the framework of WP5.4 and for reservoir characterization (WP6).

The study provides a calibration of innovative modelling methods, and tools tested through a benchmarking process, applied to the Mexican scenario, and is relevant for the assessment and characterization of these geothermal areas in the continuation of the project (WP7 and WP8) as well as for future Mexican-European collaborations.

For this, we thank Mexican partners and CFE for their support to providing geophysical background information for the preparation of the models.

1 Introduction

1.1 Objective of the task

Deliverable D5.5 refers primarily to reporting the results of Tasks 5.4.3 and 5.2.4, it is related to Task 5.4.4 and to information coming from Tasks 5.2, and the results will be used for Task 5.4.5. In this report we will describe the results of the characterization of geothermal formations by full-waveform seismic modelling including temperature. Responsible researcher: Flavio Poletto (OGS) (fpoletto@inogs.it).

The objective of the task 5.4.3 is the characterization of geothermal formations by full-waveform seismic modelling including temperature (OGS, CRES).

This report also includes the results of the Task 5.2.4. Modelling, which has the aim to:

- a. Improve methods for earthquake location, analysis of location errors, wave-form inversion;
- b. Comparison of wave-form modelling codes by designing a benchmark;
- c. Full-waveform modelling in poro-viscoelastic media with temperature (including melting and BDT analysis), using temperature maps from WP6, and estimate initial stress, pressure conditions and Arrhenius parameters from geothermal info and (if available) laboratory data provided by other partners (OGS, GFZ)

In these tasks the role of the EU partners has been to perform the data processing and modelling in cooperation with Mexican partners.

Relevant activity was dedicated to recover information about the superhot (Los Humeros) and EGS (Acoculco) Mexican sites to properly define and design their models. Significant inputs come from existing literature, from the results of geological models of GEMex WP3 (Calcagno et al., 2018), and from the results of the Seismic imaging, deliverable D5.3 (Jousset et al., 2019). Thanks also to CFE and UNAM for providing legacy active seismic data, utilized to analyse the depth models of Los Humeros.

1.2 Limitations of the report

While more extensive information was available for Los Humeros, retrieval of geophysical and geological information for Acoculco was more difficult, and some modelling parts have to be further investigated in the future (links with WP7 and WP8).

The following aspects are related to limitations of the report, hence indicate future improvements:

1. Further improvement by data integration, e.g., maximum depth of seismicity sources to estimate BDT depth.
2. Need of lab thermodynamic data (rock Arrhenius parameters), for calibration of melting conditions.
3. Pure water as geothermal fluid as an approximation estimated by NIST (Lemmon et al., 2005), further improvements by updated geothermal fluids and brine (water NaCl) tables.

4. Further improvements by linking the measured velocities and seismic properties to modelled velocities and seismic properties.
5. Present analysis by modelling in 2D can be extended to 3D.

1.3 Structure of the report

This report is based on the description of work given by the proposal and project GEMEX.

There is a link with the integration (task 5.4) and with reservoir characterization (WP6).

At the end of the report we include three published and submitted papers to scientific journals as 'GEMex papers'. Leaving the task of a more detailed reading to the lecture of the annexes, the content of the report is presented by recalling the summary, relevant results and examples, and conclusions for each of these papers.

1.3.1 Full-waveform modelling

The first chapter introduces the background theory developed by OGS in recent years, and used in the framework of this research to characterize geothermal systems by a model including creep-flow and the temperature by thermodynamic Arrhenius equation, to describe melting and brittle ductile transition (BDT) in superhot areas, and equations for poro-viscoelastic formations and pressure conditions, including supercritical fluids.

1.3.2 Sensitivity analysis

The sensitivity analysis described in Annex I studies the sensitivity of the seismic quantities with respect to the geothermal physical conditions, including fluids and temperature. This is potentially related to the task of evaluating relationships between temperature and seismic quantities (WP5.4 and D5.11).

1.3.3 Model parameters

An initial preparation of the digital seismic model was undertaken to provide the GEMex consortium with the numerical seismic grids of Los Humeros and also Acoculco. These data have been uploaded on VRE, and are usable as an initial benchmarking model by different simulation codes.

1.3.4 Elastic characterization of geothermal system

This task was aimed at characterizing the seismic reflection response of the Los Humeros active seismic lines (D5.3), by recalculating synthetic shots (full-wavefields) and processing depth images with the same parameters, compared to real results. At this stage temperature was not included.

1.3.5 Characterization of geothermal systems including temperature

This part exploits the use of full-waveform modelling in poro-viscoelastic media including temperature, and focuses over different key aspects:

1. Analysis of seismic wavefields in conductive and convective geothermal systems: This work (related to Annex II) evaluates the possible effects of the hydrothermal mechanisms on the seismic properties, relevant for the study of the geothermal system in the proximity of melting zones and to obtain information of possible recharge mechanisms.
2. Poro-viscoelastic modelling of seismic wavefields including temperature, with simulation of Los Humeros wavefields: This part (related to Annex III) is a summary of modelling approaches, with a

study of the seismic curves obtained with different Arrhenius (thermodynamic) parameters. The application of full waveform simulation is focused on Los Humeros, the superhot geothermal site of the GEMex project.

3. Poro-viscoelastic modelling of seismic wavefields including temperature, with simulation of Acoculco wavefields and relevant benchmarking of modelling methods: As in the previous point, in this case the application is focused on Acoculco, the EGS potential geothermal site of the GEMex project.

1.3.6 Conclusions

Summarize the conclusions of the different sub-parts of the Report.

1.3.7 List of Annexes

Annexed GEMex papers. All the annexed papers are GEMex papers.

1.3.8 References

These are the reference of the report. Extended references are included in the Annexed papers.

2 Full wave-form modelling (OGS)

2.1 Numerical simulation approach and method

Seismic-wave modelling is a key tool to characterize the Earth's structure, nearby geothermal areas where the presence of high temperatures can cause the existence of supercritical fluids and also partial melting. The seismic characterization of these areas is very important especially in deep drilling and high-enthalpy systems. Carcione and Poletto (2013) study the seismic properties variations in the presence of a transition between zones with brittle and ductile behaviour. Carcione et al. (2014) propose an algorithm, based on the Burgers mechanical model, to simulate full-waveform propagation in this areas.

The presented full-wave solver is based on the Burgers mechanical model, which allows us to describe the anelastic behaviour due to shear deformation and plastic flow, and the Gassmann equation to account for the fluid properties in the poro-viscoelastic model. The shear viscosity that relates the stiffness components of the brittle and ductile formation to temperature, is calculated by the Arrhenius equation and the octahedral-stress criterion. The algorithm is based on a direct grid method, and the equations of motion are solved in the time domain by using memory variables (Carcione, 2014), spatial derivatives and time integration are obtained with Fourier pseudo-spectral method and Runge-Kutta technique, respectively.

We present synthetic seismograms recorded in geothermal fields, at the surface and along vertical seismic profiles (VSP), in wet and dry viscoelastic media characterized by different temperature profiles, in order to analyse the observability of the associated variations by borehole seismic methods (Poletto and Miranda, 2004).

2.1.1 Background theory for poro-viscoelastic media (OGS)

Seismic waves can provide important information, useful to characterize the Earth's structure in particular nearby the transition zone between the brittle and the ductile part of the crust (BDT), the geothermal areas and the magmatically active areas. In these regions, temperatures can be higher than the critical temperature of water implying the possible presence of supercritical fluids.

Carcione and Poletto (2013) proposed an elastic-plastic rheology to model the BDT. They introduced a stress-strain relation including the effect of crust anisotropy, seismic attenuation and ductility to model the deformation on the basis of the shear modulus variations related to temperature.

Carcione et al. (2014) proposed a full-waveform algorithm, based on the Burgers mechanical model and the Arrhenius equation to calculate the flow viscosity, to model temperature-dependent propagation of seismic waves in geothermal and magmatic crustal areas.

Carcione et al. (2016) extended the theory and the simulation algorithm considering the poro-viscoelastic case. They explicitly modelled the effects of saturating fluids, generally water and steam at various pressure-temperature conditions also considering the possible supercritical behaviour. The full-wave solver is based on the Burgers mechanical model to describe the anelastic behaviour due to shear deformation and plastic flow and the Gassmann equation to take into account the fluid properties in the poro-viscoelastic model.

In this work we use this direct grid method to simulate P-S seismic waves in a 2D poro-viscoelastic model of the heterogeneous Earth's crust.

2.1.2 Model description

The BDT can be viewed as the transition between zones with viscoelastic and plastic behaviour, i.e., between the upper, cooler, brittle and the deeper ductile crustal zones. Its behaviour depends on stress and temperature conditions and it is principally determined by the viscosity of the crustal rocks. The contrast in properties, at this transition, is mainly due to the different shear rigidity which is higher in the brittle medium. The medium with plastic behaviour flows when subjected to deviatoric stress, expressed by the octahedral stress, which determines the character of the flow. Figure 1 shows the octahedral stress as function of strain.

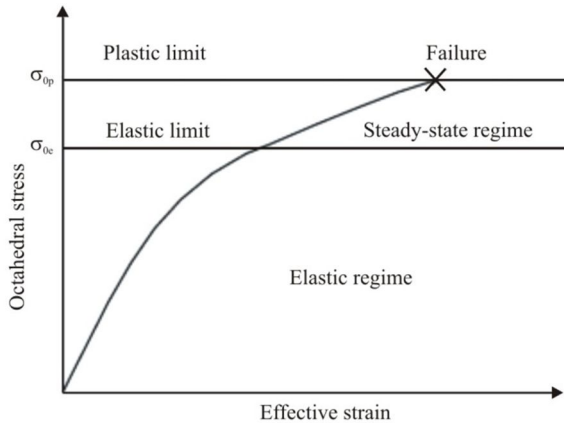


Figure 1: Octahedral stress σ_o as a function of strain. The rock starts to yield when σ_o exceeds the elastic limit σ_{oe} . Steady-state flow occurs when σ_o is between σ_{oe} and σ_{op} (modified after Carcione et al. 2014).

2.1.3 The Burgers mechanical model

The constitutive equation, used for the simulation algorithm, includes the viscoelastic and the plastic behaviour, and represents the generalization to the poro-elastic case of the stress-strain relation proposed by Carcione and Poletto (2013). The viscoelastic creep is described with the Burgers mechanical model (Carcione 2004), which is a series connection of a dashpot and a Zener model (Figure 2).

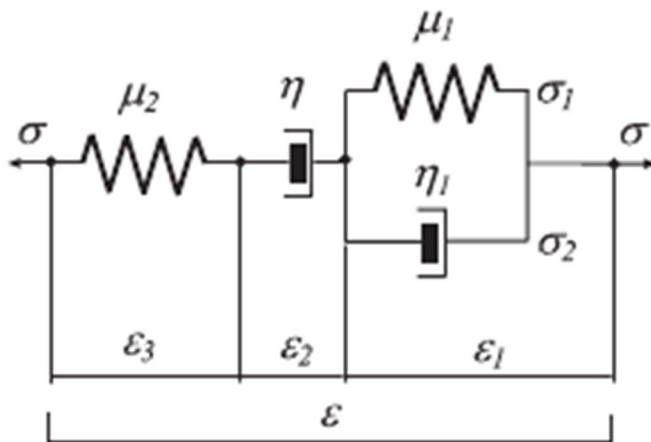


Figure 2: Burgers mechanical model for shear deformation (Carcione 2014). σ , ε , μ and η represent stress, strain, shear modulus and viscosity, respectively. The seismic relaxation is described by η_1 and the plastic flow by η .

The common expression for the creep function in the time domain is

$$\chi = \left(\frac{t}{\eta} + \frac{1}{\mu_0} \left[1 - \left(1 - \frac{\tau_\sigma}{\tau_\varepsilon} \right) \exp\left(-t/\tau_\varepsilon\right) \right] \right) H(t), \quad (1)$$

where $H(t)$ is the Heaviside function, τ_σ and τ_ε , are the seismic stress and strain relation times, respectively. They are expressed as functions of the quality factor by

$$\tau_\varepsilon = \tau_0 / Q_0 \left(1 + \sqrt{Q_0^2 + 1} \right), \quad \tau_\sigma = \tau_\varepsilon - \frac{2\tau_0}{Q_0}, \quad (2)$$

where τ_0 is the relaxation time such that $\omega_0 = 1/\tau_0$ is the centre frequency of the relaxation peak and Q_0 is the minimum quality factor (Carcione et al., 2013). The deformation of the ductile layer is calculated using the octahedral stress, which includes tectonic effects

$$\sigma_o = \frac{1}{3} \sqrt{(\sigma_v - \sigma_h)^2 + (\sigma_v - \sigma_H)^2 + (\sigma_h - \sigma_H)^2}, \quad (3)$$

where σ_v is the vertical lithostatic stress, σ_H and σ_h are the maximum and minimum horizontal stress, respectively (Carcione and Poletto 2013). The saturated wet-rock Gassmann-Burgers poro-elastic bulk and shear moduli are given by

$$K_w = K_d + \alpha^2 M \quad \text{and} \quad \mu_w(\omega) = \mu_d(\omega), \quad (4)$$

K_d and μ_d are the dry bulk and shear moduli, respectively,

$$\alpha = 1 - \frac{K_d}{K_s}, \quad M = \frac{K_s}{1 - \phi - K_d/K_s + \phi K_s/K_f}, \quad (5)$$

K_s and K_f are the solid and fluid bulk moduli, respectively, and ϕ is the porosity. The complex and frequency-dependent P- and S-wave velocities are

$$V_P = \sqrt{\frac{K_w + 4\mu_w(\omega)/3}{\rho}} \quad \text{and} \quad V_S = \sqrt{\frac{\mu_w(\omega)}{\rho}}, \quad (6)$$

where the bulk density is

$$\rho = (1 - \phi)\rho_s + \phi\rho_f, \quad (7)$$

and ρ_s and ρ_f are the grain and fluid densities, respectively.

2.1.4 Temperature dependence by Arrhenius equation

Seismic wavefields in models including creep flow and ductility from temperature, BDT (OGS)

The viscosity is related to the steady-state creep rate through the Arrhenius equation

$$\eta = \frac{\sigma_o}{2\dot{\epsilon}}, \quad (8)$$

where σ_o is the octahedral stress (eq. 3) and the dislocation creep rate is represented by the steady state power law (e.g., Violay et al. 2012)

$$\dot{\epsilon} = A\sigma_o^n \exp(-E/RT), \quad (9)$$

being A ($\text{MPa}^{-n} \text{s}^{-1}$) a material constant, n the stress exponent and E the activation energy (kJ/mole), which are experimentally determined. $R = 8.3144 \text{ J/mol/}^\circ\text{K}$ is the gas constant and T the absolute temperature.

2.1.5 Equations of motion

The equation of motion can be described using the Burgers relaxation function

$$\psi(t) = [A_1 \exp(-t/\tau_1) - A_2 \exp(-t/\tau_2)]H(t), \quad (10)$$

where

$$\tau_{1,2} = -\frac{1}{\omega_{1,2}}, \quad (11)$$

are related to the relaxation times (Eqs. 16 and 17 of Carcione et al., 2017) and

$$A_{1,2} = \frac{\mu_1\mu_2 + \omega_{1,2}\eta_1\mu_2}{\eta_1(\omega_1 - \omega_2)}, \quad (12)$$

are coefficients calculated as described in Farina et al. (2016) and Carcione et al. (2017), to write the stress-strain relations in the P-S equations of motion, considering the plane-strain conditions with propagation in the (x, z) -plane, using memory variables to overcome the temporal convolution (Carcione 2014).

2.1.6 Pressure dependence

To account for the pressure dependence, we express the dry-rock bulk moduli as

$$K_d = K_0 g_1(p_d) \quad \text{and} \quad \mu_d = \mu_B g_2(p_d), \quad (13)$$

where $g_j(p_d)$, $j = 1, 2$ defines the dependence of the moduli on the differential pressure $p_d = p_c - p$, where p_c is the confining pressure, p is the pore (fluid) pressure, and K_0 and μ_0 are the bulk and shear moduli at infinite effective pressure and $\eta = \infty$ (or $\omega = \infty$). Using μ_B in (13) means that the Burgers shear viscosity is included. The simplest form of function g , in good agreement with experimental data, is

$$g_j(p_d) = 1 - (1 - a_j) \exp\left(-\frac{p_d}{p_j^*}\right), \quad j = 1, 2, \quad (14)$$

(Kaselow and Shapiro, 2004; Poletto et al., 2018), where a_j and p_j^* are parameters. It is $g_j = 1$ for $p_d \rightarrow \infty$ (e.g., very high confining pressure) and $g_j = a_j$ for $p_d \rightarrow 0$ (pore pressure equal to the confining pressure).

2.1.7 Summary of rock properties and temperature properties

Summary of required physical and geological parameters (OGS).

The modelling methods previously described are adopted to calculate seismic properties in geothermal reservoirs, in arbitrary media. Further calculations include also permeability, depending on relation of dispersion properties and fluid mobility (e.g., Poletto et al., 2018, ANNEX I).

The application requires the estimation of the following rock parameters (Table 1),

Table 1: Rock and fluid parameters

Rock solid and dry bulk moduli	K_s and K_d
Dry shear modulus	μ
Rock solid and bulk densities	ρ_s and ρ
Fluid bulk modulus	K_f
Bulk porosity	ϕ
Fluid density	ρ_f
Rock quality (Q factors)	Q_p, Q_s

the estimation of the rock thermal (Arrhenius) constants (Table 2),

Table 2: Arrhenius parameters

The amplitude constant	A
The Activation energy	E
The exponential index	n

and the estimation of the local physical conditions (Table 3)

Table 3: Physical parameters

Octahedral stress (includes tectonic effects)	σ_o
Temperature	T
Pressure (pore and confining)	p, p_c

Not all these parameters have the same relevance and impact on the estimated results.

In the following of this report we approach the sensitivity analysis to geothermal parameters both from analytic point of view and using full-waveform modelling to evaluate effects on seismic responses.

3 Sensitivity analysis

3.1 Sensitivity analysis of seismic properties in geothermal fields

Here we insert main results from and of GEMex paper on Geothermics (OGS) (that will be in Annex to the D5.5 Report)

Summary (Annex I):

Geophysical characterization plays a key role for the definition of the deep structures of geothermal reservoirs and the consequent assessment and validation of the geothermal conceptual model. Seismic methods may provide a valuable contribution for this purpose. This involves a deep and reliable understanding of the sensitivity of seismic-wave propagation to physical and temperature variations, with complex interactions. We present the theory and sensitivity analysis based on rock's mechanical Burgers model including Arrhenius temperature equations, integrated with Gassmann model for fluid saturated porous rocks, pressure effects for bulk and shear moduli, as well as permeability and squirt flow effects. Assuming a temperature gradient model, the analysis applied at low seismic frequencies compares the interpretation of the sensitivity effects for different typical seismic elastic quantities, showing the different performance in relation to physical effects, including melting, supercritical conditions, and observability obtained in different temperature regions.

With a quantification of the physical properties, the results of the study show that in deeper zones the main expected contributions in terms of variations in seismic velocity, moduli and seismic attenuation due to temperature come from melting transition, while in shallower porous fluid-saturated formations the trends are governed by pressure effects, with minor contributions of permeability and possible effects related to soft porosity. The new calculated elastic moduli are complex-valued and frequency-dependent, and temperature dependent through the fluid properties. In this complex scenario, not always the increments in the velocity and elastic wave moduli correspond to an increment in the temperature. Moreover, with mobility decreasing as a function of depth, the analysis shows that the shear quality factor is sensitive to permeability, which introduces moderate effects for velocity and attenuation of shear waves. The analysis applies to active exploration seismic and passive seismology.

Selected representative results (Annex I):

Representative results extracted from the sensitivity analysis are shown in Figure 3 and Figure 4. In Figure 3 we observe the variation in seismic velocities to temperature calculated with and without pressure effects (porosity close to zero). These plots clearly show the strong variation in the melting zone due to the increase of creep-flow and decrease in Burgers viscosity, both for velocities of P- and S-waves. The shape of these curves strongly depend on Arrhenius' parameters of Table 2.

Figure 4 show the corresponding curves for the compressional $E_p = \rho V_p^2$ and shear $E_s = \rho V_s^2$ elastic moduli. These moduli are used for estimation of temperature by seismic properties (WP 5.4).

Conclusions (Annex I):

Understanding the sensitivity of seismic quantities to temperature is of great importance for the seismic characterization of geothermal reservoirs. Especially at high temperatures, detection and monitoring of melting and supercritical zones, as well as influence of pressure on the bulk and shear moduli require appropriate sensitivity analysis. In this paper we present the Burgers–Gassmann theory following previous studies and numerical-code developments, including permeability and involving squirt-flow effects to some extent, and study characteristic sensitivity curves in the low-frequency approximation. Results show the different observability by different elastic components, with different prevalence of the physical effects in different temperature regions. This suggests the use of an integrated analysis by more seismic elastic quantities for the characterization of geothermal areas, which can be applied either to exploration or to passive seismology data, including volcanic environments.

The characteristic sensitivity is here calculated for a set of physical models. Based on a quantification of the physical properties, the results show that in deeper zones the main expected contributions in terms of variations in seismic velocity, moduli and seismic attenuation due to temperature come from melting transition, while in shallower porous fluid-saturated formations the trends are mainly governed by pressure effects, with minor contributions of permeability and possible effects related to the compliant soft porosity. In the region corresponding to the supercritical zone, the fluid density is lower and consequently the pressure increases with a slower trend as a function of depth and temperature. Without melting (i.e., neglecting the Burgers viscosity), the wave velocities have minor variations.

Depending on porosity, we can use velocity information to retrieve the fluid saturation. The trend including pressure effects in the bulk and shear moduli presents variations even at low temperatures. The Gassmann effect is less evident in the S-wave velocity, which tends to zero at high temperatures due to melting, as expected. In the curves calculated without pressure effects for the bulk and shear moduli, the presence of fluid changes the P-wave elastic modulus which becomes lower than that calculated in the absence of fluid, but these curves are parallel, therefore they present the same sensitivity. For the S-wave elastic modulus with and without porosity and pressure effects the curves are practically superimposed. In the presence of porosity with fluid saturation the velocity and the density change, in such a way that the P-wave modulus is almost constant with temperature regarding the Gassmann effects. In the analysis of temperature as a function of seismic quantities by reciprocal sensitivity, not always the increments in the velocity and elastic wave moduli correspond to an increment in the temperature.

For example, the same increment in the S-wave velocity may correspond to an increase in the temperature in a zone where pressure effects are observed and to a decrease in the temperature in the melting zone. The fluid viscosity decreases initially as a function of temperature and then increases slowly in the

supercritical zone. At high temperatures, the fluid mobility is close to zero because the permeability decreases with depth and vanishes in the melting zone. The analysis shows that the shear quality factor is sensitive to permeability. Permeability introduces moderate effects for velocity and attenuation of shear waves. We observe these effects, especially at shallower depths and low temperatures, for the curves calculated with variable permeability, decreasing with depth. Moreover, assuming a constant-permeability model, we study the potential permeability effects for deeper zones. In this analysis, the choice and definition of the temperature distribution map, approximated by a constant gradient for our purposes, is important. The change of the rock type and its Arrhenius parameters, as well as the tectonic stresses, may change the melting temperature and this may cause a different distribution of the physical effects, partially superimposed in the sensitivity curves. The change of the geothermal fluid properties affects the supercritical point, here assumed to be that of pure water, hence the pressure and density curves used in the calculations. Next, we plan to apply the analysis to real cases, such those of the Mexican high enthalpy regions, where the main targets are to characterize seismically the super-hot geothermal systems, including the temperature, evaluate the possible presence of supercritical-fluid conditions, and contribute to map possible magmatic zones interpreted in the proximity of the investigated areas.

Annex I: Poletto, F., Farina, B., and Carcione, J. M., 2018. Sensitivity of seismic properties to temperature variations in a geothermal reservoir, *Geothermics*, 76, 149—163.

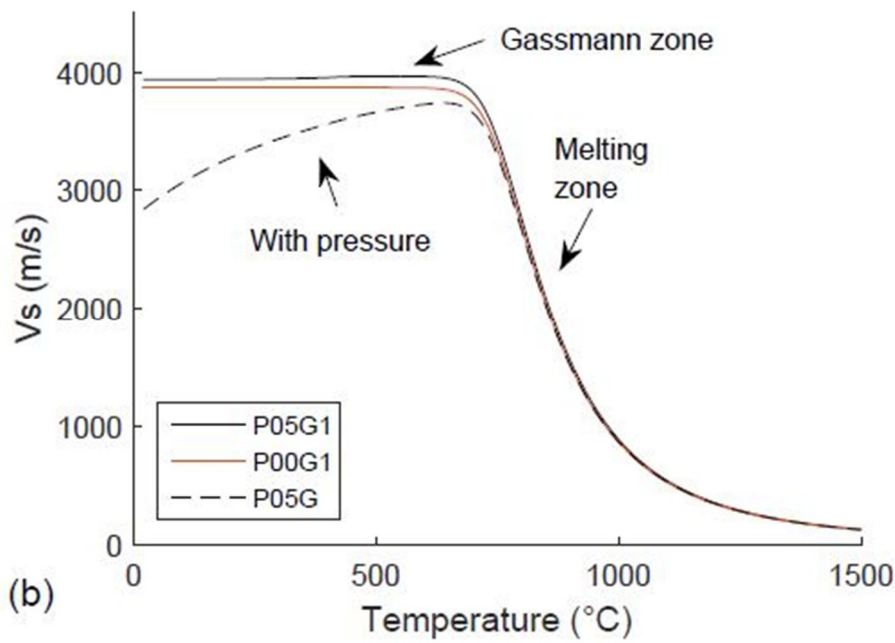
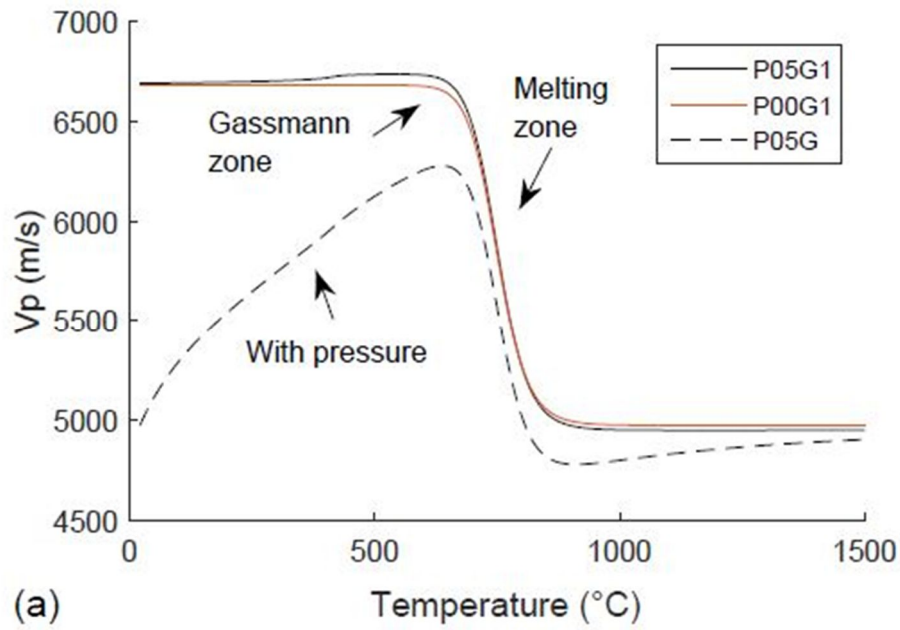


Figure 3: Plot of (a) P-wave velocity V_p , calculated with and without porosity, and pressure effects for the bulk and shear moduli. In the curve with porosity we observe the fluid Gassmann effect, while the curve without porosity is flat in the Gassmann zone. (b) S-wave velocity V_s , calculated with and without porosity, and pressure effects for the bulk modulus. The curves with and without porosity and both without pressure are superimposed.

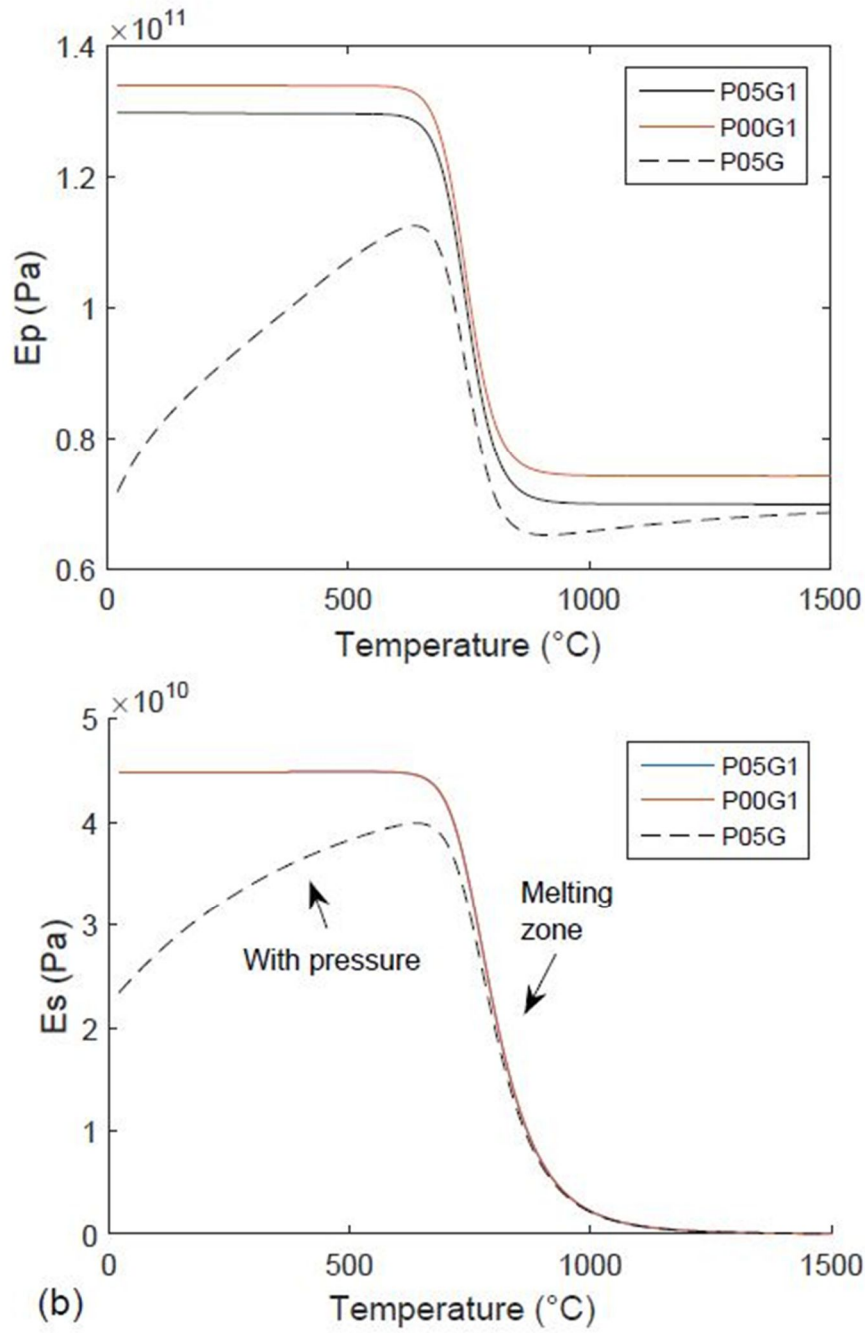


Figure 4: (a) P-wave modulus E_p curves, calculated with and without porosity, and pressure effects for the bulk and shear moduli. The curves without pressure are parallel, hence they present the same sensitivity to temperature variation. (b) S-wave modulus E_s curves, calculated with and without porosity, and pressure effects for the bulk and shear moduli.

3.2 Examples of seismic results with full waveform simulation

In this section we show that differences in the seismic properties are observable in theoretical examples selected from OGS GEMex presentation (WP 5.2 Workshop, Potsdam 2017).

The following example summarizes some analysis performed in the initial phase of the project to evaluate the variation in the poro-viscoelastic full-waveform signals for the variations in the geothermal conditions. These may include supercritical and melting (Poletto et al., EGC 2019), i.e., proximity to BDT.

The following test has the purpose to analyze the observability of variations in seismic properties in a uniform medium where only different temperature values are introduced. The background medium is assumed as a Poisson medium with $V_p = 6000$ m/s, and density 2700 kg/m³. The source is a vertical force with peak frequency $f_p=50$ Hz, the Arrhenius constants are $A = 1030$ MPa⁻ⁿs⁻¹, $n = 3.5$, the activation energy is $E = 990$ kJ/mol (after Violay et al., 2012).

In this model we assume a plume with $T=1200$ °C, the temperature of the background medium is 300 °C.

A VSP is simulated in the proximity of the plume, with a source at the surface (Figure 5 left side). The source peak frequency is 50 Hz. Figure 5 right side shows the synthetic full-waveform proximity-VSP signals, where the reflection from the plume flank (dashed red arrow in the left panel) is interpreted and evidenced by the yellow dashed line.

This example confirms with full-waveform results that seismic wavefields are sensitive to temperature, and that effects due to only temperature are seismically observable under suitable recording conditions.

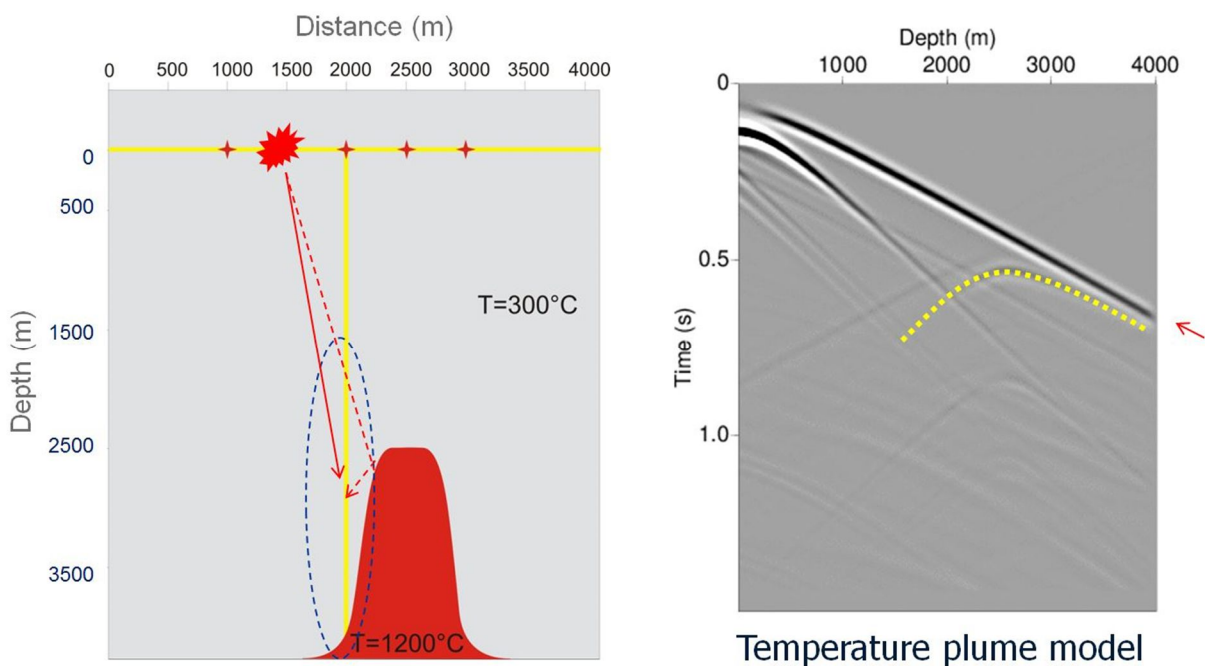


Figure 5: From OGS Contributions to WP 5.2 Seismic Imaging, Potsdam, January 2017.

4 Model parameters

4.1 Benchmarking

4.1.1 Initial benchmarking model (OGS)

Initial 3D benchmark discretized models of Los Humeros and Acoculco sites were created by OGS using the geological models of WP3 provided by GeoModeller, both at regional (Los Humeros and Acoculco) and local (Los Humeros) scales. The interfaces of the main layers have been identified and the layers filled by velocity values obtained from literature, background velocity information and geophysical evaluation where geophysical data are poorer (Acoculco site).

These models have been intended and used as initial models for improved localization purposes and as a basis for initial analysis. In subsequent steps of the project these models will be substituted by updated model obtained by project results (such as those of Section 3.3.1.2).

The digitised benchmark-model grids of Los Humeros and Acoculco prepared by OGS have been upload on GEMex VRE.

4.1.1.1 Los Humeros

The grid size of the regional model is $100 \times 100 \times 100$ m, with XYZ dimensions $56 \times 36 \times 4$ km. The grid size of the local model in the caldera area was $20 \times 20 \times 20$ m. The XYZ dimensions of the model are $9.5 \times 12.5 \times 4.2$ km. These values are summarized in Table 4 and Table 5.

The compressional P-wave velocity was extracted by Urban and Lermo (2013). To calculate S-waves from P-waves we used the Urban and Lermo (2013) V_P/V_S value 1.76.

Table 4: Parameters of Los Humeros regional model

Grid dimensions	$dX = dY = dZ = 100$ m
Model dimensions	$56 \times 34 \times 4$ km

Table 5: Parameters of Los Humeros local model

Grid dimensions	$dX = dY = dZ = 20$ m
Model dimensions	$9.5 \times 12.5 \times 4.2$ km

Figure 6 shows an open view of the local 3D velocity cube.

Files uploaded and updated by OGS on GEMex VRE (8/2/2018)

- LOS-HUMEROS-Local-MODEL_20x20x20_XYZ.Vp.dat.gz
- LOS-HUMEROS-Regional-MODEL_100x100x100_XYZ.Vp.dat.gz
- local_head.dat
- regional_head.dat

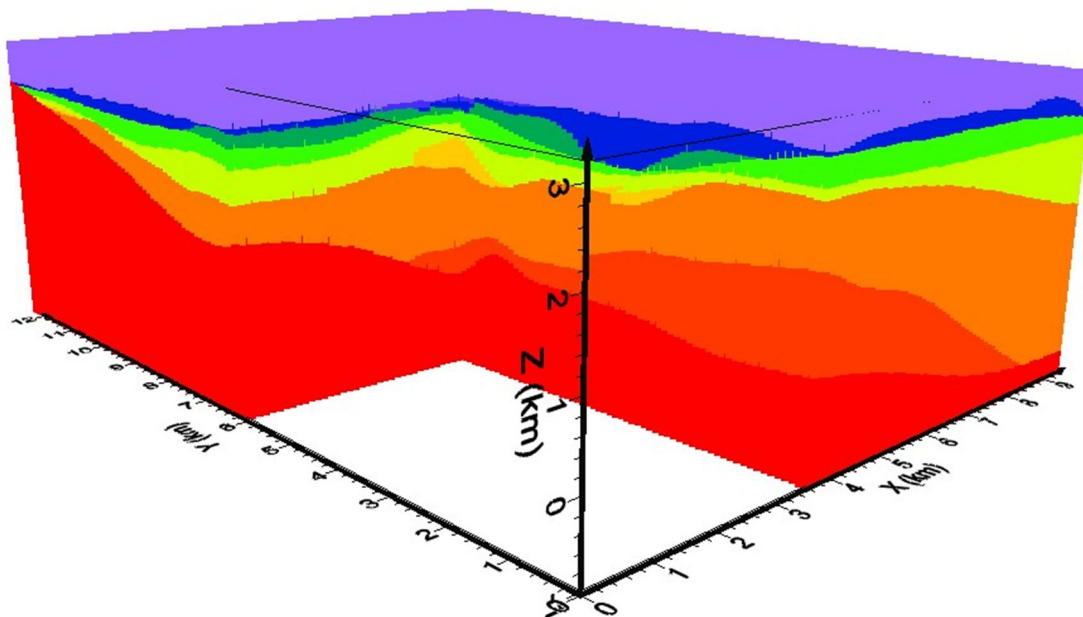


Figure 6: Open view of the 3D cube velocity model. Digitized grid version of the local model of Los Humeros (provided by OGS) using the geological model of WP3 (Calcagno et al., 2018).

4.1.1.2 Acoculco

For Acoculco the velocity information was derived from literature reporting results of seismological waves inversion, sonic logs, and considering reported density distributions and by interpreting indicative values of the sample rocks collected in the area (Lermo et al., 2009; Canet et al. 2015). This estimate represents a preliminary and provisional grid model prepared for initial analysis purposes.

With a similar procedure used for the utilization of the WP3 GeoModeller geological interpretation file (Calcagno et al., 2018), the regional model of Acoculco was discretized, with the following specifications:

Description of the two ASCII files of velocity grid of Acoculco regional model.

Format of files:

The two first records are general information (dimension, grid parameters and format).

Each following records contains the grid nodes data: X Y Z Vp

Table 6: Parameters of FILE: Acoculco_reg_100x100x100_XYZ.vox

Number of nodes	X = 550, Y = 370, Z = 105
Grid dimensions	dX = dY = dZ =100 m
Model dimensions	55 × 37 × 10.5 km
X(min – max)	560050 – 614950 m
Y(min – max)	2182050 – 2218950 m
Z(min – max)	-6950 – 3450 m

Table 7: Parameters of FILE: Acoculco_reg_200x200x50_XYZ.vox

Number of nodes	X = 275, Y = 185, Z = 210
Grid dimensions	dX = dY = 200 m, dZ =50 m
Model dimensions	55 × 37 × 10.5 km
X(min – max)	560100 – 614900 m
Y(min – max)	2182100 – 2218900 m
Z(min – max)	-6975 – 3475 m

Figure 7 shows a 3D view of the lithological interfaces of the Acoculco regional model (Calcagno et al., 2018)

Figure 8 represents the West-East section of this model with geological formations and estimated P-velocity values. Figure 9 shows an open view of the 3D digitized cube of Acoculco. The S-velocity values are calculated by averaged VP/VS value 1.783 derived from log data.

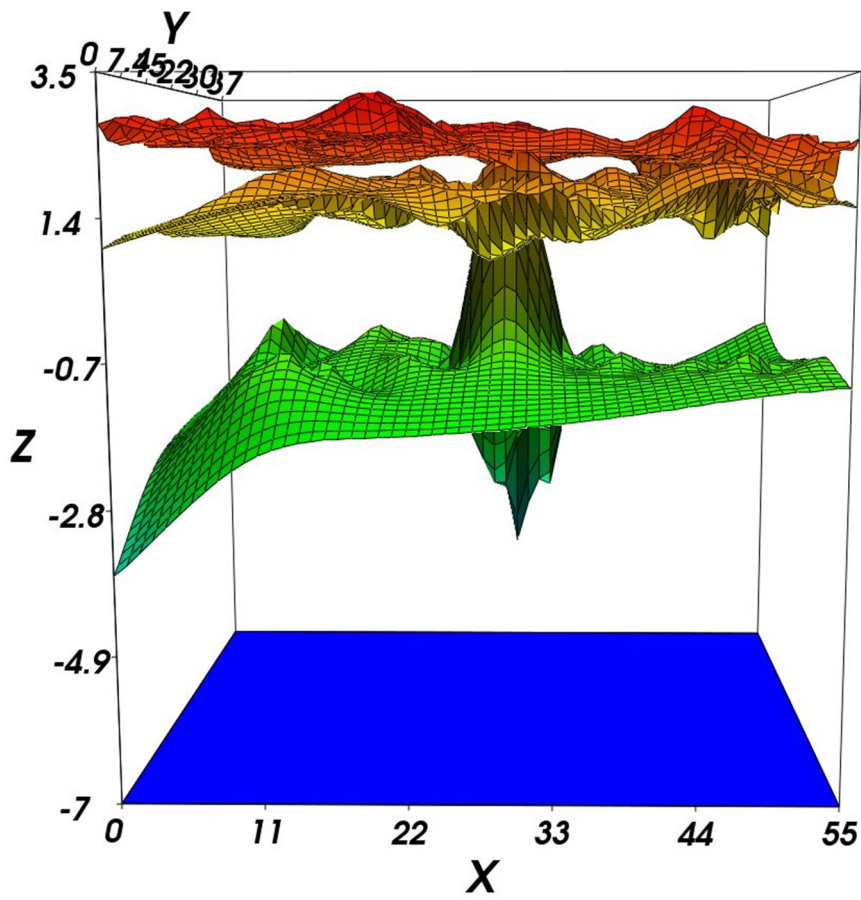


Figure 7: 3D view of the geological interfaces of Acozulco regional model (Calcagno et al., 2018).

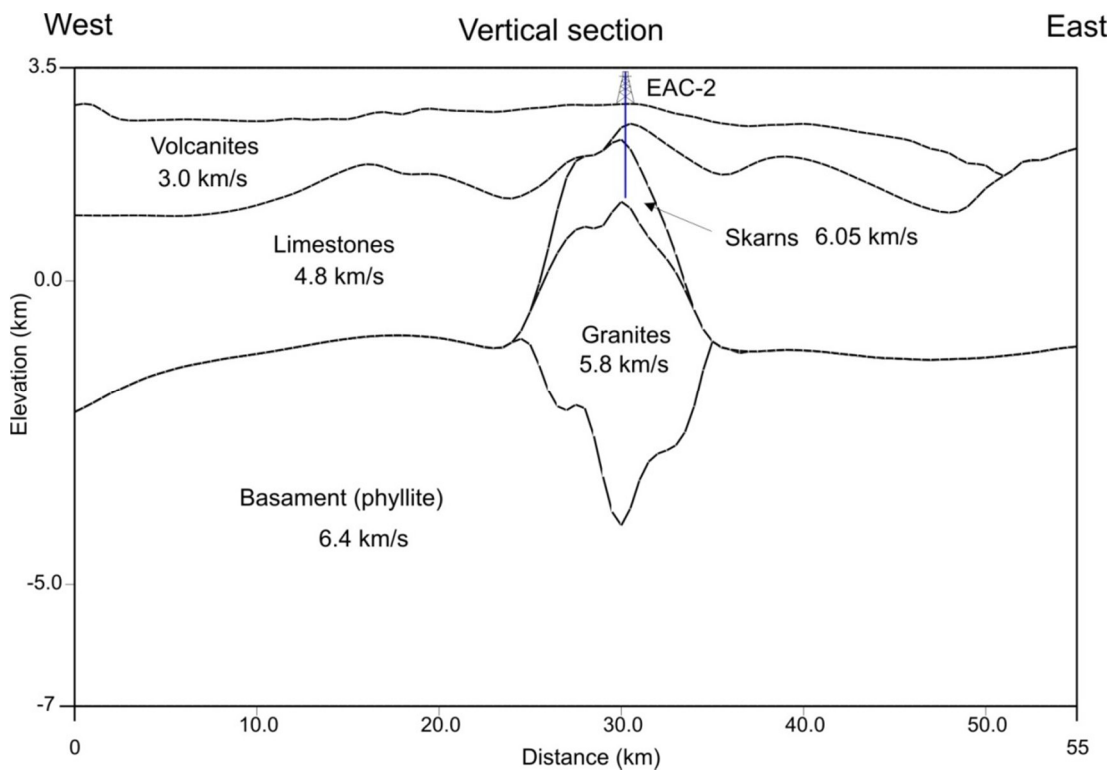


Figure 8: Section extracted from the GeoModeller model, with geological interpretation and estimated provisional-initial seismic P-velocity.

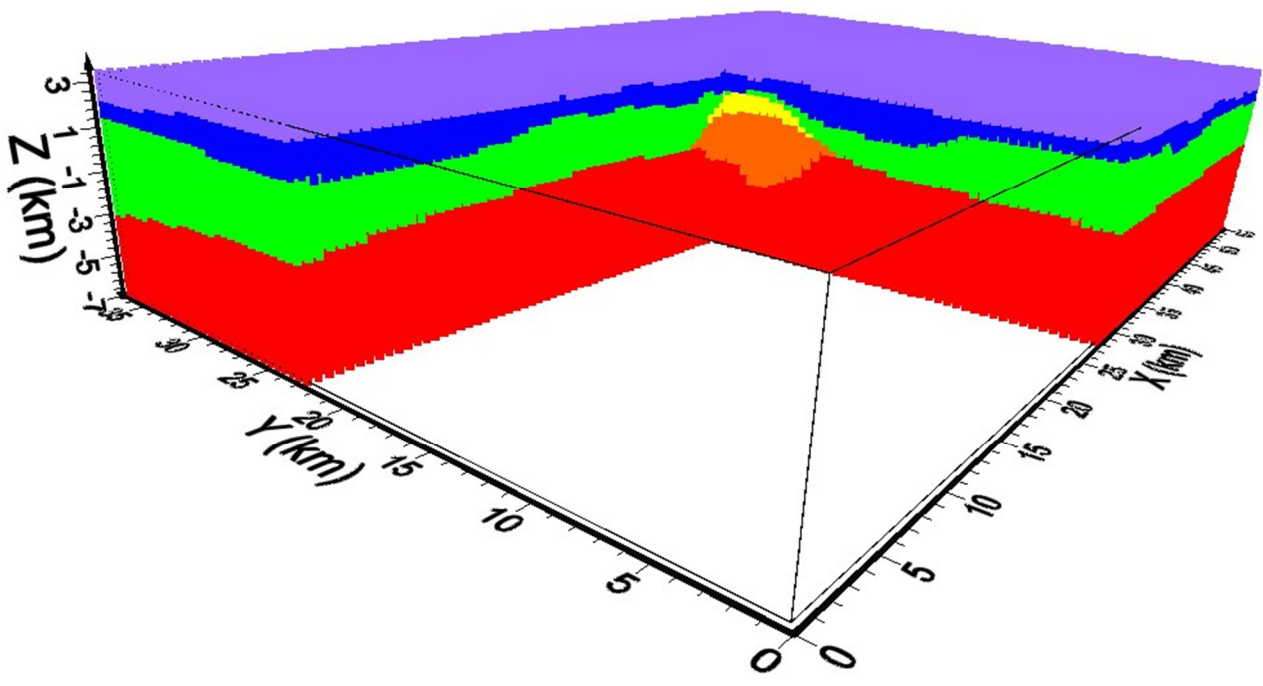


Figure 9: Open view of the 3D cube velocity model. Digitized grid version of the local model Acoculco (provided by OGS) using the geological model of WP3 (Calcagno et al., 2018).

4.1.2 Benchmarking by comparison of modelling approaches

In addition to full-waveform seismic modelling including temperature we use and compare the results obtained by other modelling approaches. We calculate the elastic modelling to simulate the conditions in which the effects of the temperature are not relevant, i.e., in particular when melting is not present.

For this purpose to calculate the synthetic seismic data, we use a fourth-order accurate space, second order accurate time, two-dimensional P-SV finite-difference code based on the Madariaga-Virieux staggered-grid formulation. The numerical scheme is developed from the first-order system of hyperbolic elastic equations of motion and constitutive laws expressed in particle velocities and stresses (Levander, 1988).

Comparison examples are shown for the Acoculco application in Section 6.3.4.

These results can be further improved, investigated and utilized for comparison methods in the continuation of the project as described in D5.3 (Jousset et al., 2019). In particular to improve methods for earthquake location, analysis of location errors, wave-form inversion, using computer facilities; and further comparison of wave-form modelling codes by designing a benchmark with the results of this report, and using the initial benchmarking models at local and regional scales described in this report.

4.1.3 Contribution P. Jousset (GFZ) to D 5.5 – Benchmarking numerical method

This report contribution summarizes results using a finite difference formulation of the wave propagation in the benchmark defined by Flavio Poletto et al. (OGS) to represent Acoculco geothermal field (Mexico).

Introduction

Using a 2-D finite-difference scheme, we model the propagation of seismic energy initiated at the surface by a single vertical force (Lamb test) in a viscoelastic medium with topography introduced by a linear mapping transformation. We model intrinsic attenuation by the linear viscoelastic theory and we approximate the media by a standard linear solid (SLS) for seismic frequencies above 2 Hz.

Method

The initial code has been developed in the framework of previous EU projects since 2003 by Philippe Jousset and updated regularly since then. It has allowed the modelling of volcanic so called Long-Period earthquakes (Jousset et al., 2004). A 3D version also exists and has been used for the modelling part of full moment tensor source inversion (e.g., Jousset et al., 2011; Jolly et al., 2012).

The initial code has been modified in this work to implement a complex geology model of P-wave and S-wave velocities and density. We model intrinsic attenuation by linear viscoelastic theory and Jousset et al. (2004) demonstrated that volcanic media can be approximated by a standard linear solid (SLS) for seismic frequencies above 2 Hz. Once the Q formulation will be refined with clearer introduction of the temperature effect on the Q, we can also introduce spatial variation of Q in the model.

The benchmarking results of this section are shown with examples of Acoculco synthetic data in Section 6.3.5.

5 Elastic characterization of geothermal system

In the next sections we model the geothermal reservoirs by calculating:

- Full-wave elastic modelling to support processing and interpretation of active seismic data of Los Humeros, deep imaging (see also GEMex deliverable D5.3);
- Characterize poro-viscoelastic geothermal systems including pressure and temperature, analytic approach;
- Characterize poro-viscoelastic geothermal systems including pressure and temperature, review by analytic approach and full-waveform synthetic simulation.

5.1 Elastic simulation of Los Humeros active seismic-lines response

Here we (OGS) simulate more extensively the elastic full-waveform response of the Los Humeros seismic lines, providing new results with respect to those of deliverable D5.3 (Jousset et al., 2019).

For this purpose we (OGS) simulate the field shots of entire seismic lines and migrate them, thus obtaining new results with comparison between Synthetic and Real PSDM migrations of full line (OGS).

Full-waveform synthetic data

Table 8: Model input parameters.

Grid dimensions (pixels)	$n_x = 970, n_z = 603$
Cell dimensions	$dX = dY = dZ = 10 \text{ m}$
Sample rate	$5 \cdot 10^{-4} \text{ s}$
Tmax	5 s
Average Richter wavelet frequency	15 Hz

5.2 Comparison of modelling with active Los Humeros seismic data results

Processing sequence applied to synthetic data:

Processing sequence applied to synthetic data:

OGS processed the synthetic data to obtain Kirchhoff Prestack Depth Migration (PSDM) sections to compare with the corresponding ones presented in D5.3.

Before the PSDM, we applied a passband filter (6/12/22/24) to the shot gathers to select the frequency range used also for the real data.

To run the Kirchhoff Prestack Depth Migration (PSDM) we use the velocity models obtained from the real data to depth-migrate the CDP gathers. These velocity models are the outcomes of a residual depth moveout analysis and a 2D Grid-based tomography of depth migrated gathers to improve the depth interval velocity section (Common Image Gather (CIG) migration analysis – See D5.3 for further details).

Then, we applied a top mute to the depth migrated gathers, stacked the data with 0.5 power and applied a frequency-space (FX) prediction deconvolution to get the final depth-migrated sections.

Figure 10 shows the comparison of a synthetic and real shot of line L4, as reported in GEMex deliverable D5.3. Figure 11 shows the comparison of synthetic and real CMP of line L4 (see D5.3).

These results are used to PSDM migrate the synthetic data, and compare them to the real results.

This comparison is shown in Figure 12. The results shown in Figure 12(a,b) are superimposed to the migration velocity model and interpretation of the CIG analysis, and compared in Figure 13.

The comparison of the synthetic and real data confirms the consistency of the analysis of the legacy active seismic data in this complex area.

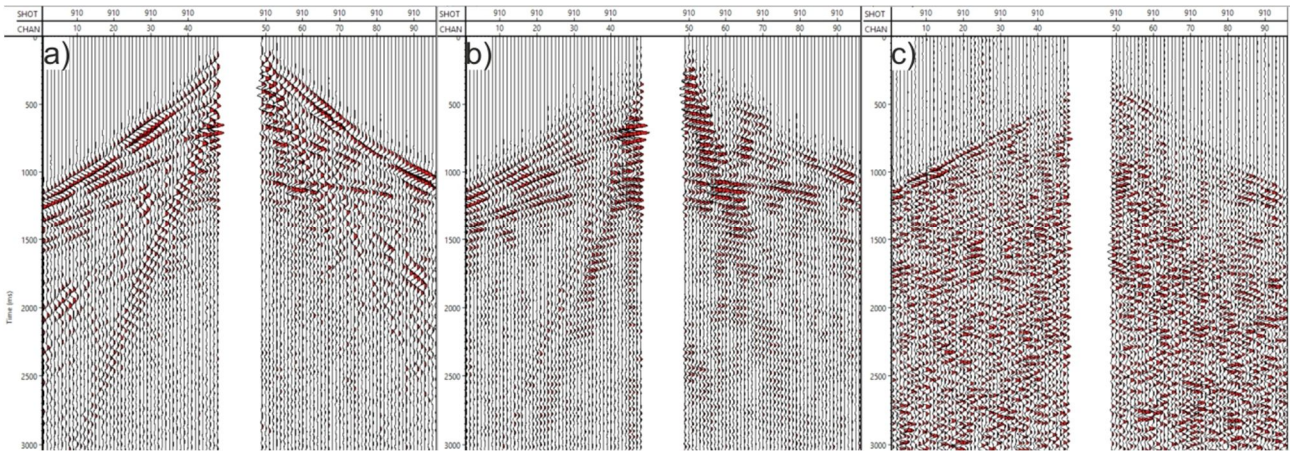


Figure 10: Comparison of a) synthetic, b) synthetic with 'pattern simulation' mixing and c) real shots of line L5.

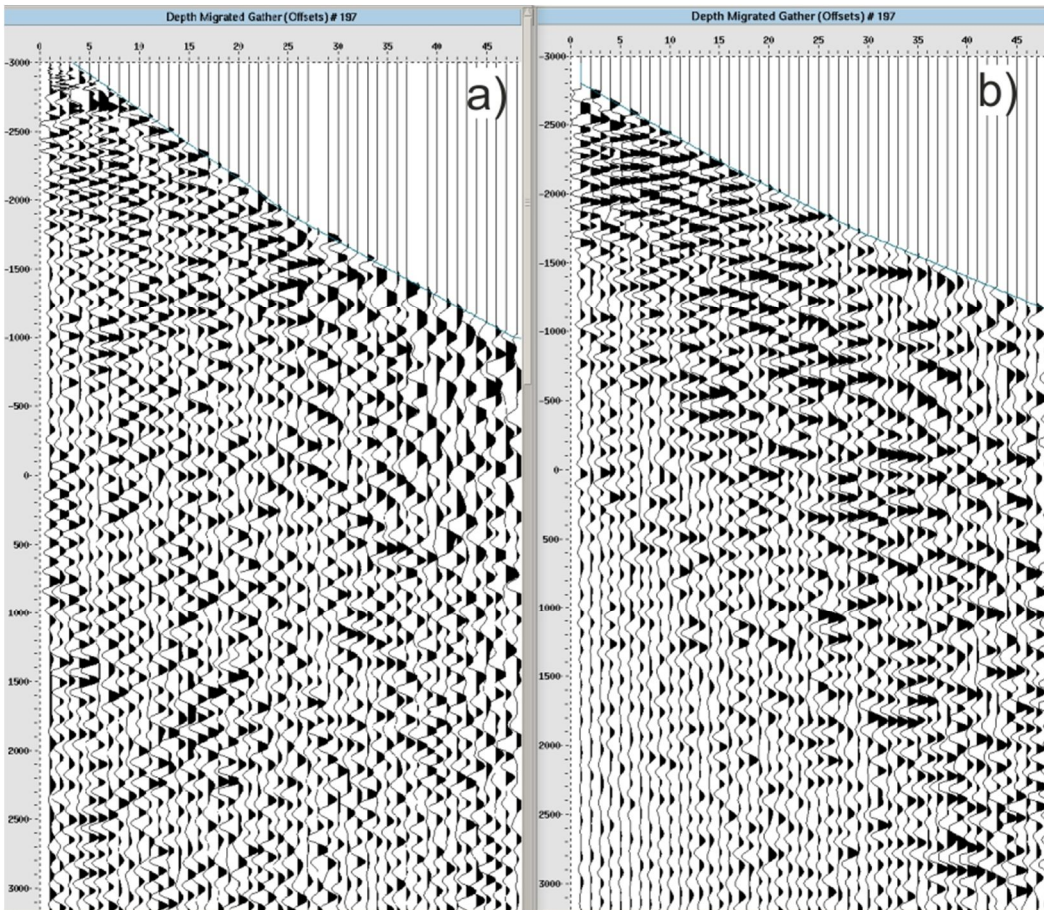


Figure 11: Comparison of a) full-waveform synthetic and b) real common mid points (CMP) of line L4. These data are used for PSDM with the same migration velocity model.

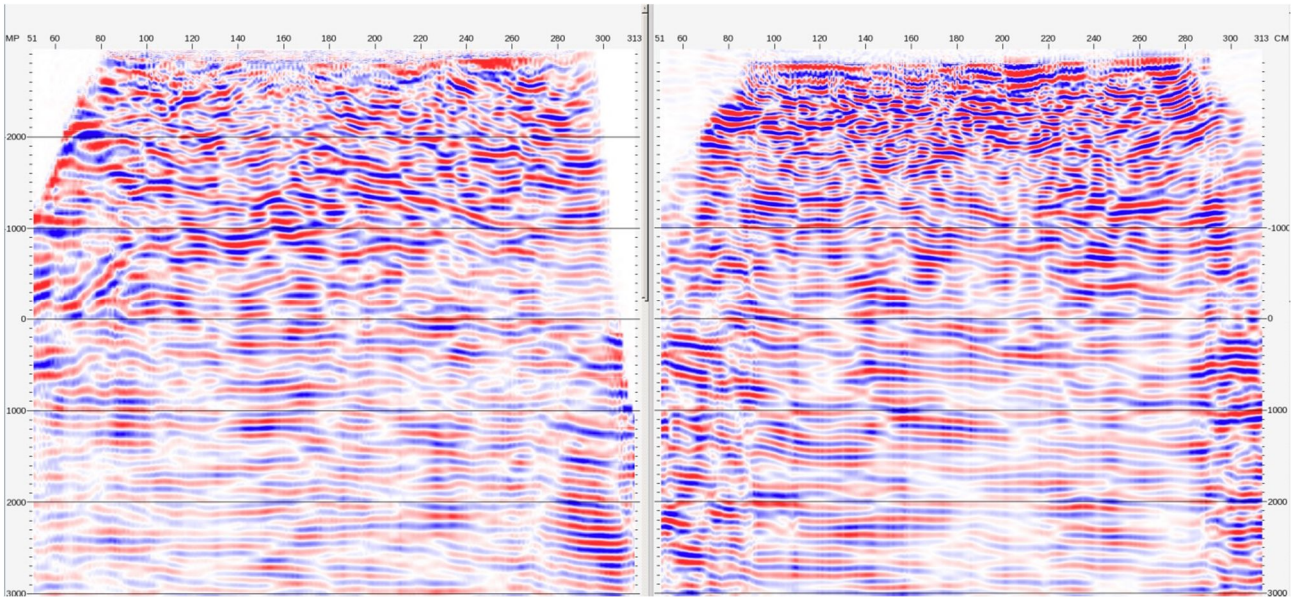


Figure 12: Comparison of a) full-waveform synthetic PSDM and b) real PSDM of line L5.

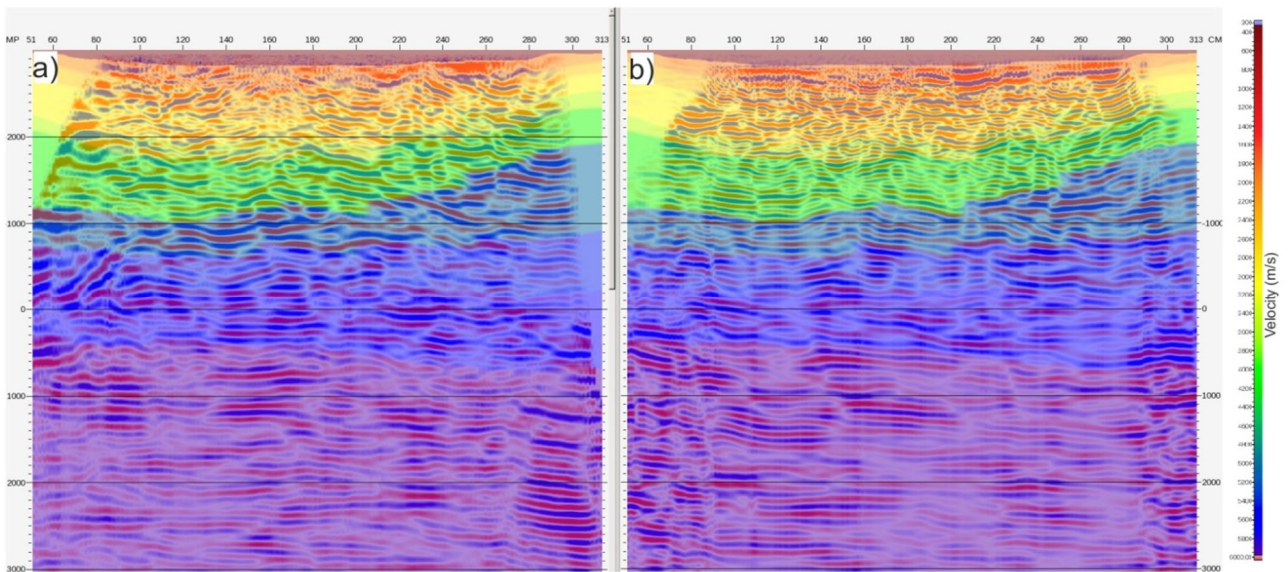


Figure 13: Comparison of a) synthetic PSDM and b) real PSDM of line L5, superimposed to the velocity model and interpretation.

6 Characterization of geothermal systems including temperature

6.1 Analysis of seismic wavefields in conductive and convective geothermal systems

Summary (Annex II):

Seismic methods contribute to the exploration of geothermal areas and characterization of existing geothermal resources. Seismic velocity and attenuation depend on the pressure and temperature conditions of the geothermal systems, which are closely related to the properties of the rock frame and geothermal fluids. We calculate the seismic velocities and attenuation in terms of the subsurface distribution of the confining and pore pressures and temperature, assuming that the heat transfer from below is convective or conductive. The pore pressure is assumed hydrostatic.

In hydrothermal systems the temperature is calculated assuming the boiling point condition at the specific pore pressure down to the reservoir. Beneath the reservoir it is assumed constant in convectively heated systems and following a constant temperature gradient in conductively heated systems. In Enhanced Geothermal Systems (EGS) conductive heat transfer and constant temperature gradient are assumed. We present three application examples, considering simplified subsurface models to describe the geothermal systems beneath the production wells. The seismic wave properties are calculated using the rock's mechanical Burgers model and the Arrhenius equation to take into account rock-properties-variability with temperature and the Gassmann model for fluid saturating the porous rocks.

Representative examples of hydrothermal mechanisms (ANNEX II):

Representative examples extracted from this analysis of the seismic wavefields in different hydrothermal systems are shown in Figure 14 and Figure 15. Figure 14 represents the fluid properties (pure water) pressure-enthalpy diagrams, in which the domains of fluid dominated systems under different phase conditions. Figure 15 shows the characteristic pressure and temperature depth profiles assumed for convective and conductive systems, which are analyzed for superhot Los Humeros and EGS Acoculco scenarios.

Conclusions (Annex II):

Our study presents a seismic characterization of convective and conductive geothermal reservoirs, with different thermodynamic properties dictated by the Arrhenius equation. The aim is to evaluate the influence of the geothermal mechanisms and temperature on the seismic properties, namely, seismic velocities, stiffness moduli and quality factors. The objective is also to discriminate between the two reservoirs at least in the hotter part, below the boiling point. The differences in the seismic properties are small when there is no melting, and are due to variations of the fluid properties. However, remarkable differences can be observed when passing from a vapor-dominated system to a liquid dominated system. Melt significantly affects the properties of the conductive reservoir, since in this case the temperature increases linearly with depth and highly affects the shear rigidity of the rocks. Conversely, in convective reservoirs, the temperature is constant with depth in the deepest region, and only partial melting can be observed for certain thermodynamic conditions.

Main results from and of GEMex paper (accepted for publication on Geothermics) (OGS) (that will be in Annex to the D5.5 Report).

Annex II: Paper accepted for publication on Geothermics (2019) entitled ‘Seismic properties in conductive and convective hot and super-hot geothermal systems’, Farina B., Poletto F., Mendrinós D., Carcione J.M., and Karytsas C.

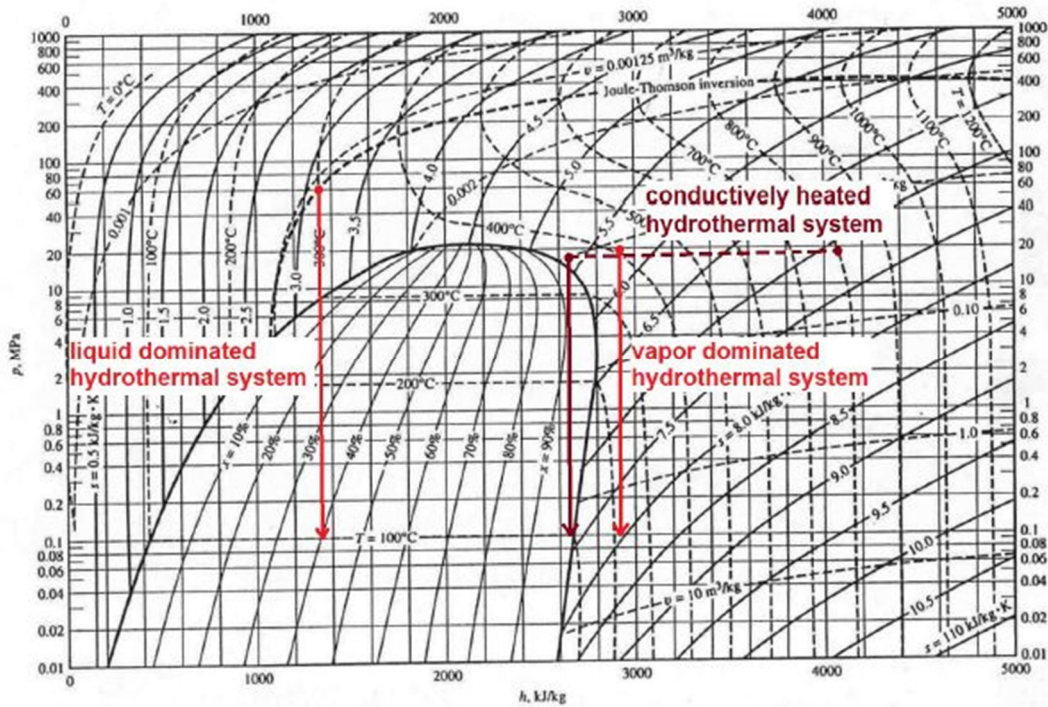


Figure 14: Fluid properties as it ascends from deep heat source to the wellhead plotted in the Mollier pressure-enthalpy diagram of pure water: examples of a liquid dominated hydrothermal system (left red line), of a convectively heated vapor dominated hydrothermal system (right red line) and of a conductively heated vapor dominated hydrothermal system (dark red line). Main assumptions are isenthalpic upwards fluid flow, as well as hydrostatic pressure for the liquid dominated system and vapor-static pressure for the deep part of the vapor dominated system.

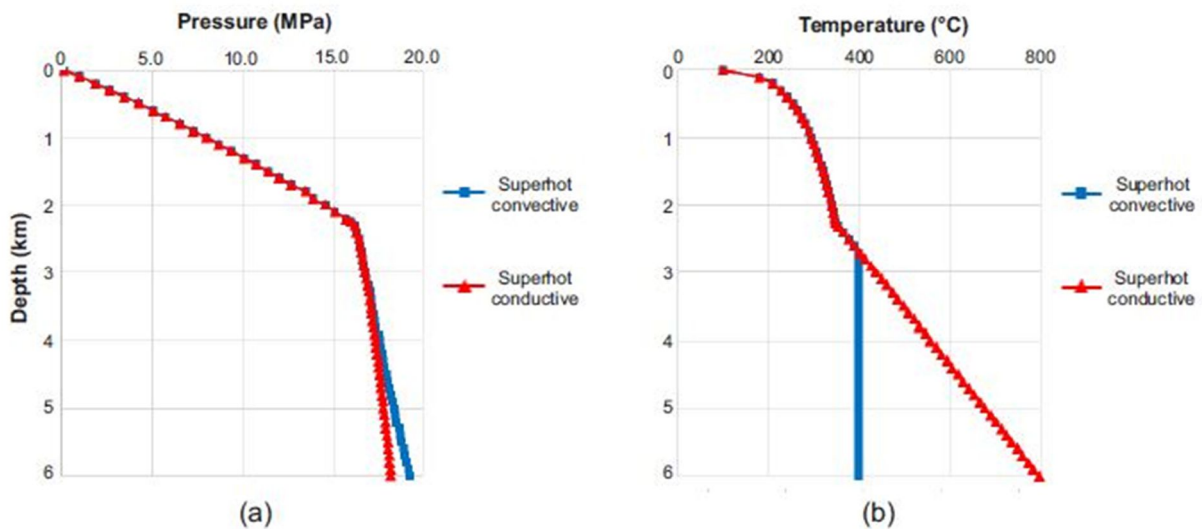


Figure 15: a) Pressure and (b) temperature profiles for a superhot geothermal reservoir with convective (blue) and conductive (red) mechanism in the deeper part.

6.2 Poro-viscoelastic modelling of seismic wavefields including temperature, with simulation of Los-Humeros wavefields

Summary (Annex III):

We present a review summary of the theory of seismic wave propagation in geothermal reservoir, including temperature and pressure effects based on the Arrhenius equation and poro-viscoelasticity. We quantify the effects of the melting rate point on the seismic velocities, and consider surface and borehole acquisition geometries. We perform wavefield simulations for geothermal areas located at different depths in dissimilar geological contexts.

Representative results and wavefield examples (Annex III):

The paper analyzes the velocity curves versus temperature in function of the different Arrhenius parameters and physical conditions. Here we introduce a new definition of melting point at depth based on seismic velocity melting-rate curve versus temperature. As discussed in the full-paper, the characteristic points for P- and S-velocity curves are different (Figure 16). An estimation of the melting depth is obtained when the melting-point curve intersect the temperature gradient, as in Figure 17 for selected parameters and signal frequency 10Hz (Poletto et al., 2019).

In the same work, we calculate synthetic full waveforms focusing on the superhot geothermal field of Los Humeros, the largest active caldera located in the northernmost part of the eastern sector of the Trans-Mexican volcanic belt (Carrasco-Núñez et al., 2017).

This is one of the two field sites studied by the joint European-Mexican GEMex project (funded from the European Union's Horizon 2020 research and innovation programme under grant agreement No. 727550).

In this context, we consider two geothermal scenarios in which the seismic response is sensitive to the high temperature and pressure conditions. Figure 18 shows the geological model for a VSP synthetic experiment with the seismic source at depth (3.6 km), located at a lateral position with respect to the right chimney, to simulate a natural micro-crack, or passive SWD measurements from a source well (Poletto and Miranda, 2004).

Assuming these lithological units and isotherms, we construct the geological model. Then we simulate the wave-fields by using the rock-frame and Arrhenius properties given in Table 9.

For all the formations we assume $V_P/V_S = 2$, porosity 5 % and pure water as geothermal fluid, as an approximation. We simulate the non-melting and melting condition by changing only the Arrhenius parameters, denoted as A1 and A2, respectively, of the last two layers, and compare the results to analyse the sensitivity of the seismic response to the thermal properties. To evaluate the melting conditions we used the analysis of the case (2, 2, 2, 2) of the Annex III. For this purpose, we extend the model to a depth of 9.9 km.

The VSP is extended from the surface to 8.5 km depth (Figure 19), thus entering the zone of melting. Obviously this condition is not realistic because of the high recording depth in melting areas, but for limited hot-zone approaching by ICDP (International Continental Scientific Drilling) wells. For the numerical simulation we use the 2D Burgers-Gassmann full-waveform propagation code in poro-viscoelastic media with temperature of Carcione et al. (2017). The grid pixel size is 30 m × 30 m.

We can observe differences in the prediction signals, namely up-going wave-fields, which can be observed from shallower positions before reaching the melting zone.

The same temperature model used for the VSP experiment without and with melting in the presence of different Arrhenius values (A1) and (A2) of Table 9, respectively, is used to calculate signals recorded by a surface seismic line (Figure 20).

Conclusions (Annex III):

We have reviewed the physics to simulate seismic-wave properties and compute synthetic wave-fields in geothermal reservoirs as a function of temperature and confining pressure. The approach is based on heterogeneous poro-viscoelastic media.

In the application to hot and superhot systems, we introduce the concept of characteristic melting depth point (for selected signal frequency), based on the melting rate observed in the seismic velocity, showing that this point is different for P and S waves. The analysis is used for the estimation of melting as a function of depth, and hence with confining pressure, according to literature results in wet rocks. The analysis is then applied for full-waveform simulation in heterogeneous media, specifically in the Los Humeros superhot Mexican caldera and geothermal site.

The simulation provides an analysis tool and makes it possible to detect differences in the seismic wave-fields due to temperature effects, in surface and borehole measurements. Obviously, the repeatability conditions obtainable by synthetic data are not obtainable in nature, and the approach has to be adapted for full-waveform analysis of seismic data, with comparison and calibration of synthetic data and real measurements of deep structures.

Main results of simulation including analysis of geothermal conditions and full wavefield propagation, from full paper recently submitted to EGC 2019 (OGS) (that will be in Annex to the D5.5 Report)

Annex III: EGC Full Paper entitled 'Analysis of seismic wave propagation in geothermal reservoirs', F. Poletto, B. Farina, J. M. Carcione and G. Pinna, submission ID [#296](#) to EGC 2019.

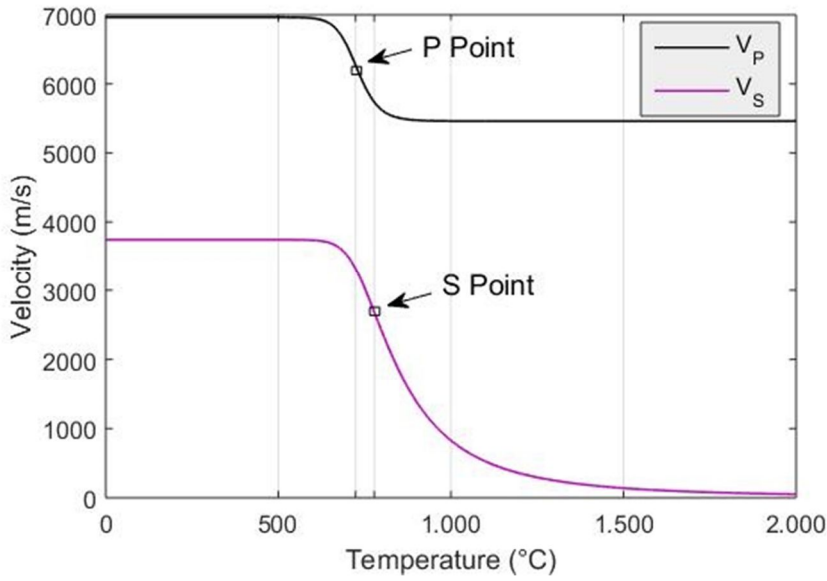


Figure 16: New definition of melting-rate point based on seismic curves (after Poletto et al., 2019).

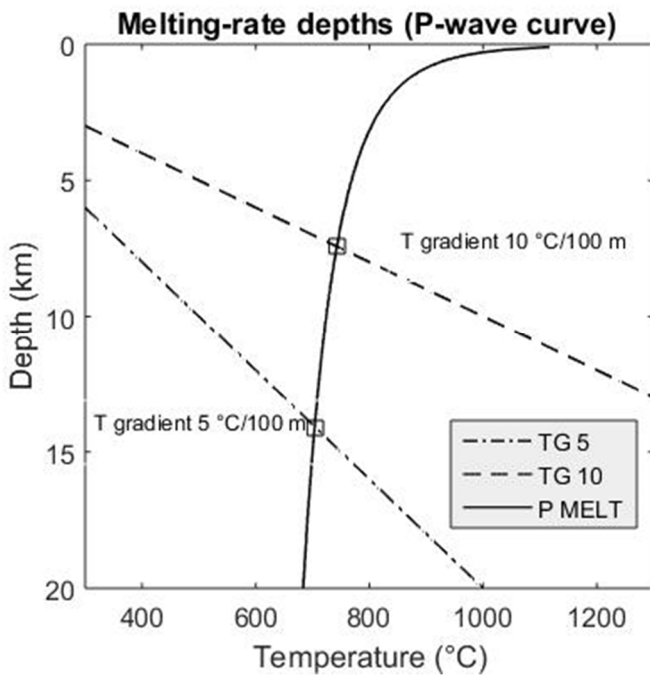


Figure 17: Estimation of melting points at depth (for selected signal frequency 10 Hz) according to the velocity-inflexion point definition (case z, 2, 2, 2 in Poletto et al. 2019).

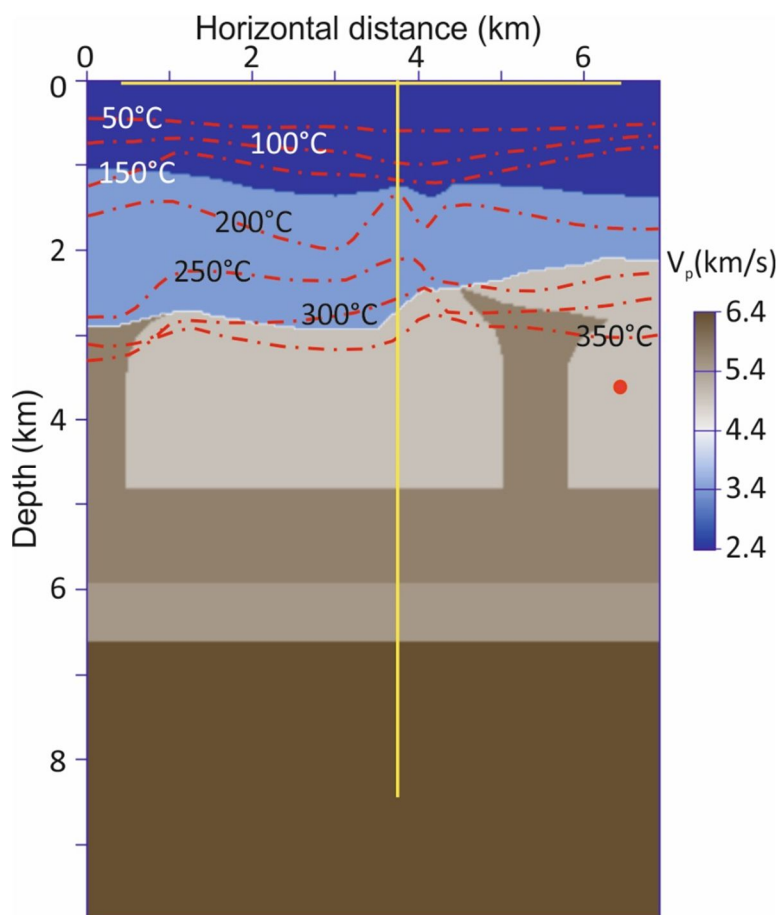


Figure 18: Input P-velocity model of the rock frame used for synthetic simulation. The yellow lines indicate the VSP and the surface profiles, the red star denotes source.

Table 9: Seismic and Arrhenius parameters used for the model of Los Humeros.

Rock Type	V_p (m/s)	ρ (g/cm ³)	References for Arrhenius parameters	A (MPa ⁻ⁿ s ⁻¹)	n	E (kJ/mol)
Tuff, Pumice, Basalt, Andesite	2400	2.140	Fernández and Ranalli (1997)	10^{-2}	1.8	151
Hornblende Andesite	3400	2.474	Ranalli (1997)	3.2×10^{-1}	2.4	293
Granite	5800	2.667	Ranalli (1997)	2×10^{-4}	1.9	137
Limestone	5000	2.600	Fernández and Ranalli (1997)	3.3×10^{-6}	2.4	134
Vesicular Andesite	5500	2.570	A1) Ranalli (1997) A2) Carcione et al. (2014)	3.3×10^{-4} 10^2	3.2 2	238 134
Basalt	6400	2.772	A1) Violay et al. (2012) A2) Carcione et al. (2014)	6.1×10^8 10^2	3.6 2	456 134

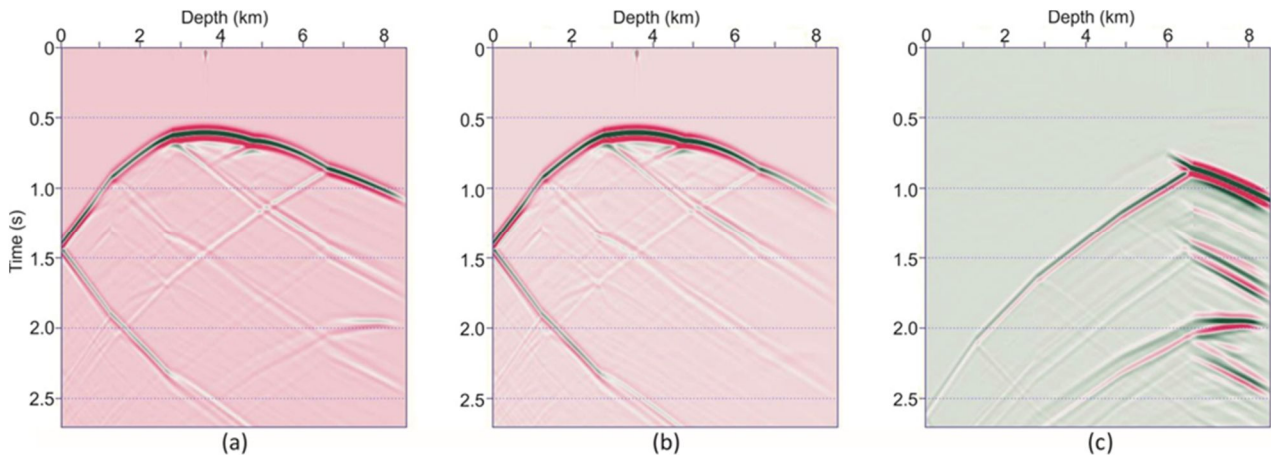


Figure 19: Modeled VSP acquired assuming a source at depth. a) In the absence of melting. b) with melting, and c) difference. We observe a clear variation of the synthetic signal in the melting zone. However also the reflection predicting the interface of the melting formation from shallower depths changes its magnitude, as shown by the upgoing events in panel (c) (Poletto et al., 2019).

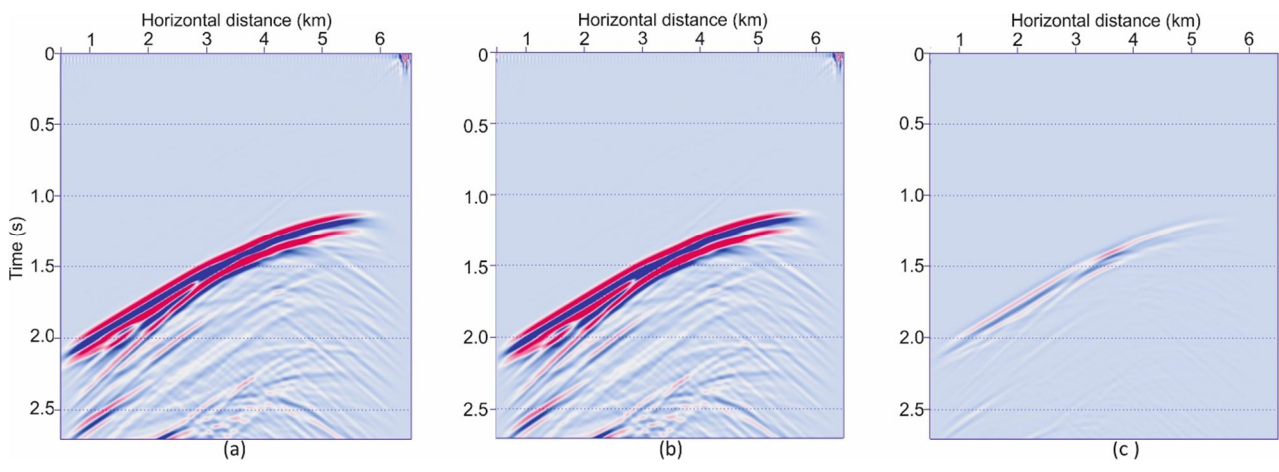


Figure 20: Signal of the surface seismic line acquired a) in the model with superhot chimney, b) in the model without superhot chimney, and c) difference of the results (a) and (b).

6.3 Poro-viscoelastic modelling of seismic wavefields including temperature, with simulation of Acoculco wavefields

6.3.1 Introduction

The Acoculco geothermal area is located in the eastern part of the Mexican volcanic belt (Canet et al., 2015). The geothermal manifestations present in this area led the Mexican Federal Electricity Company (CFE) to drill two exploration wells, 500 m apart from each other. The wells EAC-1 and EAC-2 reach a depth of 2000 m and 1900 m, respectively. The temperatures encountered in the wells are around 300 °C, their linear profiles are indicative of a conductive thermal regime (López-Hernández et al., 2009). Moreover, negligible permeability was found. This led CFE to categorise this area as a Hot Dry Rock system (Pulido et al., 2010). The two exploration wells intersected a granite intrusion at about 1600m depth.

However, the existing thermal anomaly cannot be related to such an intrusion, indicating that the magmatic source should be much deeper (Calcagno et al., 2018). Calcagno et al. (2018) proposed the Acoculco regional model with dimension of $55 \times 37 \times 6.5 \text{ km}^3$ and reaches a depth of 3 km below mean sea level. It consists of five major rock groups representing the major features of the Acoculco caldera system. These groups comprise the heterogeneous volcanic successions, the sedimentary basement built up mainly of limestones, the granite intrusion emplaced within the basement, the metamorphic contact aureole made up of marble and skarns and the overlying, very heterogeneous group of volcanites and alluvial deposits.

In the framework of WP5, in the absence of local information about the seismic properties, OGS associated seismic velocities to the lithological units proposed in the WP3 GeoModeller regional geological model, according to average seismic properties of the rocks found in literature and using an average V_p/V_s ratio of 1.783 derived from log data available for a section of well EAC2.

Farina et al. (2019) analysed the seismic properties of the Acoculco region as function of temperature and pressure calculated considering a conductive heat-transport mechanism. They used a simplified 1D seismic velocities and density model evaluating the possible presence of melted material in depth.

We use the Burgers-Gassmann mechanical model and the poro-viscoelastic code which include temperature and pressure conditions, to simulate full-waveform 2D seismic propagation. The 2D model is extracted from the 3D regional model proposed by WP3 (Calcagno et al., 2018) and we assume pure water as geothermal fluid.

6.3.2 Lithological and seismic model

Figure 21 shows the 2D model, a West-East section extracted from the 3D regional model till a depth of 6 km below the top of the wells and centred on the proposed magma chambers originating the different volcanic events (Calcagno et al., 2018). To simulate the wave propagation, we use the provisional seismic velocities proposed by OGS, we estimate the density from literature and we used the porosity values used by WP6 for the parametrization of the regional model units. For the basement we use the porosity average value proposed for Acoculco by Pan et al. (2016).

The lithological units, the seismic properties, the porosity and thermodynamic parameters used to construct the model through which simulate the wave propagation, are summarized in Table 10.

As a first approximation we consider 1D temperature and pressure profiles (Figure 21 and Figure 22). To calculate the temperature in the Acoculco field, we start from the temperature profile of well EAC1 (Pulido et al., 2010), we extrapolate in depth considering the average temperature gradient of 156 °C/km, the one needed to reach the bottom-hole temperature (Farina et al., 2019, Figure 22). To calculate the pore pressure, we start the pressure profile of well EAC1, which is in agreement with that of a hydrostatic column of water (Viggiano-Guerra et al., 2011) and we extrapolated in depth calculating the pressure corresponding to a hydrostatic column of water (Farina et al., 2019, Figure 22). Using the temperature and pore pressure profiles, we calculate the density and bulk modulus of the geothermal fluid.

The model has been discretized with 770 and 210 pixel in the horizontal and vertical direction, respectively, with pixel size of 30m, the compressional velocity model is shown in Figure 23 with the position of the sources and the vertical receiver line, and with temperature in Figure 24.

The seismic source is a Ricker wavelet of 10 Hz pick frequency.

6.3.3 Thermodynamic parameters

We study the thermodynamic parameter of Acoculco considering two different scenarios: without melting and with melting, in the presence of the same temperature conditions. We cite Calcagno et al. (2018), "Considering the measured geothermal gradient (about 100 °C km⁻¹, López-Hernández et al., 2009; Lorenzo-Pulido et al., 2010) and assuming a continental crust mechanically controlled by the rheological behaviour of quartz, a brittle/ductile transition was interpreted to occur at 4 to 4.5 km below ground level for both sites."

As discussed in ANNEX II (Farina et al., 2019), the seismic velocities of the medium, which melts at about 700°C, start decreasing at about 4 km depth, where we could expect the presence of the BDT. The effects on the quality factors start at a shallower depth. Recently, Calcagno et al. (2018) estimated the thermal gradient in the Acoculco area and the depth of the BDT zone at about 4 km depth below ground level. In this case, seismic measurements could in principle confirm this estimation.

For the Arrhenius thermodynamic parameters of the first four units, we considered average values reported for crustal rocks from Ranalli (1997) and Fernández and Ranalli (1997) for the units U1-U3, the value reported for the glassy free basalt by Violay et al. (2012) for the basement. For the unit U4, which represents the crust involved in thermal anomalies, we consider two sets of Arrhenius parameters, AC1 characteristic of the upper crust (Fernández and Ranalli, 1997) and AC2 (Carcione et al., 2014) which characterize a rock that melts at temperature around 700 °C (Table 10).

6.3.4 Poro-viscoelastic simulation with temperature and benchmarking examples

Figures from Figure 25 to Figure 30 show synthetic simulations of the ideal VSP profiles entering the formations with and without melting conditions in the presence of the assumed temperature profile. This represents a case study as an initial investigation of the behaviour of the wavefields. The use of the simulation approach will be then adapted to realistic acquisition conditions (after collecting more information on the investigated site), using active VSP geometry (direct geometry by surface sources and receivers at depth), passive or cross-well cases (with active or passive sources at depth), or reverse VSP (RVSP) geometry, such as by drill bit source (Poletto and Miranda, 2004) in which also melting zones can be approached.

In this initial phase of the study of this site, we compare also benchmarking results (from Figure 25a to Figure 27a) obtained by 2D conventional elastic modelling (as described in Section 4.1.2), to verify the trends in the calculated poro-viscoelastic wavefields including temperature at the approximation in which temperature effects are not relevant. The benchmarking confirms the consistency of the full-waveform poro-viscoelastic simulation.

The differences between poro-viscoelastic results obtained without and with melting (from Figure 28c to Figure 30c) show that changes in the seismic wavefields are observable in an area and at a depth where there are no geological and rock variations.

Effects in successive snapshots with and without melting

The effects related to variation in melting properties in high temperature zones at depth are clearly observed in seismic wavefields snapshots, calculated with signals generated by the 10-Hz source and recorded in the 2D space model at different propagation times. The snapshot examples without and with melting are shown in figures from Figure 31 to Figure 33.

Simulation of surface shots

In the following examples we simulate wavefields recorded at the surface, to study possible variations related to different melting conditions in two-way-time seismic reflection data. In Figure 34a and Figure 34b we show preliminary examples of simulation of shots recorded with a seismic line at the surface and different geothermal parameters for the models without and with melting, respectively. Panels (a), (b) and (c) in Figure 35 show the same signals of Figure 34 in the models without and with melting, and their difference, respectively. In the difference panel (c) we can interpret variations at larger seismic times. According to the VSP and snap-shot results, these effects related to deep formations are possibly observable at high recording times.

Table 10: Seismic and thermodynamic parameters used to model the West-East section represented in Figure 21.

Lithological Units	V_P (km/s)	V_S (km/s)	ρ (g/cm ³)	Φ (%)	A (MPa) ⁻ⁿ s ⁻¹	n	E (kJ/mol)
U1: Volcanics	3.0	1.68	2.3	11.2	10^{-2}	1.8	151
U2: Limestones	4.8	2.7	2.6	1.17	3.3×10^{-6}	2.4	134
U3: Skarns	6.05	3.4	2.8	1.22	3.3×10^{-4}	3.2	238
U4: Granites	5.8	3.25	2.7	2	AC1) 2×10^{-4} AC2) 10^2	1.9 2	137 134
U5: Basement	6.4	3.6	2.9	6	6.1×10^8	3.6	456

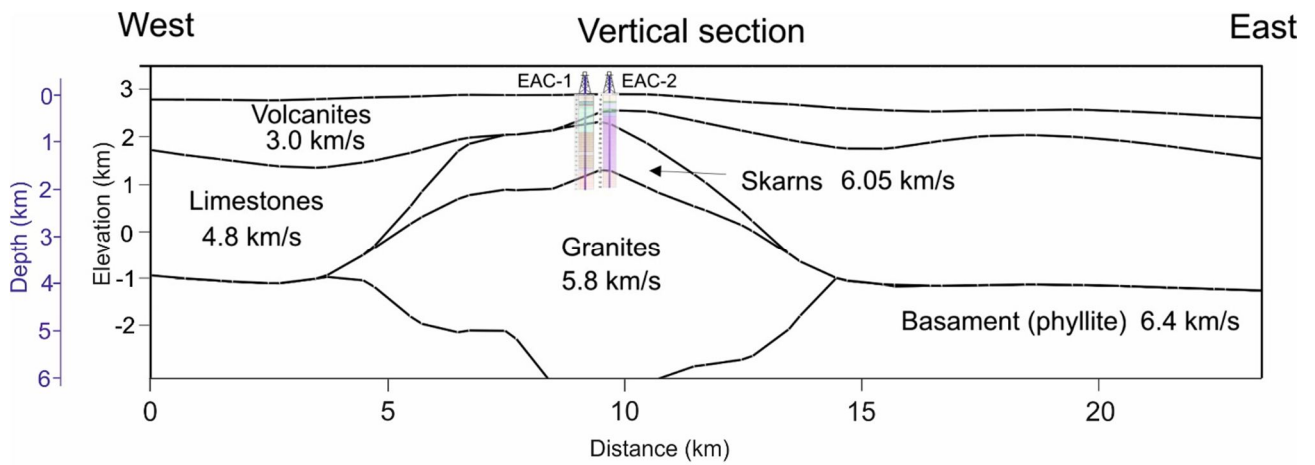


Figure 21: 2D section of Acoculco extracted from the GeoModeller 3D regional model, with geological interpretation and estimated provisional-initial seismic P-velocity. The depth, calculated with respect the top of the wells is reported in blue on the left side of the model. The lithologies of EAC1 and EAC2 wells are superimposed.

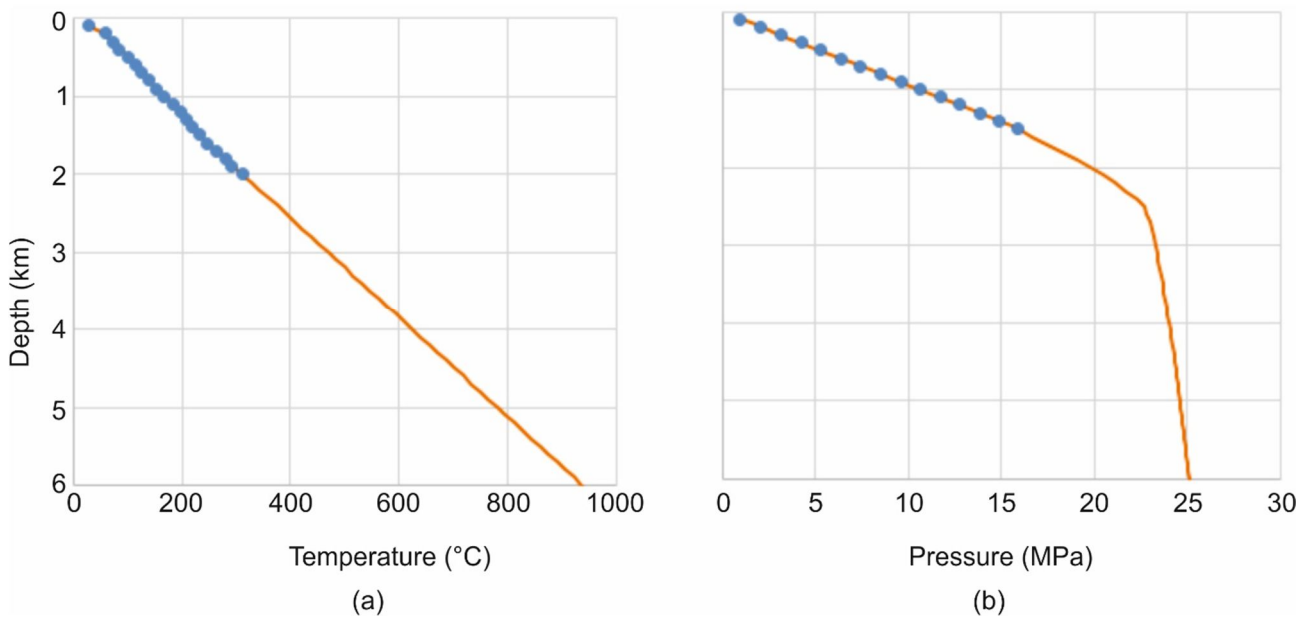


Figure 22 Models used for the Acoculco initial simulation (calculated using the local scheme of Figure 8). Two different Arrhenius parameters are used in the simulation.

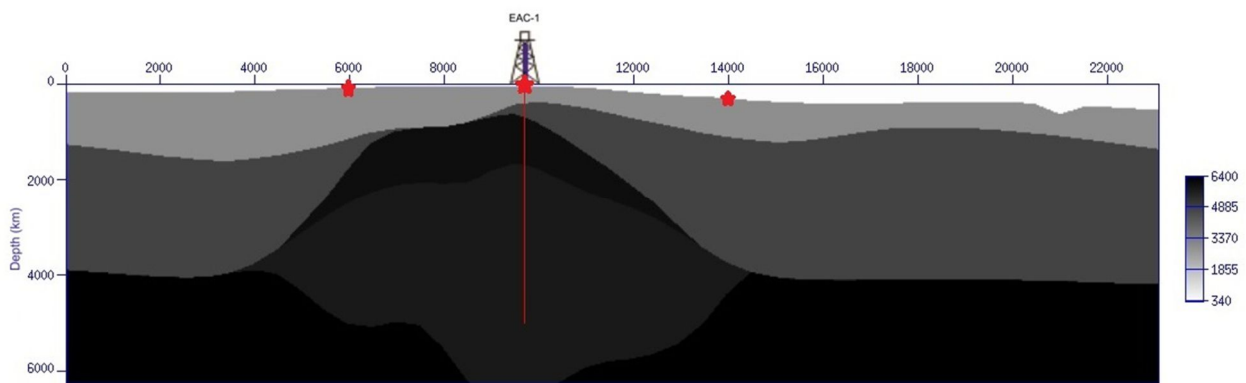


Figure 23: Compressional velocity model of Acoculco used to simulate the wave propagation. The red line represents the position of a vertical recording line, below well EAC1. The red stars represent the position of three surficial sources.

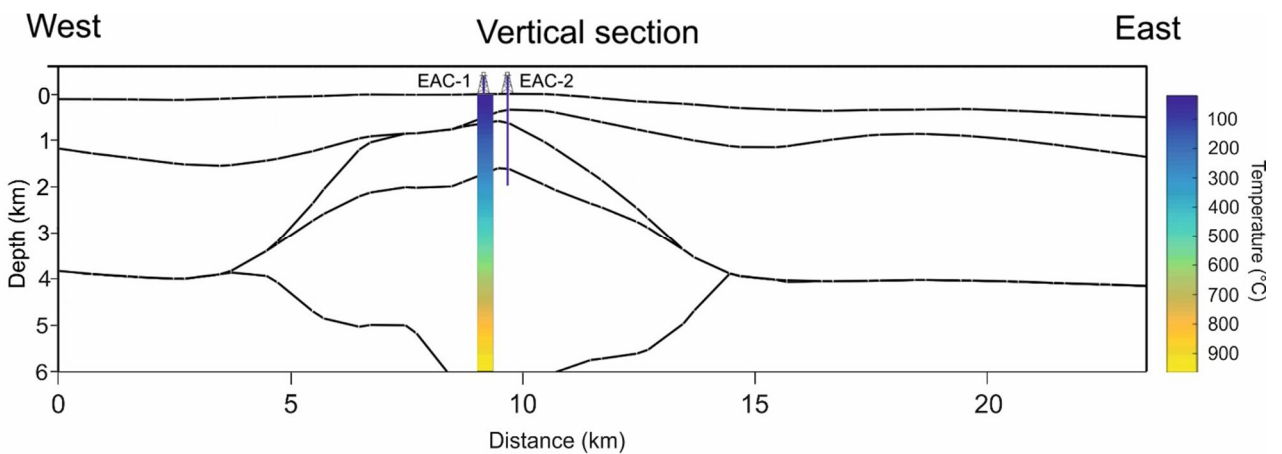


Figure 24: Acoculco section with the 1D temperature profile (see Figure 22) superimposed.

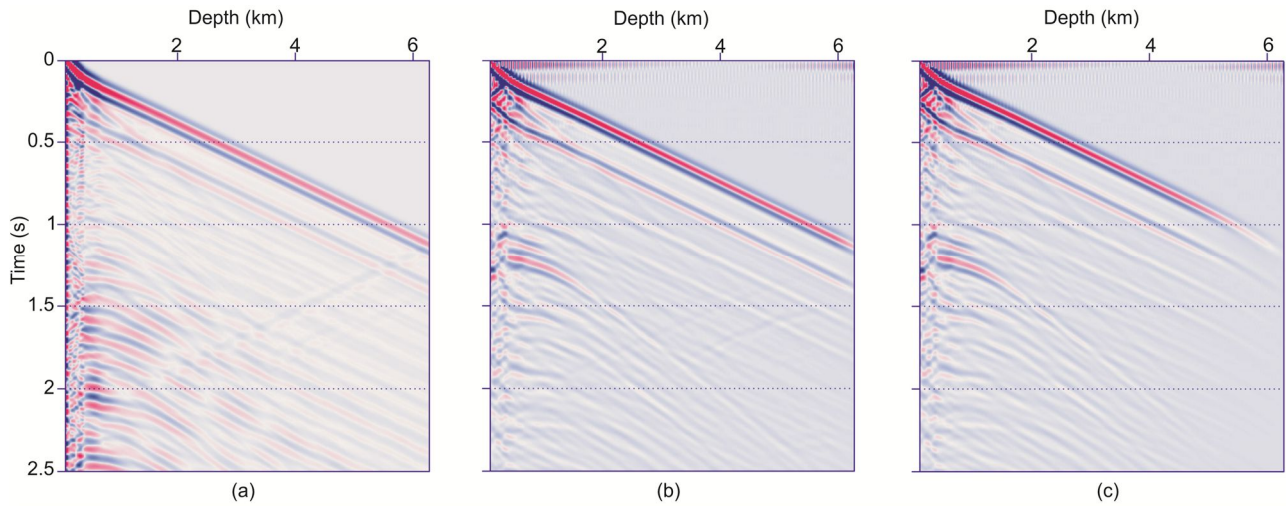


Figure 25: Zero-offset VSP (vertical Z receiver component) acquired with the source at the position of well EAC1. a) Benchmarking elastic model. Poro-viscoelastic model including temperature obtained when the lithological unit U4 (Table 10) is characterized: b) by Arrhenius set AC1 (no melting); c) by Arrhenius set AC2. In (c) the melting effects appears at about 4.5 km depth (from well ground level), where the temperature exceeds 700 °C and the profile enters the transition from the brittle to ductile rock behaviour. Note in Figure 24 that this zone is not characterized by geological changes, but only by temperature variations.

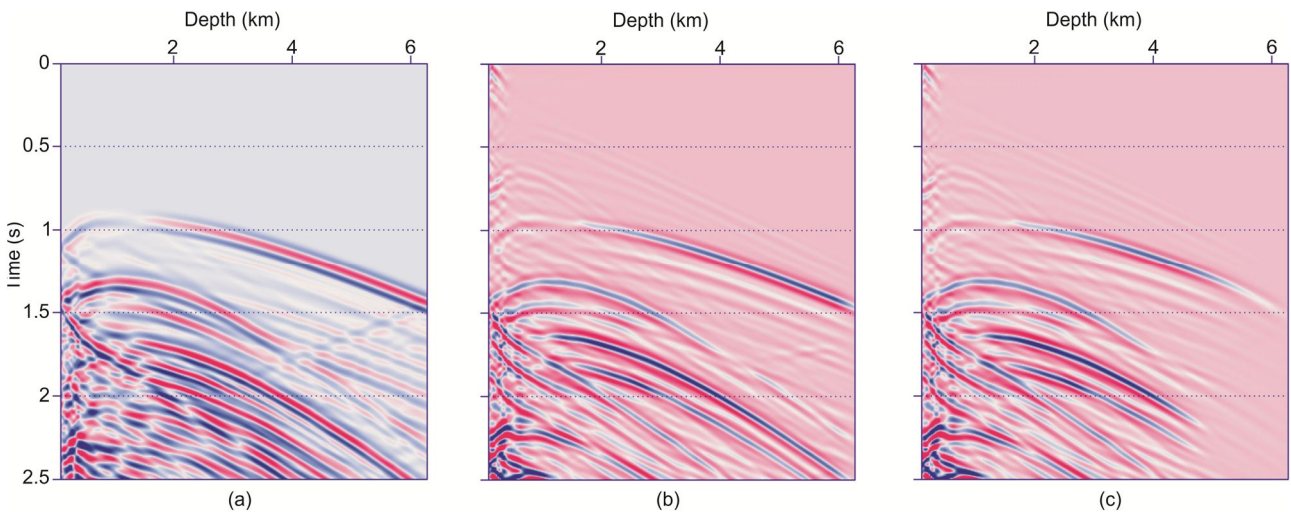


Figure 26: Offset VSP (vertical Z receiver component) acquired with the source at 4000 m lateral position from EAC1 well head. a) Shows the benchmarking elastic model. B) and c) show the poro-viscoelastic models including temperature obtained when the lithological unit U4 (Table 10) is characterized: b) by Arrhenius set AC1 (no melting); c) by Arrhenius set AC2. In (c) the melting effects appears at about 4.5 km depth (from well ground level), where the temperature exceeds 700 °C and the profile enters the transition from the brittle to ductile rock behaviour. Note in Figure 24 that this zone is not characterized by geological changes, but only by temperature variations.

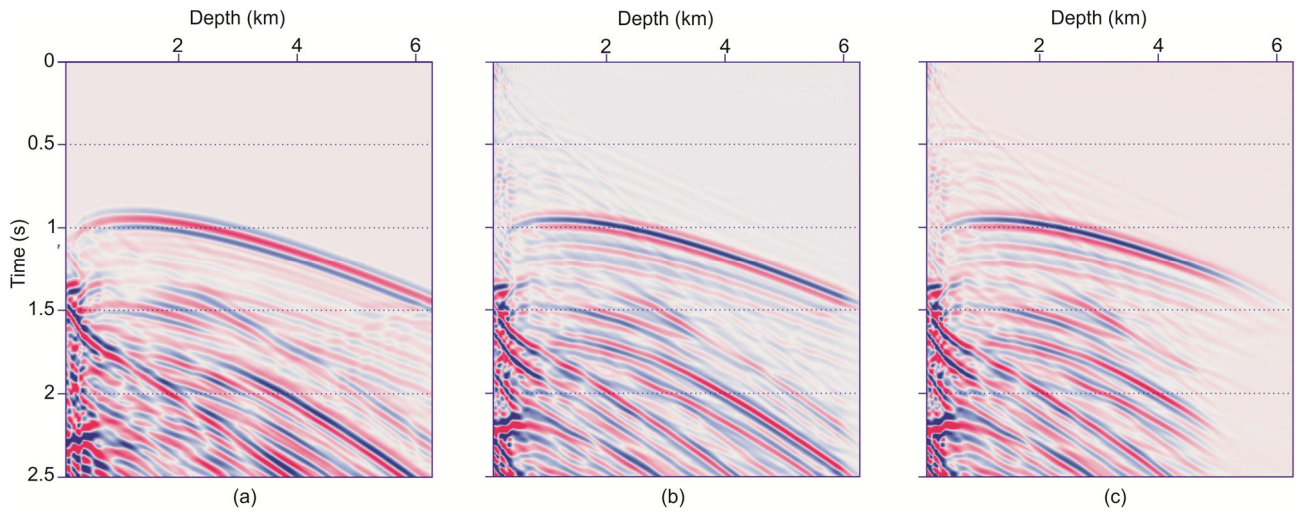


Figure 27: Offset VSP (horizontal X receiver component) acquired with the source at 4000 m lateral position from EAC1 well head. a) Shows the benchmarking elastic model. B) and c) show the poro-viscoelastic models including temperature obtained when the lithological unit U4 (Table 10) is characterized: b) by Arrhenius set AC1 (no melting); c) by Arrhenius set AC2. In (c) the melting effects appears at about 4.5 km depth (from well ground level), where the temperature exceeds 700 °C and the profile enters the transition from the brittle to ductile rock behaviour. Note in Figure 24 that this zone is not characterized by geological changes, but only by temperature variations.

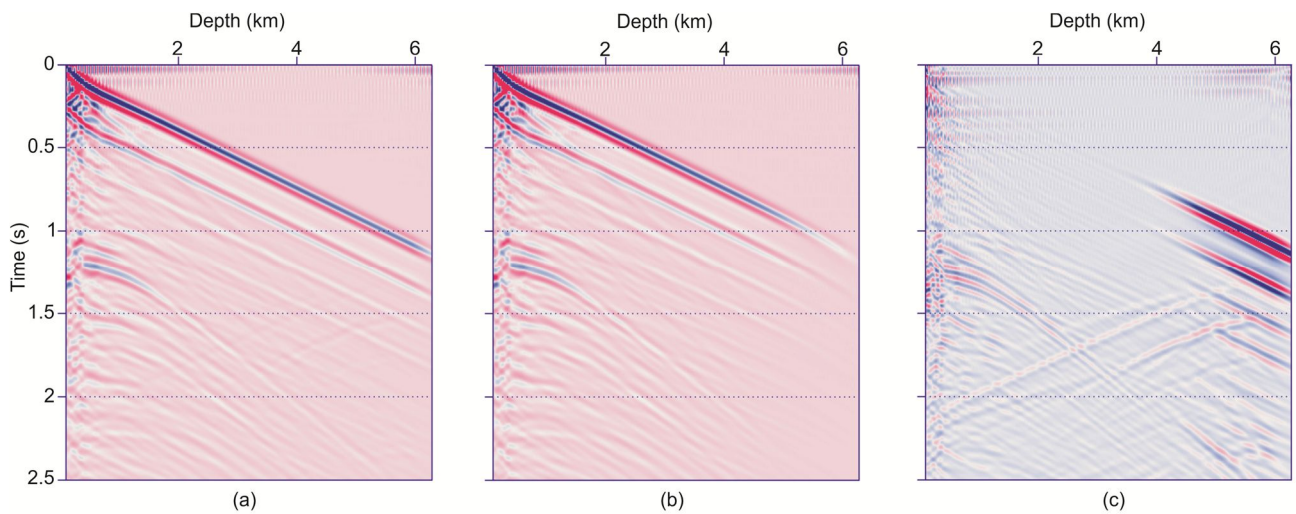


Figure 28: Zero-offset VSP (vertical Z receiver component) acquired with the source at the position of well EAC1. Poro-viscoelastic model including temperature, obtained when the lithological unit U4 (Table 10) is characterized: a) by the Arrhenius set AC1 (no melting); b) by Arrhenius set AC2 with melting effects at large depths. c) Difference between the signals in (a) and (b).

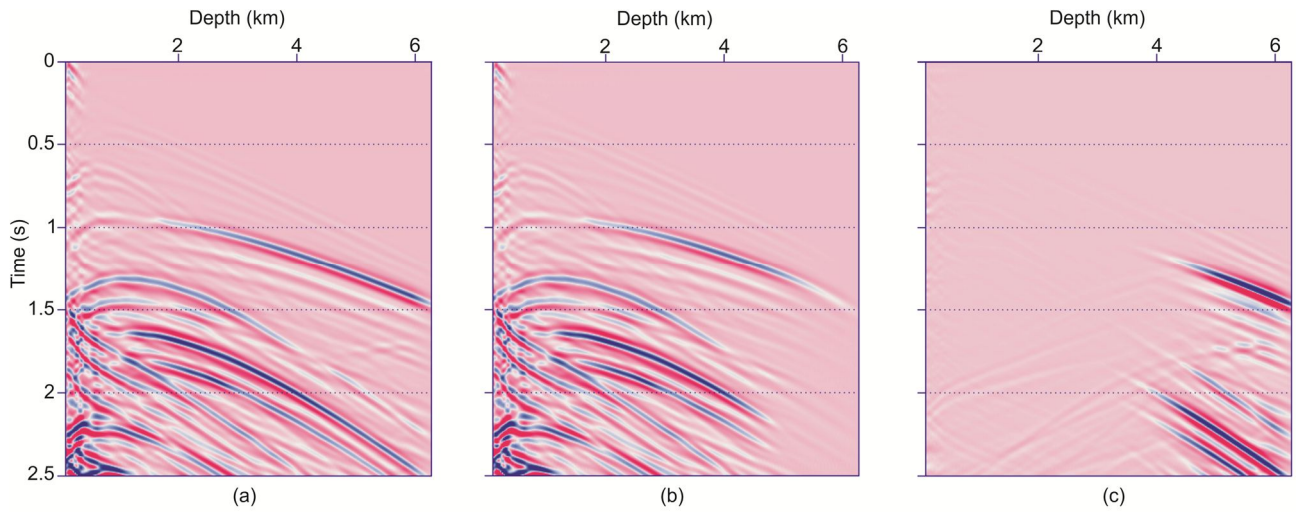


Figure 29: Offset VSP (vertical Z receiver component) acquired with the source at lateral position 4000 m from well EAC1. Poro-viscoelastic model including temperature, obtained when the lithological unit U4 (Table 10) is characterized: a) by the Arrhenius set AC1 (no melting); b) by Arrhenius set AC2 with melting effects at large depths. c) Difference between the signals in (a) and (b).

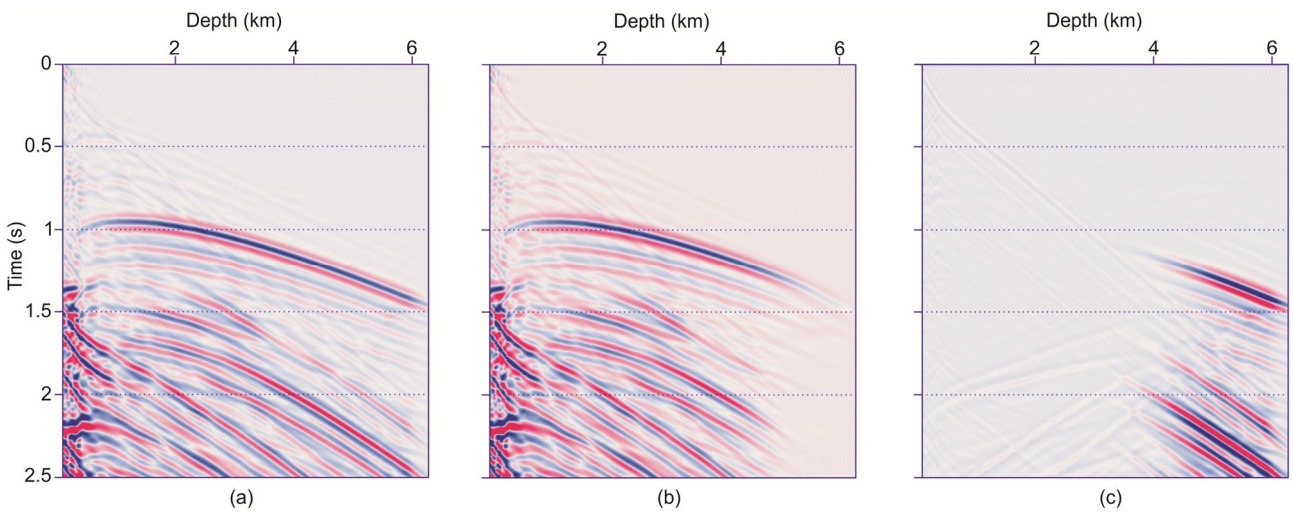


Figure 30: Offset VSP (horizontal X receiver component) acquired with the source at lateral position 4000 m from well EAC1. Poro-viscoelastic model including temperature, obtained when the lithological unit U4 (Table 10) is characterized: a) by the Arrhenius set AC1 (no melting); b) by Arrhenius set AC2 with melting effects at large depths. c) Difference between the signals in (a) and (b).

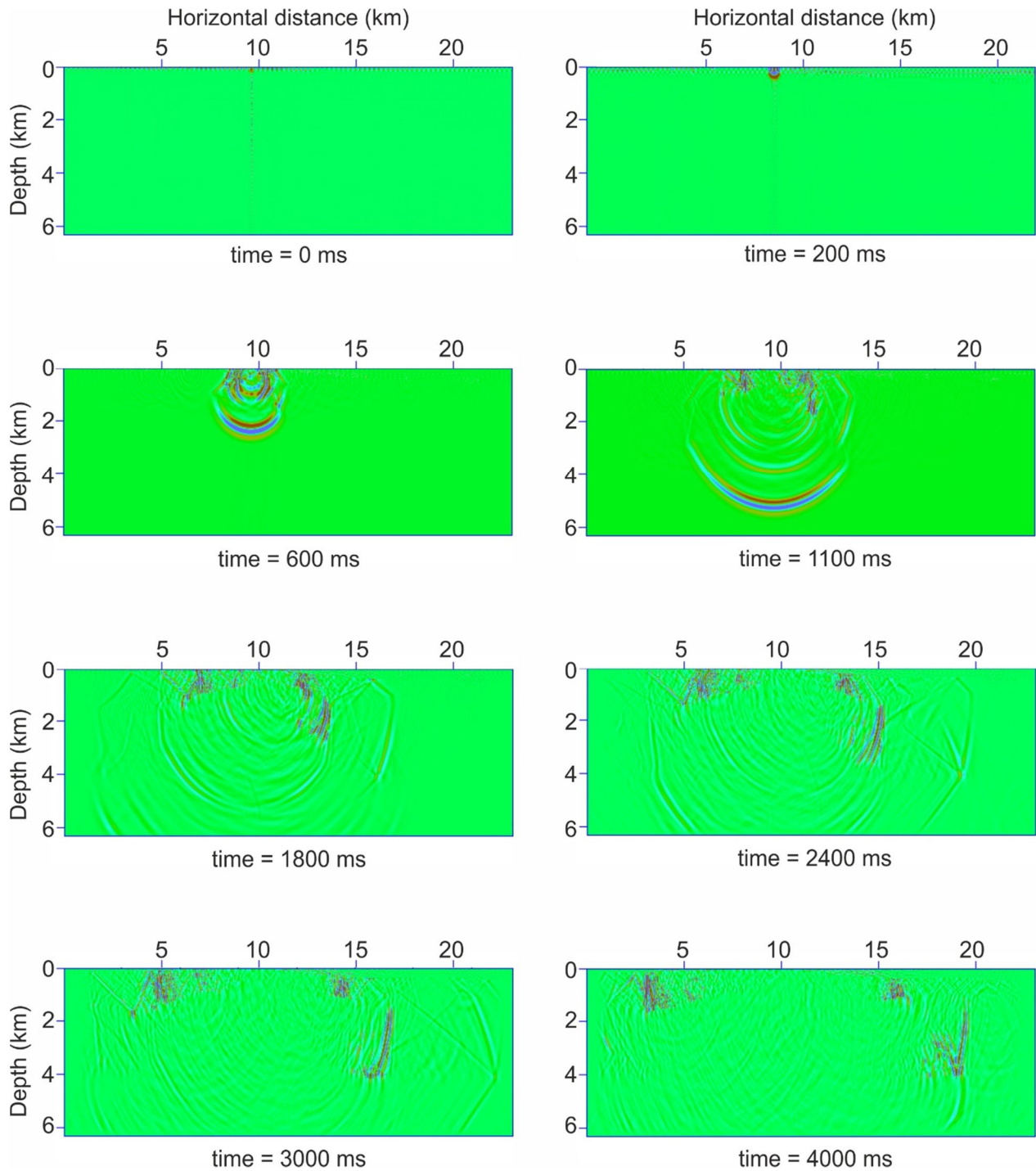


Figure 31: Successive snapshots of the amplitude of the 2D wavefield (vertical particle velocity component) propagating in the model using Arrhenius set AC1 for unit U4. With these thermal properties melting is not expected in the model zone.

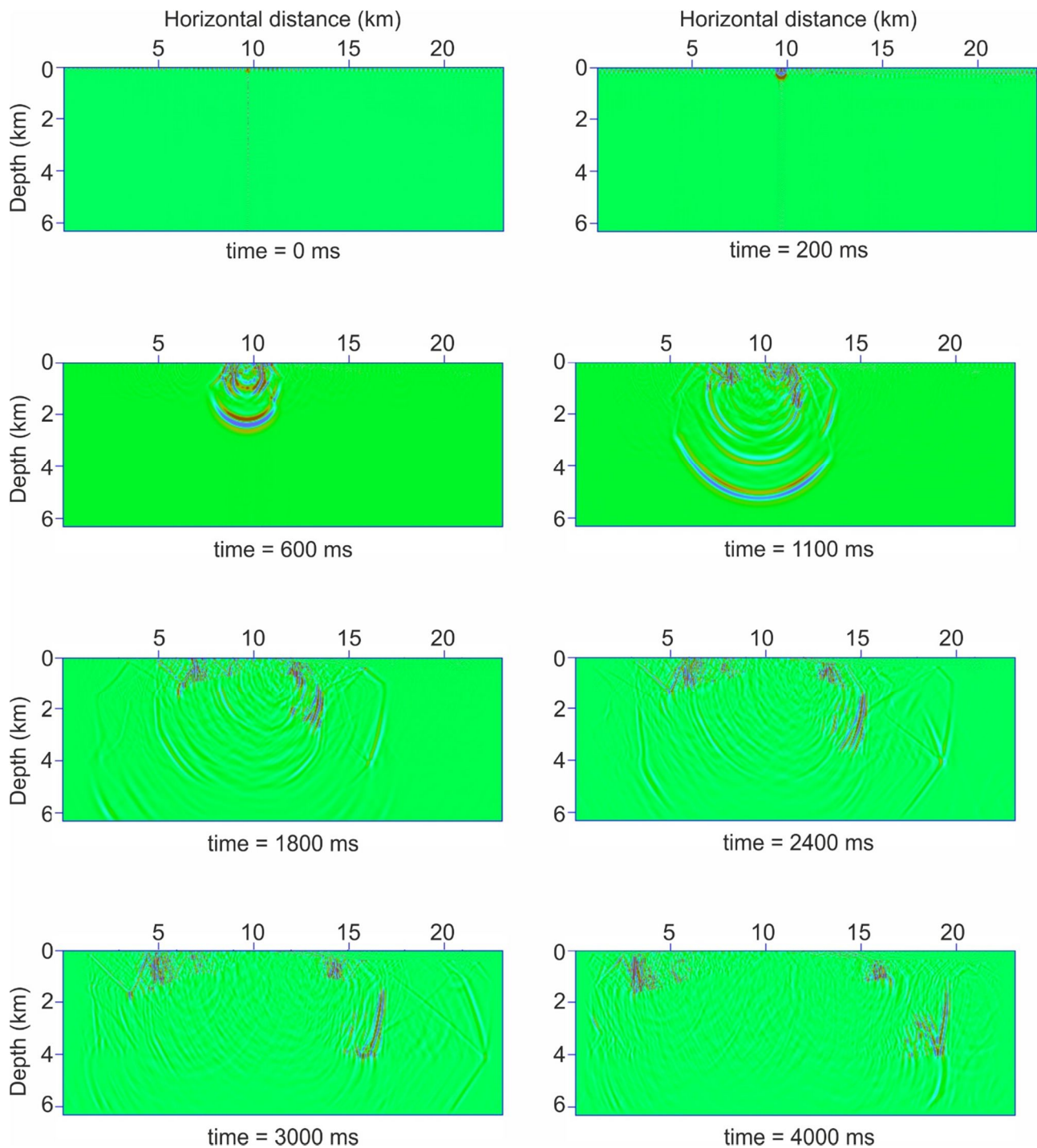


Figure 32: Successive snapshots of the amplitude of the 2D wavefield (vertical particle velocity component) propagating in the model using Arrhenius set AC2 for unit U4. With these thermal properties melting occurs in the deeper model zone, and some differences can be interpreted with respect to Figure 31. These effects can be observed in the plot of the differences in Figure 33.

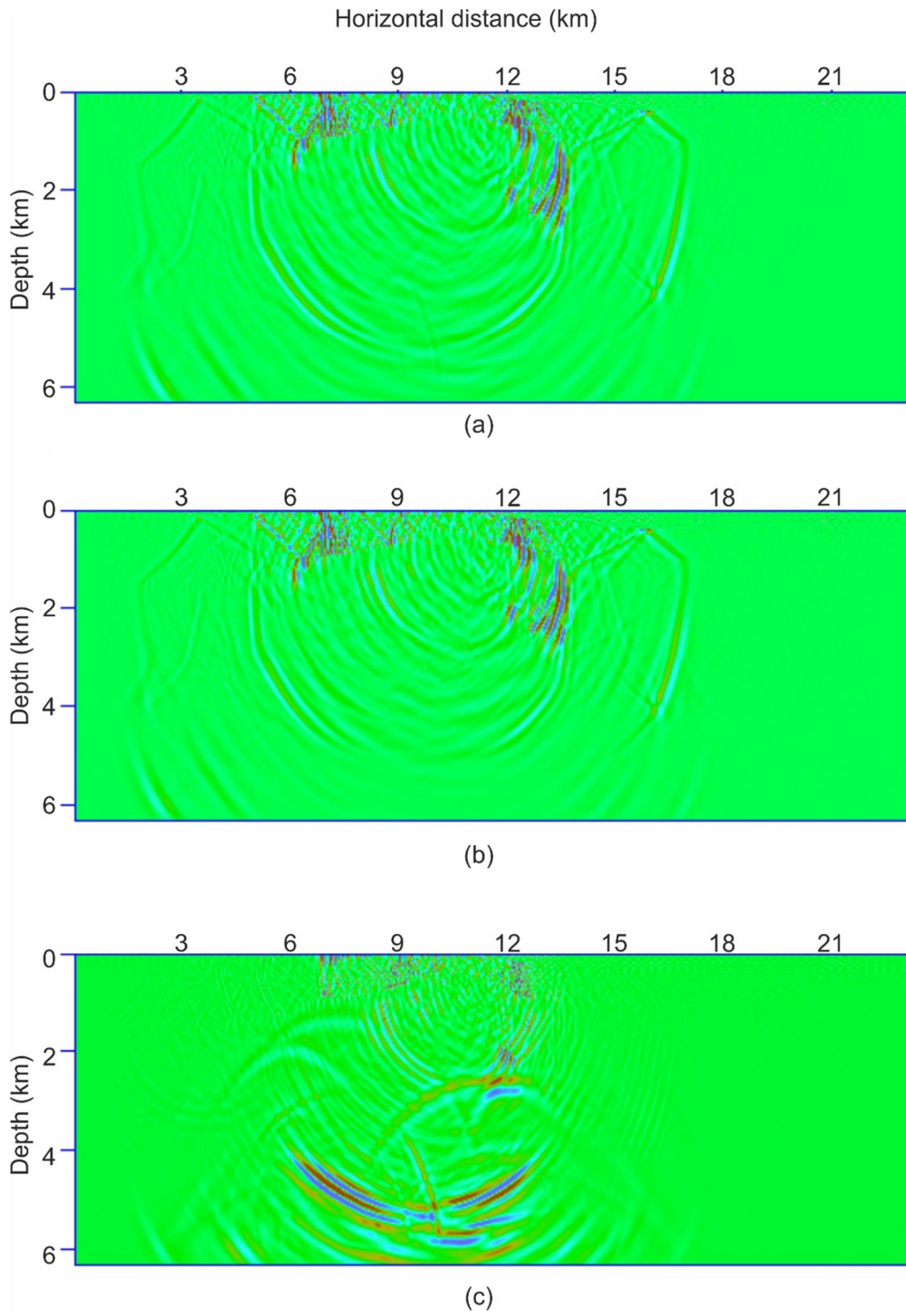


Figure 33: Snapshot at 1.8 s of the amplitude of the 2D wavefield (vertical particle velocity component) propagating in the model using for unit U4 Arrhenius set AC1 (a), AC2 (b) and their difference (c).

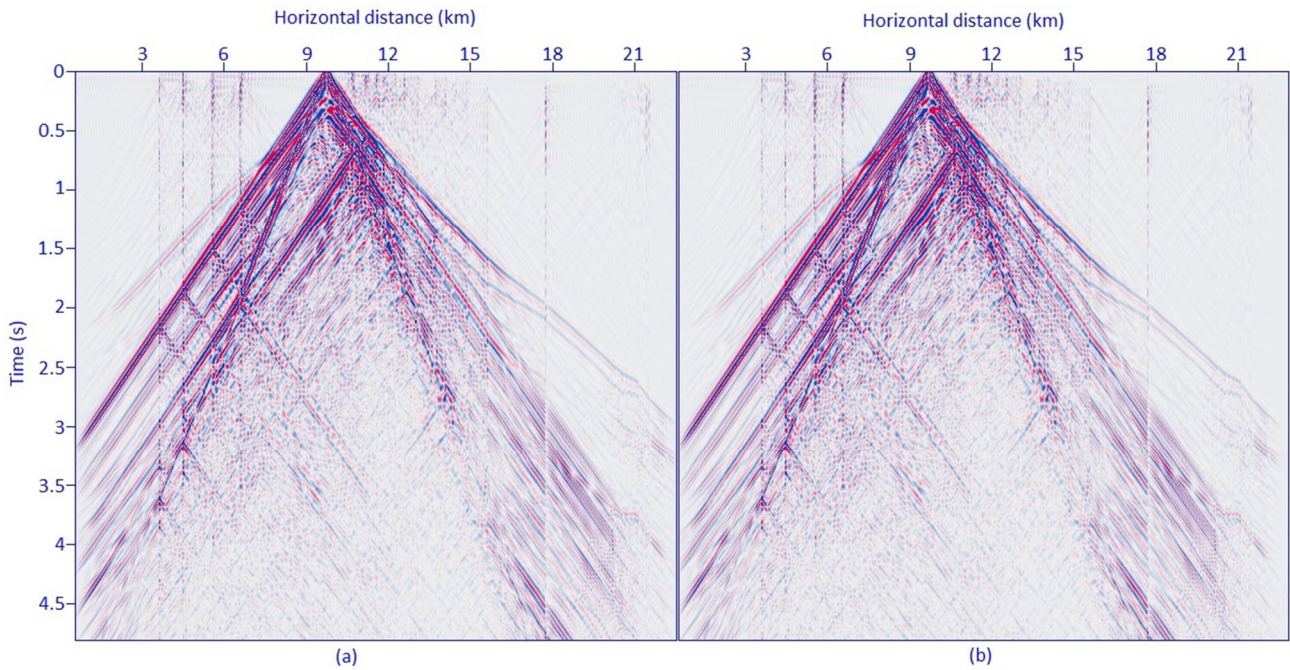


Figure 34: Simulation of signals acquired by a surface seismic line of vertical receivers and the source at the position of well EAC1. Poro-viscoelastic model including temperature, obtained when the lithological unit U4 (Table 10) is characterized: a) by the Arrhenius set AC1 (no melting); b) by Arrhenius set AC2 with melting effects at large depths and recording times.

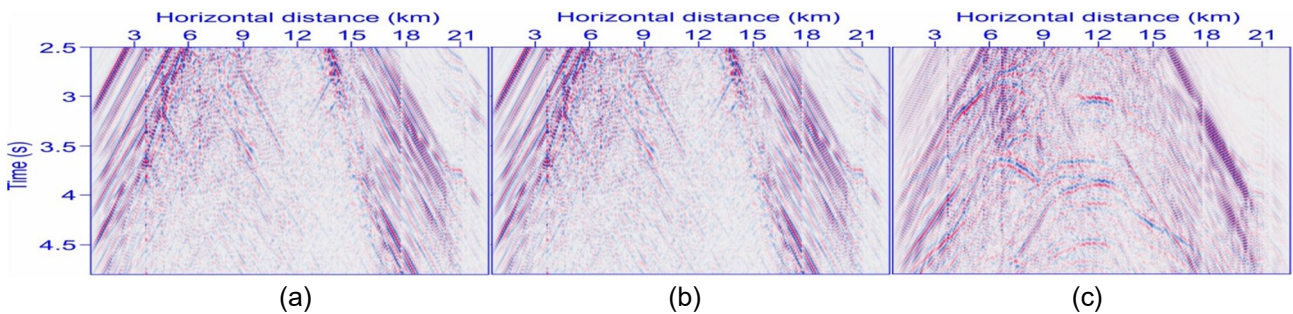


Figure 35: Detail of Figure 34. Simulation of signals acquired by a surface seismic line of vertical receivers acquired with the source at the position of well EAC1. Poro-viscoelastic model including temperature, obtained when the lithological unit U4 (Table 10) is characterized: a) by the Arrhenius set AC1 (no melting); b) by Arrhenius set AC2 with melting effects at large depths. c) Difference between the signals in (a) and (b). The panel (c) is normalized to evidence low amplitude variations in the reflection signals.

6.3.5 Contribution P. Jousset (GFZ) to D5.5 – Benchmarking simulation

In this section we present the contribution of Philippe Jousset to benchmarking using a finite difference formulation of the wave propagation (Section 4.1.3) in the benchmark defined by Flavio Poletto et al. (OGS) to represent Acoculco geothermal field (Mexico).

We use the benchmark geological model defined by OGS. This model is defined by 5 interfaces as shown in Figure 36.

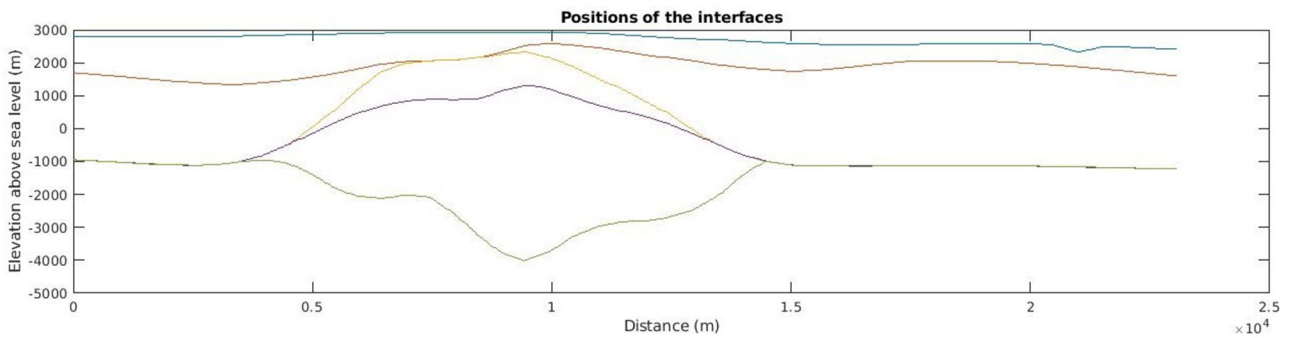


Figure 36: Interfaces created by OGS. See Figure 22 (OGS report).

The implementation of the code requires an extra domain where seismic waves will be attenuated, so that the model borders do not send back reflexions. Therefore, in order to keep the whole area of model as effectively computed, we expanded the model by 3 km on each side of the target area. Therefore the interfaces need also to be extended. We assume that their depth is the one at the border. This is shown in Figure 37 and Figure 38.

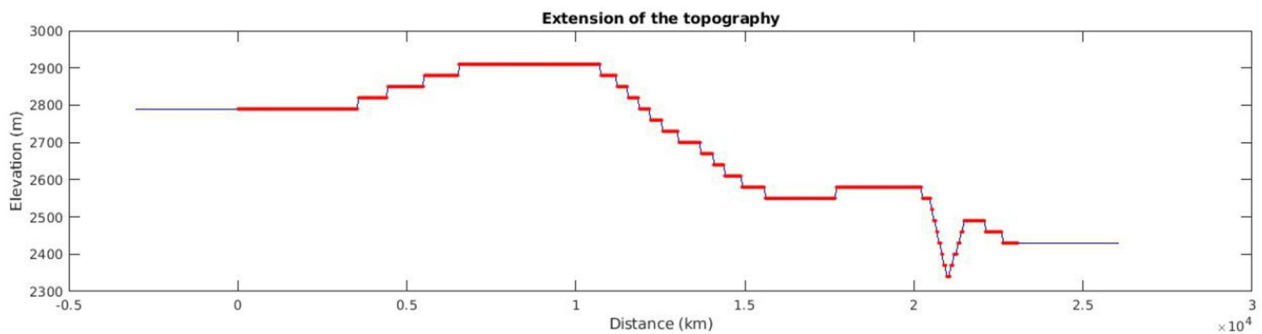


Figure 37: Extended interfaces. The initial interfaces are extended by 3 km on each side assuming a constant depth in the extended area. Illustration of this process on the topography interface. The initial interface is represented in red. The extended is represented in blue.

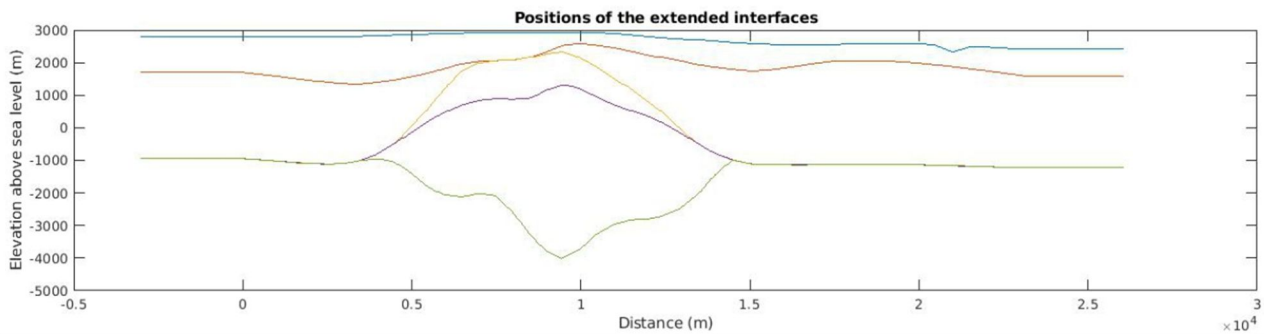


Figure 38: Extended interfaces. The initial interfaces are extended by 3 km on each side assuming a constant depth in the extended area. Illustration of this process on the topography interfaces. All interfaces are extended.

The Table 10 in Section 6.3.4 gives the values of each area in the model. Taking those values, we constructed a velocity model for V_p , V_s and the density. Figure 39 shows the initial V_p model created by OGS and the corresponding extended model by 3 km in each direction. Figure 40 shows the similar models for V_s and the density (only the extended models are shown).

There are two methods to take into account the topography. Either the surface of the topography is represented as a stair case, mapping the topography on the parametrization of the finite difference grid, or by using a linear mapping transformation, which deforms the computational grid on to the topography. In this work, the incorporation of surface topography is achieved in the code by using a linear mapping transformation (Figure 41) of the rectangular computational grid onto a curved grid (Tessmeret al., 1992).

This feature affects the whole model vertically. In order to prepare the grids for this transformation in the computation, we need to pre-deform the rectangular grid in the real world, into a linearly mapped grid in the reverse sense, so that the transformation will map the geological interfaces at their true position with respect to the topography.

Figure 42 shows this transformation in the interfaces of the model. All interfaces are deformed homotetically with respect to the topography. The topography interface is also deformed with respect to itself with the same process: it thus maps to a plane, which is then the boarder of the grid in the computation. When the transformation will be performed in the code as shown in the Figure 41, the topography will take its true position with respect to the seismic waves and so are the geological interfaces.

The velocities and density models are modified accordingly.

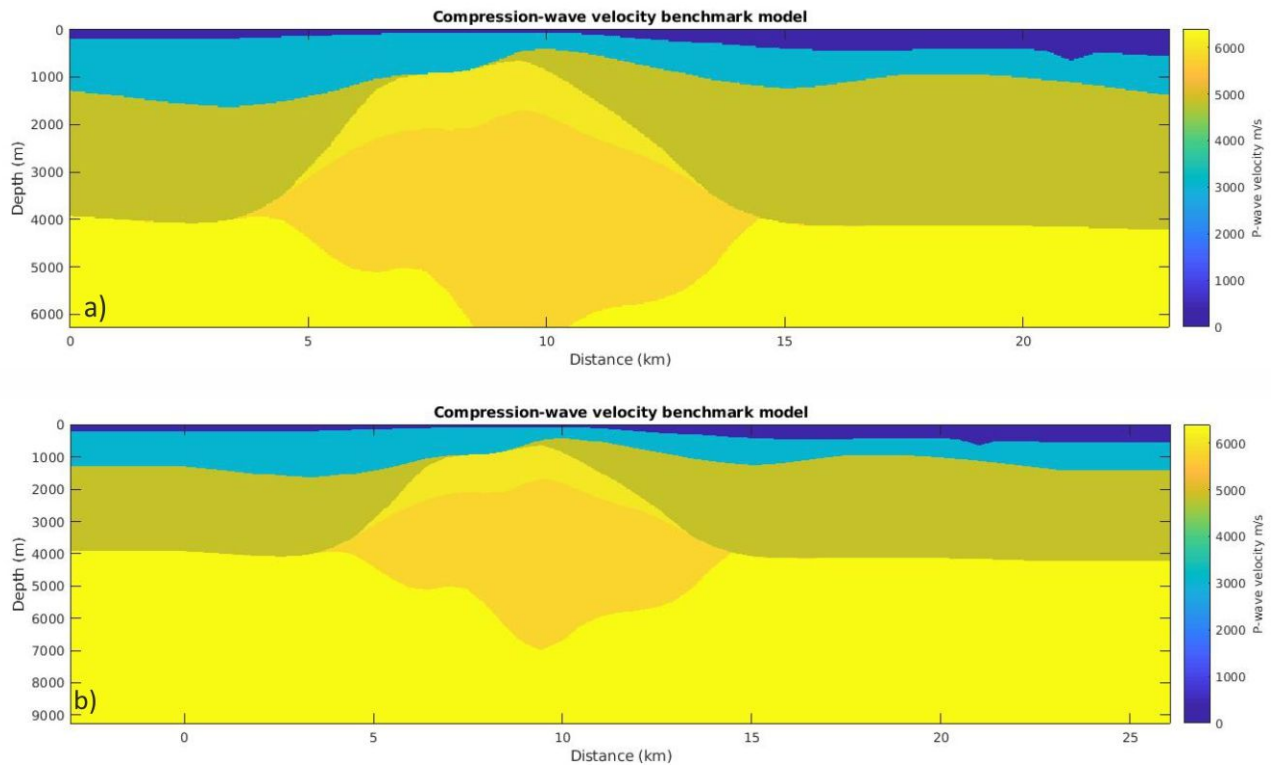


Figure 39: P-wave velocity models. a) initial model (same as in Figure 24). b) Extended model.

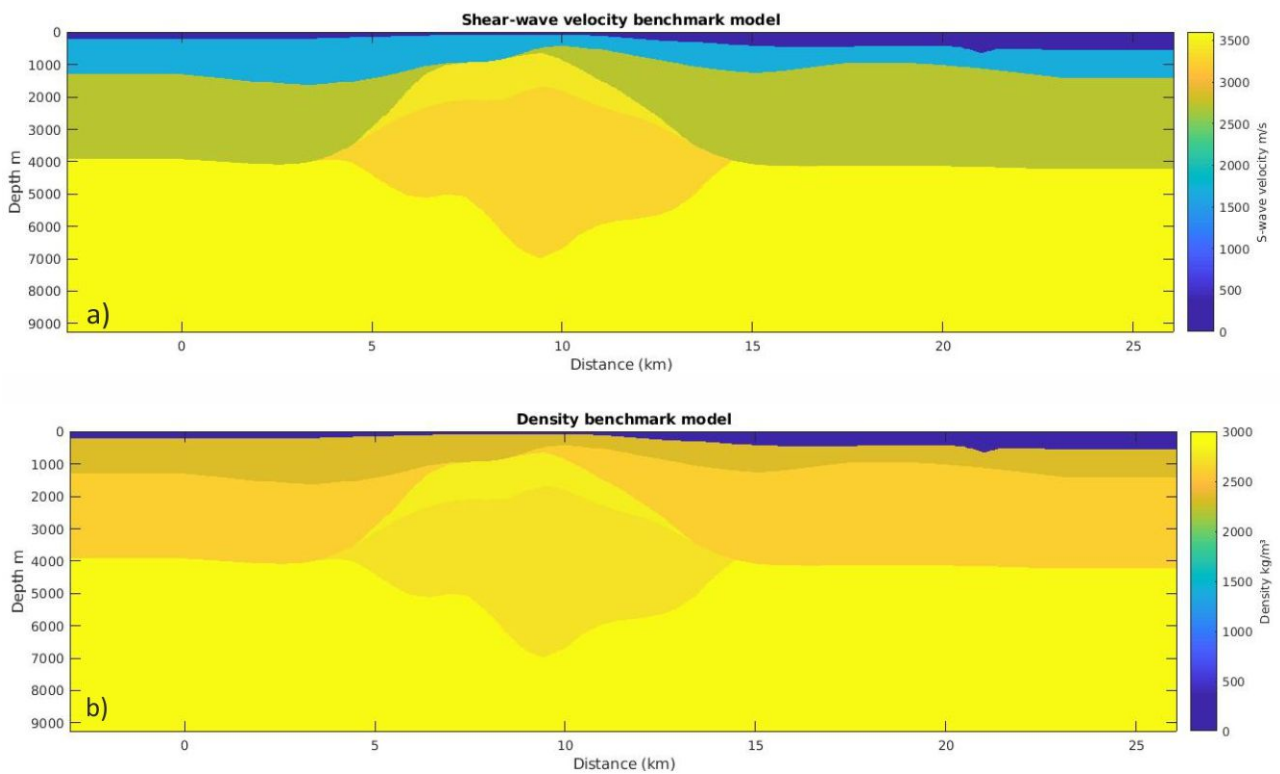


Figure 40: Extended models for a) S-wave and b) density.

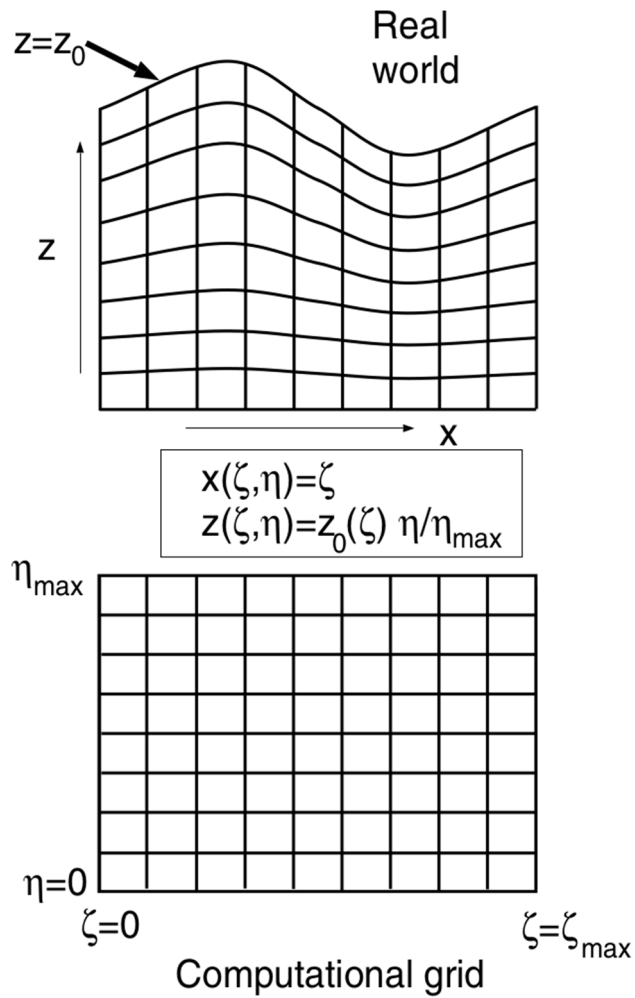


Figure 41: Curved grid in the (x, z) system and rectangular grid in the (ζ, η) system.

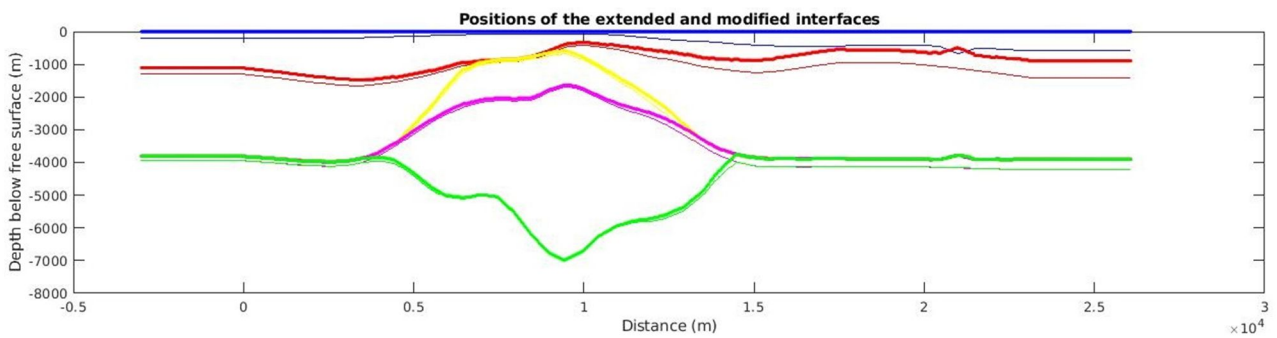


Figure 42: Stretching of the interfaces with respect to the topography. Fine lines are the original position of the interfaces, and in bold are the stretched positions. Note then the flat topography. The inverse transformation in the code will replace the interfaces at their true position and the topography will be taken into account without possible numerical instabilities due to stair case topography.

Results

In the following we assume the attenuation is constant and uniform in all media. $Q = 100$ for P-waves and $Q = 60$ for S waves.

We performed **2 experiments** using the same source locations as in the previous test by OGS. One shot at the surface as a weight drop on the ground, as for representing a VSP experiment. In our representation, as the model has 3000 m of absorbing boundary layer, the distances have 3 km shift than the ones given by OGS.

The **first source** is located at the position of the well. Figure 43 shows snapshots of the wave field propagating after the source is triggered at time 0. Snapshots reveal how the waves propagate and how they are affected by the geological model. The seismic energy tends to stay in layers of low velocities, e.g., at layers close to the surface. Compare with figures from Figure 31 to Figure 33.

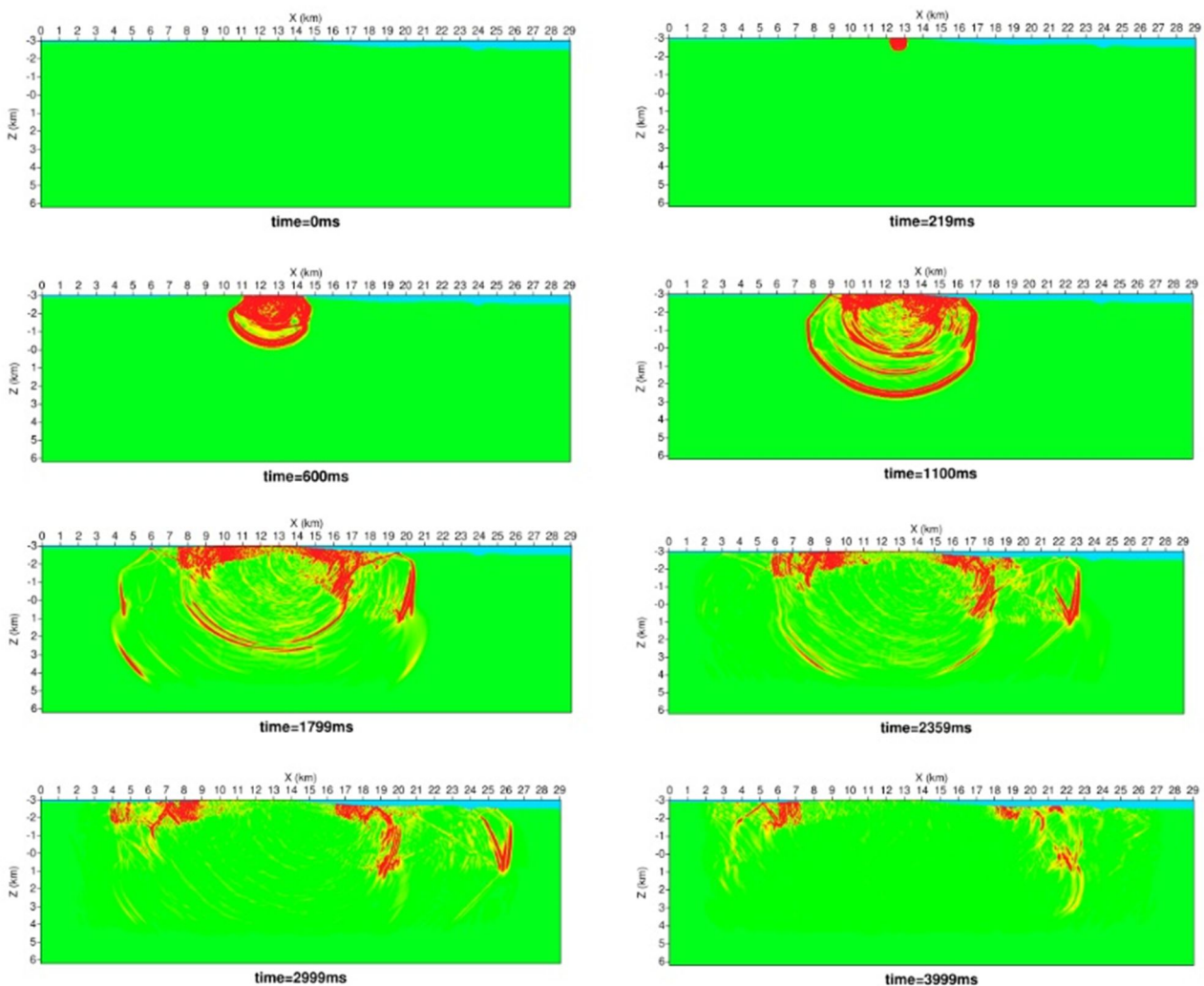


Figure 43: Successive snapshots of the amplitude of the 2D wavefield propagating in the model. Note that we can recognise the layers of the model by the wave reflections. The source appears at 12.6 km, however it is at the same location as for the OGS models there is a 3 km absorbing boundary on each side. Green color means no energy. Red color mark the locations where energy is larger.

Figure 44 shows the record at the zero VSP shot corresponding to the source set as in Figure 43. It can be compared to Figure 25 by Flavio Poletto et al. in this report. Main features can be recognised. Slight differences may be due to slight differences in the source and the implementation of the topography. In particular, surface waves are more visible and better modelled in the mapped topography as compared to the stair case topography. Figure 45 represents the records of an horizontal streamer placed at the surface of the topography.

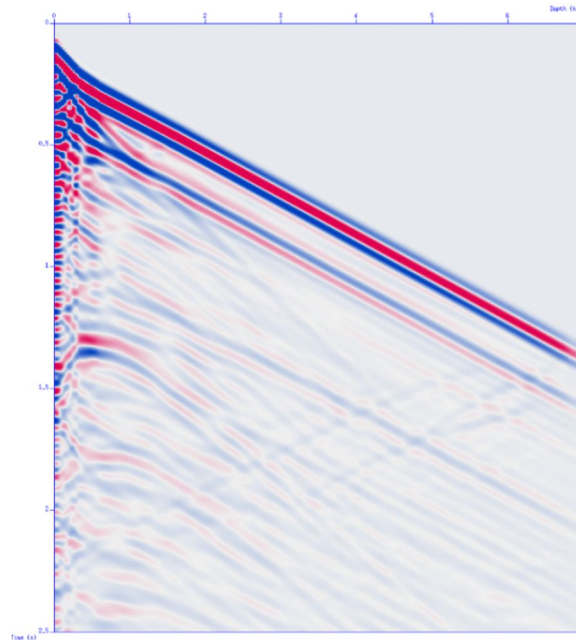


Figure 44: Zero offset VSP (vertical component) as modelled at the position of the well EAC1. The horizontal axis is depth, and ranges between 0 and 7 km. The vertical time scale ranges between 0 and 2.5 s.

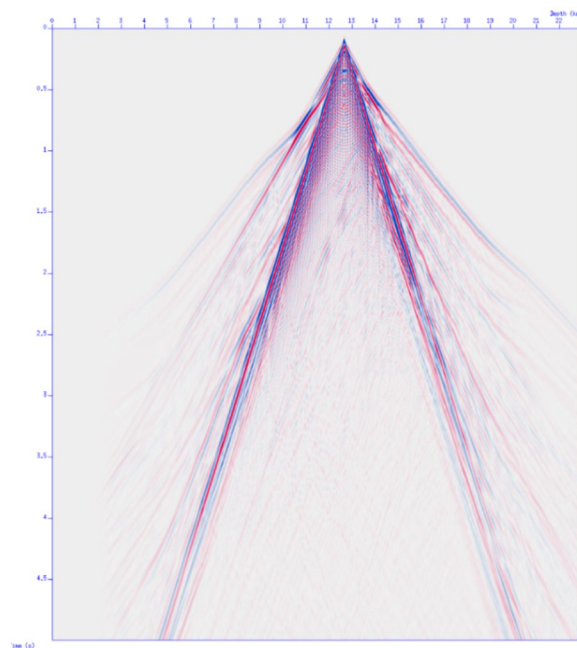


Figure 45: Vertical component are recorded by a virtual streamer placed all along the topography. The vertical time scale ranges between 0 and 5 s. The horizontal axis is horizontal distance.

The second source is located at a distance of about 4310 m from the VSP well. Results are shown in Figure 46a and Figure 46b. Note that in this case the source time function is slightly different (first case was a sinc function band passed filtered between 5 and 15 Hz, the second one is a Ricker wavelet having a peak frequency of 10 Hz). This difference in source time function does not affect the results, as the sources are in fact very similar.

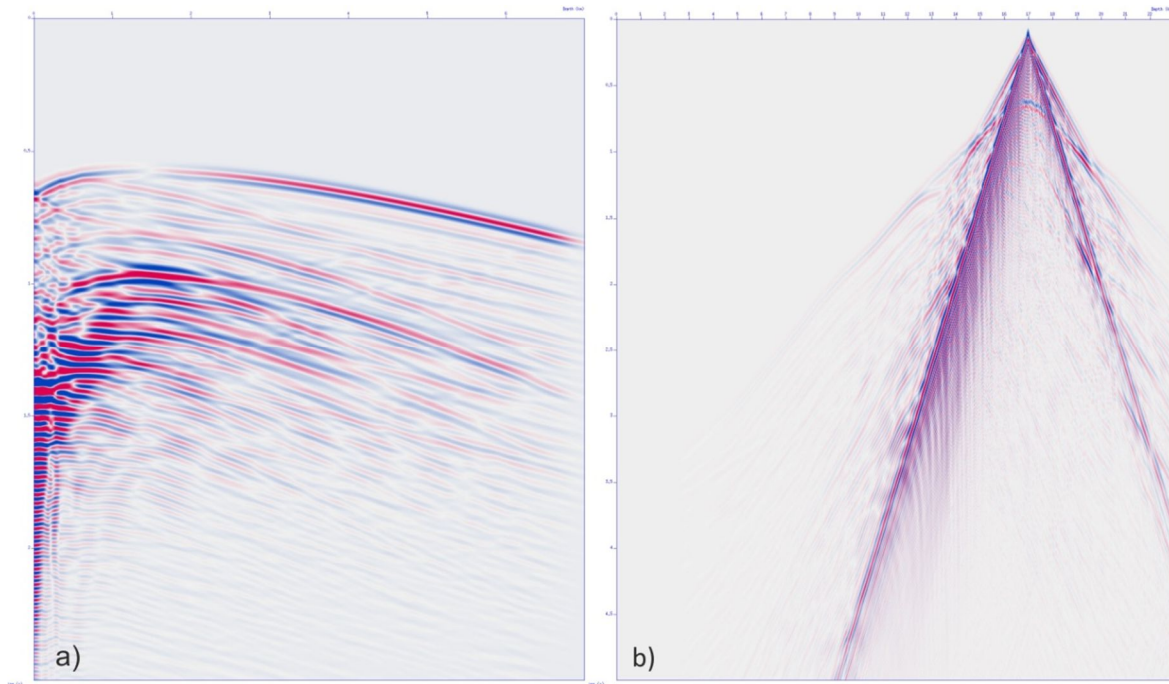


Figure 46: Vertical component records for a vertical source located at an offset of 4310 m. a) at the virtual VSP location (well EAC1). b) by receivers at the surface. The vertical axis is time and ranges from 0 to 2.5 s in (a) and from 0 to 5 s in (b). In a) the horizontal scale is depth from 0 to 7 km. In b) the horizontal scale is the horizontal distance in the model.

Conclusion and perspectives

The study conducted here allowed to model a VSP as if it would be acquired at the well EAC1 and by surface receivers along the topography. The implementation of the viscoelastic behaviour needs to be worked out in order to compare results issued from the Gassmann-Burgers model and those from the Standard Linear Solid, as modelled here. Results should be similar at earthquake seismic frequencies, and will be further investigated for Long Period seismic events (e.g., Jousset et al., 2004).

7 Conclusion

7.1 Main results achieved – milestones of the task

Main results are the achievement of a robust approach and modelling tool to characterize the geothermal sites of the GEMex project. These tools have been calibrated in a priori unknown area, for the relation between geophysical and geothermal parameters, which have been defined and calibrated in the course of the project. Thus we underline that the GEMex project can benefit from these achievements, and that these tools can be further successfully used in future projects on this hot geothermal area in Mexico, and not only.

From a methodological point of view, an overall, even if not exhaustive, analysis of the sensitivity of seismic properties to thermal and geothermal parameters has been conducted. The analysis shows that non always an increase in the temperature is related to an increase in the seismic velocity. The effects of melting are calculated for velocities, elastic quantities, and attenuation effects.

With a more conventional use of the same codes, relevant results with elastic modelling have been obtained for the characterization of active seismic lines data, and to improve the interpretation of wave-fields in the complex volcanic area characterized by faults and structural complexities.

To extend the seismic-thermodynamic analysis to a larger set of parameter, however more focused on specific sites of the project, the modelling was extended to the hydrothermal convective and conductive mechanisms. The results show that observable effects can be obtained in the possible proximity to superhot melting zones, however and substantially depending on the Arrhenius parameters of the investigated formations. Effects of supercritical conditions are evaluated.

With specific examples applied to Los Humeros and Acoculco this provide comparison datasets for further geophysical tasks of the project, in particular data integration. The benchmarking with elastic simulation of full-waveform propagation in the Acoculco model using different tools and modelling methods confirms the consistency of the full-waveform poro-viscoelastic with temperature simulation.

Milestones	Due date /data of achievement	Status
N/A	N/A	N/A

Table 11: List of Milestones

7.2 Scientific knowledge increased

Significantly increased knowledge on integrated use of seismic and geothermal, and thermodynamic parameters. Significantly increased the knowledge of the Geothermal sites of the GEMex project, with integration of geological model of GEMex WP3.

Introduced a new definition of melting point at depth based on analysis of the seismic velocity curves for selected signal frequencies. Estimation of the melting condition versus depth for selected seismic signal frequencies.

Deliverable	Due date	Status
D5.5	31.05.2019	This deliverable ☺

Table 12: List of Deliverables

7.3 Future project work and links with other WPs

This report and work has links to WP5.4, WP6, and may provide feedback for WP3. Possible link with WP4 for effects related to tectonic conditions through the estimation of the octahedral stress in the Arrhenius temperature equation.

7.3.1 Constraints

Relevant and recommended for the future the possibility to have laboratory data on thermodynamic properties of local rocks.

7.3.2 Data integration

Results are relevant for and may further benefit from integration with EM, Gravity, Geology, Temperature profiles, and in general reservoir information.

8 List of Annexes

- Annex I: Poletto, F., Farina, B., and Carcione, J. M., 2018. Sensitivity of seismic properties to temperature variations in a geothermal reservoir, *Geothermics*, 76, 149—163. (GEMex paper)
- Annex II: Paper accepted for publication on *Geothermics* (2019) entitled ‘Seismic properties in conductive and convective hot and super-hot geothermal systems’, Farina B., Poletto F., Mendrinós D., Carcione J.M., and Karytsas C.
- Annex III: EGC Full Paper entitled 'Analysis of seismic wave propagation in geothermal reservoirs', F. Poletto, B. Farina, J. M. Carcione and G. Pinna, submission ID [#296](#) to EGC 2019.

9 References

- Calcagno P., Evanno G., Trumpy E., Gutiérrez-Negrín L.C., Macías J.L., Carrasco-Núñez G., Liotta D., 2018. Preliminary 3-D geological models of Los Humeros and Acoculco geothermal fields (Mexico) – H2020 GEMex Project. *Adv. Geosci.* 45:321–333. doi: 10.5194/adgeo-45-321-2018
- Canet C., Trillaud F., Prol-Ledesma R.M., González-Hernández G., Peláez B., Hernández-Cruz B., Sánchez-Córdova M.M., 2015. Thermal history of the Acoculco geothermal system, eastern Mexico: Insights from numerical and radiocarbon dating. *Journal of Volcanology and Geothermal Research* 305, pp. 56-62.
- Carcione, J. M., 2014. Wave fields in real media: Wave propagation in anisotropic, anelastic, porous and electromagnetic media. *Handbook of Geophysical Exploration*, vol. 38, Elsevier.
- Carcione J. M. and Poletto F., 2013. Seismic rheological model and reflection coefficients of the brittle-ductile transition, *Pure and Applied Geophysics*, 170 (2), 2021-2035.
- Carcione J.M., Poletto F., Farina B. and Craglietto A., 2014. Simulation of seismic waves at the Earth crust (brittle-ductile transition) based on the Burgers model, *Solid Earth*, 5, 1001-1010.
- Carcione J. M., Poletto F., Farina B. and Craglietto A., 2017. The Gassmann-Burgers model to simulate seismic waves at the Earth crust and mantle, *Pure and Applied Geophysics*, 174, 849-863. DOI: 10.1007/s00024-016-1437-2.
- Carrasco-Núñez G., López-Martínez M., Hernández J. and Vargas V., 2017. Subsurface stratigraphy and its correlation with the surficial geology at Los Humeros geothermal field, eastern Trans-Mexican volcanic belt. *Geothermics*, 67, 1-17.
- Farina B., Poletto F., Carcione J., 2016. Seismic wave propagation in poro-viscoelastic hot rocks. In: *Proceedings, European Geothermal Congress 2016, Strasbourg, France*, p 7.
- Farina B., Poletto F., Mendrinos D., Carcione J. M. and Karytsas C., 2019. Seismic properties in conductive and convective hot and super-hot geothermal systems. Paper submitted to *Geothermics*.
- Fernández M., and Ranalli G., 1997. The role of rheology in extensional basin formation modelling. *Tectonophysics*, 282, 129-145.
- Jolly A., Neuberg J., Jousset P. and Sherburn S., 2012. A new source process for evolving repetitive earthquakes at Ngauruhoe volcano, New Zealand. *Journal of Volcanology and Geothermal Research* 215, pp. 26-39.
- Jousset P., Agustsson K., Barison E., Böhm G., Caló M., Chavarria I.G., Farina B., Gaucher E., Loer K., Martins J., Perton M., Poletto F., Saenger E., Soto A.F., Toledo T., Verdel A. and Werner C., 2019. Seismic structures of the Acoculco and Los Humeros geothermal fields. GEMex Report Deliverable D5.3, Submitted 30.04.2019.
- Jousset P., Neuberg J. and Jolly A., 2004. Modelling low-frequency volcanic earthquakes in a viscoelastic medium with topography. *Geophysical Journal International* 159, 776–802. doi: 10.1111/j.1365-246X.2004.02411
- Jousset P., Budi-Santoso A., Jolly A. D., Boichu M., Surono, Dwiyono S., Sumarti S., Hidayati S. and Thierry P., 2013. Signs of magma ascent in LP and VLP seismic events and link to degassing: An example from

the 2010 explosive eruption at Merapi volcano, Indonesia. - *Journal of Volcanology and Geothermal Research* 261, 171-192. doi: <http://doi.org/10.1016/j.jvolgeores.2013.03.014>

- Kaselow A. and Shapiro S.A., 2004. Stress sensitivity of elastic moduli and electrical resistivity in porous rocks. *J. Geophys. Eng.* 1, 1–11.
- Lemmon E. W., McLinden M. O., Friend D. G., 2005. Thermophysical properties of fluid systems. In: Lindstrom, P.J., Mallard, W.G. (eds.), *NIST Chemistry Webbook 69*, NIST Standard Reference Database, Gaithersburg, MD, USA, <http://webbook.nist.gov/chemistry/>.
- Lermo J., Antayhua Y., Bernal I., Venega S., Arredondo J., 2009. Monitoreo sísmico en la zona geotérmica de Acoculco, Pue., Mexico. *Geotermia*, Vol. 22, No.,1, January-June 2009.
- Levander A. R., 1988. Fourth-order finite-difference P-SV seismograms. *Geophysics*, 53 (11), 1425-1436.
- López-Hernández A., García-Estrada G., Aguirre-Díaz G., Gonzàles-Partida E., Palma-Guzmán H., and Quijano-León J.L., 2009. Hydrothermal activity in the Tulancingo-Acoculco Caldera Complex, central Mexico: Exploratory studies. *Geothermics*, 38, 279-293.
- Lorenzo-Pulido C., Armenta-Flores M. and Ramírez-Silva, G., 2010. Characterization of the Acoculco Geothermal Zone as a HDR System, *GRC Transactions*, 34, 369–372.
- Pan C., Chávez O., Romero C. E., Levy E. K., Corona A. A., Rubio-Maya C., 2016. Heat mining assessment for geothermal reservoirs in Mexico using supercritical CO₂ injection. *Energy*, 102, 148-160.
- Poletto F., Farina B. and Carcione J. M., 2018. Sensitivity of seismic properties to temperature variations in a geothermal reservoir, *Geothermics*, 76, 149—163.
- Poletto F., Farina B., Carcione J. M. and Pinna G., 2019, Analysis of seismic wave propagation in geothermal reservoirs. Full Paper submission ID #296 to EGC 2019.
- Poletto F. and Miranda F., 2004. *Seismic While Drilling. Fundamentals of Drill-bit Seismic for Exploration*. Elsevier, Vol. 35.
- Pulido C. L., Armenta M. F., and Silva G. R., 2010. Characterization of the Acoculco geothermal zone as HDR system. *GRC Transaction*, 34.
- Ranalli G., 1997. *Rheology of the lithosphere in space and time*. Geological Society, London, Special Publications 1997, V. 121, 19-37.
- Tessmer E., Kosloff D. and Behle A. 1992. Elastic wave propagation simulation in the presence of surface topography, *Geophys. J. Int.* 108, 621–632.
- Urban E. and Lermo F. 2013. Local seismicity in the exploitation of Los Humeros geothermal field, Mexico. *Proceedings, Thirty-Eighth Workshop on Geothermal Reservoir Engineering Stanford University, Stanford, California, February 11-13 2013*.
- Viggiano-Guerra, J. C., Armenta, M. F., and Silva, G. R., 2011. Evolución del sistema geotérmico de Acoculco, Pue., México: un estudio con base en estudios petrográficos del pozo EAC-2 y en otras consideraciones. *Geotermia*, 24(1), 14-24.
- Violay M., Gibert B., Mainprice D., Evans B., Dautria J.M., Azais P. and Pezard P.A., 2012. An experimental study of the brittle-ductile transition of basalt at oceanic crust pressure and temperature conditions. *Geophys. Res.*, 117, 1-23.

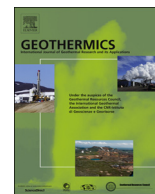
ANNEX I



ELSEVIER

Contents lists available at ScienceDirect

Geothermics

journal homepage: www.elsevier.com/locate/geothermics

Sensitivity of seismic properties to temperature variations in a geothermal reservoir



Flavio Poletto*, Biancamaria Farina, José M. Carcione

Istituto Nazionale di Oceanografia e di Geofisica Sperimentale – OGS, Borgo Grotta Gigante 42/c, 34010 Sgonico, Trieste, Italy

ARTICLE INFO

Keywords:

Sensitivity
Temperature
Seismic properties
Geothermal

ABSTRACT

Geophysical characterization plays a key role for the definition of the deep structures of geothermal reservoirs and the consequent assessment and validation of the geothermal conceptual model. Seismic methods may provide a valuable contribution for this purpose. This involves a deep and reliable understanding of the sensitivity of seismic-wave propagation to physical and temperature variations, with complex interactions. We present the theory and sensitivity analysis based on rock's mechanical Burgers model including Arrhenius temperature equations, integrated with Gassmann model for fluid saturated porous rocks, pressure effects for bulk and shear moduli, as well as permeability and squirt flow effects. Assuming a temperature gradient model, the analysis applied at low seismic frequencies compares the interpretation of the sensitivity effects for different typical seismic elastic quantities, showing the different performance in relation to physical effects, including melting, supercritical conditions, and observability obtained in different temperature regions. With a quantification of the physical properties, the results of the study show that in deeper zones the main expected contributions in terms of variations in seismic velocity, moduli and seismic attenuation due to temperature come from melting transition, while in shallower porous fluid-saturated formations the trends are governed by pressure effects, with minor contributions of permeability and possible effects related to soft porosity. The new calculated elastic moduli are complex-valued and frequency-dependent, and temperature dependent through the fluid properties. In this complex scenario, not always the increments in the velocity and elastic wave moduli correspond to an increment in the temperature. Moreover, with mobility decreasing as a function of depth, the analysis shows that the shear quality factor is sensitive to permeability, which introduces moderate effects for velocity and attenuation of shear waves. The analysis applies to active exploration seismic and passive seismology.

1. Introduction

Seismic methods may provide a valuable contribution for the geophysical characterization of geothermal reservoirs, either using exploration approaches (Batini et al., 1983; Niituma et al., 1999) or passive seismology to image the subsurface, obtain velocity information and monitor the geothermal reservoir (e.g., Blanck et al., 2016; Majer et al., 2007). This task requires a deep and reliable understanding of the sensitivity for seismic-wave propagation to physical and temperature variations, with complex interactions of the interrelated effects. This is relevant in particular for deep-drilling projects, where supercritical fluid conditions can be encountered (Farina et al., 2016; Dobson et al., 2017; Reinsch et al., 2017) and prediction, for example by reverse VSP (RVSP) (Poletto et al., 2011; Poletto and Miranda, 2004) may play a key role.

Several works consider seismic wave propagation in hot geothermal rocks worldwide (e.g., Cermak et al., 1990; Kristinsdóttir et al., 2010; Vinciguerra et al., 2006), in the presence of temperature and fluids. Jaya et al. (2010) analysed petrophysical experiments on Icelandic geothermal rock samples at simulated in situ reservoir conditions to delineate the effect of temperature on seismic velocity and attenuation, with the goal to predict the effect of the saturating pore fluid on seismic velocity using a modified Gassman equation. In their study the temperature dependence follows solely from the thermophysical characteristic of the saturating fluid in porous rock. Iovenitti et al. (2013) and Tibuleac et al. (2013), studied the seismic-temperature distribution to test the seismic component of an exploration method calibrated by integrating geological, geophysical and geochemical experimental data, including empirical temperature – P-wave velocity relationships and sensitivity analysis after removing the effects on depth, using a

* Corresponding author.

E-mail address: fpoletto@inogs.it (F. Poletto).

<https://doi.org/10.1016/j.geothermics.2018.07.001>

Received 20 September 2017; Received in revised form 2 May 2018; Accepted 1 July 2018

0375-6505/© 2018 The Authors. Published by Elsevier Ltd. This is an open access article under the CC BY license (<http://creativecommons.org/licenses/by/4.0/>).

geostatistical approach. More recently, seismic rheological analysis of the brittle ductile transition (BDT) and seismic propagation modeling in presence of temperature was performed by [Carcione and Poletto \(2013\)](#), with temperature and fluids by [Carcione et al. \(2014, 2017\)](#), [Farina et al. \(2017\)](#), including melting and supercritical condition. The numerical algorithms developed in these studies ([Carcione and Poletto, 2013](#); [Carcione et al., 2014, 2017](#); [Farina et al., 2016, 2017](#)) can be used for seismic simulation in arbitrary geological media at variable geothermal conditions, including temperature and tectonic effects at depth. After understanding the seismic behavior in geothermal environments, a model-based analysis of sensitivity for the elastic quantities together with the experimental study is essential for seismic characterization.

In particular, this work is part of the ongoing characterization of geothermal formations by full-waveform seismic modelling including temperature, planned and performed in the framework of the European Union Horizon 2020 GEMex Project ([GEMex, 2016](#)), for the study of high-temperature geothermal zones and geothermal systems in Mexico: for engineered geothermal system (EGS) development at Acoculco and for a super-hot resource near Los Humeros (e.g., [Urban and Lermo, 2013](#)). GEMex includes the analysis of the distribution of rock modulus of elasticity and correlation to temperature, namely: comparing the spatial distribution of rock modulus of elasticity with the temperature distribution data derived from the thermo-mechanical models with the purpose to estimate deep formation temperatures from seismic and gravity surveys ([GEMex, 2016](#)).

In this work, we present the theory and numerical sensitivity analysis based on rock's mechanical Burgers model including creep-flow by Arrhenius temperature equations, integrated with Gassmann model to account for fluid saturated porous rocks, and pressure effects for bulk modulus. The analysis includes permeability effects and squirt-flow, which may introduce unrelaxed effects at frequencies higher than the seismic frequencies. The analysis presented in the second part of the paper is applied at low seismic frequency, assuming a constant-gradient model for temperature. It compares the interpretation of the characteristic sensitivity effects for different typical seismic elastic quantities, showing the different performance in relation to physical effects, including melting and supercritical, and investigates results in different temperature regions in sample-case examples. Main results are related to interpretation of differences in sensitivity calculated with attenuation and propagation velocity, with interpretation of melting, fluid saturation and pressure effects in the sensitivity curves.

The scope of this work is to provide a first basis for the seismic sensitivity analysis with temperature by numerical simulation. The analysis is representative of the wave propagation behavior at different conditions.

2. Theory

2.1. The Burgers model for brittle–ductile behavior

[Carcione and Poletto \(2013\)](#) observed that the Burgers model is suitable to describe the transient viscoelastic creep for arbitrary media, because there is experimental evidence that linear viscoelastic models are appropriate to describe the behavior of ductile media. [Gangi \(1981, 1983\)](#) obtained exponential functions of time using linear viscoelastic models to fit data for synthetic and natural rocksalt. [Chauveau and Kaminski \(2008\)](#) described the effect of transient creep on the compaction process on the basis of the Burgers' model. The viscosity can be expressed by the Arrhenius' equation, accounting for thermodynamic effects, and the constants that appear in the creep rate expressions describe the properties of a specific arbitrary material at given physical conditions. For this study, we assume isotropic materials, however anisotropy is considered in [Carcione and Poletto \(2013\)](#), which can be further developed for sensitivity analysis purposes. For more details on the derivation of the constitutive equations the reader may refer to

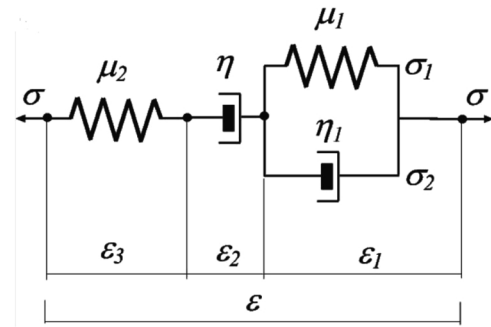


Fig. 1. Mechanical representation of the Burgers viscoelastic model for shear deformations (e.g., [Carcione, 2014](#)). σ , ϵ , μ and η represent stress, strain, shear modulus and viscosity, respectively, where η_1 describes seismic relaxation while η is related to plastic flow and processes such as dislocation creep.

previous works ([Carcione and Poletto, 2013](#); [Carcione et al., 2014, 2017](#)).

The constitutive equation, including both the shear viscoelastic and ductile behavior, can be described with the Burgers model as reported in [Carcione and Poletto \(2013\)](#) and [Carcione et al. \(2014\)](#). The Burgers model is a series connection of a dashpot and a Zener model ([Fig. 1](#)) and its complex shear modulus can be written as

$$\mu_B = \frac{\mu_0(1 + i\omega\tau_\epsilon)}{1 + i\omega\tau_\sigma - \frac{i\mu_0}{\omega\eta}(1 + i\omega\tau_\epsilon)} \quad (1)$$

The quantities τ_σ and τ_ϵ are seismic relaxation times, μ_0 is the relaxed shear modulus (see below) and η is the flow viscosity describing the ductile behavior, $i = \sqrt{-1}$ and $\omega = 2\pi f$ is the angular frequency. The relaxation times can be expressed as

$$\tau_\epsilon = \frac{\tau_0}{Q_0}(\sqrt{Q_0^2 + 1} + 1), \quad \tau_\sigma = \tau_\epsilon - \frac{2\tau_0}{Q_0} \quad (2)$$

where τ_0 is a relaxation time such that $\omega_0 = 1/\tau_0$ is the center frequency of the relaxation peak and Q_0 is the minimum quality factor.

The limit $\eta \rightarrow \infty$ in Eq. (1) recovers the Zener kernel to describe the behavior of the brittle material, while $\tau_\sigma \rightarrow 0$ and $\tau_\epsilon \rightarrow 0$ yield the Maxwell model used by [Dragoni and Pondrelli \(1991\)](#): $\mu_B = \mu_0(1 - i\mu_0/\omega\eta)^{-1}$ (e.g., [Carcione, 2014](#)). For $\eta \rightarrow 0$, $\mu_B \rightarrow 0$ and the medium becomes a fluid. Moreover, if $\omega \rightarrow \infty$, $\mu_B \rightarrow \mu_0\tau_\epsilon/\tau_\sigma$, where μ_0 is the relaxed ($\omega = 0$) shear modulus of the Zener element ($\eta = \infty$).

The viscosity η can be expressed by the Arrhenius equation (e.g., [Carcione et al., 2006](#); [Montesi, 2007](#)). It is related to the steady-state creep rate $\dot{\epsilon}$ by

$$\eta = \frac{\sigma_o}{2\dot{\epsilon}}, \quad \dot{\epsilon} = A_\infty \sigma_o^n \exp(-E/R_G T) \quad (3)$$

where σ_o is the octahedral stress (e.g., [Gangi, 1981, 1983](#); [Carcione et al., 2006](#); [Carcione and Poletto, 2013](#)), A_∞ and n are constants, E is the activation energy, $R_G = 8.3144 \text{ J/mol}^\circ\text{K}$ is the gas constant and T is the absolute temperature. The octahedral stress is

$$\sigma_o = \frac{1}{3}\sqrt{(\sigma_v - \sigma_h)^2 + (\sigma_v - \sigma_H)^2 + (\sigma_h - \sigma_H)^2}, \quad (4)$$

where the σ 's are the stress components in the principal system, corresponding to the vertical (v) lithostatic stress, and the maximum (H) and minimum (h) horizontal tectonic stresses.

The temperature is a function of depth through the geothermal gradient G . A linear approximation is $T - T_0 = z G$, where z is the depth and T_0 is the temperature at the surface ($z = 0$).

2.2. The modified Gassmann model

Gassmann's equations are used to calculate changes in seismic velocity and elastic quantities due to different fluid saturations. In this

work we assume that the porous material is isotropic, and homogeneous. The Gassmann bulk and shear moduli are

$$K_G = K_m + \alpha(K_m)^2 M(K_m) \quad \text{and} \quad \mu_G = \mu_m = \mu_B, \quad (5)$$

where

$$\alpha(K_m) = 1 - \frac{K_m}{K_s}, \quad (6)$$

and

$$M(K_m) = \frac{K_s}{1 - \phi - K_m/K_s + \phi K_s/K_f}, \quad (7)$$

where ϕ is the porosity, K_m and μ_m are the bulk and shear moduli of the drained matrix, and K_s and K_f are the solid and fluid bulk moduli, respectively (e.g., [Carcione, 2014](#)).

To account for the pressure dependence, we express the dry-rock bulk moduli as

$$K_m = K_0 g_1(p_d), \quad \text{and} \quad \mu_m = \mu_0 g_2(p_d), \quad (8)$$

where $g_j(p_d)$, $j = 1, 2$ defines the dependence of the moduli on the differential pressure $p_d = p_c - p$, where p_c is the confining pressure, p is the pore (fluid) pressure, and K_0 and μ_0 are the bulk and shear moduli at infinite effective pressure and $\eta = \infty$ (or $\omega = \infty$). Using μ_B in (8) means that the Burgers shear viscosity is included. The simplest form of function g , in good agreement with experimental data, is

$$g_j(p_d) = 1 - (1 - a_j) \exp(-p_d/p_j^*), \quad j = 1, 2 \quad (9)$$

([Kaselow and Shapiro, 2004](#)), where a_j and p_j^* are parameters. It is $g_j = 1$ for $p_d \rightarrow \infty$ (e.g., very high confining pressure) and $g_j = a_j$ for $p_d \rightarrow 0$ (pore pressure equal to the confining pressure).

The bulk density is

$$\rho = (1 - \phi)\rho_s + \phi\rho_f, \quad (10)$$

where ρ_s and ρ_f are the grain and fluid densities, respectively. In the following analysis we distinguish between stiff grain porosity and soft compliant porosity in the gap area of grain contact. The compliant porosity is typically so small – nearly 0.001 for most rocks – that the total porosity ϕ can be assumed to be equal to the stiff porosity.

2.3. Phase velocity, attenuation and wave modulus

The phase velocity and attenuation, or dissipation factor (inverse of the quality factor), including the Burgers, Biot, permeability and squirt-flow losses (see next sections), are

$$v_p = \left[\text{Re} \left(\frac{1}{v_c} \right) \right]^{-1}, \quad (11)$$

and

$$Q^{-1} = \frac{\text{Im}(v_c^2)}{\text{Re}(v_c^2)}, \quad (12)$$

where v_c is the complex velocity (e.g., [Carcione, 2014](#)). For shear waves

$$v_c = \sqrt{\frac{\mu}{\bar{\rho}}}, \quad (13)$$

where

$$\bar{\rho} = \rho - \rho_f^2/\rho_1 \quad \text{and} \quad \rho_1 = \frac{\rho_f \mathcal{T}}{\phi} + \frac{\eta_f}{i\omega\kappa}, \quad (14)$$

where \mathcal{T} is the rock tortuosity and κ is the permeability. In our simulations we assume $\mathcal{T} = 1 - 0.5(1 - 1/\phi)$ ([Mavko et al., 2009](#); [Berryman, 1980](#)). Eq. (14) can be reformulated as

$$\rho_1 = \frac{\rho_f \mathcal{T}}{\phi} + \frac{1}{i\omega M}, \quad (15)$$

where the quantity $M(p, T) = (\kappa/\eta_f)$ is mobility, ratio of permeability and viscosity ([Batzle et al., 2006](#)), introducing dispersion and attenuation effects in the shear-wave Eqs. (12) and (13), as well as in Eq. (18) for compressional waves, depending on pressure and temperature through fluid properties and permeability. [Manning and Ingebritsen \(1999\)](#) inferred permeability from thermal modeling and metamorphic systems suggesting the following dependence with depth z ,

$$\log \kappa = -3.2 \log z - 14 = -3.2 \log \left(\frac{T - T_0}{G} \right) - 14. \quad (16)$$

where $T_0 = T(0)$ is the surface temperature, z is the depth in km and the permeability is given in m^2 . With constant-gradient approximation, the second expression assumes a linear geothermal law, $T - T_0 = z G$.

The complex velocity of the P waves is obtained from the following second-order equation in v_c^2 :

$$\bar{\rho} \rho_1 v_c^4 + a_1 v_c^2 + a_0 = 0, \quad (17)$$

where

$$a_1 = (2\alpha\rho_f - \rho)M - \rho_1 \left(K_G + \frac{4}{3}\mu_G \right), \\ a_0 = \left(K + \frac{4}{3}\mu \right) M \quad (18)$$

(e.g., [Carcione, 2014](#) Eq. (7.324)).

The P-wave and S-wave stiffness moduli are given by

$$E_P = \rho v_p(P)^2 \quad \text{and} \quad E_S = \rho v_p(S)^2, \quad (19)$$

respectively.

3. Sensitivity analysis

The approach we adopt to investigate the sensitivity of the seismic properties to temperature T is as follows. Consider the quantities

$$\rho = \rho(T), \quad v_{P,S} = v_{P,S}(T), \quad Q_{P,S} = Q_{P,S}(T), \quad (20)$$

where ρ , $v_P = v_p(P)$ and $v_S = v_p(S)$ are formation density, and compressional and shear velocities, respectively, and Q is the quality factor (12) accounting for attenuation related to temperature. We define the stiffness (modulus, denoted by subscript ‘M’) and impedance (denoted by subscript ‘I’) sensitivities as

$$s_M^{(J)} = \frac{\partial(\rho v_J^2)}{\partial T} = \frac{\partial \rho}{\partial T} v_J^2 + 2\rho v_J \frac{\partial v_J}{\partial T}, \quad (21)$$

$$s_I^{(J)} = \frac{\partial(\rho v_J)}{\partial T} = \frac{\partial \rho}{\partial T} v_J + \rho \frac{\partial v_J}{\partial T}, \quad (22)$$

and that of attenuation by

$$s_Q^{(J)} = \frac{\partial Q_J}{\partial T}, \quad (23)$$

where the subscript and superscript ($J = P, S$) denote the compressional- or shear-wave type index. Eq. (21) expresses the effect of temperature on the stress–strain relations through the moduli of elasticity, while Eq. (22) refers to the radiation impedance, since it includes density and not only wave velocity. Note that the sensitivity for the Bulk modulus is given by

$$s_M^{(KB)} = s_M^{(P)} - \frac{4}{3} s_M^{(S)}. \quad (24)$$

The quantities in Eqs. (21) and (22) can simply be expressed as a function of ρ , $(\partial\rho/\partial T)$, v_J and $(\partial v_J/\partial T)$. In poro-viscoelastic media, for a given type of rock and saturating fluid, it is in general

$$\rho = \rho[\phi, \rho_f(p, T)], \quad (25)$$

where ϕ is porosity, ρ_f is the fluid density and p is pressure. In general at variable depths and in the proximity of melting conditions we also consider the dependence $\phi = \phi(T, p)$. Moreover, the quantities v_J and

Q_J also depend on local stress conditions and typically they exhibit non negligible dispersion effects, since they depend on frequency ω . Namely, we have

$$\nu_J = \nu_J(T, \omega, \sigma_o, \phi, p, \kappa), \quad Q_J = Q_J(T, \omega, \sigma_o, \phi, p, \kappa), \quad (26)$$

where we introduced the octahedral stress σ_o and the permeability κ is included. With these premises, we analyze the sensitivity quantities $s_K^{(J)}$ where the subscript $K = M, I, Q$. These curves provide tools to evaluate the reliability and the effectiveness of the temperature analysis methods by seismic signals.

To achieve this task using different seismic quantities, we calculate and compare also the relative-sensitivity curves $S(T)$ for the investigated quantities, generically denoted by W_J , with respect to the value of the same quantity at the same temperature,

$$S_W^{(J)} = \frac{1}{W_J} \frac{\partial(W_J)}{\partial T}, \quad (27)$$

which provides an estimator of the performance of the different quantities W_J to characterize seismically the geothermal variation. For example, with slow and negligible variations of the impedance $W_J(T) = \rho \nu_J$ in limited temperature intervals, Eq. (27) gives an approximation of twice the magnitude of the acoustic reflection coefficient per unit temperature increment, and can be used to evaluate the impact of the investigation by the seismic reflection response once the dependence of the seismic quantity on temperature and the local temperature gradient are known, hence for inversion purposes.

Finally, note that the reciprocal of the sensitivity of seismic quantities to temperature, say, of a given measurable quantity W_J ,

$$s_T^{(W_J)} = \frac{1}{s_W^{(J)}} = \frac{\partial T}{\partial W_J}, \quad (28)$$

provides the rate of variation (sensitivity) of temperature with respect to said measurable seismic quantity, which can be investigated and utilized for evaluation of stability conditions in the seismic prediction of geothermal temperature distribution and variation between depth intervals. When the reciprocal sensitivity of Eq. (28) is low, a variation in the seismic quantity correspond to a lower variation in temperature, and the prediction is locally more stable.

4. Physics of the fluid-saturated rocks

The rheological conditions we study to analyze seismically geothermal fields include solid rock properties, fluid properties, temperature, pressure, tectonic conditions, porosity and permeability versus depth and temperature. Possible squirt flow effects are also evaluated.

4.1. Rock parameters

For our analysis, we consider sample KTB 61C9b (amphibolite) reported in Popp and Kern (1994) (their Table II and Fig. 3), for which $\rho_s = 3000 \text{ kg/m}^3$, $K_s = 74.2 \text{ GPa}$, and $\phi = 0.05$, $K_0 = 69.84 \text{ GPa}$ and $\mu_0 = 43.57 \text{ GPa}$ (see also Carcione et al., 2017).

4.2. Pressure, tectonic stress and thermal parameters

The pressure dependence at seismic frequencies (Eq. (8)) is

$$\begin{aligned} g_1 &= 1 - (1 - 0.39)\exp(-p_d/65), \\ g_2 &= 1 - (1 - 0.52)\exp(-p_d/62), \end{aligned} \quad (29)$$

where p_d is given in MPa (Carcione et al., 2017) and the constants a_j and p_j^* in Eq. (9) are calculated from Popp and Kern (1994).

The shear seismic loss parameter is obtained from empirical equations derived by Castro et al. (2008) for the crust in Southern Italy. They report $Q_0 = 18.8 f^{1.7}$ for the upper crust and up to a frequency of 10 Hz. In the examples we consider a frequency of $f = 3 \text{ Hz}$, with

$\omega_0 = 2 \pi f$, which gives $Q_0 = 122$. The temperature is a function of depth through the geothermal gradient G as $T = (20 + z G \times 10^{-3})$, where z (m) is depth and $G = 50, 60$ and $90 \text{ }^\circ\text{C/km}$ in our calculations for different examples. The lithostatic stress is $\sigma_v = -\bar{\rho}gz = -p_e$, where $\bar{\rho} = 2400 \text{ kg/m}^3$ is the average density and $g = 9.81 \text{ m/s}^2$ is the gravity constant. To obtain the octahedral stress (4) we consider a simple model based on the gravity contribution at depth z . The horizontal stresses are estimated as

$$\sigma_H = \frac{\nu \sigma_v}{1 - \nu}, \quad \text{and} \quad \sigma_h = \xi \sigma_H \quad (30)$$

where $\nu = \nu(K_0, \mu_0)$ is the Poisson ratio at infinite effective pressure. The factor $\nu/(1 - \nu)$ lies between 0.25 and 1 for ν ranging from 0.2 to 0.5, with the latter value corresponding to a liquid (hydrostatic stress). The parameter $\xi \leq 1$ has been introduced to model additional effects due to tectonic activity (anisotropic tectonic stress) (Carcione and Poletto, 2013). Furthermore, we consider $A_\infty = 100 \text{ (MPa)}^{-n} \text{ s}^{-1}$, $E = 134 \text{ kJ/mol}$ and $n = 2$, and take $\xi = 0.8$. The above degree of stress anisotropy is consistent with values at prospective depths provided by Hegret (1987) for the Canadian Shield, and in agreement with data reported in Engelder (1993, p. 91).

4.3. Fluid physical properties

Without loss of generality, in our examples the geothermal fluid is pure water. The water properties as a function of pressure and temperature are obtained from the fluid thermo-physical database provided in the website of the National Institute of Standards and Technology (NIST), collected from laboratory measurements by Lemmon et al. (2005). In ‘‘Thermophysical Properties of Fluid Systems’’, we choose water (1) and Isothermal Properties (3). The range of allowable values are $[0, 1000] \text{ }^\circ\text{C}$ and $[0, 1000] \text{ MPa}$. In order to analyse the seismic properties in the presence of overpressure and anomalous temperatures, we extract the water density, ρ_w , sound velocity, c_w , and viscosity from the NIST website for the range $[0, 900] \text{ }^\circ\text{C}$ and $[0, 200] \text{ MPa}$. A 3D plot is shown in Fig. 2. The zone in excess to $T = 374 \text{ }^\circ\text{C}$ and $p_w = 22.1 \text{ MPa}$ corresponds to the supercritical phase. The fluid bulk modulus is given by $K_f = \rho_w c_w^2$.

With only liquid, a state of hydrostatic pore pressure is given by $p = \bar{\rho}_f gz$, where $\bar{\rho}_f = 1000 \text{ kg/m}^3$ is an average fluid density. In the presence of different, liquid, vapour and supercritical phases at depth, we use an iterative method to calculate the hydrostatic pressure by NIST (Farina et al., 2016). In Fig. 2 we consider a depth range $[5, 15] \text{ km}$, where pore pressure and temperature vary from 50 to 150 MPa and 300 to 900 $^\circ\text{C}$, respectively (in this example the geothermal gradient is $60 \text{ }^\circ\text{C/km}$). The experimental density, sound velocity and viscosity of water are shown together with the pressure and temperature profiles. Compare these values to the ones at ambient conditions, defined by a temperature of $20 \text{ }^\circ\text{C}$ and a pressure of 0.1 MPa : a water density of 998 kg/m^3 and a sound velocity of 1482 m/s .

4.4. Porosity and permeability

Let us consider now variations in the rock porosity ϕ , assuming stiff porosity approximation $\phi \cong \phi_s$. This implies that the bulk and shear moduli depend on porosity by Gassmann model as well as on the permeability. The dry bulk and shear moduli of the samples are determined by the Krief model (Krief et al., 1990),

$$\frac{K_m}{K_s} = \frac{\mu_m}{\mu_s} = (1 - \phi)^{3/(1-\phi)}, \quad (31)$$

where K_s and μ_s are the bulk and shear moduli of the solid. Permeability is obtained as

$$\kappa = \frac{R_s^2 \phi^3}{45(1 - \phi)^2} \quad (32)$$

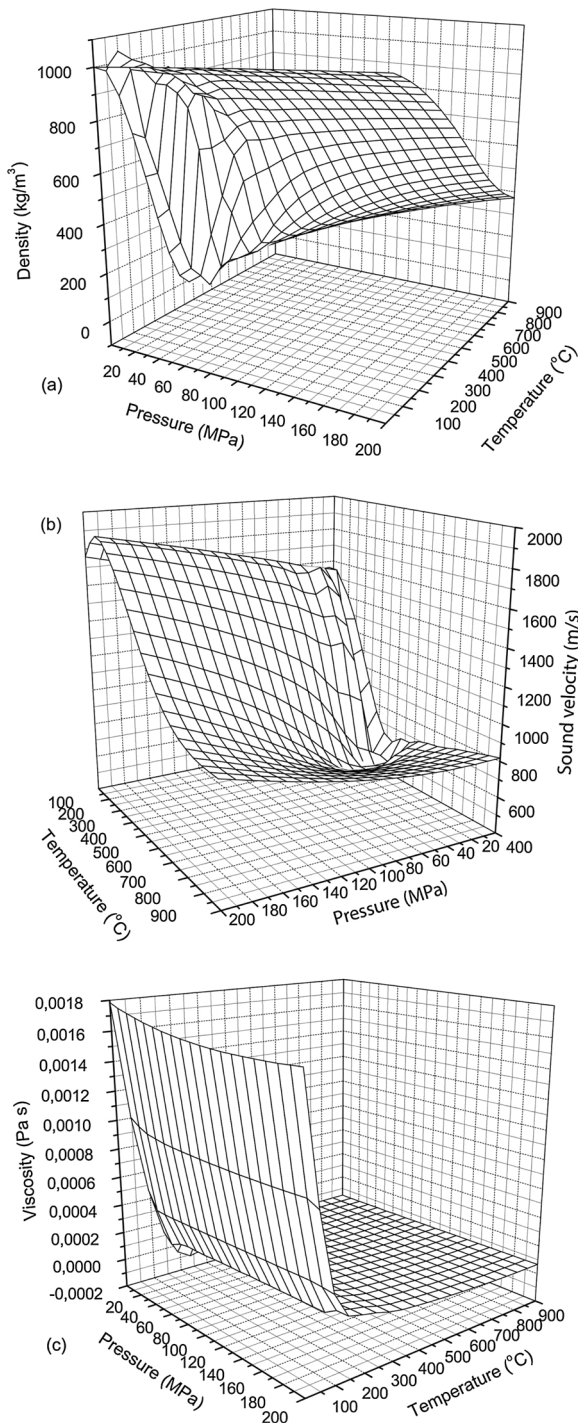


Fig. 2. Water density (a), sound velocity (b) and viscosity (c) for a wide range of pressures and temperatures (data taken from the NIST website).

(Carcione et al., 2000), where R_s is the average radius of the grains. Here, we assume $R_s = 20 \mu\text{m}$. As we can see below, this relation is in agreement with rheological estimations with temperature in different types of rocks, and we assume it as a generalized approximated relation, with possible deviations for metamorphic rocks. Moreover, significant deviations can be expected for permeability in formations with secondary crack porosity but low stiff porosity in rocks with flow paths in faulting and fractures, both when considering natural systems (Hickman et al., 1995; Ito and Zoback, 2000) and EGS systems with enhanced fracturation (Majer et al., 2007; Hashida et al., 2001). To account for the dependence of permeability from depth and

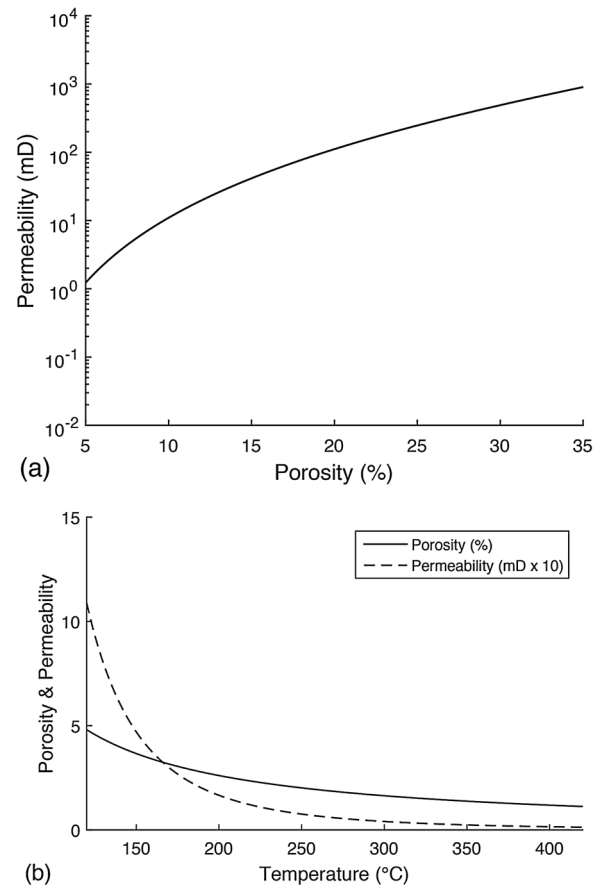


Fig. 3. (a) Permeability versus porosity. (b) Permeability and porosity versus temperature assuming a constant-gradient $G = 50 \text{ }^\circ\text{C}/\text{km}$ in the depth interval [2, 8] km.

temperature, we invert Eq. (32) for porosity by solving

$$R_s^2 \phi^3 - \hat{\kappa} \phi^2 + 2\hat{\kappa} \phi - \hat{\kappa} = 0, \quad (33)$$

where $\hat{\kappa} = 45\kappa$ and $\kappa = \kappa(T)$ is given from Eq. (16). The plot of permeability as a function of porosity shown in Fig. 3a is in agreement with the curves estimated empirically for sandstone and carbonate rocks by Ehrenberg and Nadeau (2005, in particular in Fig. 4 of their paper). In this example, the dependence on temperature is calculated as $T = zG + T_0$ with $T_0 = 20 \text{ }^\circ\text{C}$ and a gradient $G = 50 \text{ }^\circ\text{C}/\text{km}$ in order to avoid melting zones. In order to display the curves in the same numerical range, Fig. 3b shows the permeability expressed in (mDarcy $\times 10$) unit and porosity (%) versus temperature in the depth interval [2, 8] km. In this analysis, according with Ehrenberg and Nadeau (2005), we neglect the shallower layers with higher porosity and, in agreement with Fig. 3b, we consider examples with the porosity in the range $\phi = [0, 5]$ (%).

4.5. Stiff and soft pores and squirt-flow effects

The squirt flow interaction model between stiff and soft pores takes into account the fact that the pore space of many rocks has a binary structure composed of relatively stiff pores, which constitute the majority of the pore space, and relatively compliant (or soft) pores, which are responsible for the pressure dependency of the poroelastic moduli. Fluid saturates both stiff and soft pores. When the frequency is higher than the so-called characteristic squirt relaxation frequency f_{CS} , the fluid pressure does not have enough time to equilibrate between stiff and compliant pores during a half-wave cycle. Above f_{CS} the system is in the so called unrelaxed state. Then, compliant pores at the grain

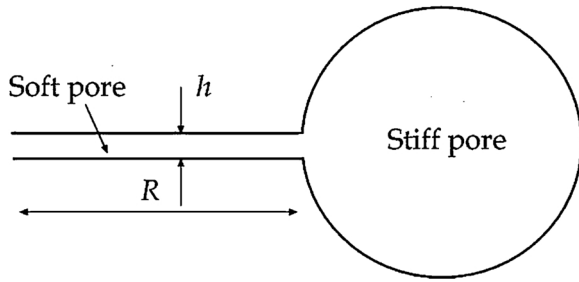


Fig. 4. Sketch of the squirt-flow model, where two sandstone grains in contact are shown. The soft pores are the grain contacts and the stiff pores constitute the main porosity. The quantity R is the radius of the disk-shaped soft pore (half disk is represented in the plot) (modified after Gurevich et al., 2010).

contacts are effectively isolated from the stiff pores and hence become stiffer with respect to normal (but not tangential) deformation.

In order to model the frequency dependency of the partially-relaxed moduli, Gurevich et al. (2010) assumed a geometrical configuration by which a compliant pore forms a disk-shaped gap between two grains, and its edge opens into a toroidal stiff pore (Fig. 4). Gurevich et al. (2009, 2010) analyzed the ultrasonic behaviour, and the *low*-, *intermediate*- and *high*-frequency approximations for squirt-induced attenuation. They obtained the modified partially-relaxed (at sufficient low frequency) dry moduli, i.e., whereby soft pores are fluid-filled whereas stiff pores are dry, as

$$\frac{1}{K} = \frac{1}{K_h} + \left[\left(\frac{1}{K_m} - \frac{1}{K_h} \right)^{-1} + \left(\frac{1}{K_f^*} - \frac{1}{K_s} \right)^{-1} \phi_c^{-1} \right]^{-1},$$

$$\frac{1}{\mu} = \frac{1}{\mu_m} - \frac{4}{15} \left(\frac{1}{K_m} - \frac{1}{K} \right), \quad (34)$$

where K_m and μ_m represent the dry-rock bulk and shear moduli at the confining pressure p_c , K_h is the dry-rock bulk modulus at a confining pressure where all the compliant pores are closed, i.e., that of a hypothetical rock without the soft porosity, and ϕ_c is the compliant (soft) porosity. For a more detailed description of the numerical modeling approach see Carcione and Gurevich (2011). The key quantity in Eqs. (34) is the effective bulk modulus $K_f^* = K_f^*(k \cdot R, K_f)$ of the fluid saturating the soft pores, where

$$k \cdot R = 2 \left(\frac{R}{h} \right) \sqrt{-\frac{3i\omega\eta_f}{K_f}}, \quad (35)$$

and k is the wavenumber, R is the radius of the crack and h is its thickness (Fig. 4). When the fluid modulus satisfies $K_f \gg 8\phi_c K$ with $K^{-1} = (K_m^{-1} - K_h^{-1})$ we may assume the approximation $K_f^* = i\omega\eta_f^*$, where

$$\eta_f^* = \frac{3}{2} \left(\frac{R}{h} \right)^2 \eta_f \quad (36)$$

is an effective viscosity. The peak relaxation frequency of the squirt-flow model is

$$f_{CS} \approx \frac{1}{3\pi\eta_f} \left(\frac{h}{R} \right)^2 \phi_c K, \quad (37)$$

using the approximations $K_h \approx K_m$ and assuming $K_s \gg (\phi_c K)$ (Carcione and Gurevich, 2011). Hence, the peak frequency decreases with increasing fluid viscosity and decreasing aspect ratio (h/R) of the crack.

Using Eqs. (34) in the Gassmann model Eqs. (5)–(7) gives the modified squirt-Gassmann moduli. The explicit functional form of α and M on K_m is in fact convenient for replacing K_m by the modified matrix (or frame) complex modulus K including the squirt-flow mechanism (Eq. (34)). Similarly, μ_m is replaced by μ . The new moduli are complex-valued and frequency-dependent, and relevant for our study, also temperature dependent through the fluid properties.

As discussed by Carcione et al. (2018a,b), the squirt-flow model is consistent with Gassmann's theory in the low-frequency limit, and with Mavko–Jizba unrelaxed moduli in the high-frequency limit (Mavko and Jizba, 1991). All the parameters of the model have a clear physical meaning. There is only one adjustable parameter: the aspect ratio of compliant pores (grain contacts) h/R . However, the model approximations in different frequency regions are different for different fluid phases, i.e., not only fluid but also gas (Gurevich et al., 2010; Carcione and Gurevich, 2011) and supercritical. The squirt physical effect, here introduced for a preliminary evaluation for the purposes of the sensitivity analysis, needs further investigations with multi-phase fluids to evaluate its relevance at seismic frequencies with temperature.

5. Examples

5.1. Case study for seismic and physical quantities

Using rock and geothermal parameters of the reference literature, we calculate the seismic elastic quantities to obtain characteristic sensitivity curves for a small set of explanatory physical models. We compare the sensitivities $(\partial\rho/\partial T)$, $(\partial v_f/\partial T)$ and $(\partial Q_s/\partial T)$ together with the normalized sensitivity curves of Eqs. (21) and (22), for a uniform formation with background temperature-unperturbed compressional velocity $v_p = 6670$ m/s, shear velocity $v_s = 3851$ m/s and unperturbed density $\rho = 3000$ kg/m³, for the following parametrizations in the low-frequency approximation at seismic frequencies (Table 1). Burgers and thermal parameters are listed in Table 2. The discussion is focused on sensitivity calculated by Burgers model including shear loss with temperature, Gassmann model with fluid saturation, as well as bulk modulus dependence on pressure (as expressed by Eq. (9)), stiff porosity and permeability. Examples with squirt flow are presented.

Fig. 5a shows the fluid density calculated with the values of Tables 1 and 2 and the temperature gradient of 90 °C/km shown in Fig. 6a. Fig. 5b plots the water pressure versus temperature, where the supercritical zone for temperature and pressure in excess to $T = 374$ °C and 22.1 MPa, respectively, is evidenced. Note that in the region of (a) corresponding to the supercritical zone in (b), the density is lower and consequently the pressure increases with a slower trend as a function of depth and temperature in the supercritical zone of (b).

5.1.1. Seismic velocity

Signals are calculated at the reference frequency $f = 10$ Hz (Table 2), using the linear temperature-depth model $T(z) = z G \times 10^{-3} + T_0$, where $T_0 = T(0) = 20$ °C, with constant gradient $G = 90$ °C/km of Fig. 6a. Fig. 6b shows the wave velocity for P and S waves. Without melting (i.e., neglecting the Burgers viscosity), the wave velocities have minor variations.

In the following figures we interpret contributions due to different physical effects in the plots of the seismic quantities versus temperature. First we compare different behaviors in the responses obtained by velocity and elastic moduli. Fig. 7 represents v_p and v_s in the presence and absence of saturating geothermal fluids, therefore with and without porosity and with and without pressure effects for the moduli. Here and in the following we use the term ‘without porosity’ or ‘zero porosity’ to denote negligible porosity, e.g., less than 0.1 %. In Fig. 7a and b we

Table 1
Rock properties.

Quantity name	Symbol	Value
Solid density	ρ_s	3000 kg/m ³
Solid compressional velocity	v_p	6670 m/s
Solid shear velocity	v_s	3851 m/s
Bulk modulus ($p_d = \infty$) ^a	K_0	69.84 GPa
Shear modulus ($p_d = \infty$) ^a	μ_0	43.57 GPa

^a See Eq. (8).

Table 2
Arrhenius and Burgers model properties.

Quantity name	Symbol	Value
Arrhenius constant	A_∞	100 MPa ⁻ⁿ
Arrhenius exponent	n	2
Activation energy	E	134 kJ/mol
Central frequency	f_0	3 Hz
Relaxation quality factor	Q_0	61
Reference signal frequency	f	10 Hz
Temperature gradient	G	90 °C/km
Tectonic stress anisotropy parameter ^a	ξ	0.8

^a See Eq. (30). Lithostatic stress is calculated with average $\rho_m = 2400 \text{ kg/m}^3$.

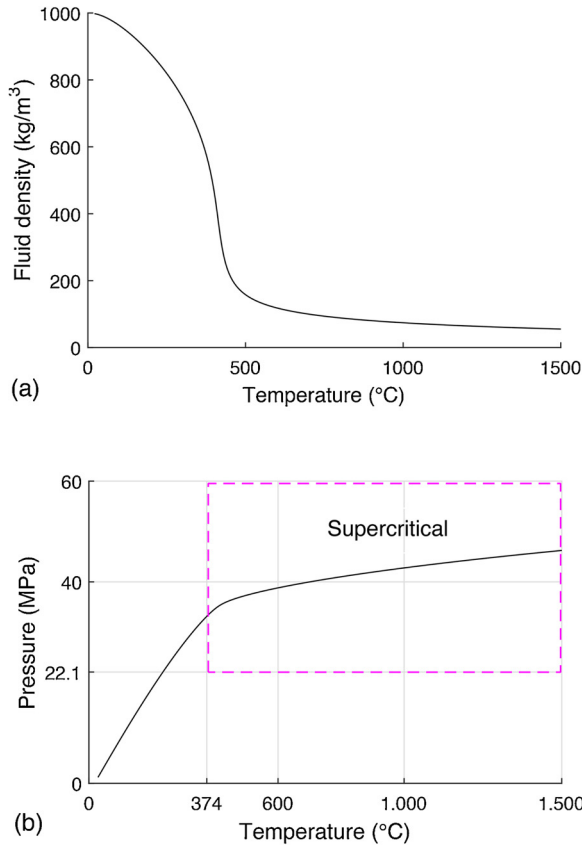


Fig. 5. (a) Fluid (water) density and (b) pressure versus temperature, where the supercritical zone for temperature and pressure in excess to $T = 374 \text{ °C}$ and 22.1 MPa is evidenced.

observe the large effect for v_p and v_s , respectively, in the melting zone, similar for all the curves of the same panels. In the curve of v_p calculated with porosity, shown by the red line in Fig. 7a (stiff porosity $\phi = 0.05$), we observe the zone where the fluid saturation effect, indicated as the ‘Gassman zone’, is more evident, while the curve without porosity is flat in that zone. From this result we deduce that, depending on porosity value, we can use velocity information to investigate the geothermal fluid saturation effects in the model, also when the pressure effects for the bulk modulus are not included. The curve with pressure effects for the bulk modulus (dashed line) presents variations also at lower temperatures, below the melting zones. This corresponds to different sensitivity curves, as we will see what follows. Fig. 7b shows the corresponding curves for the S-wave components, where the Gassmann effect is much less evident. In this case, different from P-wave, the shear velocity tends to zero at high temperatures as expected beyond the melting zone, where the rock is fluid.

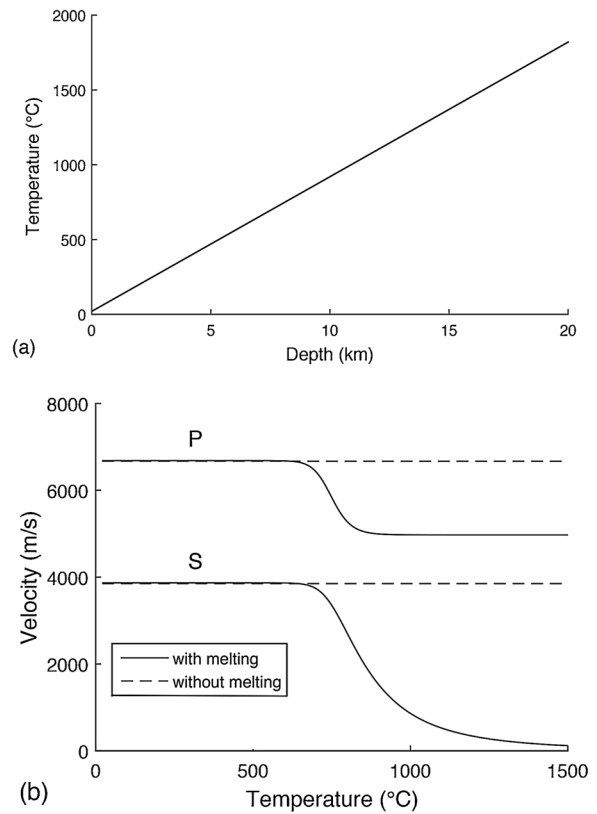


Fig. 6. (a) Constant-gradient linear temperature model starting from surface temperature of 20 °C. (b) P- and S-wave velocities versus temperature. The solid and dashed lines correspond to the cases with and without the Burgers viscosity. The frequency is 10 Hz. In these examples we do not include the effects of fluid pressure on the moduli, to better evidence the effects of the viscosity as a function of temperature.

5.1.2. Seismic stiffness and density

The corresponding curves calculated with the P-wave and S-wave elastic moduli show similar trends with melting. However, as it can be observed in Figs. 8a and b, the same considerations in relation to Gassmann fluid saturation effects in the presence of porosity are not valid for the sensitivity analysis with the elastic moduli. In Fig. 8a we show the P-wave elastic modulus E_p with and without porosity, and pressure effects. We observe that the presence of fluid changes the P-wave elastic modulus in the curves without pressure effects, which becomes lower, but these curves are parallel, therefore they present the same sensitivity. Moreover in the absence of the pressure correction they are both flat below the melting zone. Fig. 8b shows the S-wave elastic modulus E_s with and without porosity and pressure effects for the bulk and shear moduli. In this case the curves with and without porosity are superimposed.

In the presence of porosity and fluid saturation the velocity changes and also the density changes, in such a way that the change in $v_{p,s}^2$ is inversely proportional to that of density, and this creates a compensation effect in the elastic moduli. The compensation effect observed in the flat regions of Fig. 8 is explained using Fig. 9. The result is that there is not variation in $E_{p,s}$ relative to temperature for Gassmann effects. Fig. 9 shows these trends in normalized curves calculated with porosity and without pressure, in this case using both P-wave and S-wave elastic moduli. We compare v_p^2 , v_s^2 and $1/\rho$ by amplitudes normalized at the temperature origin (with unit relative amplitude at $T = 0$). In the region below the melting zone these curves are superimposed, since the product of density and v^2 eliminates the variations relative to temperature due to fluid saturation.

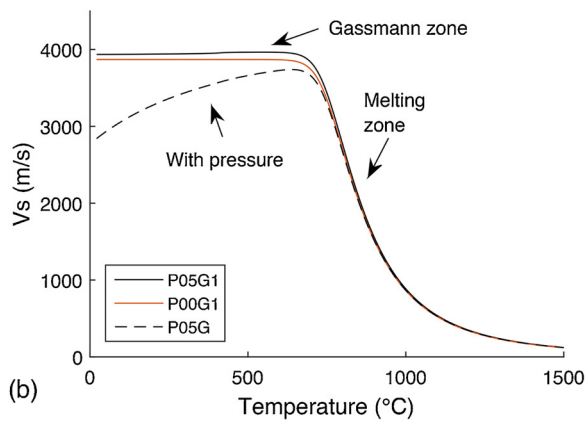
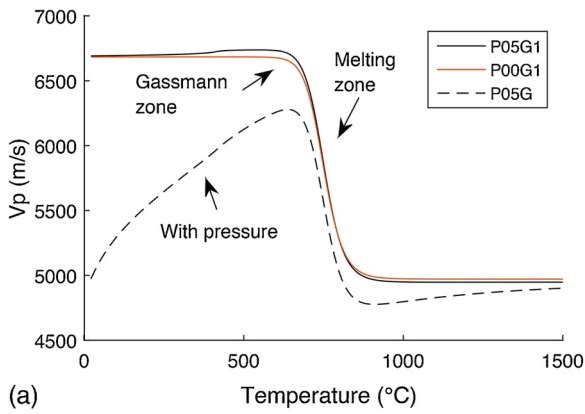


Fig. 7. Plot of (a) P-wave velocity v_p , calculated with and without porosity, and pressure effects for the bulk and shear moduli. In the curve with porosity we observe the fluid Gassmann effect, while the curve without porosity is flat in the Gassmann zone. (b) S-wave velocity v_s , calculated with and without porosity, and pressure effects for the bulk modulus. The curves with and without porosity and both without pressure are superimposed. (See Table 3 for the list of the symbols).

5.1.3. Temperature as a function of seismic quantities

In temperature-velocity regression analysis, e.g., such as in Iovenitti et al. (2013), it is sometimes convenient to exchange the plot axes, and to represent the temperature versus velocity, or other seismic parameters. Fig. 10a shows the plots of temperature as a function of velocity, both using P-wave and S-wave velocities calculated with fluid saturation ($\phi = 5\%$) and pressure effects for the Bulk and shear wave's moduli. Fig. 10b shows the similar plots for the P-wave and S-wave moduli. Obviously, this type of representation depends on the temperature trend versus depth, in this case a gradient. Fig. 11 shows a detail of the same curves of Fig. 10 in a restricted temperature region [100, 600] °C, to better evidence the trends below the melting zone.

5.1.4. Permeability, mobility and attenuation

We extend the poro-viscoelastic model to include the permeability (Carcione et al., 2018a,b). Permeability, according with the depth dependence given by Eq. (16) decreases versus depth, and it can be assumed negligible in the melting zone for the purposes of our sensitivity analysis. The effect is governed by fluid mobility and is dispersive. Fig. 12 shows (a) the fluid viscosity versus temperature and (b) the mobility in the temperature interval [100, 800] °C, below the lower limit of the melting zone. At higher temperatures, mobility is close to zero because the permeability decreases with depth and vanishes in the proximity of the melting zone (Fig. 3b).

The analysis shows that the shear quality factor is sensitive to permeability. Fig. 13a shows the shear-wave Q_s quality factor calculated in

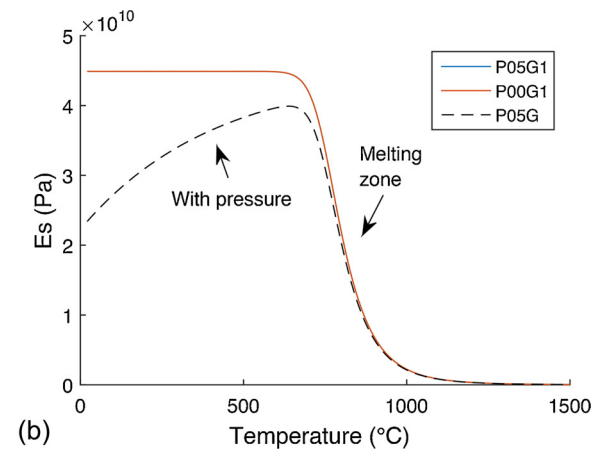
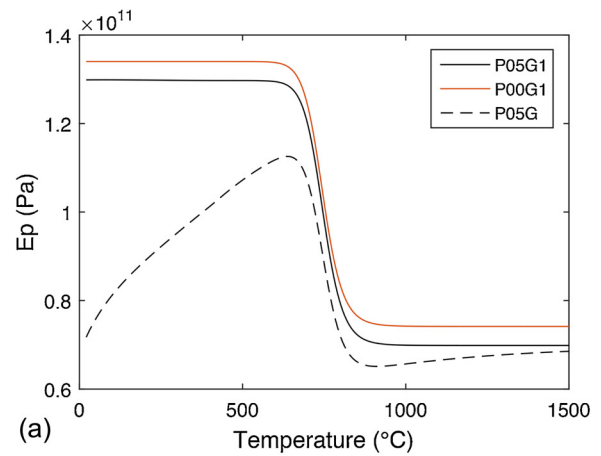


Fig. 8. (a) P-wave modulus E_p curves, calculated with and without porosity, and pressure effects for the bulk and shear moduli. The curves without pressure are parallel, hence they present the same sensitivity to temperature variation. (b) S-wave modulus E_s curves, calculated with and without porosity, and pressure effects for the bulk and shear moduli.

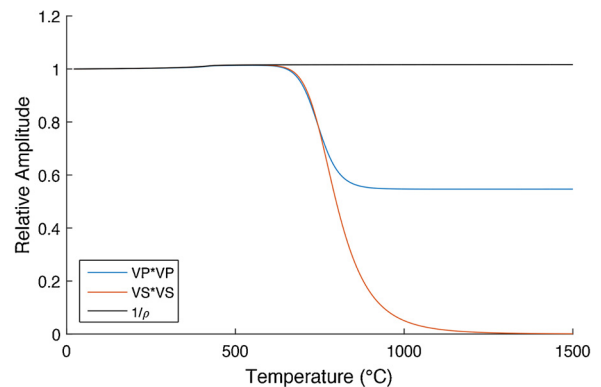


Fig. 9. Normalized compressional and shear squared velocities and normalized reciprocal of density curves. In the zone below the Burgers melting effects the curves are superimposed. No pressure effects are included for the bulk and shear moduli.

the temperature interval [0, 800] °C without and with permeability. The signal frequency is 200 Hz. In this example the unperturbed intrinsic attenuation is low. For permeability, we use the variable function of depth given by Eq. (16). The result shows observable variations with respect to the case without permeability, especially at lower temperatures, where permeability is higher. To evidence possible effects also at higher depths, we test also the approach using constant permeability $\kappa_c = 1.5 \times 10^{-14} \text{ m}^2$ (blue curve in Fig. 13a). In this case

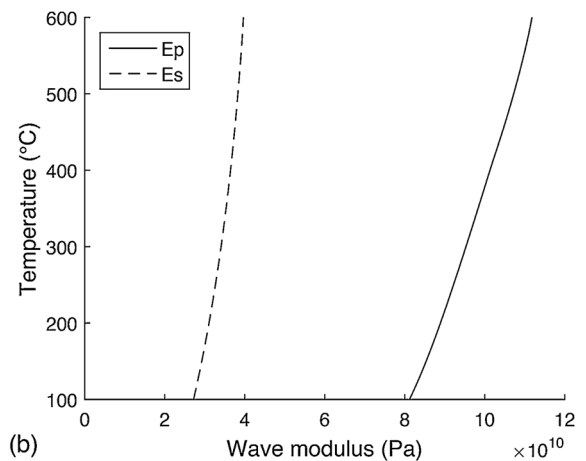
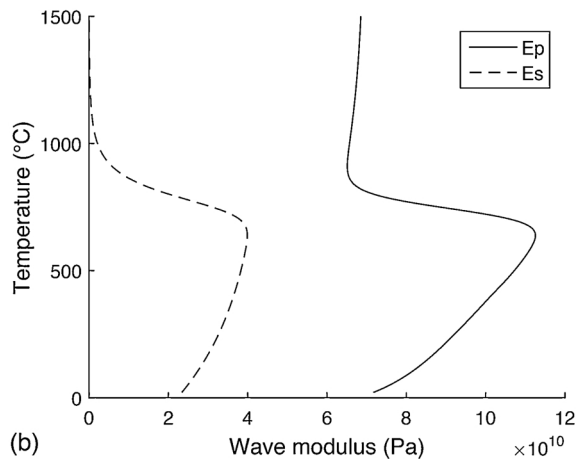
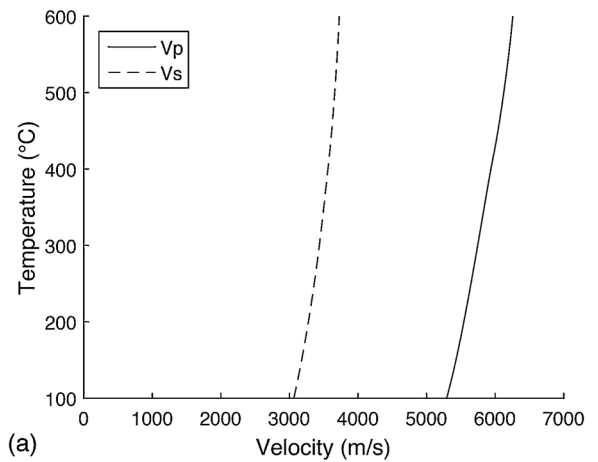
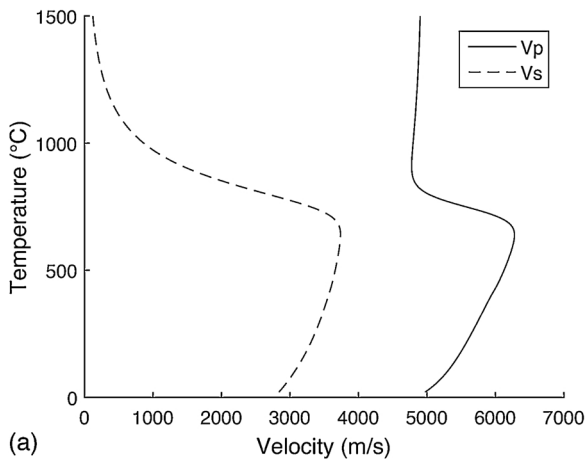


Fig. 10. (a) Plot of temperature as a function of velocity. Curves are calculated for both for P-waves (solid line) and S-waves (dashed line). (b) Plot of temperature versus wave modulus. The curves are calculated both for P-wave (solid line) and S-wave (dashed line) moduli E_p and E_s .

the variation is only due to fluid viscosity. Above $T = 500$ °C, close to the melting zone, all the curves are similar. Fig. 13b shows shear-wave attenuation Q_s^{-1} curves as a function of frequency, and calculated for different mobility values, corresponding to the shallower zone of the model, namely: $M_1 = 1.94 \times 10^{-8}$, $M_2 = 7.13 \times 10^{-9}$, $M_3 = 3.4310^{-9}$ and $M_4 = 1.2110^{-9}$ ($m^2/(Pa \cdot s)$). The result with frequency-shifted attenuation peaks is in agreement with the analysis of Batzle et al. (2006) and the estimation by VSP and open hole in the work of Zhubayev et al. (2013).

5.1.5. Squirt flow

Assuming the presence of stiff and soft porosity (Fig. 4), the squirt flow modulus is calculated using the following parameters: solid density $\rho_s = 3000 \text{ kg/m}^3$ and $K_s = 74.2 \text{ GPa}$ (this value is deduced from Table II of Popp and Kern (1994), intrinsic velocity data at 200 MPa), $h/R = 0.00001$, $K_h = 66.2 \text{ GPa}$ and $\phi_c = 0.00001$. Closure of cracks with confining pressure is reflected in the values of the compliant porosity given in Table II of Popp and Kern (1994), ranging from 0.28% at 12 MPa to 0.01% at 200 MPa. We investigate possible dispersion effects introduced by squirt flow. We observe that K_h , a key value that is the bulk modulus of the hypothetical rock without compliant porosity (Gurevich et al., 2010), determines also the trends of K at low ϕ_c in Eq. (34). To prevent from distorted physical effects at low pressure, otherwise we obtain large differences in K and K_m at shallower depths and lower temperatures with negligible ϕ_c , we have to consider the variability in the compliant porosity with depth. Following Gurevich et al. (2010) the trend in the compliant porosity should satisfy the approximation

Fig. 11. (a) Plot of temperature versus velocity. Detail of Fig. 10a, showing the curves in the temperature interval [100, 600] °C, below melting. The curves are calculated for both for P-waves (solid line) and S-waves (dashed line). (b) Plot of temperature versus wave modulus. Detail of Fig. 10b, showing the curves in the temperature interval [100, 600] °C, below melting. The curves are calculated for both for P-wave (solid line) and S-wave (dashed line) moduli E_p and E_s .

$$\phi_{c(\text{var})} \approx \frac{K_m^{-1} - K_h^{-1}}{\hat{K}_f^{-1} - K_s^{-1}}, \quad (38)$$

where for \hat{K}_f we try both K_f and K_f^* . We also take advantage from the laboratory results reported by Popp and Kern to infer a decay curve for the compliant porosity. These curves are compared in Fig. 14 in the temperature range [0, 900] (°C).

Fig. 15 shows the velocity of (a) P-waves and (b) S-waves calculated with only Burgers (B) at fixed frequency 10 Hz, and Burgers plus squirt flow calculated with variable ϕ_c estimated by Pop and Kern (1994) (P & K), and by Eq. (38) using K_f^* . The model includes porosity and pressure effects. More evident for the P-waves (a), below the melting zone (in this case this is the interpretation zone) the velocity calculated with only Burgers increases when the Burgers model is used together with squirt flow. Fig. 16 shows the corresponding quality factor Q_p and Q_s of (a) P-waves and (b) S-waves, respectively, calculated with only Burgers (B) at fixed frequency 10 Hz, and Burgers plus squirt flow calculated with variable ϕ_c estimated by Pop and Kern (1994) (P & K), and by Eq. (38) using K_f^* . Although the magnitude of the simulated velocities and attenuation can be revised and could be matter of further evaluation for a suitable choice of the rheological parameters in order to calibrate the model in a geothermal context, this result shows that the squirt flow may introduce effects at low frequencies (in this case 10 Hz) depending on compliant porosity estimate.

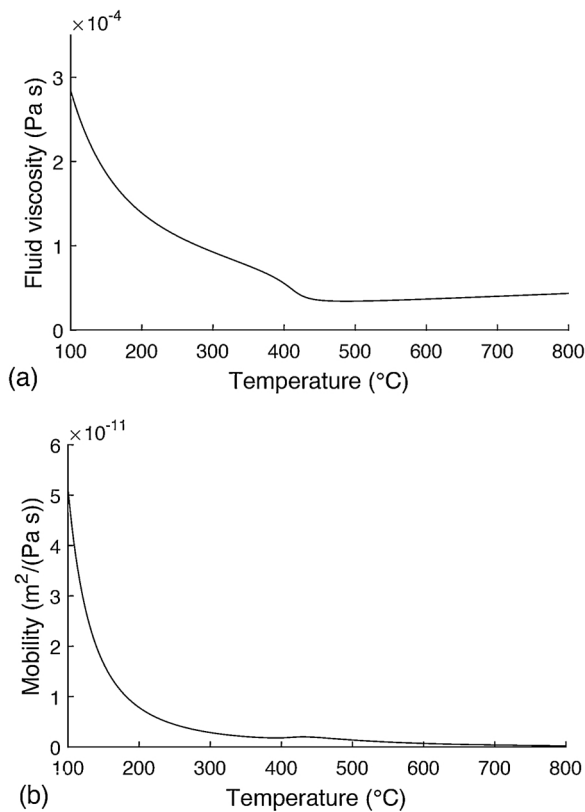


Fig. 12. Plot of (a) fluid viscosity and (b) mobility in the temperature interval [100, 800] °C, below and at the lower limit of the melting zone. At higher temperatures mobility is close to zero because permeability decreases with depth and vanishes in the proximity of the melting zone.

5.2. Sensitivity analysis and interpretation

The numerical sensitivity analysis is performed using the Burgers-Gassmann poro-viscoelastic model with pressure, for four different conditions summarized in Table 3: with and without porosity effects (P05 and P00, respectively), and without and with pressure effects (G1 and G, respectively) for the bulk and shear moduli. Namely, G1 and G denote that no pressure effect is accounted for, and that the pressure effect is accounted for, respectively. For example, the notation P05G in the figures denotes that the porosity $\phi = 0.05$ is used to account for the Gassmann behavior and pressure effects are accounted for to calculate the bulk modulus (see Table 3). Each panel compares these four different sensitivity curves for a selected quantity, by showing the absolute value of the sensitivity in Figs. from 17 to 21.

The interpretative analysis shows the different temperature regions where the sensitivity variations related to the physical effects are more important, for the different model curves. Not all the curves in the panels are affected by the same effects. In all the panels, the Burgers melting is the more important effect. Superimposed are the Gassmann fluid effect with porosity and fluid saturation, and the effect related to pressure-induced bulk modulus variation. Permeability introduces moderate effects for velocity and attenuation of shear waves.

Fig. 17a shows the sensitivity curves for v_p . In the presence of porosity and fluid-saturation we observe Gassmann effects. With pressure-bulk modulus correction we observe evidence of trends at low temperatures. The arrows indicate schematically the zones in which the different effects are more relevant for the sensitivity, displayed by absolute value. Similar to Fig. 17a, Fig. 17b shows the sensitivity curves for v_s . Note the different extension along the temperature axis of the Burgers melting sensitivity region with respect to v_p . Fig. 18a shows the sensitivity curves for the P-wave elastic modulus E_p . A weaker

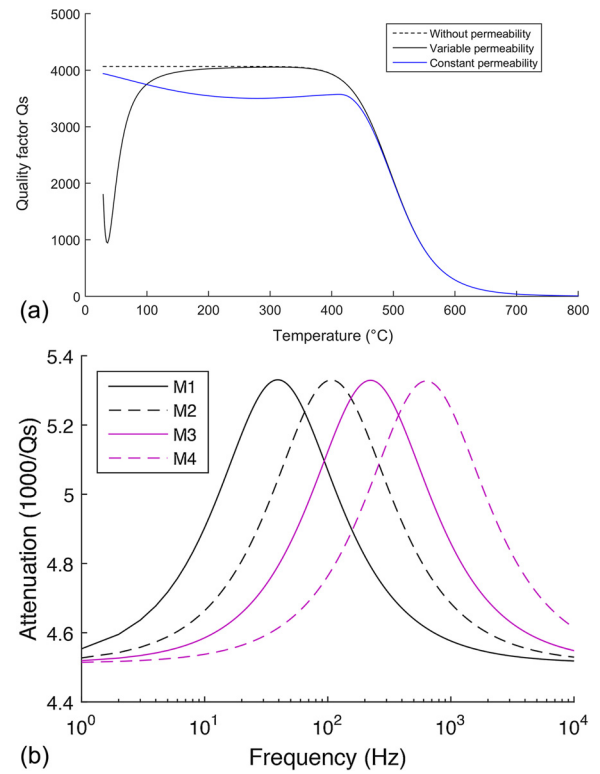


Fig. 13. (a) Plot of the shear-wave Q_S quality factor calculated in the temperature interval [0, 800] °C without and with variable and constant permeability. (b) Shear-wave attenuation Q_S^{-1} curves plotted versus frequency, and calculated with different mobility values.

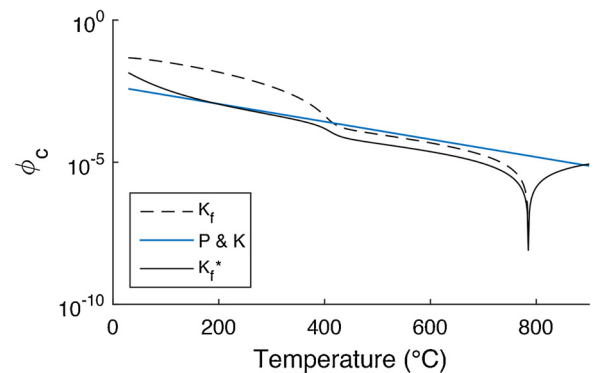


Fig. 14. Soft porosity ϕ_c variable with depth and temperature. Curves are estimated by K_f , Popp and Kern graphic regression (1994), and K_f^* .

Gassmann effect is observable, only with both porosity and pressure-bulk correction. Fig. 18b shows the sensitivity curves for the S-wave elastic modulus E_s . As expected, Gassmann effects are not observable in the shear sensitivity plots.

The analysis is also applied to attenuation effects. Fig. 19a shows the sensitivity curves for the Q_p factor. Prevalent effect of Burgers melting can be observed, also at high temperatures, where the sensitivity of Q_p increases. Fig. 19b shows the sensitivity curves for Q_s . All the curves are superimposed, and only the effect of Burgers melting is present, in this case only in the melting zone around the peak approximately at 500 °C. For Q_s , we observe that there is no increase in the sensitivity for increasing temperature as for Q_p , since after melting the shear waves do not propagate in the magma fluid. Finally, in Fig. 20a we see the sensitivity (absolute value) of the shear quality factor Q_S calculated without and with – variable and constant – permeability. These sensitivity data are calculated using the signals shown in Fig. 13a in the

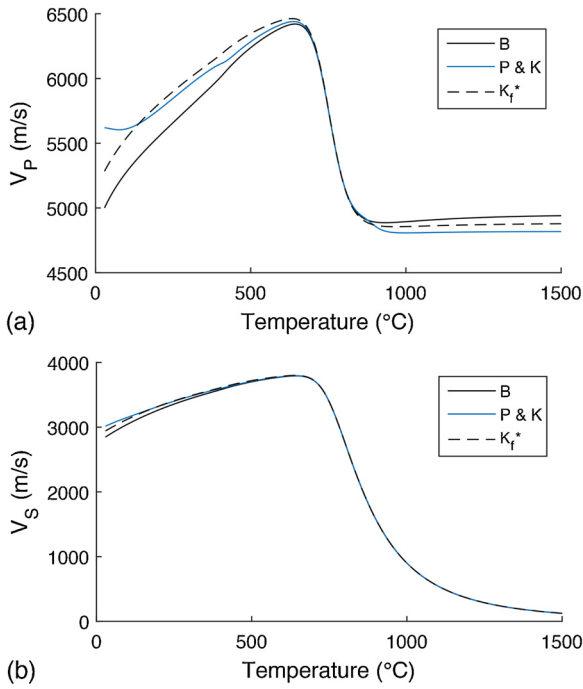


Fig. 15. Velocity of (a) P-waves and (b) S-waves including porosity and pressure calculated with only Burgers (B) at fixed frequency 10 Hz, and Burgers plus squirt flow calculated with variable ϕ_c estimated by Pop and Kern (1994) (P & K), and by Eq. (38) using K_f^* .

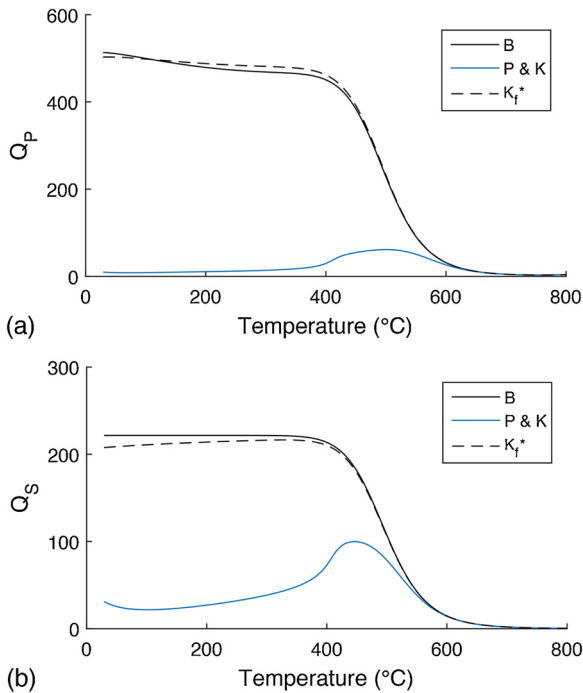


Fig. 16. Quality factor of (a) P-waves and (b) S-waves including porosity and pressure calculated with only Burgers (B) at fixed frequency 10 Hz, and Burgers plus squirt flow calculated with variable ϕ_c estimated by Pop and Kern (1994) (P & K), and by Eq. (38) using K_f^* .

temperature interval [0, 800] °C. We observe, especially at shallower depths and lower temperatures, significant variations of sensitivity for the curves calculated with variable permeability, decreasing with depth, and constant permeability (see the example of Fig. 13a).

Fig. 20b shows the sensitivity curves calculated for density ρ . Relevant variation of its sensitivity calculated with porosity and fluid

Table 3

Scheme of symbols used to denote labels for physical parameters.

Label marker	Quantity name	Symbol and/or value
P00	Stiff porosity	$\phi = 0$
P05	Stiff porosity	$\phi = 0.05$
G1	Flag – pressure-effect for bulk and shear moduli	No
G	Flag – pressure-effect for bulk and shear moduli	Yes

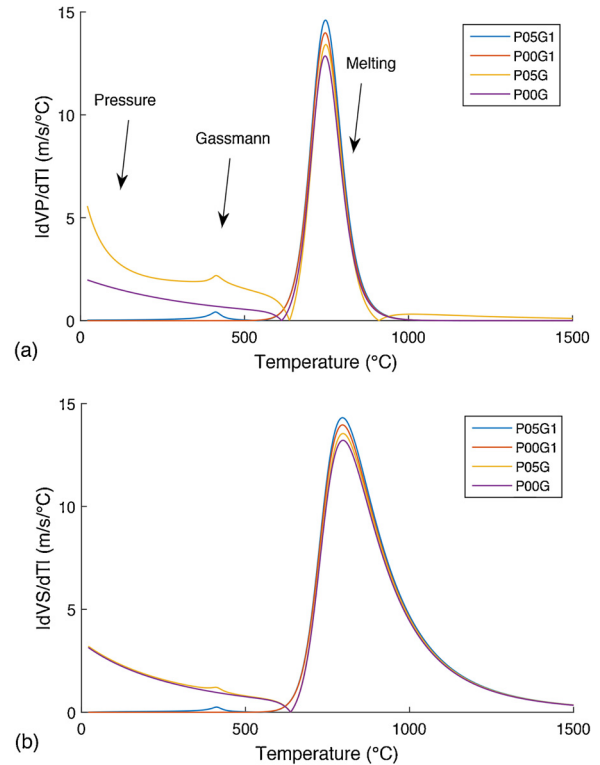


Fig. 17. (a) Characteristic sensitivity curves for v_p . With porosity we observe Gassmann effects, including the supercritical zone. With bulk and shear moduli correction for pressure we observe effects and trends at low temperatures. (b) Characteristic sensitivity curves for v_s . Note the different extension of the Burgers melting sensitivity zone with respect to v_p .

saturation is observable, and interpreted also as related to supercritical effects assuming as geothermal fluid pure water.

All these examples show that the different quantities provide, with different extents and case by case, better estimations of sensitivity in different temperature regions. In Fig. 21 we compare the absolute values of the normalized sensitivity curves of different elastic quantities. The curves in this superposition cover with different responses different temperature regions. Note that, as observable in the previous plots, the peaks of the sensitivity are at different temperatures for velocity (at approximately 800 °C) and quality factor (at approximately 500 °C). We may better observe the out-of phase trends of attenuation and dispersion in the next figure.

In Fig. 22a we compare the corresponding relative sensitivity responses (S by Eq. (27)) for the same quantities of Fig. 21, i.e., each curve represents its relative variation with respect to its physical value at the given temperature per temperature degree. In this case the sensitivity curves are plotted with positive and negative signs, to show the polarity of the relative variations. In this figure, the out-of-phase behavior of velocity and Q-factor is more evident. This is similar to the fact that for causal physical signals dispersion and attenuation are Kramers-Krönig pairs (e.g., Sun et al., 2009). We may see that a relevant

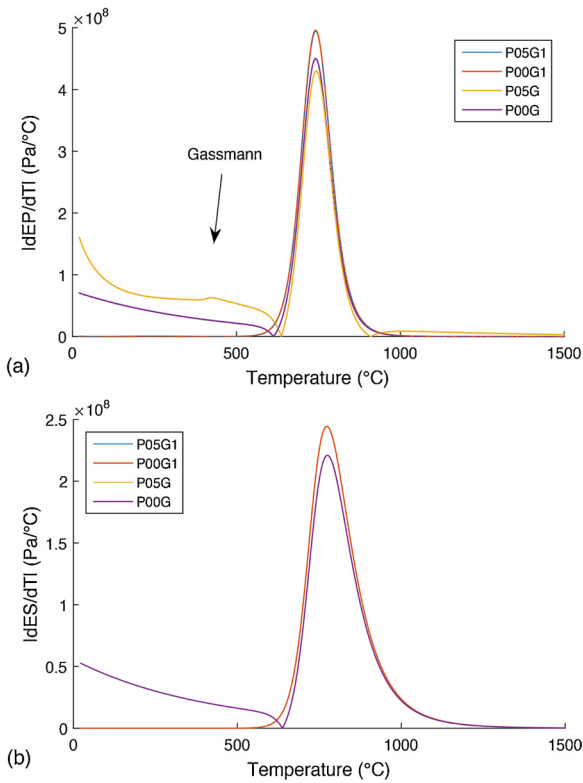


Fig. 18. (a) Characteristic sensitivity curves for P-wave elastic modulus E_p . A weaker Gassmann effect is observable only with both porosity and pressure-bulk correction. (b) Characteristic sensitivity curves for S-wave elastic modulus E_s . Gassmann effects are not observable.

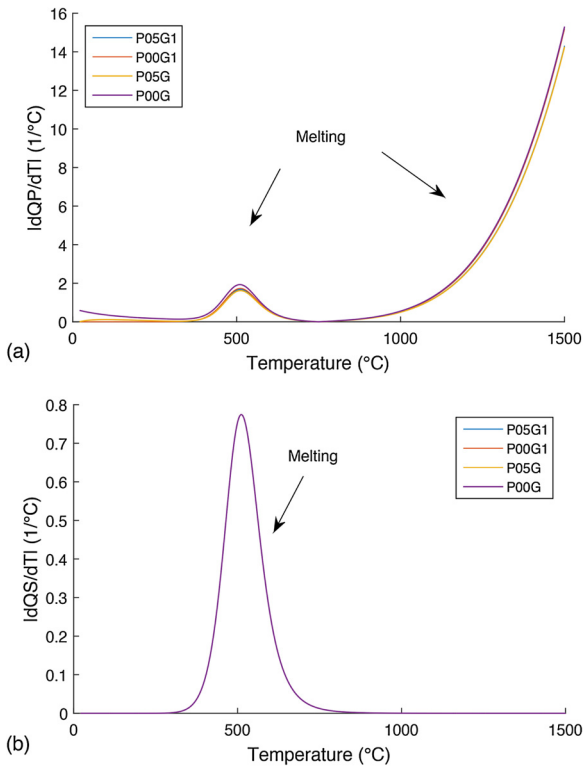


Fig. 19. (a) Characteristic sensitivity curves for Q_p . Prevalent effect of Burgers melting is observable, also at high temperatures. (b) Characteristic sensitivity curves for Q_s . All the curves are superimposed, only the effect of Burgers melting is present.

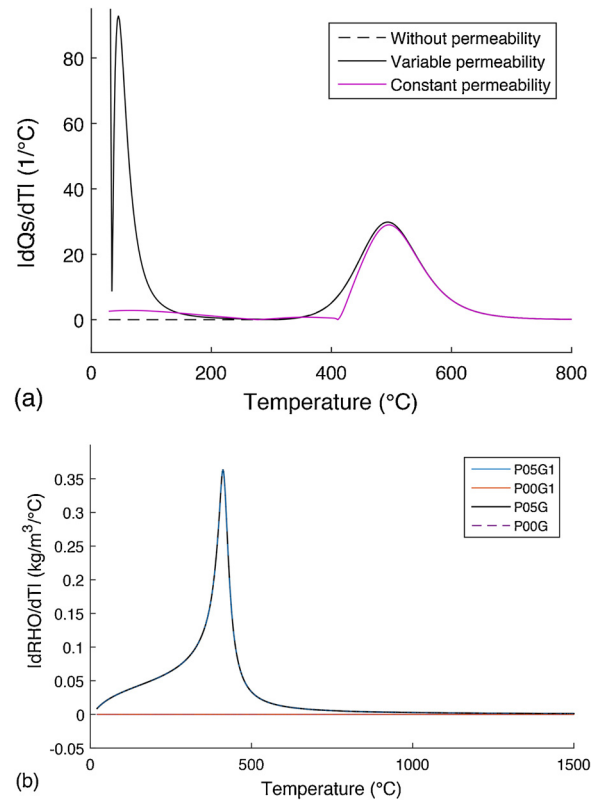


Fig. 20. (a) Sensitivity (absolute value) of the shear quality factor Q_s calculated without and with – variable and constant – permeability. Data correspond to the physical signals shown in Fig. 13a. (b) Characteristic sensitivity curves for density. Relevant variation can be observed only with porosity and fluid saturation.

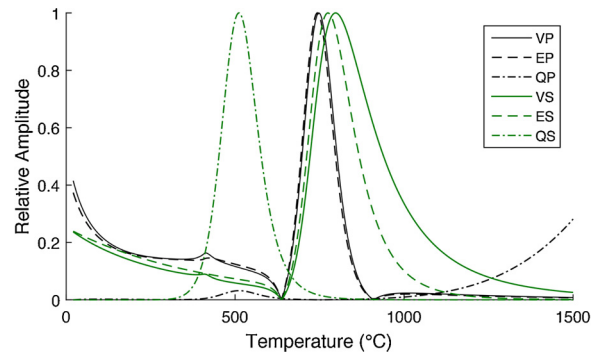


Fig. 21. Comparison of normalized sensitivity curves of different viscoelastic quantities.

observability effect is obtained in the melting zone using the Q-factor, and in general more prominent with shear components. Fig. 22b shows the estimated, and approximated as previously discussed, reflection coefficient calculated by $S_r \times \Delta T$ at each T value using Eq. (27) for compressional- and shear-wave impedances and a temperature interval $\Delta T = 10^\circ\text{C}$, as with a step ΔT between two uniform temperature zones. Also in this plot we display the curves with positive and negative signs. This provides an estimation of the reflection response related only to the temperature model.

Finally, it is typically convenient using the reciprocal of sensitivity to predict (in stable regions, i.e., where the sensitivity is different from zero) temperature variations for an increment of velocity. Fig. 23 shows the predicted temperature variation

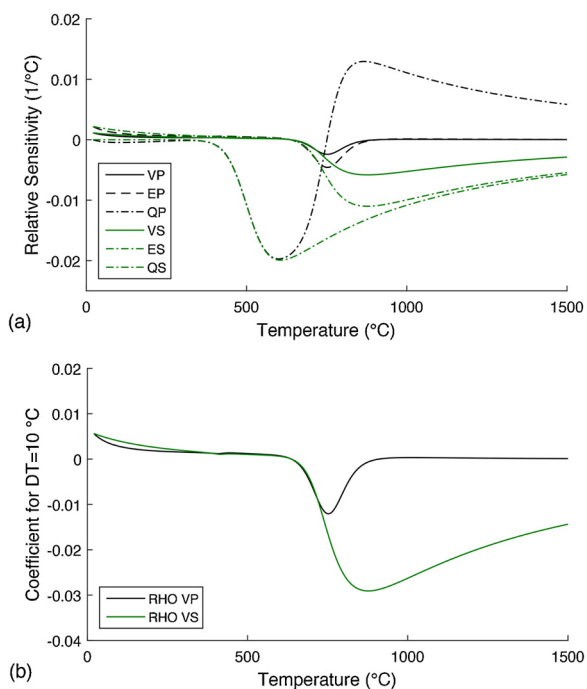


Fig. 22. (a) Comparison of relative sensitivity curves of different viscoelastic quantities. (b) Comparison of relative sensitivity curves (semi amplitude plot) calculated for compressional and shear impedances with a temperature interval of 10 °C.

$$\Delta T_{p,s} = \left(\frac{1}{s_{p,s}} \right) \Delta v_{p,s}, \quad (39)$$

calculated for P- and S-velocities using the reciprocal sensitivity $s_{p,s}^{-1} = \partial T / \partial v_{p,s}$ (a) with a velocity increment $\Delta v_p = 100$ m/s and (b) $\Delta v_s = 58$ m/s. In both the P-wave and S-wave plots we observe zones where an increment in the velocity can correspond both to an increment or to a decrease of the temperature in the different regions interpreted in the figures. Note that higher sensitivity means higher detectability of velocity changes induced by temperature, and a more stable result for a given velocity variation when we predict temperature from velocity. For example, a large P-wave velocity variation of 100 m/s at $v_p = 5800$ m/s in the melting zone in Fig. 23a corresponds to a decrease in the temperature of approximately 10 °C, while in the pressure zone it corresponds to an increase in temperature of approximately 50 °C.

6. Discussion and research perspectives

The paper presents a comprehensive analysis of temperature effects for fluid-saturated rock together with a theoretical basis and models for the seismic characterization of geothermal formations. The interpretation of results points out different trends and effects in the sensitivity analysis. These are related to different models corresponding to specific physical effects. The interaction of these physical conditions and effects is typically complex. In this analysis, the choice and definition of the temperature distribution map, approximated by a constant-gradient model for our purposes, is of great importance.

The characteristic sensitivity examples shown here for a case study are numerically calculated at fixed parameters, using a set of physical configurations, and low frequency, and are not exhaustive for a characterization of geothermal systems belonging to different and much more complex geological scenarios. For example, the change of the rock type and of its Arrhenius parameters, as well as tectonic stresses, may change the melting temperature and this may cause a different superposition of the physical effects in the sensitivity curves versus

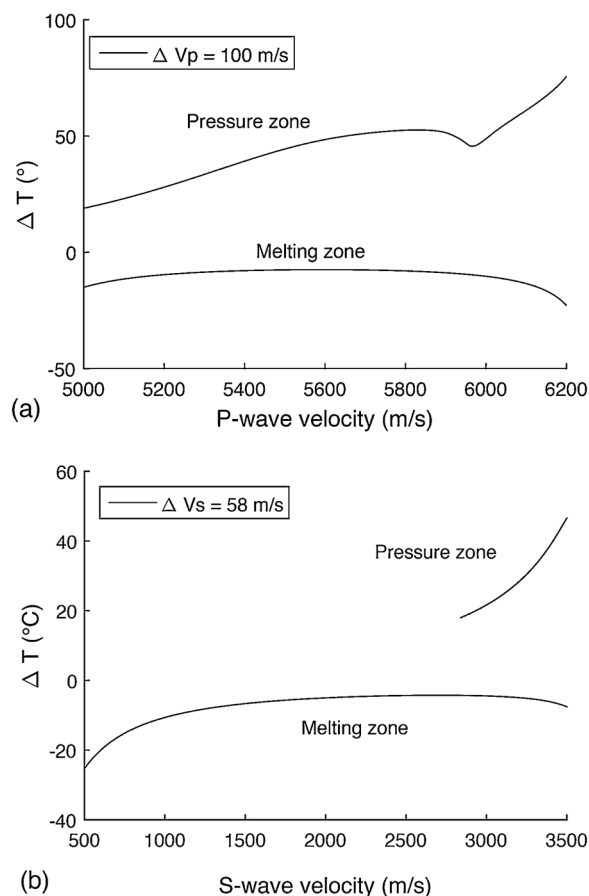


Fig. 23. Temperature variation ΔT calculated using the reciprocal sensitivity s^{-1} (Eq. (28)) (a) with a velocity increment $\Delta v_p = 100$ m/s in the P-velocity interval [5000, 6200] m/s, and (b) $\Delta v_s = 58$ m/s in the S-velocity interval [500, 3500] m/s. In both the compressional and shear panels we observe zones where an increment in the velocity can correspond both to an increment or to a decrease of the temperature.

temperature. The change of the geothermal fluid properties (e.g., [Jaya et al., 2010](#)) may change the supercritical point, here assumed to be that of pure water, hence pressure and density curves used in the numerical calculations. Further corrections and improvements can be introduced to take into account further physical effects and relationships, as well as experimental evidences in the modeling and sensitivity analysis of geothermal seismic properties and wave fields, such as those of the Mexican high-enthalpy areas (GEMex Project, 2016). In this case, the main targets will be to characterize seismically the super-hot geothermal systems, investigate the permeability and fracturation conditions, evaluate the possible presence of fluids at supercritical conditions, and contribute to map possible magmatic zones (BDT) interpreted in the proximity of the investigated areas, thus supporting geothermal exploration and future exploration and production drilling.

7. Conclusions

Understanding the sensitivity of seismic quantities to temperature is of great importance for the seismic characterization of geothermal reservoirs. Especially at high temperatures, detection and monitoring of melting and supercritical zones, as well as influence of pressure on the bulk and shear moduli require appropriate sensitivity analysis. In this paper we present the Burger–Gassmann theory following previous studies and numerical-code developments, including permeability and involving squirt-flow effects to some extent, and study characteristic sensitivity curves in the low-frequency approximation. Results show the

different observability by different elastic components, with different prevalence of the physical effects in different temperature regions. This suggests the use of an integrated analysis by more seismic elastic quantities for the characterization of geothermal areas, which can be applied either to exploration or to passive seismology data, including volcanic environments.

The characteristic sensitivity is here calculated for a set of physical models. Based on a quantification of the physical properties, the results show that in deeper zones the main expected contributions in terms of variations in seismic velocity, moduli and seismic attenuation due to temperature come from melting transition, while in shallower porous fluid-saturated formations the trends are mainly governed by pressure effects, with minor contributions of permeability and possible effects related to the compliant soft porosity. In the region corresponding to the supercritical zone, the fluid density is lower and consequently the pressure increases with a slower trend as a function of depth and temperature. Without melting (i.e., neglecting the Burgers viscosity), the wave velocities have minor variations. Depending on porosity, we can use velocity information to retrieve the fluid saturation. The trend including pressure effects in the bulk and shear moduli presents variations even at low temperatures. The Gassmann effect is less evident in the S-wave velocity, which tends to zero at high temperatures due to melting, as expected. In the curves calculated without pressure effects for the bulk and shear moduli, the presence of fluid changes the P-wave elastic modulus which becomes lower than that calculated in the absence of fluid, but these curves are parallel, therefore they present the same sensitivity. For the S-wave elastic modulus with and without porosity and pressure effects the curves are practically superimposed. In the presence of porosity with fluid saturation the velocity and the density change, in such a way that the P-wave modulus is almost constant with temperature regarding the Gassmann effects. In the analysis of temperature as a function of seismic quantities by reciprocal sensitivity, not always the increments in the velocity and elastic wave moduli correspond to an increment in the temperature. For example, the same increment in the S-wave velocity may correspond to an increase in the temperature in a zone where pressure effects are observed and to a decrease in the temperature in the melting zone.

The fluid viscosity decreases initially as a function of temperature and then increases slowly in the supercritical zone. At high temperatures, the fluid mobility is close to zero because the permeability decreases with depth and vanishes in the melting zone. The analysis shows that the shear quality factor is sensitive to permeability. Permeability introduces moderate effects for velocity and attenuation of shear waves. We observe these effects, especially at shallower depths and low temperatures, for the curves calculated with variable permeability, decreasing with depth. Moreover, assuming a constant-permeability model, we study the potential permeability effects for deeper zones.

In this analysis, the choice and definition of the temperature distribution map, approximated by a constant gradient for our purposes, is important. The change of the rock type and its Arrhenius parameters, as well as the tectonic stresses, may change the melting temperature and this may cause a different distribution of the physical effects, partially superimposed in the sensitivity curves. The change of the geothermal fluid properties affects the supercritical point, here assumed to be that of pure water, hence the pressure and density curves used in the calculations.

Next, we plan to apply the analysis to real cases, such those of the Mexican high enthalpy regions, where the main targets are to characterize seismically the super-hot geothermal systems, including the temperature, evaluate the possible presence of supercritical-fluid conditions, and contribute to map possible magmatic zones interpreted in the proximity of the investigated areas.

Acknowledgements

This project has received funding from the European Union's Horizon 2020 research and innovation programme under grant agreement No. 727550. Fruitful discussion and suggestions on relations between temperature and seismic velocity and elastic moduli were given by Dimitrios Mendrinou.

References

- Batini, F., Bertini, G., Gianelli, G., Pandeli, E., Puxeddu, M., 1983. Deep structure of Larderello field: contribution from recent geophysical and geological data. *Mem. Soc. Geo. It* 25, 219–235.
- Batzle, M., Han, D., Hofmann, R., 2006. Fluid mobility and frequency-dependent seismic velocity direct measurements. *Geophysics* 71 (1), N1–N9.
- Berryman, J.G., 1980. Confirmation of Biot's theory. *Appl. Phys. Lett.* 37, 382–384.
- Blanck, H., Jousset, P., Ágústsson, K., Hersir, G.P., Flóvenz, Ó.G., 2016. Analysis of seismological data on Reykjanes peninsula, Iceland. In: *Proceedings, European Geothermal Congress*. Strasbourg, France 2016.
- Carcione, J.M., 2014. Wave fields in real media: wave propagation in anisotropic, an elastic, porous and electromagnetic media. *Handbook of Geophysical Exploration*, 3rd ed. Elsevier, Amsterdam revised and extended.
- Carcione, J.M., Helle, H.B., Gangi, A.F., 2006. Theory of borehole stability when drilling through salt formations. *Geophysics* 71, F31–F47.
- Carcione, J.M., Gurevich, B., 2011. Differential form and numerical implementation of Biot's poroelasticity equations with squirt dissipation. *Geophysics* 76, N55–N64.
- Carcione, J.M., Gurevich, B., Cavallini, F., 2000. A generalized Biot–Gassmann model for the acoustic properties of shaly sandstones. *Geophys. Prosp.* 48, 539–557.
- Carcione, J.M., Poletto, F., 2013. Seismic rheological model and reflection coefficients of the brittle–ductile transition. *Pure Appl. Geophys.* <https://doi.org/10.1007/s00024-013-0643-4>.
- Carcione, J.M., Poletto, F., Farina, B., 2018a. The Burgers/squirt-flow seismic model of the crust and mantle. *Phys. Earth Planet. Interiors* 274, 14–22.
- Carcione, J.M., Poletto, F., Farina, B., Bellezza, C., 2018b. 3D seismic modeling in geothermal reservoirs with a distribution of steam patch sizes, permeabilities and saturations, including ductility of the rock frame. *Phys. Earth Planet. Interiors* 279, 67–78.
- Carcione, J.M., Poletto, F., Farina, B., Craglietto, A., 2014. Simulation of seismic waves at the Earth's crust (brittle–ductile transition) based on the Burgers model. *Solid Earth Discuss.* 6, 1371–1400.
- Carcione, J.M., Poletto, F., Farina, B., Craglietto, A., 2017. The Gassmann–Burgers model to simulate seismic waves at the Earth crust and mantle. *Pure Appl. Geophys.* 174, 849–863. <https://doi.org/10.1007/s00024-016-1437-2>.
- Castro, R.R., Gallipoli, M.R., Mucciarelli, M., 2008. Crustal Q in southern Italy determined from regional earthquakes. *Tectonophysics* 457 (2), 96–101.
- Cermak, V., Bodri, L., Rybach, L., Buntebarth, G., 1990. Relationship between seismic velocity and heat production: comparison of two sets of data and test of validity. *Earth Planet. Sci. Lett.* 99 (1–2), 48–57.
- Chauveau, B., Kaminski, E., 2008. Porous compaction in transient creep regime and implications for melt, petroleum, and CO₂ circulation. *J. Geophys. Res.* 113, B09406.
- Dobson, P., Asanuma, H., Huenges, E., Poletto, F., Reinsch, T., Sanjuan, B., 2017. Supercritical geothermal systems – a review of past studies and ongoing research activities. *Proceedings, 41st Workshop on Geothermal Reservoir Engineering*. Stanford University, Stanford, California, pp. 13.
- Dragoni, M., Pondrelli, S., 1991. Depth of the brittle–ductile transition in a trans-crustal boundary zone. *Pure Appl. Geophys.* 135, 447–461.
- Engelder, T., 1993. *Stress Regimes in the Lithosphere*. Princeton University Press.
- Ehrenberg, S.N., Nadeau, P.H., 2005. Sandstone vs. carbonate petroleum reservoirs: a global perspective on porosity–depth and porosity–permeability relationships. *AAPG Bull.* 89 (April (4)), 435–445.
- Farina, B., Poletto, F., Carcione, J., 2016. Seismic wave propagation in poro-viscoelastic hot rocks. In: *Proceedings, European Geothermal Congress*. Strasbourg, France, pp. 7.
- Farina, B., Poletto, F., Carcione, J.M., 2017. Seismic wave propagation in geothermal hot rocks: a review of simulation analysis and results based on Burgers models. *79th EAGE Conference and Exhibition, Workshop*. <https://doi.org/10.3997/2214-4609.201701769>.
- Gangi, A.F., 1981. A constitutive equation for one-dimensional transient and steady-state flow of solids. *Mech. Behav. Crustal Rocks Geophys. Monogr.* 24 (AGU), 275–285.
- Gangi, A.F., 1983. Transient and steady-state deformation of synthetic rocksalt. *Tectonophysics* 91, 137–156.
- GEMex, 2016. H2020 Project: GEMex: Cooperation in Geothermal Energy Research Europe-Mexico for Development of Enhanced Geothermal Systems and Superhot Geothermal Systems: European Union's Horizon 2020 Research and Innovation Programme Under Grant Agreement No. 727550.
- Gurevich, B., Makarynska, D., Pervukhina, M., 2009. Ultrasonic moduli for fluid-saturated rocks: Mavko–Jizba relations rederived and generalized. *Geophysics* 74 (4), N25–N30. <https://doi.org/10.1190/1.3123802>.
- Gurevich, B., Makarynska, D., Pervukhina, M., De Paula, O., 2010. A simple model for squirt-flow dispersion and attenuation in fluid-saturated granular rocks. *Geophysics* 75 (6), N109–N120. <https://doi.org/10.1190/1.3509782>.
- Hashida, T., Bignall, G., Tsuchiya, N., Takahashi, T., Tanifuji, K., 2001. Fracture generation and water-rock interaction process in supercritical deep-seated geothermal reservoirs. *Geotherm. Resour. Council Trans.* 25, 225–229.

- Hegret, G., 1987. Stress assumption for underground excavation in the Canadian Shield. *Int. J. Rock Mech. Min. Sci. Geomech. Abstr.* 24, 95–97.
- Hickman, S., Sibson, R., Bruhn, R., 1995. Introduction to special section: mechanical involvement of fluids in faulting. *J. Geophys. Res.* 100 (B7) pages 12, 831–12, 840 July 10.
- Iovenitti, J., Sainsbury, J., Tibuleac, I.M., Karlin, R., Wanamaker, P., Maris, V., Blackwell, D., Thakur, M., Ibsen, F.H., Lewicki, J., Kennedy, B.M., Swyer, M., 2013. EGS exploration methodology project using the Dixie Valley geothermal system, Nevada, status update. 38th Workshop on Geothermal Reservoir Engineering. Stanford University, Stanford, California, February 11–13.
- Ito, T., Zoback, M.D., 2000. Fracture permeability and in situ stress to 7 km depth in the KTB Scientific Drillhole. *Geophys. Res. Lett.* 27 (April (7)), 1045–1048.
- Jaya, M.S., Shapiro, S.A., Kristinsdóttir, L.H., Bruhn, D., Milsch, H., Spangenberg, E., 2010. Temperature dependence of seismic properties in geothermal rocks at reservoir conditions. *Geothermics* 39 (1), 115–123. <https://doi.org/10.1016/j.geothermics.2009.12.002>.
- Kaselow, A., Shapiro, S.A., 2004. Stress sensitivity of elastic moduli and electrical resistivity in porous rocks. *J. Geophys. Eng.* 1, 1–11.
- Krief, M., Garat, J., Stellingwerff, J., Ventre, J., 1990. A petrophysical interpretation using the velocities of P and S waves (full waveform sonic). *Log Anal.* 31, 355–369.
- Kristinsdóttir, L.H., Flóvenz, Ó., Árnason, K., Bruhn, D., Milsch, H., Spangenberg, E., Kulenkampff, J., 2010. Electrical conductivity and P-wave velocity in rock samples from high-temperature Icelandic geothermal fields. *Geothermics* 39 (1), 94–105.
- Majer, E.L., Baria, R., Stark, M., Oates, S., Bommer, J., Smith, B., Asanuma, H., 2007. Induced seismicity associated with Enhanced Geothermal Systems. *Geothermics* 36, 185–222.
- Mavko, G., Mukerji, T., Dvorkin, J., 2009. *The Rock Physics Handbook: Tools for Seismic Analysis in Porous Media*. Cambridge Univ. Press.
- Mavko, G., Jizba, D., 1991. Estimating grain-scale fluid effects on velocity dispersion in rocks. *Geophysics* 56, 1940–1949.
- Manning, C.E., Ingebritsen, S.E., 1999. Permeability of the continental crust: the implications of geothermal data and metamorphic systems. *Rev. Geophys.* 37, 127–150.
- Montesi, L.G.J., 2007. A constitutive model for layer development in shear zones near the brittle-ductile transition. *Geophys. Res. Lett.* 34, L08307. <https://doi.org/10.1029/2007GL029250>.
- Niitsuma, H., Fehler, M., Jones, R., Wilson, S., Albright, J., Green, A., Baria, R., Hayashi, K., Kaieda, H., Tezuka, K., Jupe, A., Walrothy, T., Cornet, F., Asanuma, H., Moriya, H., Nagano, K., Phillips, W.S., Rutledge, J., House, L.S., Beauce, A., Aldge, D., Aster, R., 1999. Current status of seismic and borehole measurements for HDR/HWR development. *Geothermics* 28 (4-5), 475–490.
- Poletto, F., Corubolo, P., Schleifer, A., Farina, B., Pollard, J., Grozdanic, B., 2011. Seismic while drilling for geophysical exploration in a geothermal well. *Geothermal Resources Council Transactions* 1737–1741.
- Poletto, F., Miranda, F., 2004. *Seismic While Drilling. Fundamentals of Drill-Bit Seismic for Exploration*. Elsevier, Amsterdam.
- Popp, T., Kern, H., 1994. The influence of dry and water saturated cracks on seismic velocities of crustal rocks – a comparison of experimental data with theoretical model. *Surveys in Geophysics* 15, 443–465.
- Reinsch, T., Dobson, P., Asanuma, H., Huenges, E., Poletto, F., Sanjuan, B., 2017. Utilizing supercritical geothermal systems – a review of past ventures and ongoing research activities. *Geotherm. Energy* 5 (16). <https://doi.org/10.1186/s40517-017-0075-y>.
- Sun, L.F., Milkereit, B., Schmitt, D.R., 2009. Measuring velocity dispersion and attenuation in the exploration seismic frequency band. *Geophysics* 74, 113–122.
- Tibuleac, I.M., Iovenitti, J., von Seggern, D., Sainsbury, J., Biasi, G., Anderson, J.G., 2013. Development of exploration methods for engineered geothermal systems through integrated geophysical, geologic and geochemical interpretation: The seismic analysis component. In: 38th Workshop on Geothermal Reservoir Engineering Stanford University. Stanford, California, February 11–13.
- Urban, E., Lermo, J.F., 2013. Local seismicity in the exploration of Los Humeros geothermal fields, Mexico. In: 38th Workshop on Geothermal Reservoir Engineering. Stanford University, Stanford, California, February 11–13.
- Vinciguerra, S., Trovato, C., Meredith, P.G., Benson, P.M., Troise, C., Natale, G.D., 2006. Understanding the seismic velocity structure of Campi Flegrei Caldera (Italy): from the laboratory to the field case. *Pure Appl. Geophys.* 163, 2205–2221.
- Zhubayev, A., Jihai, Y., Jun, C., Borodin, B., Sanders, M., Lim, T.K., Menkiti, H., Ghose, R., 2013. Fluid mobility in reservoir rocks from integrated VSP and openhole data. Expanded Abstracts, SEG Houston 2013 Annual Meeting, 2964–2968. <https://doi.org/10.1190/segam2013-0213.1>.

ANNEX II

Seismic properties in conductive and convective hot and super-hot geothermal systems

Biancamaria Farina^(*), Flavio Poletto^(*), Dimitrios Mendrinis^(),
José M. Carcione^(*) and Constantine Karytsas^(**)**

(*) OGS - Istituto Nazionale di Oceanografia e di Geofisica Sperimentale,
Borgo Grotta Gigante 42c, 34010 Sgonico, Trieste, Italy. E-mail: bfarina@inogs.it

(**) CRES Centre for Renewable Energy Sources and Saving
19 km Marathonos ave., 19009, Pikerimi, Greece

Paper to be considered for publication on Geothermics

(Submitted 4th February 2019; Accepted 7th May 2019)

Keywords: Seismic velocity, seismic attenuation, heat transfer, hot geothermal systems.

ABSTRACT

Seismic methods contribute to the exploration of geothermal areas and characterization of existing geothermal resources. Seismic velocity and attenuation depend on the pressure and temperature conditions of the geothermal systems, which are closely related to the properties of the rock frame and geothermal fluids. We calculate the seismic velocities and attenuation in terms of the subsurface distribution of the confining and pore pressures and temperature, assuming that the heat transfer from below is convective or conductive. The pore pressure is assumed hydrostatic. In hydrothermal systems the temperature is calculated assuming the boiling point condition at the specific pore pressure down to the reservoir. Beneath the reservoir it is assumed constant in convectively heated systems and following a constant temperature gradient in conductively heated systems. In Enhanced Geothermal Systems (EGS) conductive heat transfer and constant temperature gradient are assumed. We present three application examples, considering simplified subsurface models to describe the geothermal systems beneath the production wells. The seismic wave properties are calculated using the rock's mechanical Burgers model and the Arrhenius equation to take into account rock-properties-variability with temperature and the Gassmann model for fluid saturating the porous rocks.

INTRODUCTION

Seismic methods are used for the exploration of geothermal areas and characterization of existing natural and potentially enhanced geothermal resources (EGS) (Mayer et al., 2007; Aqui and Zarrouk, 2011; Iovenitti et al., 2013) basically, to understand and verify the conceptual model, explore new resources, and identify and characterize the fracture/fault systems (e.g., Majer et al., 2007; Hashida et al., 2001). Appraisal methods make use of surface and borehole seismic measurements (Poletto et al., 2011; Niitsuma et al., 1999) for the location and characterization of geothermal reservoirs. Passive seismic methods are also useful, e.g., in volcanic areas (Blanck et al., 2016), even though they are less accurate for well siting. Simiyu (2010) applied micro-seismic methods to geothermal exploration, Bannister et al. (2015) obtained the 3-D seismic velocity and attenuation to investigate the deep geothermal resources in a volcanic area. Surface reflection seismic response together with passive seismic has been used for the characterization of deep structures and shallow layers in different geothermal regions (e.g., Batini et al., 1983; Bannister, 1992; Majer, 1978; Majer and McEvilly, 1982; Henrys et al., 1986; Kristinsdóttir et al., 2010).

Knowledge of the physical properties and microstructure of the geothermal rocks is important to understand their seismic response as a function of pressure, temperature and fluid properties (Kristinsdóttir et al., 2010). To support deep geothermal exploration, extensive works have been conducted on numerical simulations of geothermal systems focused on developing improved geophysical models to describe the properties associated to the presence of brittle-ductile transition (BDT) (e.g., Montesi, 2007) or supercritical fluids (Dobson et al., 2017; Reinsch et al., 2017; Farina et al., 2017; Hashida et al., 2001). Carcione and Poletto (2013) modeled the BDT using the Burgers mechanical model to describe the ductility effects, and the octahedral stress criterion and the Arrhenius equation to calculate the flow viscosity as function of temperature and pressure. Carcione et al. (2014) developed an algorithm to simulate the full-waveform propagation including the effects of ductility and the temperature dependence of flow viscosity. More recently, Carcione et al. (2017) extended the theory and the simulation algorithm to poro-viscoelastic media using the Gassmann equation to take into account the presence of geothermal fluids.

On the basis of these studies, Poletto et al. (2018) calculated the sensitivity of seismic wave propagation to physical properties and temperature variation using the Burgers model augmented with the Arrhenius relation and integrated in a modified Gassmann model to determine the sensitivity of the elastic properties, stiffnesses, impedance and attenuation to temperature, including frequency dependent effects related to permeability (Manning and Ingebritsen, 1999), fluid mobility (Batzle et al., 2006; Zhubayev et al., 2013), and squirt flow (Carcione et al., 2018; Carcione and Gurevich, 2011; Gurevich et al. 2010). The analysis of the seismic quantities is extended to the dependence of elastic moduli to temperature variations (Jaya et al. 2010; Poletto et al., 2018). All these aspects are related, with different relevance depending on the specific geological context, to the seismic characterization of a geothermal reservoir. From the conceptual-system point of view, a key issue in the characterization of a geothermal reservoir is to understand the nature, whether conductive or convective, of the heat-transfer mechanism. This nature, under different conditions in different geological scenarios, determines the fluid-rock temperature

regimes at depth and may have important impacts for the exploitation of geothermal reservoirs and for the production of geothermal resources (Edwards et al., 1982). In this work, we use the numerical approach of Poletto et al. (2018) to calculate seismic velocity and attenuation in poro-viscoelastic media where the temperature profiles are calculated considering models of conductive and convective heat flow systems. The aim of this analysis is to clarify a series of key issues, namely:

1. The seismic characterization and identification of the conductive and convective processes.
2. Determination of the most sensitive visco-elastic properties.
3. The influence of super critical fluids in very hot geothermal regions.
4. How the seismic properties are affected by melting.

The potential use of the proposed approach is studied by using known petrophysical rock properties, and envisaged for different geothermal sites and temperature-pressure profiles, including existing and potential Mexican geothermal sites investigated in the framework of the GEMex project (GEMex, 2016).

We first review the poro-visco elastic seismic modeling theory, extended to include temperature, pressure as well as melting effects. Then, we introduce the characteristic properties of conductive and convective geothermal systems, provide examples of seismic analysis with known crustal rock parameters, and discuss the results for different reservoir scenarios assuming pure water as geothermal fluid.

THEORY: THE BURGERS - GASSMANN MODEL

The anelastic behaviour due to shear deformation and plastic flow is described using the Burgers mechanical model (Carcione and Poletto, 2013; Carcione, 2014; Carcione et al., 2104), whose frequency dependent shear modulus is

$$\mu_B = \frac{\mu_0(1 + i\omega\tau_\epsilon)}{1 + i\omega\tau_\sigma - \frac{i\mu_0}{\omega\eta_S}(1 + i\omega\tau_\epsilon)}. \quad (1)$$

where ω is the angular frequency, $i = \sqrt{-1}$, μ_0 is the relaxed shear modulus of the Zener element describing the brittle material, τ_σ and τ_ϵ are seismic relaxation times expressed by the relations

$$\tau_\epsilon = \frac{\tau_0}{Q_0} \left(\sqrt{Q_0^2 + 1} + 1 \right), \quad \tau_\sigma = \tau_\epsilon - \frac{2\tau_0}{Q_0}, \quad (2)$$

where Q_0 is the minimum quality factor and τ_0 is a relaxation time such that $\omega_0 = 1/\tau_0$ is the center frequency of the relaxation peak.

The shear viscosity η_S , which describes the medium ductile behaviour, is obtained by the Arrhenius equation (e.g., Carcione et al., 2006; Montesi, 2007) accounting for

thermodynamic rheological effects. This quantity is related to the steady-state creep rate $\dot{\epsilon}$ by

$$\eta_S = \frac{\sigma_o}{2\dot{\epsilon}}, \quad \dot{\epsilon} = A_\infty \sigma_o^n \exp(-E/R_G T) \quad (3)$$

where σ_o is the octahedral stress (e.g., Gangi, 1981, 1983; Carcione et al., 2006; Carcione and Poletto, 2013), A_∞ and n are constants, E is the activation energy, $R_G = 8.3144$ J/mol/°K is the gas constant and T is the absolute temperature. All these parameters govern the ductile creep and melting behavior. The octahedral stress is

$$\sigma_o = \frac{1}{3} \sqrt{(\sigma_v - \sigma_h)^2 + (\sigma_v - \sigma_H)^2 + (\sigma_h - \sigma_H)^2}, \quad (4)$$

where the σ 's are the stress components in the principal system. In our analysis we assume that these components correspond to the vertical (v) confining stress, and the maximum (H) and minimum (h) horizontal tectonic stresses, given by

$$\sigma_v(x, y, z) = \int_0^z \rho(x, y, z') g dz', \quad (5)$$

where x and y are the horizontal coordinates, z is depth, $z = 0$ corresponding to the surface, ρ is the medium density, g is the acceleration of gravity, and, omitting for simplicity the dependence on lateral coordinates x and y ,

$$\sigma_H(z) = \frac{\nu \sigma_v(z)}{1 - \nu}, \quad \text{and} \quad \sigma_h(z) = \xi \sigma_H(z). \quad (6)$$

The parameter $\xi = \xi(x, y, z) \leq 1$ accounts for the additional effects due to tectonic stresses (Carcione and Poletto, 2013) and $\nu = \nu(x, y, z)$ is the Poisson's ratio of the formation.

In addition to the Burgers mechanical model, the Gassmann model allows us to predict the low-frequency limit of the wet-rock bulk modulus with complete saturation (Carcione et al., 2017). This model considers the elastic effects due to the mineral components, rock-frame bulk modulus (K_s), dry-rock elastic moduli (K_m and μ_m), porosity (ϕ) and pore fluid bulk modulus (K_f). According to the Gassmann model, the saturated-rock bulk and shear moduli are given by (e.g., Carcione, 2014)

$$K_G = K_m + \alpha^2 M \quad \text{and} \quad \mu_G = \mu_m, \quad (7)$$

where

$$\alpha = 1 - \frac{K_m}{K_s}, \quad (8)$$

and

$$M = \frac{K_s}{1 - \phi - K_m/K_s + \phi K_s/K_f}. \quad (9)$$

The elastic behavior of granular material composing the dry rock depends on pressure and is non-linear. In general, velocity rises with increasing confining pressure,

and this effect is probably due to pores/cracks closure and hence increases the density. At low effective pressure, cracks are open and easily closed with an increase in pressure (Chen et al., 2015). The elastic moduli typically vary as power functions of mean stress (Houlsby, Amorosi and Rojas, 2005). The pressure dependence of dry-rock-moduli can be expressed as (Kaselow and Shapiro, 2004)

$$K_m(p_d) = K_0 \cdot [1 - (1 - a_1) \cdot \exp(-p_d/p_1)], \quad (10)$$

and

$$\mu_m(p_d) = \mu_B \cdot [1 - (1 - a_2) \cdot \exp(-p_d/p_2)], \quad (11)$$

where K_0 and μ_0 are the dry-rock bulk and shear moduli at infinite (i.e., very high) confining pressure, a_1 , a_2 , p_1 and p_2 are constants and $p_d = p_c - p_o$ is the differential pressure, p_o and p_c are the pore and the confining pressure, respectively. In equation (11) we use $\mu_0 = \mu_B$, where $\mu_B = \mu_B(\omega)$ is the frequency dependent Burgers shear modulus given by equation (1) that takes into account the rock modulus variation in the presence of high temperature and melting.

The complex seismic velocities are given by

$$v_P(\omega) = \sqrt{\frac{K_G + 4\mu_G(\omega)/3}{\rho_w}}, \quad (12)$$

and

$$v_S(\omega) = \sqrt{\frac{\mu_G(\omega)}{\rho_w}}, \quad (13)$$

where

$$\rho_w = (1 - \phi)\rho_s + \phi\rho_f, \quad (14)$$

is the bulk density, and ρ_s and ρ_f are the grain and fluid densities, respectively. The phase velocities and quality factors are

$$V_{P,S} = \left[\text{Re} \left(\frac{1}{v_{P,S}} \right) \right]^{-1}, \quad (15)$$

and

$$Q_{P,S} = \frac{\text{Re} \left(v_{P,S}^2 \right)}{\text{Im} \left(v_{P,S}^2 \right)}, \quad (16)$$

respectively. These equations have been used, together with terms including frequency-dependent effects related to permeability and fluid flow, to study the sensitivity of seismic properties to temperature variations in a geothermal reservoir (Polletto et al., 2018), assuming linear gradient temperature models typical of conductive environments. In this work, we extend the analysis to other realistic geothermal models.

CONDUCTIVE AND CONVECTIVE SYSTEMS

Temperature and presence of fluids are key conditions for the characterization of a geothermal reservoir. In particular, temperature is a key parameter for the evaluation of geothermal resources. The temperature profile versus depth can be determined only with direct access to the rocks, through measurements in drilled wells. In the absence of direct measurements, it is possible to use temperature models derived from geophysical, geological and geochemical prospecting (e.g., Manzella 2010). The models can be characterized by different behaviors in different environments. An important classification is based on the distinction between conductive and convective heat-transport systems summarized below (Axelsson and Steingrímsson, 2012; Moeck and Beardsmore, 2014).

1. Conductive systems

In a purely conductive system, the heat flow remains almost constant with depth, as stated by the first law of thermodynamics, while the thermal gradient varies according to the conductive properties of the rocks (Beardsmore and Cooper, 2009). This means that the temperature profiles varies with depth. EGS are cases of conductive systems, as in situ permeability is too small to allow the movement of fluids.

2. Convective systems

A convective system differs from a conductive one, because in its upflow zone the fluid specific enthalpy is nearly constant. For a liquid-only rising fluid this implies a nearly constant temperature with depth. The same is approximately valid for a vapor-only rising fluid if the pressure within the reservoir is nearly constant. For a two-phase rising fluid (liquid and vapor), where boiling occurs as the pressure decreases upwards, the temperature and pore pressure are inter-related following the boiling point with depth curve (BPD) down to the geothermal reservoir, which is the exploitation target. This is due to the convective-fluid exchange mechanism. Convection cells are emanated by a deeper heat source, which usually is a cooling magma chamber located beneath the geothermal reservoir. The heat transfer mechanism from below can be either convective, where convection cells extend down to the brittle-ductile transition (BDT) level (convectively heated hydrothermal system), or conductive (conductively heated hydrothermal system).

Convective geothermal systems can have different behaviors depending on the fluid regimes, phase and pressure. We distinguish the following subcases (Donaldson, 1982):

Liquid-dominated system.—The deeper reservoir fluid is in the liquid phase with temperature below the critical point of water, even though the wells may deliver a two-phase fluid. An indicative graph of fluid properties shown on the Mollier pressure enthalpy diagram (Elders and Fridleifsson 2010), as it ascends from the deep heat source to the surface is presented in Figure 1, assuming isenthalpic upward flow.

Vapor dominated system.—The deeper reservoir fluid is in the vapor phase, while the wells deliver mainly steam vapor. Two indicative graphs of fluid properties shown on a pressure enthalpy diagram, as it ascends from the deep heat source to the surface are presented in Figure 1, distinguished by the heat transfer mechanisms (convective or conductive).

The efforts in geothermal exploration of natural resources are typically focused on up-flow zones of hydrothermal convection system. The reference lowest bound of the temperature profiles is the linear thermal conduction curve with an average continental geothermal gradient of 30 °C/km (Suzuki, Ioka and Muraoka, 2014). The highest temperature profiles in those zones are normally limited by the BPD temperature curve (Haas, 1971). To simulate the upper part of the hydrothermal system, we calculate the temperature $T(z)$ versus depth z in the conductive and convective models from surface to 2.25 km depth using the BPD curve (Henley et al., 1984), by the James equation (James, 1970), assumed as valid in the depth range $0.030 < z < 3.0$ km,

$$T(^{\circ}\text{C}) = 69.56 \times z^{0.2085}. \quad (17)$$

Below 2.25 km, we assume a temperature gradient of $T = 120$ °C/km to reach the condition of $T = 400$ °C at 2.7 km. In the deeper part, the temperature in the convective model is constant, whereas in the conductive model it increases with depth with the above temperature gradient.

Below 2.25 km, the fluid properties as a function of depth are calculated every $\Delta z = 100$ m intervals from top downwards as follows. The fluid density is calculated from the temperature at depth z and the pressure of the overlying interval, while the pressure at depth z is calculated from the fluid density assuming fluid-static conditions, i.e., for the i -th interval

$$p(i) = p(i - 1) + \rho_f(i - 1)g\Delta z. \quad (18)$$

The rock pressure is calculated from the rock density assuming lithostatic conditions, while the rock temperature is assumed equal to the fluid temperature.

Fluid convective systems require fluid circulation conditions, related, to some extent, to permeability (Sorey, 1978; Chatles et al., 1997; Lipsey, 2014; Lipsey et al., 2016). Conversely, finite permeability is not necessarily required for a conductive system. Complex micro fracture systems, faulting and melting have a big influence (e.g., Saemundsson, 2013; Arnórsson, 2014). These factors may affect seismic wave propagation, such as variations in the Poisson ratio, attenuation and anisotropy associated to fracture orientation, that, in principle, can be investigated with seismic methods (e.g., Carcione, 2014). The effects related to temperature, including porosity and permeability, are discussed in Carcione et al. (2018). Here, we model porosity,

but we do not include permeability in the calculation of the seismic properties, even if the assumption of a convective system requires to consider permeability. We mainly focus on the effects induced by the thermodynamic properties, related to temperature and pressure changes expected for convective or conductive systems.

In the following analysis, we denote ‘conductively heated hydrothermal systems’ as ‘conductive’, and ‘convectively heated hydrothermal systems’ as ‘convective’. We also consider the EGS scenario. Figure 2 shows (a) the pore pressure and (b) the temperature profiles as a function of depth for the conductive (red lines) and convective (blue lines) models, respectively. In the first part, until depth of 2.25 km, the heat transfer is dominated by the convective mode. In the interval 2.25–2.7 km, we assume a transition from the BPD curve to 400 °C by conduction, using the temperature gradient of 120 °C/km. In the deeper part, we assume conductive and convective conditions. Both, these hydrothermal systems are ‘vapor dominated’. The conductively heated hydrothermal system is characterized by much higher temperatures at depth, and by lower pressures, resulting from the lower fluid density. Depending on pressure and fluid properties, supercritical conditions may develop at these high temperatures (Dobson et al., 2017). This implies different physical conditions that affect the seismic properties.

EXAMPLES

To characterize the convective and conductive systems seismically, we need the temperature conditions, the pressure of the saturating fluids, and the seismic properties of the formations, in terms of the elastic moduli of the the dry rock and their dependence on the effective pressure. All these factors are involved in the Arrhenius equation (Eq. 3). The characterization requires the collection of integrated information from geophysical, geological, and laboratory data.

Here, we focus on three representative examples, two of which related to a superhot geothermal reservoir and one related to an EGS geothermal reservoir. The properties of the geothermal fluids are assumed those of pure water. For a superhot geothermal system (examples 1 and 2), we consider the pore pressure and temperature conditions shown in Figure 2, where below 2.7 km depth, we assume conductive and convective models.

We estimate the fluid properties by using the pore pressure and temperature profiles shown in Figure 2, that characterize a vapour dominated superhot geothermal reservoir. We derive the density, the acoustic velocity and the bulk modulus of the fluid using CoolProp codes (Bell et al., 2014) based on the thermo-physical database provided by the National Institute of Standards and Technology (NIST). Figure 2 shows the curves of (a) density, (b) acoustic velocity and (c) bulk modulus of the pore fluid for the conductive (red line) and convective (blue dashed line) models. The fluid properties are different only in the deeper layer, where the pressure and temperature conditions of the geothermal reservoir differ. Figure 2d shows the difference between the fluid bulk moduli calculated for the two heat-transport modes $\Delta K_f = K_{f(\text{CD})} - K_{f(\text{CV})}$, where subscripts ‘CD’ and ‘CV’ denote conductive and convective, respectively. For an EGS system (example 3) we consider a conductive-only

model.

Example 1: Crustal rock geophysical and thermal parameters

We consider a schematic model of a superhot geothermal reservoir with three layers. We use the geophysical and rheological properties of three crustal rocks reported in the literature including the dependence of the elastic dry-rock moduli on the differential pressure calculated in laboratory (Brace, 1965; Simmons and Brace, 1965; Popp and Kern, 1993). The Arrhenius parameters are derived from generic crustal formations (Fernández and Ranalli, 1997). The aim is to evaluate if, how and when the conceptual conductive and convective models can be seismically characterized and identified. We vary the porosity of the deeper layer to study the influence of the geothermal pore fluid in the presence of convective and conductive heat-transport mechanisms.

Then, we calculate the seismic properties of the saturated formation, assuming a given porosity, using the temperature and pore pressure conditions of a convective-liquid-dominated geothermal reservoir and compare the results with those of the conductive model. We vary also the Arrhenius parameters of the deeper layer, to see how the seismic properties change when the thermal properties melt the rock.

The profiles as functions of depth of the density, bulk modulus of the solid and porosity of the formations are shown in Figures 3a, 3b and 3c, respectively. The dry-rock bulk and shear moduli at infinite confining pressure, the solid density and bulk modulus, with the sample’s intrinsic porosity in brackets, are reported in Table 1. Properties for samples S-1 and S-2 (granite from Georgia and granite from Rhode Island) are reported in Brace (1965) and Simmons and Brace (1965), and those of samples KTB 61C9b, in Popp and Kern (1993). The frame bulk modulus at infinite confining pressure is calculated with the equation proposed by Krief et al. (1990), which relates the grain property to the dry-rock bulk modulus and the porosity

$$K_0 = K_s(1 - \phi)^{3/(1-\phi)}, \quad (19)$$

considering the intrinsic porosity, i.e., neglecting compliant porosity (e.g., Poletto et al., 2018), of each sample and the dry-rock bulk modulus at infinite confining pressure. Constants a_1 , a_2 , p_1 and p_2 , used in equations (10) and (11) to calculate the dry-rock bulk and shear moduli dependence on differential pressure, are reported in Table 2 for each sample. These constants are obtained from Brace (1965) and Simmons and Brace (1965) for samples S-1 and S-2, and from Popp and Kern (1993) for sample KTB 61C9b.

The parameters that appear in the Arrhenius equation, used to characterize the three layers, are reported in Table 3, retrieved from representative rheological values for the wet upper crust reported in Fernández and Ranalli (1997). Castro et al. (2008) propose the shear seismic loss parameters for the crust in Southern Italy,

$$Q_0 = 18.8 \cdot f^{1.7}, \quad (20)$$

where f is the frequency, an equation valid till 10 Hz. We calculate the relaxation times using $Q_0 = 122$ as the minimum quality factor, corresponding to a frequency

$f = 3$ Hz. We use the Gassmann equation (7) to obtain the bulk moduli of the saturated formation (Fig. 3a). These moduli are substituted in equations (15) and (16) to calculate the seismic properties as a function of depth, pressure and temperature. The difference of the saturated-rock moduli $\Delta K_G = K_{G(\text{CD})} - K_{G(\text{CV})}$, is shown in Figure 3b.

The compressional velocities of the conductive (red line) and convective (blue dashed line) geothermal systems are shown in Figure 4a. Their difference $\Delta V_P = V_{P(\text{CD})} - V_{P(\text{CV})}$ (Fig. 4b), has a maximum of 15 m/s, when the temperature difference between the two models is the highest. Similar trends can be observed for the compressional elastic moduli of the two heat flow models (Fig. 4c) and their difference (Fig. 4d). The shear velocities are shown in Figure 4a, where the difference has a maximum of 9 m/s at the highest temperature gap (see Fig. 4b). The behaviour of the shear elastic moduli are shown in Figures 4c and 4d.

The compressional (Q_P) and shear (Q_S) quality factors as a function of depth for both models are shown in Figures 5a and 5b. The variability of the seismic properties is solely due to the properties of the fluid, since there is no melting. The fluid is in a vapour phase for both models, and the fluid properties do not significantly change in the deeper part, even if the temperature difference reaches 400 °C. This results in small variations of the seismic velocities and quality factors. To investigate the variations of the visco-elastic quantities in a superhot geothermal system due to the presence of geothermal fluids in a vapour phase, we focus only on the deeper part below 2.7 km. Here, the pore pressure and temperature conditions change according to the conductive and convective heat transport mechanisms. This zone is modeled with the properties of the rock sample KTB 61C9b (Table 1). We vary the average porosity of the medium from 5 % to 50 %. Figures 5a, 5b and 5c show the difference in the bulk density ($\Delta\rho = \rho_{(\text{CD})} - \rho_{(\text{CV})}$), the difference in the compressional phase velocity ($\Delta V_P = V_{P(\text{CD})} - V_{P(\text{CV})}$) and that of the shear phase velocity ($\Delta V_S = V_{S(\text{CD})} - V_{S(\text{CV})}$). As the porosity increases, the effect due to the presence of the saturating fluid is more relevant, as can be seen in the variations of the bulk density and seismic velocities. The seismic quality factors are hardly affected.

For comparison, we calculate the seismic properties of a geothermal reservoir considering the temperature and pressure of a convective liquid-dominated (LD) system, where the temperature increases following the boiling-point to depth (BPD) curve until 1 km, where it reaches 300 °C and then it remains constant. The petrophysical properties do not change, while the geothermal fluid properties and the dry-rock moduli variation with differential pressure are calculated using the pore pressure and temperature profiles shown in Figures 6a and 6b, respectively. The fluid density, acoustic velocity and bulk modulus for the conductive (red line) and convective LD (blue dashed line) systems are shown in Figures 7a, 7b and 7c, respectively. The difference between the fluid bulk moduli calculated for the two heat transport models $\Delta K_f = K_{f(\text{CD})} - K_{f(\text{LD})}$, where ‘CD’ and ‘LD’ denote conductive and convective liquid-dominated, respectively, is shown in Figure 7d. This difference is approximately three orders of magnitude larger than that calculated for the vapour dominated reservoir (Fig. 2d). The change from vapor to liquid, related to the two different pressure-temperature conditions of Figure 6, causes significant variations in the seismic properties. The compressional and shear velocities calculated with the conductive and convective LD mechanisms and their difference are shown in Figure 7.

The maximum difference between the velocities of the conductive system, where the fluid is in a vapour phase, and the convective liquid-dominated system, is 246 m/s (P wave) and 137 m/s (S wave). The corresponding compressional and shear quality factors are shown in Figure 8. The difference is small, with the compressional quality factor more sensitive.

To investigate the changes due to variations of the rock properties, we analyze the deeper layer, considering the pressure and temperature conditions of the vapor-dominated convective and conductive models. We vary only the Arrhenius parameters of the layer. We use the four sets of thermodynamic parameters reported in Table 4. Set A1 is the same used to calculate the seismic properties shown in Figures 4, 4 and 5 below 2.25 km depth. Set A2 is obtained from Violay et al. (2012). As for set A1, it characterizes rocks that melt at very high temperature, higher than 800 °C. Rocks with the Arrhenius parameters and activation energy of set A3 (Poletto et al., 2018) and A4 (Fernández and Ranalli, 1997) start melting at around 700 °C and 500 °C, respectively.

Figure 8 shows the viscosity variation as a function of depth for the conductive (bold line) and convective (dashed line) heat flow models. The viscosity decreases with increasing temperature. Viscosity values lower than 10^{11} Pa s are obtained for temperatures higher than 400 °C in the conductive case, when the rock is characterized by sets A3 and A4. These low viscosity values are associated to the presence of melted material (Mavko, 1980; Solomon, 1972; Poletto et al., 2018), and this significantly affects the velocity (Fig. 9) and attenuation (Fig. 10) profiles. Conversely, in the convective model there is no melting because the maximum temperature is 400 °C, and the rock viscosity does not change, remaining higher than 10^{11} Pa s, without appreciable variations in the elastic moduli of the saturated rocks. Therefore, the seismic velocities calculated for saturated rocks with different thermal properties do not change.

More in detail, the compressional phase velocities calculated with the conductive and convective models are shown in Figures 9a and 9b, respectively and their difference ΔV_P in Figure 9c. For rocks with Arrhenius parameters A1 and A2, there is no melt and the compressional seismic velocity increases by about 15 m/s when temperature increases from 400 °C to 800 °C. This variation is interpreted as due to the variations in the fluid properties. On the other hand, for rocks with properties A3 and A4, the compressional velocity decreases with increasing temperature with a maximum reduction of 1230 m/s and 1780 m/s, respectively, as expected in the presence of partially molten rocks (Solomon, 1972; Williams and Garnero, 1996; Carcione and Poletto, 2013; Poletto et al., 2018). The shear phase velocities calculated with the conductive and convective models are shown in Figures 9d and 9e, respectively and their difference ΔV_S in Figure 9f. The difference is about 8 m/s for rocks with Arrhenius parameters A1 and A2. A large reduction in the shear velocity, reaching zero with complete melting, is observable in rocks with thermal parameter A3 and A4, when the conductive model is assumed, because the temperature exceeds the values at which melting starts. In principle, assuming the conductive heat transport mechanism, the seismic observations can reveal the temperature variations and the presence of molten phases related to the sharp discontinuities in velocity and quality factor (Spetzler and Anderson, 1968; Carcione and Poletto, 2013; Poletto et al., 2018).

Figure 10 shows the calculated compressional and shear quality factors in the conductive and convective models and their difference. P-wave attenuation results from the relaxation of both the shear and the bulk moduli (Carcione et al., 2017). The compressional quality factors (Q_P) calculated with the four sets are shown in Figures 10a and 10b for the conductive and convective models, respectively, and their difference is shown in Figure 10c. The shear wave attenuation results from relaxation of the shear modulus. Figure 10d and 10e show the shear quality factors (Q_S) of the conductive and convective systems, respectively, and their differences are shown in Figure 10f. Seismic attenuations of rocks which start melting at temperatures greater than 800 °C (A1 and A2) do not show relevant variations between the conductive and convective mechanisms. The attenuation, which is more related to thermally activated relaxation processes (Solomon, 1972) shows a very rapid decrease as the melting point is approached (Spetzler and Anderson, 1968; Carcione and Poletto, 2013), before reaching the brittle-ductile transition (BDT) zone, and this behaviour can be observed also in the convective model for set A4, which starts melting at about 500 °C (Figs. 10b and 10d). Figure 11 shows the seismic velocities and quality factors as function of temperature for the conductive model. The compressional and shear velocity curves (Figs. 11a and 11b, respectively) abruptly decrease around 700 °C and 500 °C for rocks with parameters A3 and A4, respectively. The seismic compressional and shear attenuations start increasing at 400 °C and 350 °C for the two sets.

Example 2: Los Humeros geothermal system

We focus the analysis on the superhot geothermal field of the Los Humeros volcanic complex (Fig. 12) (GEMex, 2016), which is the largest active caldera located in the northernmost part of the eastern sector of the Trans-Mexican volcanic belt (Carrasco-Núñez et al., 2017). We consider the simplified lithological model of Gutiérrez-Negrin and Izquierdo-Montalvo (2010), derive the solid and dry-rock properties from the literature in addition to the average porosity and density (Aragón-Aguilar et al. 2017; García-Estrada 1992).

Los Humeros is one of the oldest producing geothermal fields in Mexico (Arzate et al., 2018), the second after Los Azufres to produce electricity in the area of the Mexican Volcanic Belt (Prol-Ledesma, 1998). Many studies have been done to understand better the behaviour of the geothermal reservoir focusing on geophysics and geology (e.g., Arzate et al., 2018; Carrasco-Núñez et al., 2017; Urban and Lermo, 2013; Gutiérrez-Negrin and Izquierdo-Montalvo, 2010; Lermo et al., 2008; Cedillo, 2000), hydrogeology and hydrodynamic (e.g., Cedillo, 2000; Portugal et al., 2002), petrology and volcanology (e.g., Contreras, Domínguez and Rivera, 1990; Ferriz and Mahood, 1984; Carrasco-Núñez et al., 2012), thermal and pressure conditions (e.g., Arellano et al., 2008; Arellano et al., 2000; Verma, Gómez-Arias and Andaverde, 2011; Verma, 1985).

Arellano et al. (2000) studied the distribution of pressure and temperature of the Los Humeros geothermal field analyzing information from 42 wells drilled in the field. They proposed the existence of at least two reservoirs. The shallower one, located at 1.6–1.025 km above sea level (a.s.l) is liquid-dominant with a pressure

profile corresponding to a 300–330 °C boiling water column. Arellano et al. (2003) used well pressure logs and observed that the data show high correlation with the boiling point pressure for this depth. The deeper one, located at 0.85–0.1 km a.s.l., with low-liquid-saturation, has a temperature ranging between 300 and 400 °C (Urban and Lermo, 2013).

Gutiérrez-Negrin and Izquierdo-Montalvo (2000) analyzed several Los Humeros wells, and showed that their temperatures follow the boiling point to depth curve down to a depth of about 2.5 km. However, beneath a depth of about 1.75 km, a cluster of production wells shows temperature values with a gradient of approximately 120 °C/km, higher than those of the BPD curve and reaching a maximum temperature of 400 °C at about 2.25 km depth. Pulido (2008) reported a maximum bottom-hole temperature of 395.4 °C for well H-43, García-Gutiérrez et al. (2002) estimated that the maximum static formation temperature (SFT) of well H-26 is 407 °C.

In this example, we assume the conductive and convective heat-flow models. For the geological model of the Los Humeros geothermal field, we consider the four main lithological units proposed by Gutiérrez-Negrin and Izquierdo-Montalvo (2010), according with the rock cuts provided by the geothermal wells and based on previous works (e.g., Viggiano and Robles, 1988). These units are shown in Table 5. Starting from this lithological partition, we built a simple 1-D four-layers model. For the calculation of the shear velocity, we use the reference ratio $V_P/V_S = 1.76$ (Lermo et al., 2008). We consider that additional petrophysical data, provided by the ongoing GEMex project (GEMex, 2016), will be used for a refinement of this investigation. Average porosity values have been assigned using porosity measurements in core samples (Aragón-Aguilar et al., 2017; Contreras et al., 1990).

The 1-D velocities, density and porosity profiles are shown in Figure 13 and the averaged seismic and thermodynamic properties are reported in Table 6. To select the corresponding Arrhenius parameters, we used the characteristic values of crustal formations, provided by Fernández and Ranalli (1987) for the first three layers. To evaluate the seismic response near the BDT, assuming the proximity of a magma chamber as a possible scenario, we consider the two sets of parameters ALH1 and ALH2 for the last and fourth layers, which correspond to two different behaviors of the rock at high temperatures. The set ALH1 characterizes a rock that melts at temperatures greater than 900 °C (Violay et al., 2012), and set ALH2 characterizes a rock that melts at temperature around 700 °C (Carcione and Poletto, 2013; Poletto et al., 2017).

The P-velocity values are taken from the literature values. Starting from these values, we calculate the frame bulk modulus K_s , and using the porosity reported in Table 6, we invert the Krief relation given by equation 19 (Krief, 1990) to derive the bulk modulus of the dry matrix at infinite pressure (K_0). Using the shear velocity and the density, we calculate the shear modulus at infinite pressure μ_0 . The values of the tectonic parameter $\xi = 0.8$ in equation 6, of the minimum quality factor $Q_0 = 122$ and the frequency $f = 10$ Hz, used to calculate the relaxation times (Eq. 2), are the same without variations in the different lithologies of the model. With these parameters, we obtain the seismic velocities and attenuations.

The seismic compressional and shear phase velocities of the saturated media corresponding to the conductive (red line) and convective (blue dashed line) case, for the model with the deeper layer characterized by set ALH1, are shown in Figures 14a and

14b, respectively. The compressional and shear quality-factors are shown in Figures 14c and 14d, respectively. In this case the variability in the seismic properties due to the different pressure and temperature profiles is only related to the fluid properties variations. At the maximum temperature and pressure differences, it is about 0.2 % for the seismic phase velocities and 2 % for the seismic quality factors.

The seismic velocities for set ALH2 are shown in Figures 14a and 14b, respectively, while the compressional and shear quality factors are shown in Figures 14c and 14d, respectively. In this case, the variability is mainly due to melting, i.e., close to the BDT zone. The phase velocities start decrease at about 5 km depth, where the thermodynamic conditions allow rock melting. The maximum seismic phase velocities difference between the two analyzed temperature-pressure conditions, is 20 %. As expected, the quality factors related to the thermally activated relaxation processes (Poletto et al., 2018), show a rapid decrease starting approximately at 3 km, before reaching the melting point.

Example 3: Acoculco geothermal system

We consider the Acoculco Mexican site, where the geothermal conditions for a potential EGS site are investigated (Fig. 15) (GEMex, 2016). This area, situated near the town of Chignahuapan in the Mexican state of Puebla, is located in a volcanic complex that extends over the Ouebla-Hidalgo state boundary, in the eastern part of the Mexican Volcanic Belt (Canet et al., 2015; Pulido, Armenta and Silva, 2010). Studies on two wells drilled in the Acoculco area have shown that the temperature profiles are linear, indicative of a conductive thermal regime (López-Hernández et al., 2009). We calculate the seismic properties of a four-layer stratified model, assuming a conductive heat-transport mechanism.

The geothermal area of Acoculco is hosted by a volcanic caldera complex in the eastern part of the Mexican Volcanic Belt. Studies on this geothermal area have been performed to assess the feasibility of developing it as an enhanced geothermal system (EGS) for power generation (Pulido et al., 2010, 2011; GEMex, 2016). The heat source is interpreted as related to the presence of magma, which heats the surrounding formation (Pulido et al., 2010). The Comisión Federal de Electricidad (CFE) drilled two exploratory wells in the southernmost area, and located not too far from each other, well EAC-1 in 1995 and well EAC-2 in 2008 reaching a depth of 1810 and 1900 m, respectively (Canet et al., 2015; Viggiano-Guerra et al., 2011). The area is characterized by the presence of active gas emissions. Thermal logs from the exploratory wells EAC-1 and EAC-2 show a conductive heat transfer regime with bottom-hole temperature greater than 300 °C (López-Hernández et al., 2009; Viggiano-Guerra et al., 2011).

In this example, we use the conductive heat-transport mechanism to calculate the temperature and pressure conditions shown in Figures 16a and 16b, respectively. The temperature profile shown in Figure 16a is that of well EAC-1 (blue bullets), obtained from Pulido et. (2010). This profile is extrapolated in depth with a temperature gradient of 156 °C/km (orange line), which is the average gradient required to reach the bottom-hole temperature. The pressure in Figure 16b is that of well

EAC-1 (blue bullets, obtained from Viggiano-Guerra et al., 2011). This pressure profile is in agreement with the pressure corresponding to a hydrostatic column of water (Viggiano-Guerra et al., 2011), and it is extrapolated in depth (orange line) calculating the hydrostatic pressure from water densities associated to the temperature profile of Figure 16a derived from the NIST database. The water density, velocity and bulk modulus are shown in Figures 16a, 16b and 16c, respectively. We can see that at about 2.4 km depth, the conditions are those of a transition from liquid (blue line) to supercritical (green line) water phase.

For the geological model, we consider a simplified 1-D four-layers model representing the main lithologic units penetrated by well EAC-1 (López-Hernández et al., 2009) shown in Table 7. We assume compressional velocity and density values obtained from the literature. For the calculation of the shear velocity, we use the same ratio $V_P/V_S = 1.76$ used for Los Humeros. The 1-D rock-frame compressional (blue line) and shear (red line) velocities and density profiles of the are shown in Figures 17a and 17b, respectively. In the future, we will use data provided by the ongoing GEMex project (GEMex, 2016). We assume an average porosity of 6 %, as proposed by Pan et al. (2016) for the Acoculco geothermal area. For the Arrhenius parameters, we use the same values of Los Humeros. The geophysical and thermal parameters are summarized in Table 8. For the last layer, we consider two thermodynamic sets, AAC1 and AAC2, which correspond to two different behaviour of the rock at high temperatures. The Arrhenius parameters AAC1 = ALH1 characterize a rock which melts at temperatures higher than 900 °C (Violay et al., 2012), and those of set AAC2 = ALH2 characterize a rock which melts at temperature around 700 °C (Carcione and Poletto, 2013; Poletto et al., 2018). Figure 17 shows the seismic compressional (a) and shear (b) phase velocities, and the compressional (c) and shear (d) quality factors, when the thermodynamic parameters do not allow melting (set AAC1, blue line), and when they allow the last layer to melt (set AAC2, red line). The seismic velocities of the medium, which melts at about 700 °C, start decreasing at about 4 km depth, where we could expect the presence of the BDT. The effects on the quality factors start at a shallower depth. Recently, Calcagno et al. (2018) estimated the thermal gradient in the Acoculco area and the depth of the BDT zone at about 4 km depth below ground level. In this case, seismic measurements could in principle confirm this estimation.

DISCUSSION

The paper presents a comprehensive analysis of the temperature effects on the seismic properties of geothermal reservoirs with different heat-transport mechanisms, focusing on convective and conductive systems in hot and very-hot regions. The analysis uses pure water as geothermal fluid, and the thermodynamic properties predicted by the Arrhenius equation. The study is based on simulation equations developed in previous works. One of the difficulties is to determine the input parameters for the simulations, related to the geological, geophysical, thermodynamic and fluid-transport properties. To afford this task, we have assumed a simplified layer system, using typical crustal parameters and basing on known scenarios of two reservoirs along the Mexican Volcanic Belt, one of them in operation.

We simplify the heat-recharge system, but the method can be useful to study more complex recharge reservoirs mechanisms, which are subject to controversial investigations. Here, we assume equilibrium between the thermal properties of the rock frame and of the saturating fluid. Laboratory experiments are required to characterize the rocks near the BDT, where partial melt occurs. In this sense, this work is intended as a first step for future and more extensive characterizations of high temperature (HT) geothermal reservoirs, such as super-hot and EGS ones.

CONCLUSIONS

Our study presents a seismic characterization of convective and conductive geothermal reservoirs, with different thermodynamic properties dictated by the Arrhenius equation. The aim is to evaluate the influence of the geothermal mechanisms and temperature on the seismic properties, namely, seismic velocities, stiffness moduli and quality factors. The objective is also to discriminate between the two reservoirs at least in the hotter part, below the boiling point. The differences in the seismic properties are small when there is no melting, and are due to variations of the fluid properties. However, remarkable differences can be observed when passing from a vapor-dominated system to a liquid dominated system. Melt significantly affect the properties of the conductive reservoir, since in this case the temperature increases linearly with depth and highly affects the shear rigidity of the rocks. Conversely, in convective reservoirs, the temperature is constant with depth in the deepest region, and only partial melting can be observed for certain thermodynamic conditions.

ACKNOWLEDGMENTS

This project has received funding from the European Union's Horizon 2020 research and innovation programme under grant agreement No. 727550.

REFERENCES

- Aqui, A. R., and Zarrouk, S., 2011. Permeability Enhancement of Conventional Geothermal Wells. New Zealand Geothermal Workshop, Auckland, New Zealand.
- Aragón-Aguilar, A., Izquierdo-Montalvo, G., López-Blanco, S., Arellano-Gómez, V., 2017. Analysis of heterogeneous characteristics in a geothermal area with low permeability and high temperature. *Geoscience Frontiers*, 8, 1039–1050.
- Arellano, V. M., Aragón, A., Barragán, R. M., Armenta, M. F., Montes, M. R., and Aguado, R. T., 2008. Análisis de datos de producción y condiciones termodinámicas del fluido de alimentación de pozos de Los Humeros, Pue. *Geotermia*, 21 (2), 21–28.
- Arellano, V. M., García, A., Barragán, R. M., Izquierdo, G., Aragón, A., and Pizano, A., 2000. Distribución inicial de presión y temperatura del campo geotérmico de Los Humeros, Puebla. *Ingeniería hidráulica en México*, XVI (3), 75–84.
- Arnórsson, S., 2014. The roots of volcanic geothermal systems their birth, evolution and extinction. Proceedings 5th African Rift geothermal Conference Arusha, Tanzania.
- Arzate, J., Corbo-Camargo, F., Carrasco-Núñez, G., Hernández, J., and Yutsis, V., 2018. The Los Humeros (Mexico) geothermal field model deduced from new geophysical and geological data. *Geothermics*, 71, 200–211.
- Axelsson, G., and Steingrímsson, B., 2012. Logging, testing and monitoring geothermal wells, Presented at “Short Course on Geothermal Development and Geothermal Wells”, organized by UNU-GTP and LaGeo (Santa Tecla, El Salvador).
- Bannister, S., 1992. Seismic exploration in geothermal areas - effect of the surface layer. Proceedings 14th New Zealand Geothermal Workshop.
- Bannister, S., Bourguignon, S., Sherburn, S., and Bertrand, T., 2015. 3-D seismic velocity and attenuation in the Central Taupo Volcanic zone, New Zealand: Imaging the roots of geothermal systems. Proceedings World Geothermal Congress, Australia.
- Batini, F., Bertini, G., Gianelli, G., Pandeli, E., and Puxeddu, M., 1983. Deep structure of Larderello field: Contribution from recent geophysical and geological data. *Mem. Soc. Geo. It.*, 25, 219–235.
- Batzle, M., D. Han, and R. Hofmann, 2006. Fluid mobility and frequency-dependent seismic velocity direct measurements. *Geophysics*, 71, no. 1, N1–N9.
- Beardsmore, G. R., and Cooper, G.T., 2009. Geothermal system assessment Identification and mitigation of EGS exploration risk. Proceedings 34th Workshop on Geothermal Reservoir Engineering (Stanford, California).

- Bell, I. H., Wronski, J., Quoilin, S. and Lemort, V., 2014. Pure and pseudo-pure fluid thermophysical property evaluation and the open-source thermophysical property library CoolProp. *Ind. Eng. Chem. Res.*, 53 (6), 498–2508.
- Blanck, H., Jousset, P., Àgústsson, K., Hersir, G. P., Flóvenz, Ó. G., 2016. Analysis of seismological data on Reykjanes peninsula, Iceland. Proceedings, European Geothermal Congress (Strasbourg, France).
- Brace, W. F., 1965. Some new measurements of linear compressibility of rocks. *Jou. Geop. Research*, 70 (2), 391–398.
- Calcagno, P., Evanno, G., Trumpy, E., Gutiérrez-Negrin, L. C., Macías, J. L., Carrasco-Núñez, G., and Liotta D., 2018. Preliminary 3-D geological models of Los Humeros and Aocolco geothermal fields (Mexico) H2020 GEMex Project. *Adv. Geosci.*, 45, 321–333.
- Canet, C., Trillaud, F., Prol-Ledesma, R. M., González-Hernández, G., Peláez, B., Hernández-Cruz, B., Sánchez-Córdova, M., 2015. Thermal history of the Aocolco geothermal system, eastern Mexico: Insights from numerical modeling and radiocarbon dating. *Journal of Volcanology and Geothermal Research*, 305, 56–62.
- Carcione, J. M., 2014. Wave fields in real media: Wave propagation in anisotropic, anelastic, porous and electromagnetic media. *Handbook of Geophysical Exploration*, Elsevier, Amsterdam (3rd edition, revised and extended).
- Carcione, J. M., and Gurevich, B., 2011. Differential form and numerical implementation of Biot’s poroelasticity equations with squirt dissipation. *Geophysics*, 76, N55–N64.
- Carcione, J. M., and Poletto, F., 2013. Seismic rheological model and reflection coefficients of the brittle-ductile transition. *Pure and Applied Geophysics*, DOI 10.1007/s00024-013-0643-4.
- Carcione, J. M., Poletto, F., Farina, B., 2018a. The Burgers/squirt-flow seismic model of the crust and mantle. *Physics of the Earth and Planetary Interiors*, 274, 14–22.
- Carcione, J. M., Poletto, F., Farina, B., Bellezza, C., 2018b. 3D seismic modeling in geothermal reservoirs with a distribution of steam patch sizes, permeabilities and saturations, including ductility of the rock frame. *Physics of the Earth and Planetary Interiors*, 279, 67–78.
- Carcione, J. M., Poletto, F., Farina, B. and Craglietto, A., 2014. Simulation of seismic waves at the Earth crust (brittle-ductile transition) based on the Burgers model. *Solid Earth*, 5, 1001–1010.
- Carcione, J. M., Poletto, F., Farina, B., and Craglietto, A., 2017. The Gassmann-Burgers model to simulate seismic waves at the Earth crust and mantle, *Pure and Applied Geophysics*, 174, 849-863. DOI: 10.1007/s00024-016-1437-2.

- Carrasco-Núñez, G., López-Martínez, M., Hernández, J., and Vargas, V., 2017. Subsurface stratigraphy and its correlation with the surficial geology at Los Humeros geothermal field, eastern Trans-Mexican volcanic belt. *Geothermics*, 67, 1–17.
- Carrasco-Núñez, G., McCurry, M., Branney, M. J., Norry, M., and Willcox, C., 2012. Complex magma mixing, mingling and withdrawal associated with an intra-Plinian ignimbrite eruption at a large silicic caldera volcano: Los Humeros of central Mexico. *GSA Bulletin*, 124 (11/12) 1793–1809.
- Cedillo Rodríguez, F., 2000. Hydrogeologic model of the geothermal reservoirs from Los Humeros, Puebla, Mexico. *Proceedings World Geothermal Congress, Japan*.
- Cermak, V., Bodri, L., Rybach, L., and Buntebarth, G., 1990. Relationship between seismic velocity and heat production: comparison of two sets of data and test of validity. *Earth and Planetary Science Letters*, 99 (1-2), 48–57.
- Cathles, L. M., Erendi, A. H. J., and Barrie, T., 1997. How long can a hydrothermal system be sustained by a single intrusive event? *Economic Geology*. 92. 10.2113/gsecongeo.92.7–8.766.
- Chen, X., Schmitt, D. R., Kessler J. A., Evans J., and Kofman, R., 2015. Empirical relations between ultrasonic P-wave velocity, porosity and uniaxial compressive strength. *CSEG Recorder*, 40(5), 24–29.
- Contreras, E., Domínguez, B., and Rivera, O., 1990. Petrophysical measurements in drill cores from the Los Humeros geothermal field. *Geothermia*, 6 (1), 7–42.
- Dobson, P., Asanuma, H., Huenges, E., Poletto, F., Reinsch, T., Sanjuan, B., 2017. Supercritical geothermal systems - a review of past studies and ongoing research activities. In: *Proceedings, 41st Workshop on Geothermal Reservoir Engineering, Stanford University (Stanford, California)*.
- Donaldson, I. G., 1982. Heat and mass circulation in geothermal systems. *Ann. Rev. Earth Planet. Sci.*, 377–395.
- Edwards, L. M., Chilingar, G. V., Rieke, H. H., and Fertl, W. H., 1982. *Handbook of Geothermal Energy*. Gulf Publishing Company, Houston, Texas, pp. 1–12, 36–41, 44–74, 471.
- Elders, W., and Fridleifsson G., 2010. The Science Program of the Iceland Deep Drilling Project (IDDP): a Study of Supercritical Geothermal Resources, *Proceedings World Geothermal Congress (Bali, Indonesia)*.
- Engelder, T., 1993. *Stress regimes in the lithosphere*. Princeton University Press.
- Farina, B., Poletto, F., Carcione, J., 2016. Seismic wave propagation in poroviscoelastic hot rocks. *Proceedings, European Geothermal Congress (Strasbourg, France)*.

- Farina, B., Poletto, F., and Carcione, J. M., 2017. Seismic wave propagation in geothermal hot rocks: a review of simulation analysis and results based on Burgers models. 79th EAGE Conference and Exhibition, Workshop, DOI: 10.3997/2214-4609.201701769.
- Fernández, M., and Ranalli, R., 1997. The role of rheology in extensional basin formation modelling. *Tectonophysics*, 282, 129–145.
- Ferriz, H., and Mahood, G. A., 1984. Eruption rates and compositional trends at Los Humeros Volcanic Center Puebla, Mexico. *Journal of Geophysical research*, 89, 8511–8524.
- García-Estrada, G. H., 1992. Study for the development of new interpretative criteria for gravity studies of geothermal areas case study of Los Humeros, Pue., Mexico. *Geothermal Res. Coun. Trans.*, 16, 227–232.
- García-Gutiérrez, A., Arellano V., Barragán R.M., and Espinosa-Paredes G., 2002. Initial temperature field in the Los Humeros geothermal reservoir. *Geofísica Internacional*, 41 (3), 303–312.
- Gutiérrez-Negrin, L. C. A., and Izquierdo-Montalvo, G., 2010. Review and update of the main features of the Los Humeros geothermal field, Mexico. *Proceedings World Geothermal Congress (Bali, Indonesia)*.
- GEMex, 2016. H2020 Project: GEMex: Cooperation in Geothermal energy research Europe-Mexico for development of Enhanced Geothermal Systems and Superhot Geothermal Systems: European Union’s Horizon 2020 research and innovation programme under grant agreement No. 727550.
- Gurevich, B., Makarynska, D., Pervukhina, M. and De Paula, O., 2010. A simple model for squirt-flow dispersion and attenuation in fluid-saturated granular rocks. *Geophysics*, 75 (6), N109–N120, doi: 10.1190/1.3509782.
- Haas, J. L., Jr, 1971. The effect of salinity on the maximum thermal gradient of a hydrothermal system at hydrostatic pressure. *Econ. Geol.*, 66, 940–946.
- Hashida, T., Bignall, G., Tsuchiya, N., Takahashi, T., and Tanifuji, K., 2000. Fracture Generation and Water-Rock Interaction Process in Supercritical Deep-Seated Geothermal Reservoirs. *Geothermal Resources Council Transactions*, 25, 225–229.
- Henley, R. W., Truesdell, A. H., Barton, P. B., Whitney, J. A., 1984. Fluid-Mineral Equilibria in Hydrothermal Systems. *Reviews in Economic Geology*, 1, 9–15.
- Henry, S. A., Levander, A. R., Hill, N. R., and Gibson, B. S., 1986. Seismic response of the surface layer at the Ohaaki geothermal field, New Zealand. 56th Annual Int. Mtg., SEG, Expanded abstract, ENG1.7.
- Houlsby, G. T., Amorosi, A., and Rojas, E., 2005. Elastic moduli of soils dependent on pressure: a hyperelastic formulation. *Geotechnique*, 55 (5), 383–392.

- Iovenitti, J., Sainsbury, J., Tibuleac, I. M., Karlin, R., Wanamaker, P., Maris, V., Blackwell, D., Thakur, M., Ibser, F. H., Lewicki, J., Kennedy B. M., and Swyer, M., 2013. EGS exploration methodology project using the Dixie Valley geothermal system, Nevada, status update. 38th Workshop on Geothermal reservoir Engineering Stanford University, (Stanford, California), 11–13.
- James, R., 1970. Factors controlling borehole performance. UN. Symp. On the Development and Utilization of Geothermal Resources. Pisa, Proceedings (Geothermics Spec. Iss. 2) 2 (2), 1502.
- Jaya, M. S., Shapiro, S. A., Kristinsdóttir, L. H., Bruhn, D., Milsch, H., Spangenberg, E., 2010. Temperature dependence of seismic properties in geothermal rocks at reservoir conditions. *Geothermics*, 39, 1, 115123.
- Kaselow, A., and Shapiro, S. A., 2004. Stress sensitivity of elastic moduli and electrical resistivity in porous rocks. *J. Geophys. Eng.*, 1, 1–11.
- Krief, M., J. Garat, J. Stellingwerff, and J. Ventre, 1990. A petrophysical interpretation using the velocities of P and S waves (full-waveform sonic). *The Log Analyst*, 31 (6), 355–369.
- Kristinsdóttir, L. H., Flvenz, O., rason, K., Bruhn, D., Milsch, H., Spangenberg, E., and Kulenkampff, J., 2010. Electrical conductivity and P-wave velocity in rock samples from high-temperature Icelandic geothermal fields. *Geothermics*, 39 (1), 94–105.
- Lermo, J., Antayhua, Y., Bernal, I., Venegas, S., Arredondo, J., 2009. Monitoreo sísmico en la zona geotérmica de Acozulco, Pue., México. *Geotermia*, 22 (1), 40–58.
- Lermo, J., Antayhua, Y., Quintanar, L., and Lorenzo, C., 2008. Estudio sísmológico del campo geotérmico de Los Humeros, Puebla, México. Parte I: Sísmicidad, mecanismos de fuente y distribución de esfuerzos. *Geotermia*, 21 (1), 25–41.
- Lipsey, L. C., 2014. Numerical modelling of thermal convection related to fracture permeability: implication for geothermal exploration and basin modeling. MSc Thesis, Utrecht University.
- Lipsey, L., Pluymaekers, M., Goldberg, T., van Oversteeg, K., Ghazaryan, L., Cloetingh S., Jan-van Wees, D., 2016. Numerical modelling of thermal convection in the Luttelgeest carbonate platform, the Netherlands. *Geothermics*, 64, 135–151.
- López- Hernández A., García-Estrada G., Aguirre-Díaz G., González-Partida E., Palma-Guzmán H., and Quijano-León J.L., 2009. Hydrothermal activity in the Tulancingo-Acozulco Caldera Complex, central Mexico: Exploratory studies. *Geothermics*, 38, 279–293.
- Majer, E. L., 1978. Seismological Investigations in Geothermal Regions. Ph.D. Thesis.

- Majer, E. L., and McEvilly, T. V., 1982. Seismological studies at the Cerro Prieto Field: 1978-1982. 4th symposium on Cerro Prieto Geothermal Field, Guadalajara, Mexico.
- Majer, E. L., Baria, R., Stark, M., Oates, S., Bommer, J., Smith, B., and Asanuma, H., 2007. Induced seismicity associated with Enhanced Geothermal Systems. *Geothermics*, 36, 185–222.
- Manning, C.E., and Ingebritsen, S. E., 1999. Permeability of the continental crust: the implications of geothermal data and metamorphic systems. *Reviews of Geophysics*, 37, 127–50.
- Manzella, A., 2010. Technological Challenges in Exploration and Investigation of EGS and UGR, Proceedings World Geothermal Congress (Bali, Indonesia).
- Mavko, G. M., 1980. Velocity and attenuation in partially molten rocks. *Journal of Geophysical research*, 85 (B10), 5173–5189.
- Moeck, I. S., and Beardsmore, G., 2014. A new ‘geothermal play type’ catalog: Streamlining exploration decision making. Proceedings, 39th Workshop on Geothermal Reservoir Engineering Stanford University, (Stanford, California), SGP-TR-202.
- Montesi, L. G. J., 2007. A constitutive model for layer development in shear zones near the brittle-ductile transition. *Geophys. Res. Lett.*, 34, L08307, doi:10.1029/2007GL029250.
- Niitsuma, H., Fehler, M., Jones, R., Wilson, S., Albright, J., Green, A., Baria, R., Hayashi, K., Kaieda, H., Tezuka, K., Jupe, A., Wallrothy, T., Cornet, F., Asanuma, H., Moriya, H., Nagano, K., Phillips, W.S., Rutledge, J., House, L.S., Beauce, A., Aldge, D., and Aster, R., 1999. Current status of seismic and borehole measurements for HDR/HWR development. *Geothermics*, 28 (4-5), 475–490.
- Pan, C., Chávez, O., Romero, C. E., Levy, E. K., Corona, A. A., Rubio-Maya, C., 2016. Heat mining assessment for geothermal reservoirs in Mexico using supercritical CO₂ injection. *Energy*, 102, 148-160.
- Poletto, F., Corubolo, P., Schleifer, A., Farina, B., Pollard, J., Grozdanich, B., 2011. Seismic while drilling for geophysical exploration in a geothermal well. *Geothermal resource Council Transactions*, 1737–1741.
- Poletto, F., Farina, B., and Carcione, J. M., 2018. Sensitivity of seismic properties to temperature variations in a geothermal reservoir. *Geothermics*, 76, 149–163.
- Poletto, F., and Miranda, F., 2004. *Seismic while drilling. Fundamentals of drill-bit seismics for exploration.* Elsevier, Amsterdam.
- Popp, T., and Kern, H., 1994. The influence of dry and water saturated cracks on seismic velocities of crustal rocks – A comparison of experimental data with theoretical model. *Surveys in Geophysics*, 15, 443–465.

- Portugal, E., Izquierdo, G., Barragán, R. M., and Romero, B. I., 2012. Hydrodynamic model of Los Humeros geothermal field, Mexico, based on geochemical, mineralogical and isotopic data. *Geofísica Internacional*, 41, 415–420.
- Prol-Ledesma, R. M., 1998. Pre- and post-exploitation variations in hydrothermal activity in Los Humeros geothermal field, Mexico. *Journal of Volcanology and geothermal research*, 83, 313–333.
- Pulido, C. L., 2008. Borehole geophysics and geology of well H-43, Los Humeros geothermal field, Puebla, Mexico. Report 23, Geothermal training Program, United Nations university, Iceland.
- Pulido, C. L., Armenta, M. F., and Silva, G. R., 2010. Characterization of the Acoculco geothermal zone as HDR system. *GRC Transaction*, 34.
- Pulido, C. L., Armenta, M. F., and Silva, G. R., 2011. Caracterización de un yacimiento de roca seca caliente en la zona geotérmica de Acoculco, Pue. *Geotermia*, 24(1), 59–69.
- Raymer, L. L., Hunt, E. R., and Gardner, J. S., 1980. An improved sonic transit time-to-porosity transform. *SPWLA 21 Ann. Logging Symp.*, 1–12.
- Reinsch, T., Dobson, P., Asanuma, H., Huenges, E., Poletto, F., and Sanjuan, B., 2017. Utilizing supercritical geothermal systems: a review of past ventures and ongoing research activities. *Geothermal Energy*, 5–16.
- Saemundsson, K., 2013. Geothermal systems in global perspective. Short Course VIII on Exploration for Geothermal Resources.
- Simiyu, S. M., 2010. Application of micro-seismic methods to geothermal exploration: examples from the Kenys rift. Presented at Short Course V on Exploration for Geothermal Resources, Kenya.
- Simmons, G., and Brace, W. F., 1965. Comparison of static and dynamic measurements of compressibility of rocks. *Jou. Geop. Research*, 70(22).
- Solomon, S. C., 1972. Seismic-wave attenuation and partial melting in the upper mantle of North America. *Journal of Geophysical Research*, 77 (8), 1483–1502.
- Sorey, M. L., 1978. Numerical modelling of liquid geothermal systems. U.S. Geological Survey Professional Paper 1044, D1–D25.
- Spetzler, H., and Anderson, D. L., 1968. The effect of temperature and partial melting on velocity and attenuation in a simple binary system. *Journal of Geophysical Research*, 73 (18), 6051–6060.
- Suzuki, Y., Ioka, S., and Muraoka, H., 2014. Determining the maximum depth of hydrothermal circulation using geothermal mapping and seismicity to delineate the depth to brittle-plastic transition in Northern Honshu, Japan. *Energies*, 7, 3503–3511.

- Tibuleac, I. M., Iovenitti, J., von Seggern, D., Sainsbury, J., Biasi, G., and Anderson, J. G., 2013. Development of exploration methods for engineered geothermal systems through integrated geophysical, geologic and geochemical interpretation: The seismic analysis component. 38th Workshop on Geothermal reservoir Engineering Stanford University (Stanford, California).
- Urban, E., and Lermo, J. F., 2013. Local seismicity in the exploration of Los Humeros geothermal fields, Mexico. 38st Workshop on Geothermal reservoir Engineering Stanford University (Stanford, California).
- Verma, M. P., Verma, S. P. and Sanvicente, H., 1990. Temperature field simulation with stratification model of magma chamber under Los Humeros caldera, Puebla, Mexico. *Geothermics*, 19 (2), 187-197.
- Verma, S. P., 1985. Heat source in Los Humeros geothermal area, Puebla, Mexico. *Transactions Geotherm. Resour. Counc.* 9 (Part 1).
- Verma, S. P., and Andaverde, J., 1995. Temperature field distribution from cooling of a magma chamber. *Proc. World Geothermal Congress, Florence*, 1119–1124.
- Verma, S. P., Gómez-Arias, E., and Andaverde, J., 2011. Thermal sensitivity analysis of emplacement of the magma chamber in Los Humeros caldera, Puebla, Mexico. *International Geology Review*, 53 (8), 905–925.
- Viggiano-Guerra, J. C., Armenta, M. F., and Silva, G. R., 2011. Evolución del sistema geotérmico de Acoculco, Pue., México: un estudio con base en estudios petrográficos del pozo EAC-2 y en otras consideraciones. *Geotermia*, 24(1), 14-24.
- Violay, M., Gibert B., Mainprice D., Evans B., Dautria J. M., Azais P., and Pezard P., 2012. An experimental study of the brittle-ductile transition of basalt at oceanic crust pressure and temperature conditions. *Journal of Geophysical Reserch*, 117.
- Wyllie, M. R. J., Gregory, A. R., and Gardner, L. W., 1956. Elastic wave velocities in heterogeneous and porous media. *Geophysics*, 21, 41-70.
- Zhubayev, A., Jihai, Y., Jun, C., Borodin, B., Sanders, M., Lim, T. K., Menkiti, H., and Ghose, R., 2013. Fluid mobility in reservoir rocks from integrated VSP and openhole data. Expanded Abstracts, SEG Houston Annual Meeting, 2964–2968, DOI <http://dx.doi.org/10.1190/segam2013-0213.1>

TABLES

TABLE 1. Petrophysical properties of the rock samples used in the layered model.

Depth (km)	Sample	Dry bulk modulus	Dry shear modulus	Density	Solid bulk modulus
		K_0 (GPa)	μ_0 (GPa)	ρ_s (g/cm ³)	K_s (GPa)
0 ÷ 1.0	S-1	56.5	37.0	2.631	57.0 ($\phi = 0.3\%$)
1.0 ÷ 2.25	S-2	55.8	33.8	2.646	58.0 ($\phi = 1.1\%$)
> 2.25	61C9b	67.1	41.4	3.0	89.44 ($\phi = 8.4\%$)

TABLE 2. Constants used for the bulk- and shear-moduli dependence on pressure.

Sample	a_1	p_1	a_2	p_2
S-1	0.26	90.9	0.48	55.55
S-2	0.43	86.9	0.60	71.07
61C9b	0.38	60	0.55	63

TABLE 3. Values of the Arrhenius parameters for the model layers.

Layer	A_∞ (MPa) $^{-n}$ s $^{-1}$	n	E (kJ/mol)
1	10^{-2}	1.8	151
2	$2 \cdot 10^{-4}$	1.9	134
3	$2.9 \cdot 10^{-3}$	1.8	150

TABLE 4. Arrhenius thermodynamic parameter-sets used to evaluate the melting effect.

Set number	A_∞ (MPa) $^{-n}$ s $^{-1}$	n	E (kJ/mol)
A1	$2.9 \cdot 10^{-3}$	1.8	150
A2	$1.3 \cdot 10^{-9}$	3.7	59
A3	10^2	2	134
A4	$5 \cdot 10^6$	3	190

TABLE 5. Los Humeros lithology proposed by Gutiérrez-Negrin and Izquierdo-Montalvo (2010).

Depth (km)	Lithology
0 ÷ 1.0	Andesites, basalts, rhyolites, dacites, tuffs, ashes, pumices
1.0 ÷ 1.8	Vitreous and lithic ignimbrites
1.8 ÷ 3.0	Augite andesites and hornblende andesites
> 3.0	Limestones, marble, granitic rocks

TABLE 6. Seismic and thermodynamic average properties of the rock frame composing the media in the Los Humeros layered model. In the last layer we distinguish two thermodynamic rock behaviours related to two different Arrhenius parameters (A_∞ , n and E) sets named A1 and A2.

Depth (km)	V_P (m/s)	V_S (m/s)	ρ (g/cm ³)	ϕ (%)	A_∞ (MPa) ^{-n} s ⁻¹	n	E (kJ/mol)
0 ÷ 1.0	1600	909	1.8	19.1	1.3×10^{-3}	2.4	219
1.0 ÷ 1.8	2700	1530	2.15	10.3	2.0×10^{-4}	1.9	141
1.8 ÷ 3.0	3800	2160	2.3	16.3	2.9×10^{-3}	1.8	150
> 3.0	6000	3410	2.7	16.3	ALH1. 1.3×10^{-9}	3.7	59
					ALH2. 10^2	2	134

TABLE 7. Acoculco lithology model based on the main lithologic units penetrated by well EAC-1 (Lopez-Hernandez et al., 2009).

Depth (km)	Lithology
0 ÷ 0.20	Volcanic rocks including rhyodacite and dacite
0.20 ÷ 0.57	Ignimbrite
0.57 ÷ 1.66	Metamorphic rocks composed mainly of skarns
> 1.66	Hornblende granite

TABLE 8. Seismic and thermodynamic average properties of the rock frame composing the media in the Acoculco model. In the last layer we distinguish two thermodynamic rock behaviours related to two different Arrhenius parameters (A_∞ , n and E) sets named A1 and A2.

Depth (km)	V_P (m/s)	V_S (m/s)	ρ (g/cm ³)	ϕ (%)	A_∞ (MPa) ^{-n} s ⁻¹	n	E (kJ/mol)
0 ÷ 0.20	1600	909	1.8	6	1.3×10^{-3}	2.4	219
0.20 ÷ 0.57	2700	1530	2.15	6	2.0×10^{-4}	1.9	141
0.57 ÷ 1.66	4000	2270	2.4	6	2.9×10^{-3}	1.8	150
> 1.66	6000	3410	2.7	6	AAC1. 1.3×10^{-9}	3.7	59
					AAC2. 10^2	2	134

FIGURES

FIG. 1. Fluid properties as it ascends from deep heat source to the wellhead plotted in the Mollier pressure-enthalpy diagram of pure water: examples of a liquid dominated hydrothermal system (left red line), of a convectively heated vapor dominated hydrothermal system (right red line) and of a conductively heated vapor dominated hydrothermal system (dark red line). Main assumptions are isenthalpic upwards fluid flow, as well as hydrostatic pressure for the liquid dominated system and vapor-static pressure for the deep part of the vapor dominated system.

FIG. 2. (a) Pressure and (b) temperature profiles for a superhot geothermal reservoir with convective (blue) and conductive (red) mechanism in the deeper part.

FIG. 2. Saturating fluid properties calculated for the conductive (red line) and the convective (blue dashed line) models: a) density, b) acoustic velocity, c) bulk modulus (K_f), and d) bulk moduli difference (ΔK_f).

FIG. 3. 1-D rock-frame properties: a) density, b) bulk modulus, and c) porosity.

FIG. 3. (a) Gassmann bulk modulus for the saturated formation using conductive (red line) and convective (blue dashed line) models, and (b) bulk moduli difference.

FIG. 4. a) Compressional velocities in the conductive (red line) and convective (blue dashed line) models and b) their difference; c) compressional elastic moduli in the conductive (red line) and convective (blue dashed line) models and d) their difference.

FIG. 4. a) Shear velocities in the conductive (red line) and convective (blue dashed line) models and b) their difference; c) shear elastic moduli in the conductive (red line) and convective (blue dashed line) models and d) their difference.

FIG. 5. (a) Compressional and (b) shear quality factors in the conductive (red line) and convective (blue dashed line) models.

FIG. 5. Difference in (a) the bulk density, (b) the compressional and (c) the shear phase velocities as function of depth calculated in the conductive and convective models with the porosity values shown in the legend equal for all the panels.

FIG. 6. (a) Pressure and (b) temperature profiles for a superhot geothermal reservoir with conductive (red) and convective LD (blue) heat flow mechanism.

FIG. 7. Saturating fluid properties in the conductive (red line) and the convective liquid dominated (blue dashed line) systems: a) density, b) acoustic velocity, c) bulk moduli (K_f) and d) their difference (ΔK_f).

FIG. 7. a) Compressional velocities for conductive (red line) and convective LD (blue dashed line) models and b) their difference; c) shear velocities for conductive (red line) and convective LD (blue dashed line) models and d) their difference.

FIG. 8. (a) Compressional and (b) shear quality factors for conductive (red line) and convective LD (blue dashed line) models.

FIG. 8. Viscosity as a function of depth for the four thermodynamic sets of Table 4 in the conductive (bold line) and the convective (dashed line) models.

FIG. 9. Compressional phase velocities (V_P) calculated in (a) the conductive and (b) convective models and (c) their difference (ΔV_P). Shear phase velocities (V_S) calculated in (d) the conductive and (d) convective models and (f) their difference (ΔV_S). The legend of the used Arrhenius sets (see Table 4) is common to all panels.

FIG. 10. Compressional attenuation factors (Q_P) calculated in (a) the conductive and (b) convective models and (c) their difference (ΔQ_P). Shear attenuation factors (Q_S) calculated in (d) the conductive and (d) convective models and (f) their difference (ΔQ_S). The legend of the used Arrhenius sets (see Table 4) is common to all panels.

FIG. 11. (a) Compressional and (b) shear phase velocities. (c) Compressional and (d) shear quality factors as functions of temperature. The legend of the used Arrhenius sets (see Table 4) is common to all panels.

FIG. 12. (a) Location of the Los Humeros volcanic complex in the Trans-Mexican Volcanic Belt. (b) Location of the Los Humeros geothermal field (green circle) at the northern boundary of the Serdán-Oriental basin (Arzate et al., 2018).

FIG. 13. (a) Compressional (blue line) and shear (red line) velocities, (b) density and (c) porosity of the rock frame composing the geological section.

FIG. 14. (a) Compressional and (b) shear phase velocities. (c) Compressional and (d) shear quality factors calculated with conductive (blue line) and convective (red dashed line) models using the Arrhenius set A1 for the deeper layer of the Los Humeros model.

FIG. 14. (a) Compressional and (b) shear phase velocities. (c) Compressional and (d) shear quality factors calculated with conductive (blue line) and convective (red dashed line) models using the Arrhenius set A2 for the deeper layer of the Los Humeros model.

FIG. 15. Map of the geothermal area of Acoculco, Puebla (modified after Pulido et al., 2011).

FIG. 16. (a) Temperature of well EAC-1 (blue bullets) obtained from Pulido et al. (2010) and extension to deeper depths using the geothermal gradient of 156 °C/km (orange line). (b) Pressure of well EAC-1 (blue bullets) and extension using the hydrostatic pore pressure associated to the chosen temperature gradient.

FIG. 16. (a) Density, (b) acoustic velocity and (c) bulk modulus of water under

temperature and pressure conditions of Figure 16. The blue and green lines indicate the liquid and supercritical behaviour of water, respectively.

FIG. 17. (a) Compressional (blue line) and shear (red line) velocities and (b) density of the rock frame composing the geological section.

FIG. 17. (a) Compressional and (b) shear phase velocities, (c) compressional and (d) shear quality factors as functions of depth for the saturated media composing the Acozulco model with the last layer characterized by the Arrhenius sets A1 (blue line) and A2 (red line).

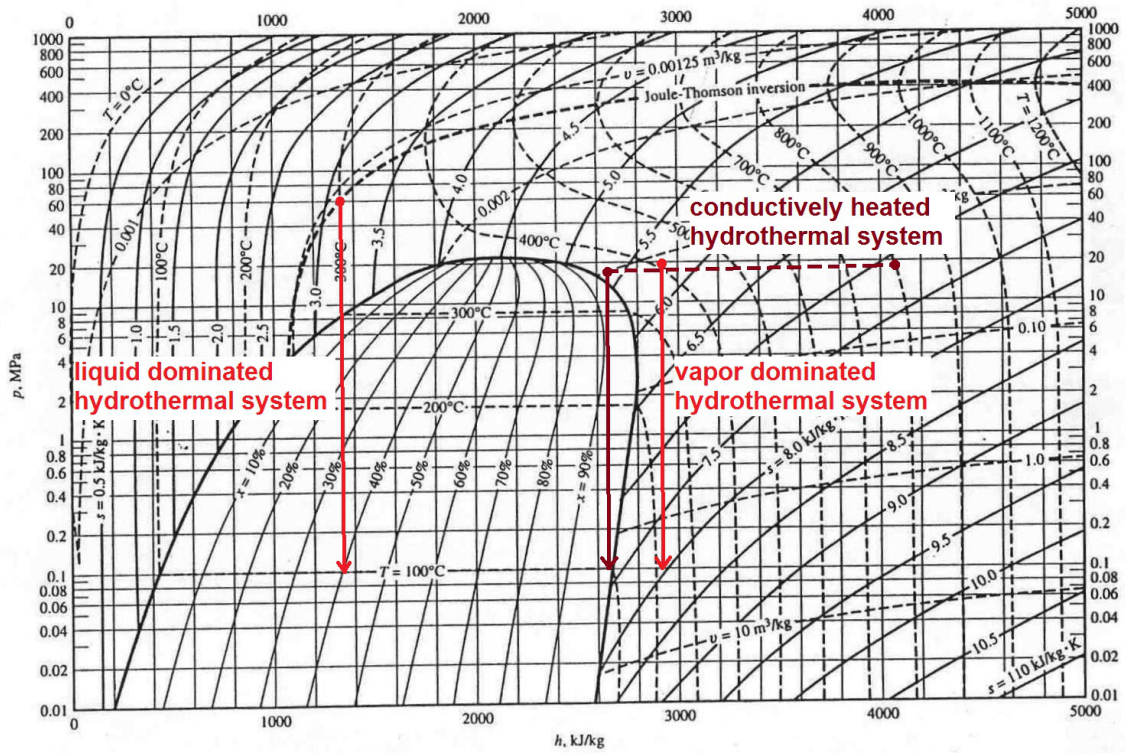


FIG. 1. Fluid properties as it ascends from deep heat source to the wellhead plotted in the Mollier pressure-enthalpy diagram of pure water: examples of a liquid dominated hydrothermal system (left red line), of a convectively heated vapor dominated hydrothermal system (right red line) and of a conductively heated vapor dominated hydrothermal system (dark red line). Main assumptions are isenthalpic upwards fluid flow, as well as hydrostatic pressure for the liquid dominated system and vapor-static pressure for the deep part of the vapor dominated system.

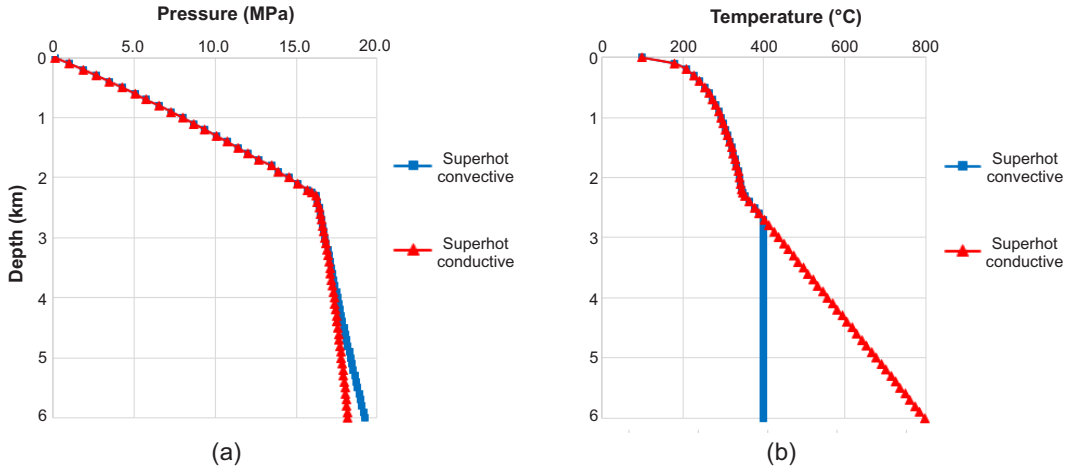


FIG. 2. (a) Pressure and (b) temperature profiles for a superhot geothermal reservoir with convective (blue) and conductive (red) mechanism in the deeper part.

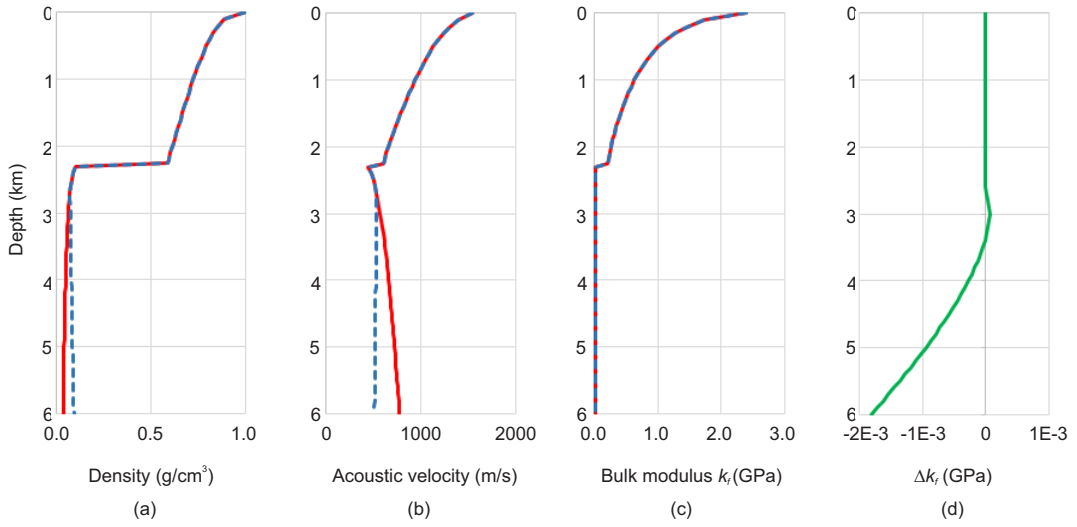


FIG. 2. Saturating fluid properties calculated for the conductive (red line) and the convective (blue dashed line) models: a) density, b) acoustic velocity, c) bulk modulus (K_f), and (d) bulk moduli difference (ΔK_f).

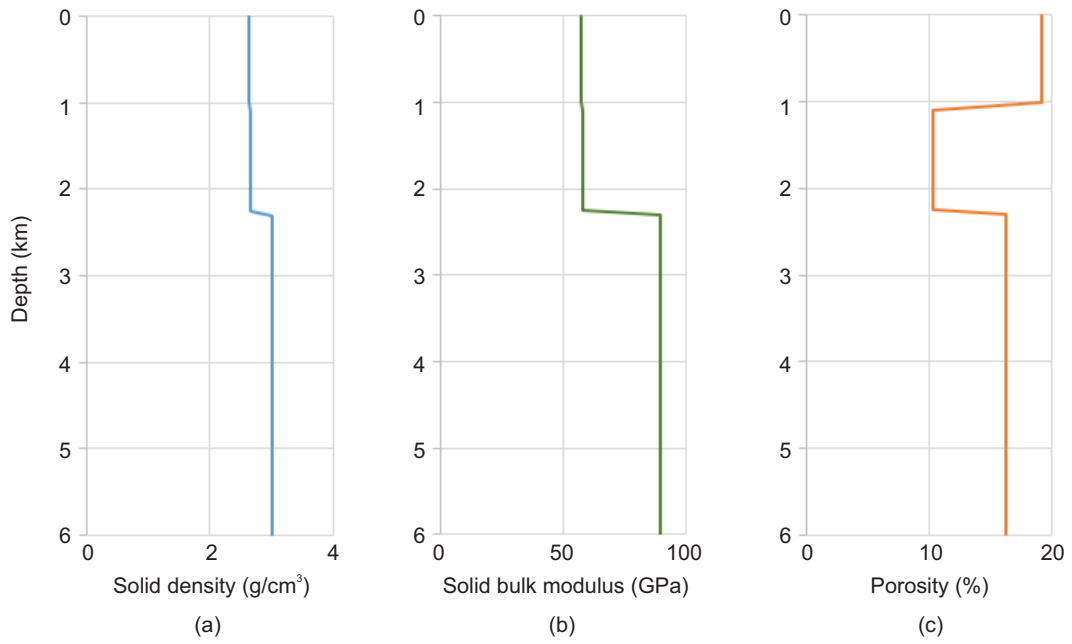


FIG. 3. 1-D rock-frame properties: a) density, b) bulk modulus, and c) porosity.

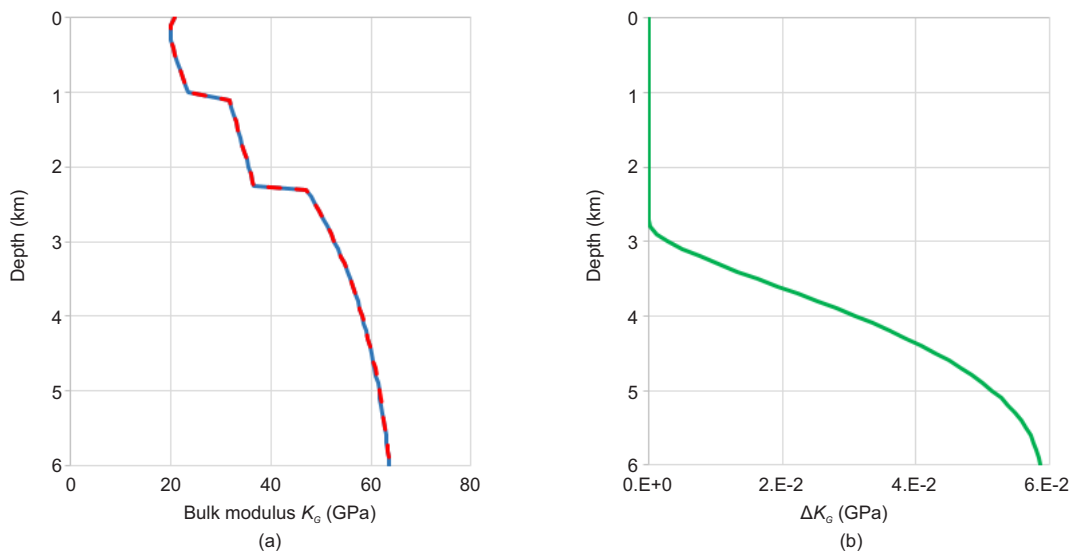


FIG. 3. (a) Gassmann bulk modulus for the saturated formation using conductive (red line) and convective (blue dashed line) models, and (b) bulk moduli difference.

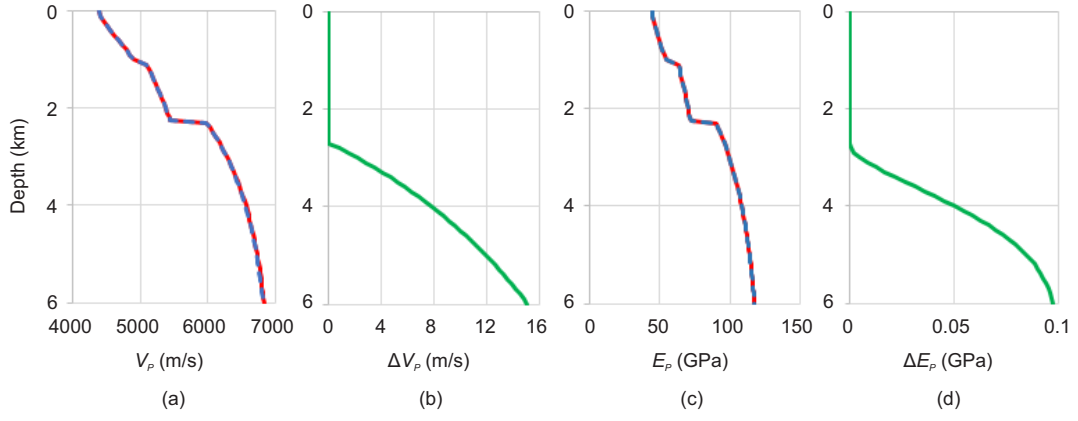


FIG. 4. a) Compressional velocities in the conductive (red line) and convective (blue dashed line) models and b) their difference; c) compressional elastic moduli in the conductive (red line) and convective (blue dashed line) models and d) their difference.

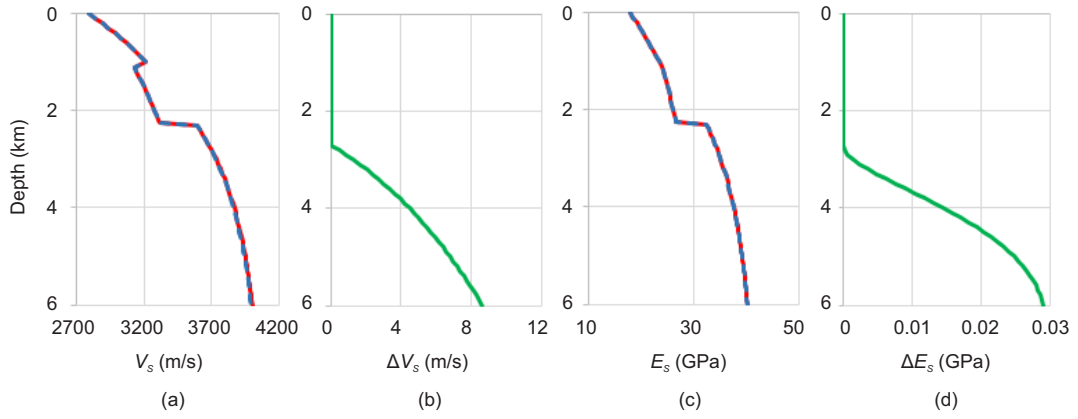


FIG. 4. a) Shear velocities in the conductive (red line) and convective (blue dashed line) models and b) their difference; c) shear elastic moduli in the conductive (red line) and convective (blue dashed line) models and d) their difference.

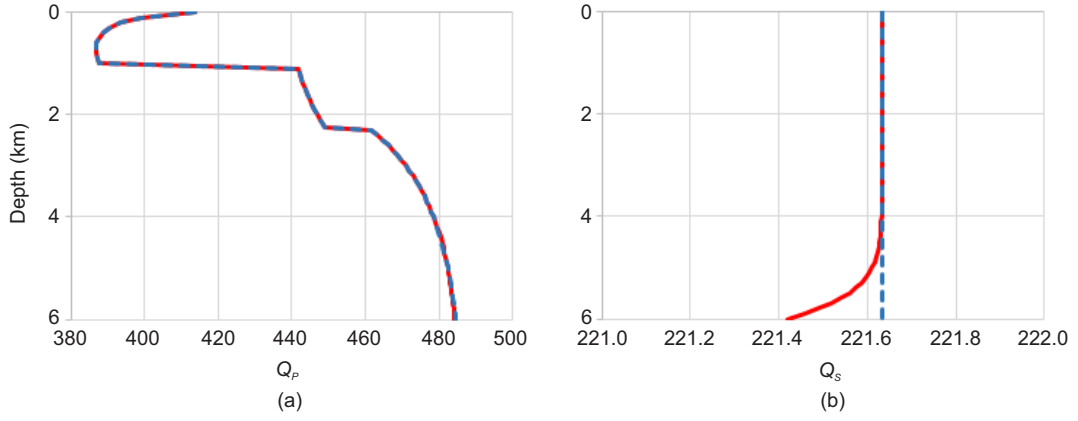


FIG. 5. (a) Compressional and (b) shear quality factors in the conductive (red line) and convective (blue dashed line) models.

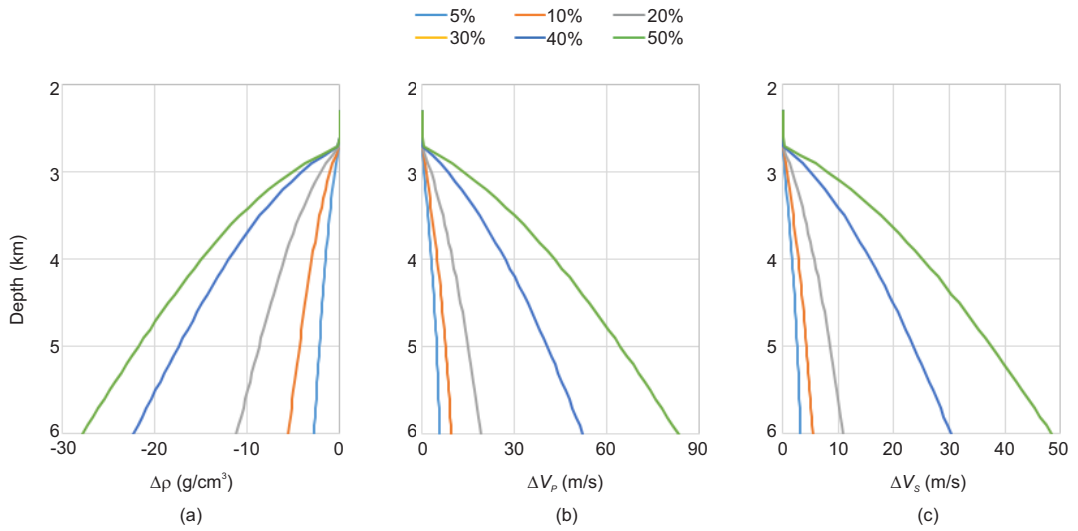


FIG. 5. Difference in (a) the bulk density, (b) the compressional and (c) the shear phase velocities as function of depth calculated in the conductive and convective models with the porosity values shown in the legend equal for all the panels.

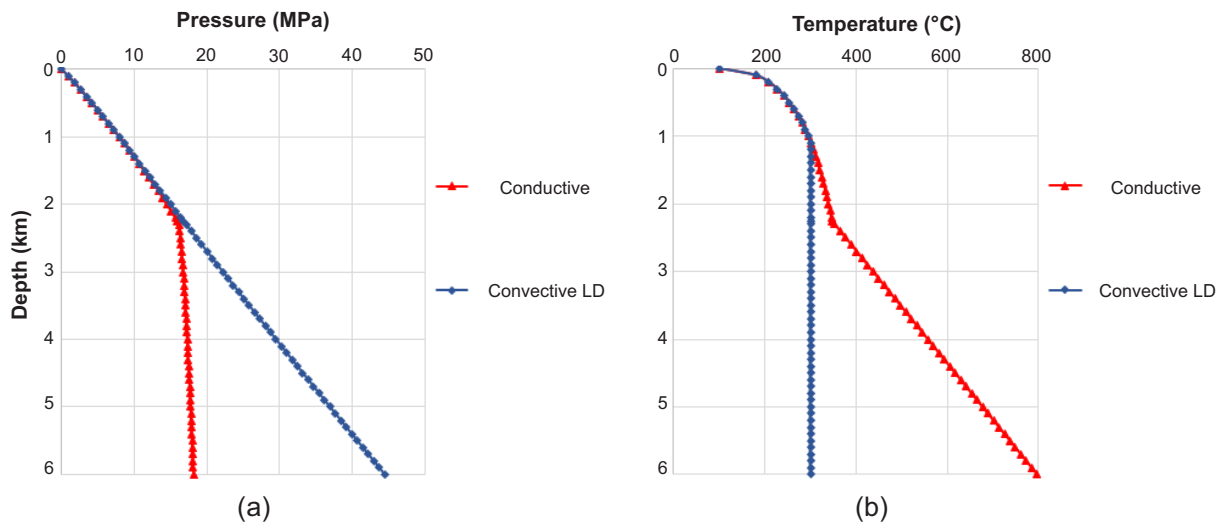


FIG. 6. (a) Pressure and (b) temperature profiles for a superhot geothermal reservoir with conductive (red) and convective LD (blue) heat flow mechanism.

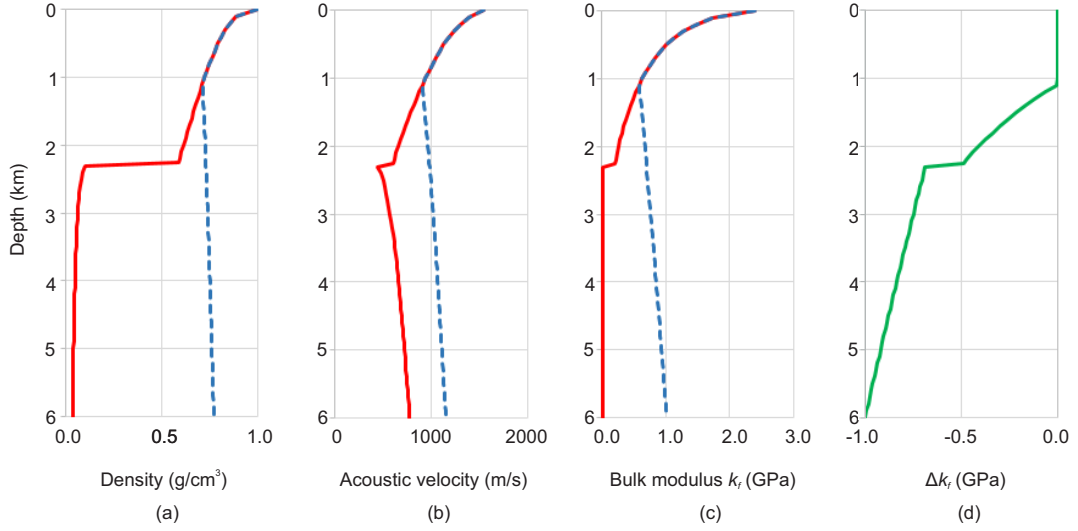


FIG. 7. Saturating fluid properties in the conductive (red line) and the convective liquid dominated (blue dashed line) systems: a) density, b) acoustic velocity, c) bulk moduli (K_f) and d) their difference (ΔK_f).

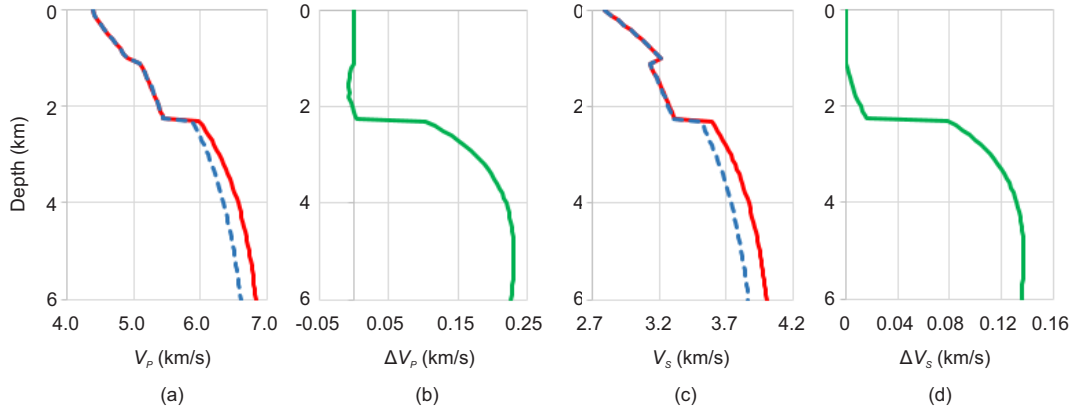


FIG. 7. a) Compressional velocities for conductive (red line) and convective LD (blue dashed line) models and b) their difference; c) shear velocities for conductive (red line) and convective LD (blue dashed line) models and d) their difference.

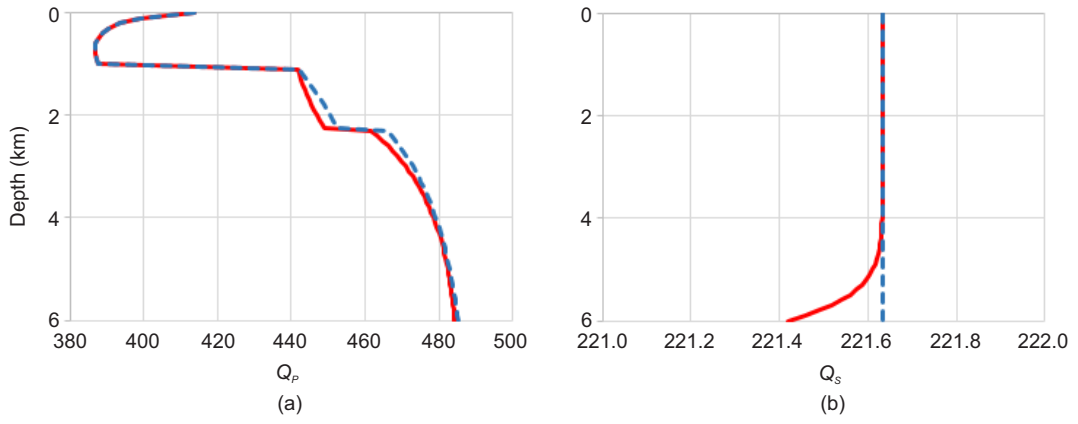


FIG. 8. (a) Compressional and (b) shear quality factors for conductive (red line) and convective LD (blue dashed line) models.

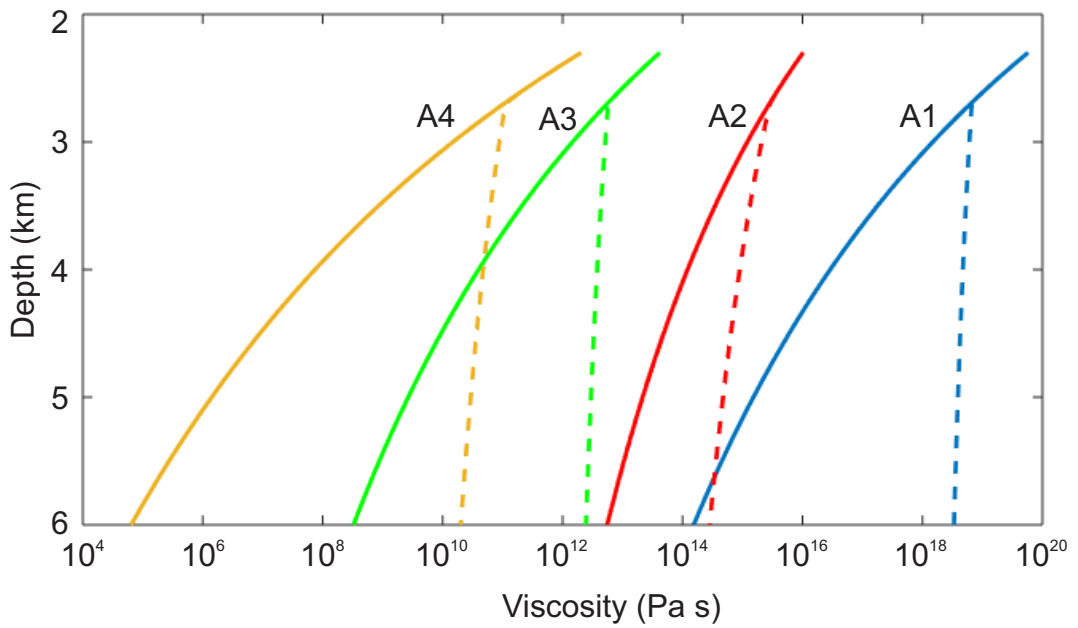


FIG. 8. Viscosity as a function of depth for the four thermodynamic sets of Table 4 in the conductive (bold line) and the convective (dashed line) models.

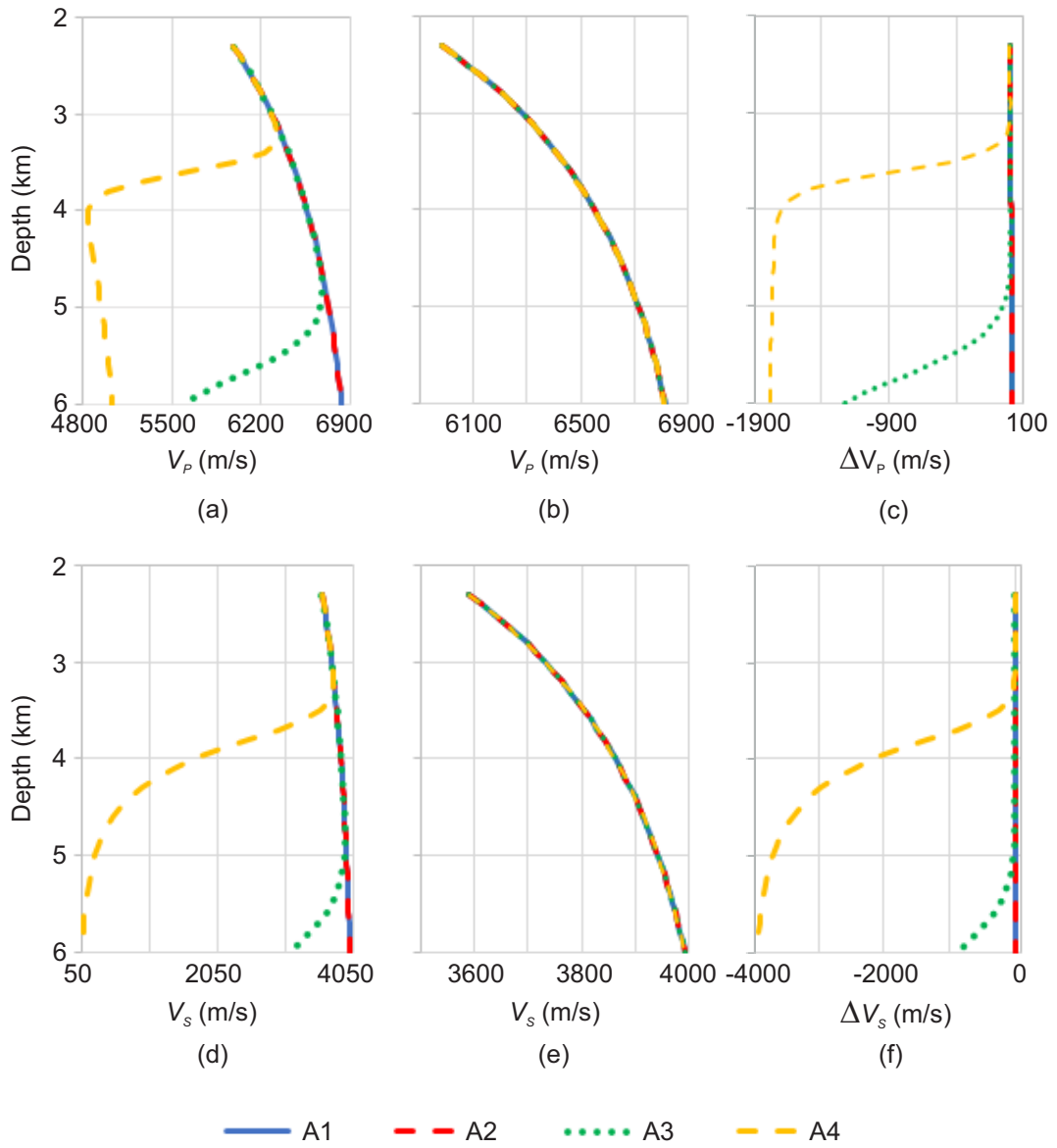


FIG. 9. Compressional phase velocities (V_P) calculated in (a) the conductive and (b) convective models and (c) their difference (ΔV_P). Shear phase velocities (V_S) calculated in (d) the conductive and (d) convective models and (f) their difference (ΔV_S). The legend of the used Arrhenius sets (see Table 4) is common to all panels.

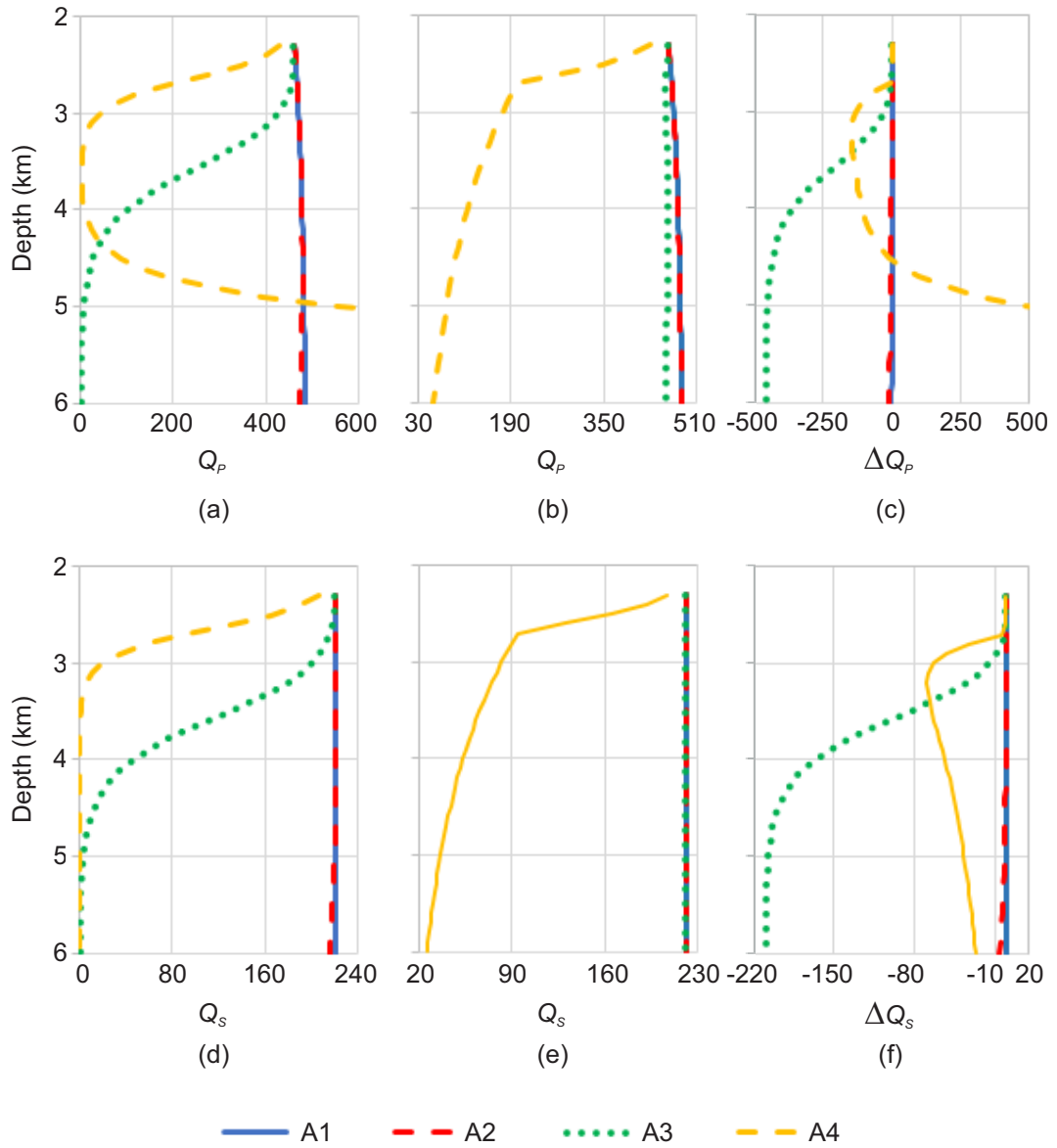


FIG. 10. Compressional attenuation factors (Q_P) calculated in (a) the conductive and (b) convective models and (c) their difference (ΔQ_P). Shear attenuation factors (Q_S) calculated in (d) the conductive and (d) convective models and (f) their difference (ΔQ_S). The legend of the used Arrhenius sets (see Table 4) is common to all panels.

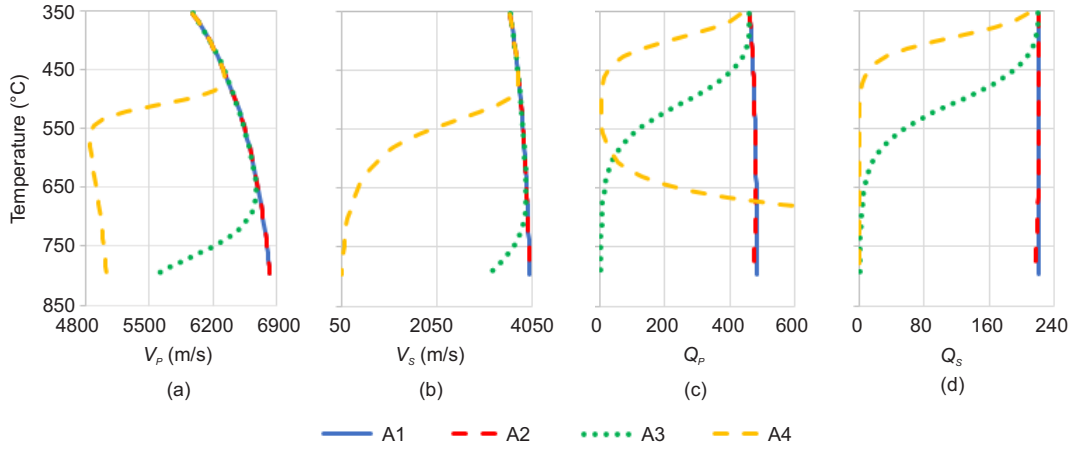


FIG. 11. (a) Compressional and (b) shear phase velocities. (c) Compressional and (d) shear quality factors as functions of temperature. The legend of the used Arrhenius sets (see Table 4) is common to all panels.

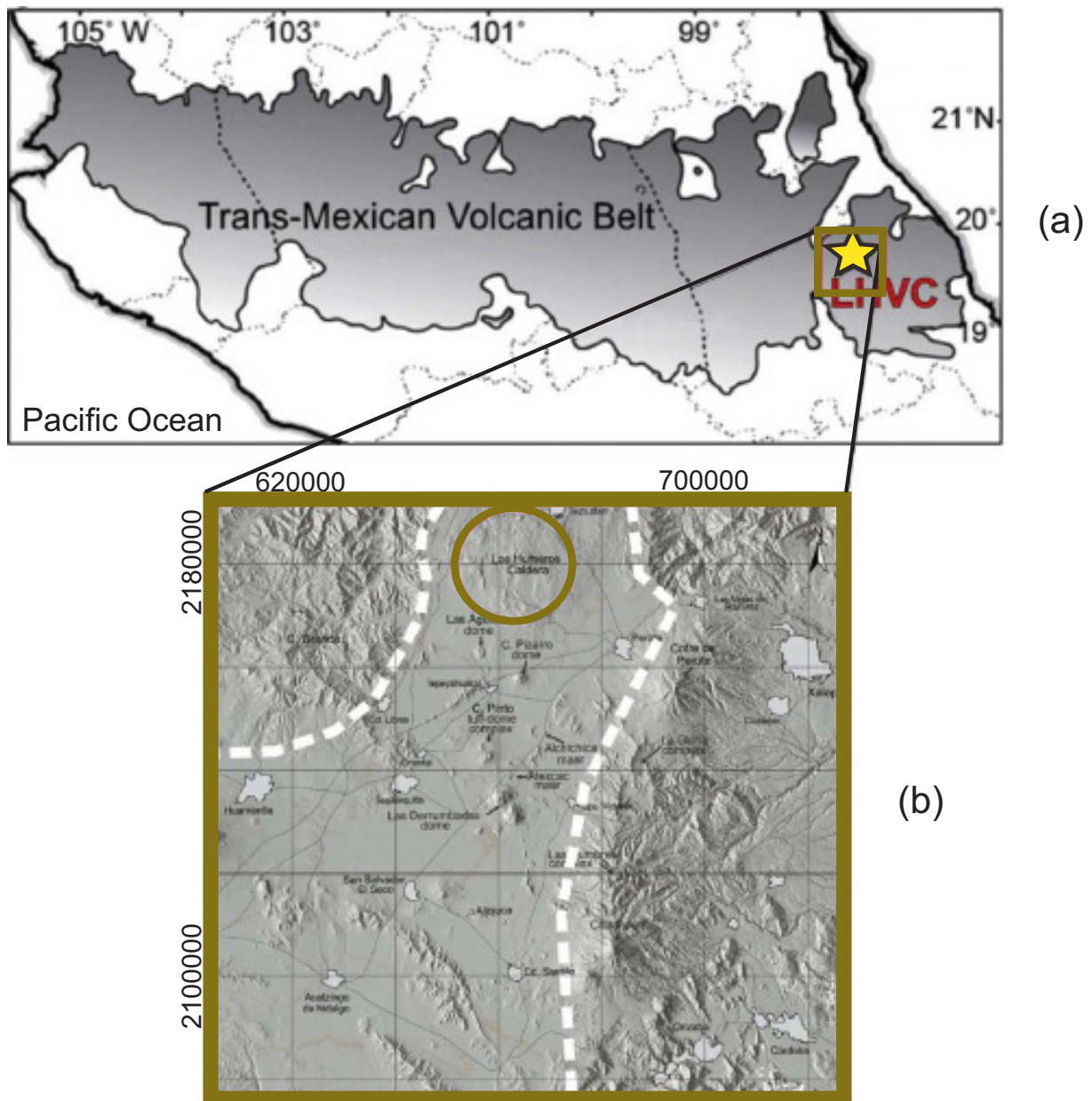


FIG. 12. (a) Location of the Los Hornos volcanic complex in the Trans-Mexican Volcanic Belt. (b) Location of the Los Hornos geothermal field (green circle) at the northern boundary of the Serdán-Oriental basin (Arzate et al., 2018).

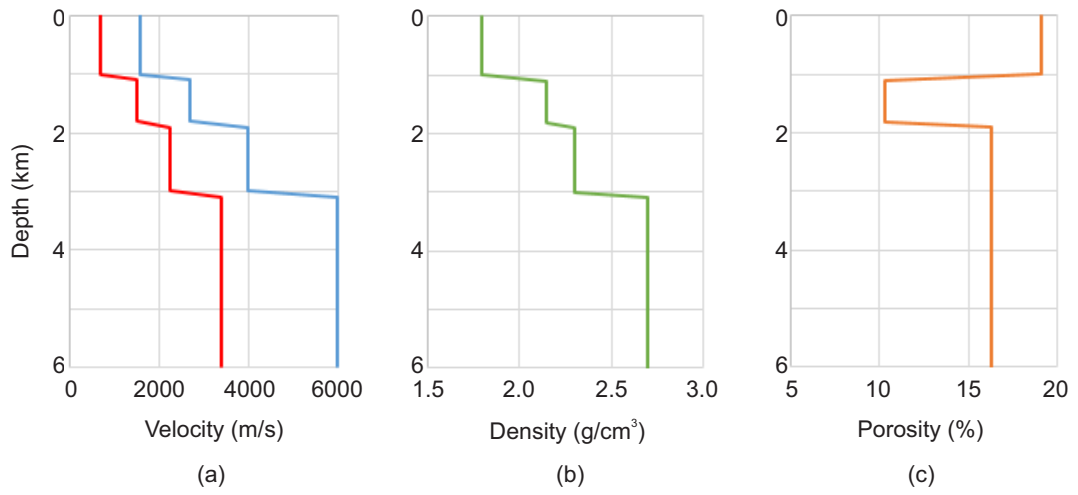


FIG. 13. (a) Compressional (blue line) and shear (red line) velocities, (b) density and (c) porosity of the rock frame composing the geological section.

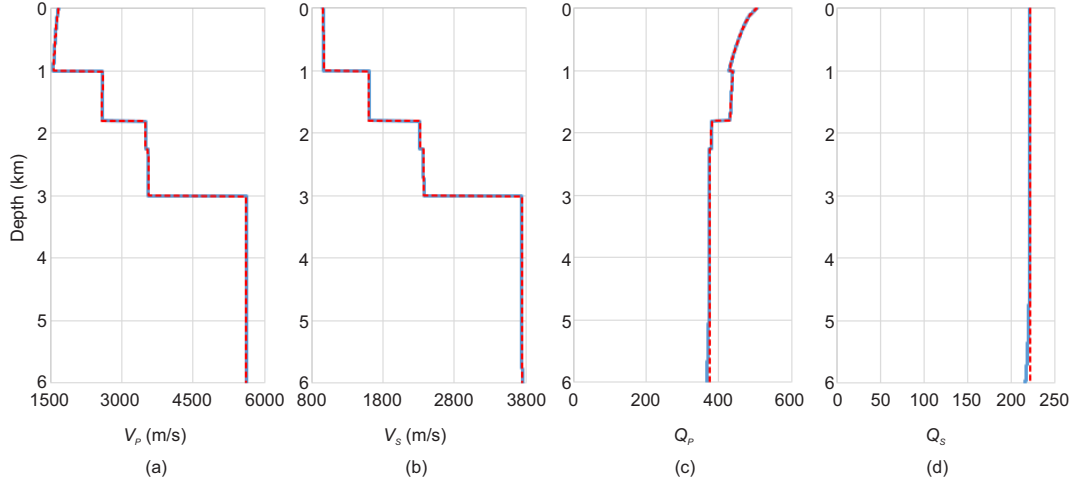


FIG. 14. (a) Compressional and (b) shear phase velocities. (c) Compressional and (d) shear quality factors calculated with conductive (blue line) and convective (red dashed line) models using the Arrhenius set A1 for the deeper layer of the Los Humeros model.

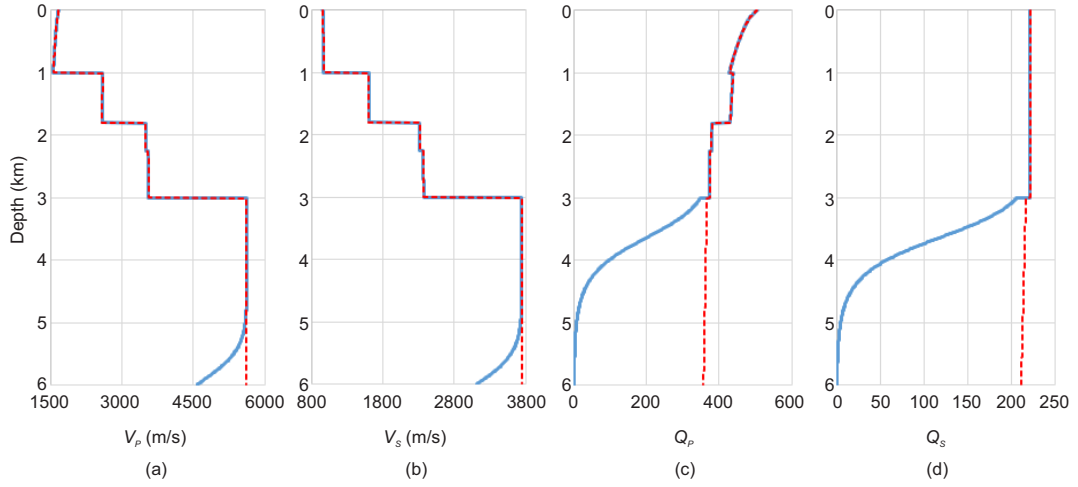


FIG. 14. (a) Compressional and (b) shear phase velocities. (c) Compressional and (d) shear quality factors calculated with conductive (blue line) and convective (red dashed line) models using the Arrhenius set A2 for the deeper layer of the Los Humeros model.

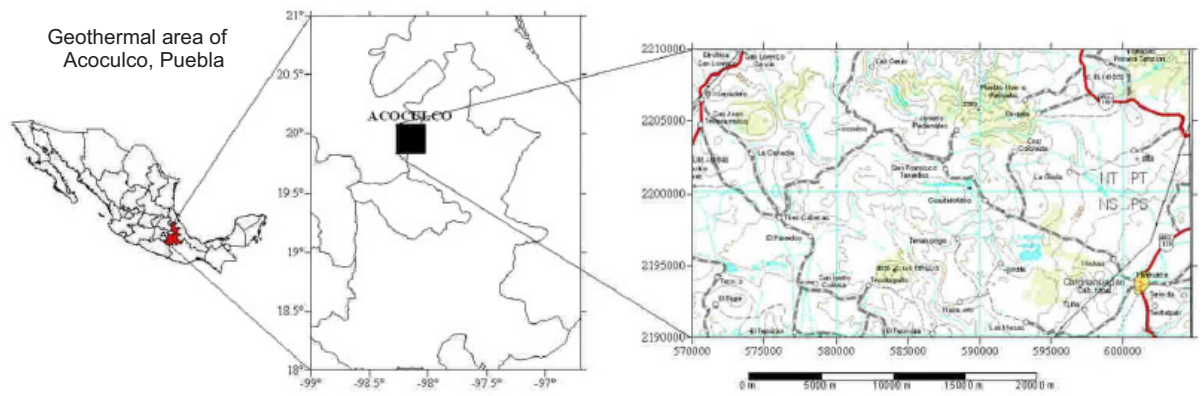


FIG. 15. Map of the geothermal area of Acozulco, Puebla (modified after Pulido et al., 2011).

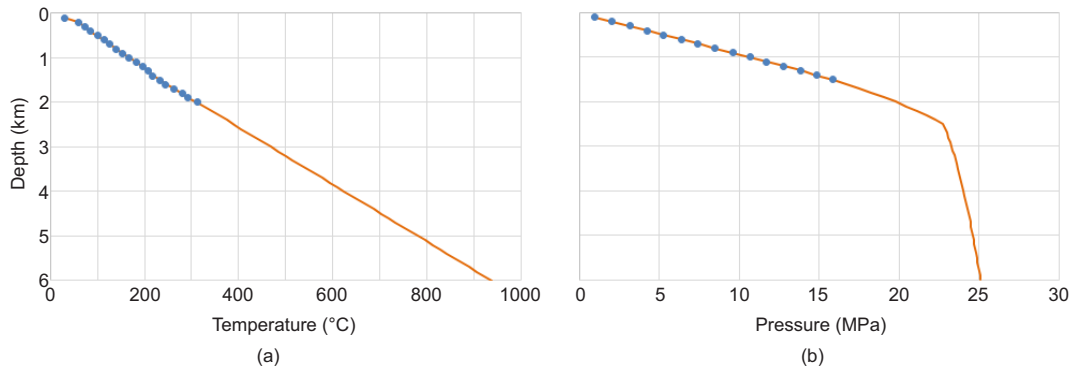


FIG. 16. (a) Temperature of well EAC-1 (blue bullets) obtained from Pulido et al. (2010) and extension to deeper depths using the geothermal gradient of $156\text{ }^{\circ}\text{C}/\text{km}$ (orange line). (b) Pressure of well EAC-1 (blue bullets) and extension using the hydrostatic pore pressure associated to the chosen temperature gradient.

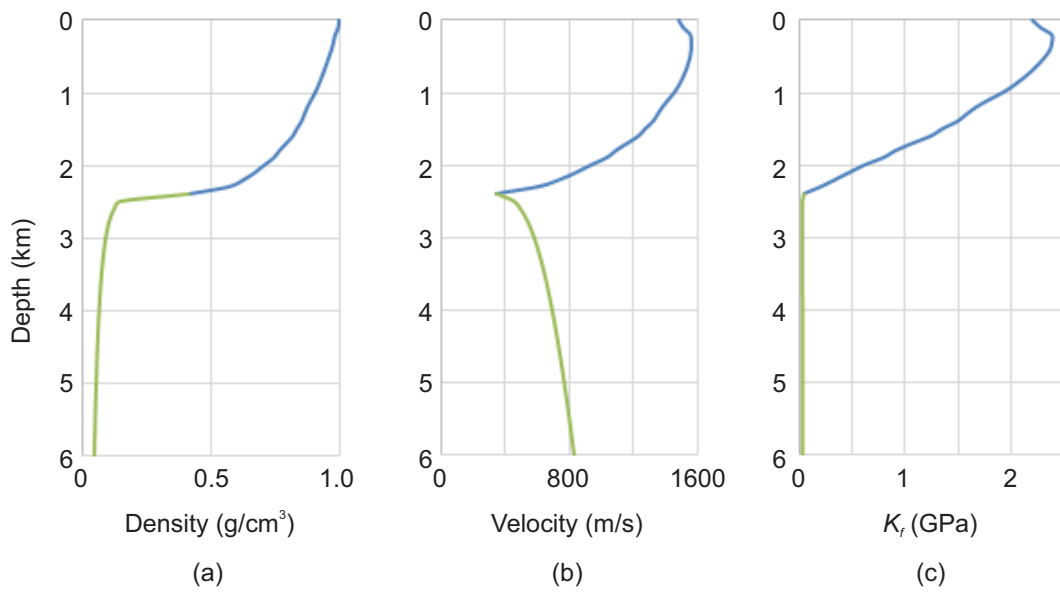


FIG. 16. (a) Density, (b) acoustic velocity and (c) bulk modulus of water under temperature and pressure conditions of Figure 16. The blue and green lines indicate the liquid and supercritical behaviour of water, respectively.

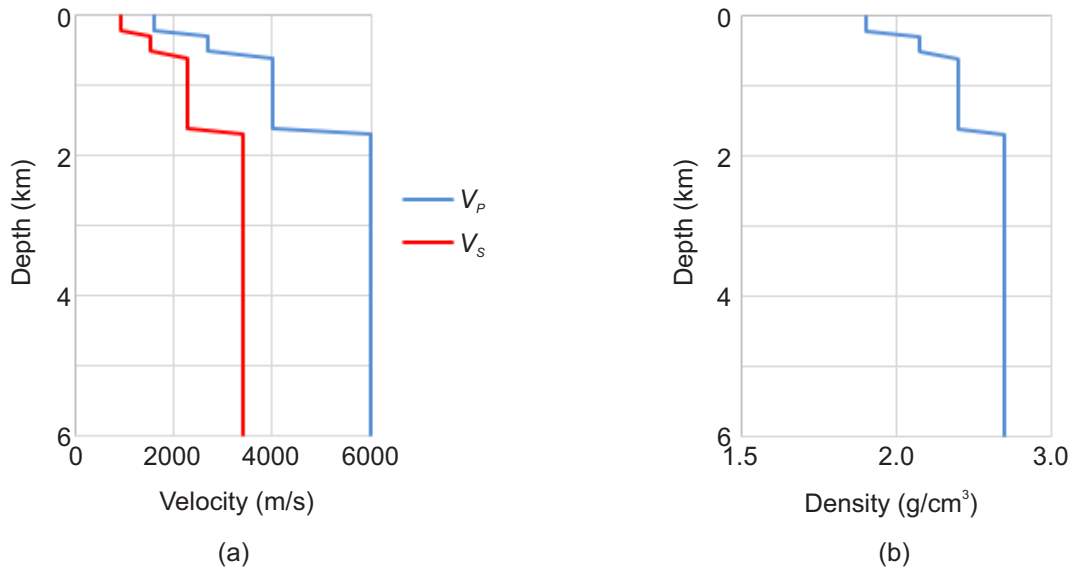


FIG. 17. (a) Compressional (blue line) and shear (red line) velocities and (b) density of the rock frame composing the geological section.

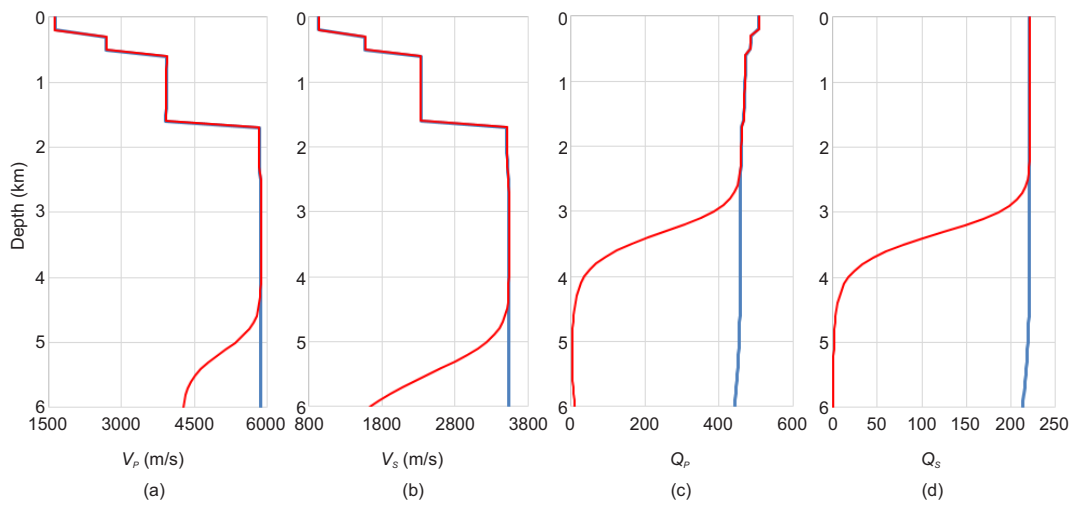


FIG. 17. (a) Compressional and (b) shear phase velocities, (c) compressional and (d) shear quality factors as functions of depth for the saturated media composing the Acoculco model with the last layer characterized by the Arrhenius sets A1 (blue line) and A2 (red line).

ANNEX III

Analysis of seismic wave propagation in geothermal reservoirs

Flavio Poletto, Biancamaria Farina, José M. Carcione and Giorgia Pinna

OGS – Istituto Nazionale di Oceanografia e di Geofisica Sperimentale,
Borgo Grotta Gigante 42/c 34010 Sgonico (Trieste), Italy

fpoletto@inogs.it

Keywords: Seismic waves, temperature, pressure, geothermal reservoirs.

ABSTRACT

We present a review summary of the theory of seismic wave propagation in geothermal reservoir, including temperature and pressure effects based on the Arrhenius equation and poro-viscoelasticity. We quantify the effects of the melting rate point on the seismic velocities, and consider surface and borehole acquisition geometries. We perform wavefield simulations for geothermal areas located at different depths in dissimilar geological contexts.

1. INTRODUCTION

In recent years, rheological studies have been focused to incorporate temperature and melting in the study of seismic wave properties (Jaya et al. 2010) and develop a theory of wave propagation in hot and very-hot geothermal regions with partial melting or melting conditions, such as the brittle-ductile transition (BDT) (Carcione and Poletto, 2013). These approaches have been subsequently used to enable the utilization of seismic methods by developing full-waveform viscoelastic simulation codes for arbitrary geothermal environments (Carcione et al., 2014), including temperature effects through the Arrhenius equation, and confining and pore pressure, with fluids at different phase states (Carcione et al., 2017). The methodology provides synthetic seismograms for geothermal regions, that can be used for a sensitivity analysis of the seismic properties at different rheological conditions (Poletto, et al. 2018), and the study of conductive and convective geothermal systems (Farina et al., 2019).

A preliminary analysis was applied to models obtained from the literature, including geothermal scenarios in Mexico, investigated in the framework of the GEMex H2020 project. This involves a calibrated choice of the rheological, structural and geothermal parameters at the subsurface conditions (Farina et al., 2016). This task required an estimation of the characteristic properties with suitable approximations for the given geological conditions.

Here, we present a review summary of the theory and numerical simulation of seismic wave propagation focused on surface and borehole geometries, and a

discussion of the physical modelling conditions for geothermal areas located at different depths and at different geological contexts. We present examples of wave-field simulation and analysis of the related physical and seismic parameters, and discuss their impact for the calculation of the results.

2. THEORY

2.1 Burgers-Arrhenius model

According to experimental studies, linear viscoelastic models can be used to describe the behaviour of ductile media. Carcione and Poletto (2013) studied the seismic properties of rocks with a ductile behaviour on the basis of variations of the shear modulus as a function of temperature. They proposed a rheology based on the Burgers mechanical model, which is obtained by adding a dashpot (Burgers viscosity), responsible for the steady-state viscous flow, to the Zener model.

The Zener model is used to describe viscoelastic deformation without viscous flow, obtained as the limit of infinite Burgers viscosity. Carcione and Poletto (2013) modelled the effects of anisotropy, seismic attenuation and steady-state creep flow. The frequency-domain Burgers shear modulus is expressed as a function of the seismic relaxation times (τ_σ and τ_ε) of the unrelaxed shear modulus μ_0 , and of the flow viscosity η that describes the ductile behaviour related to the shear deformation:

$$\mu_B(\omega) = \frac{\mu_0(1 + i\omega\tau_\varepsilon)}{1 + i\omega\tau_\sigma - \frac{i\mu_0}{\omega\eta}(1 + i\omega\tau_\varepsilon)}, \quad [1]$$

where ω is the angular frequency and $i = \sqrt{-1}$.

The high temperature effects on seismic wave losses are related to the Burgers viscosity and are solely due to shear deformations. Carcione and Poletto (2013) introduced the viscosity η related to the steady-state creep rate $\dot{\varepsilon}$, which is in turn related to the temperature T through the Arrhenius equation:

$$\eta = \frac{\tau_0}{2\dot{\varepsilon}} = \frac{1}{2A_\infty} \tau_0^{1-n} \exp(E/RT), \quad [2]$$

where τ_0 is the octahedral stress used to describe deformation of the ductile medium. The octahedral stress (see Carcione and Poletto, 2013) is a function of

the stress components along the principal axes and takes into account the additional effects due to the anisotropic tectonic stress related to tectonic activity. A_∞ and n are Arrhenius constants, and E is the activation energy of the medium. $R=8.3144$ J/mol/K is the gas constant and T is the absolute temperature. The complex frequency-dependent compressional (P) and shear (S) phase-velocities are

$$V_p = \sqrt{\frac{K + \frac{4\mu_B(\omega)}{3}}{\rho}} \quad \text{and} \quad V_s = \sqrt{\frac{\mu_B(\omega)}{\rho}}, \quad [3]$$

where K and ρ are the rock modulus and density, respectively.

2.2 Gassman-Burgers model

To simulate full-waveform seismic propagation in poro-viscoelastic geothermal reservoirs including temperature, Carcione et al. (2014) implemented an algorithm based on the Burgers mechanical model, which includes the transient creep of the Zener model and the steady-state creep of the Maxwell model. They simulated seismic wave propagation in heterogeneous anelastic media in the presence of the brittle-ductile transition (BDT), where memory variables were implemented to solve the differential equations in the time domain. The equations are developed in the velocity-stress formulation by using eight memory variables for 2D P-S wave propagation.

Carcione et al. (2017) extended the theory to poro-viscoelastic media. They explicitly modelled the effects of saturating fluids, using water and steam at various pressure-temperature conditions, considering supercritical states. The approach yields the wet-rock Gassmann-Burgers bulk and shear moduli

$$K_G = K_m + \alpha^2 M \quad \text{with} \quad \alpha = 1 - \frac{K_m}{K_s}, \quad [4]$$

and

$$M = \frac{K_s}{1 - \phi - \frac{K_m}{K_s} + \phi \frac{K_s}{K_f}}, \quad [5]$$

where K_m , K_s and K_f are the dry-rock, mineral and fluid bulk moduli, respectively, and ϕ is the porosity .

2.3 Seismic velocity

The properties in poro-viscoelastic media are characterized by seismic velocity and attenuation Q^{-1} , where Q is the quality factor. Here, we pay attention to the velocity.

The complex phase velocities are obtained on the basis of equations (3) (Carcione and Poletto, 2013), by substituting the rock-frame bulk modulus K with the wet-rock bulk modulus K_G and the rock density ρ with the bulk density $\rho_b = (1 - \phi)\rho + \phi\rho_f$, where ρ_f is

the fluid density. Important and characteristic velocity variations are calculated for melting conditions and the presence of the BDT.

3. MELTING CONDITIONS

To illustrate typical seismic properties in reservoirs as a function of temperature, we present a preliminary overview of the rock's melting behaviour in relation to the thermodynamic conditions, which are expressed in our analysis by the Arrhenius parameters (eq. [2]). For this purpose, we assume a medium with uniform properties, neglecting the presence of fluids and pore pressure as an approximation. In these examples we refer to the amphibolite rock sample of Popp and Kern (1994), as representative of the properties of a crustal rock, including intrinsic attenuation Q_0 (Table 1).

We use the confining pressure at variable depth z to calculate the octahedral stress (Carcione and Poletto, 2013). Then, keeping constant the other properties, we vary the Arrhenius stress parameter-exponent n , the amplitude A (for convenience here we use the simplified notation A for A_∞), and the rock sample activation energy E .

This provides us a set of characteristic curves representing the behaviour of the partially or completely melted rock versus depth and temperature. This analysis, based on literature laboratory rheological data, is mainly aimed at describing and better understanding the seismic properties in the presence of shear viscosity by creep flow, a function of the Arrhenius parameters. A similar analysis can be extended to rocks of other types, such as those of volcanic environments.

Table 1: Rock parameters used for the calculation of the melting conditions.

Property	Value	Unit
ρ	3000	Kg/m ³
K_0	67.1	GPa
K_s	89.4	GPa
μ_0	41.4	GPa
Q_0 (at 10 Hz)	122	

To perform the analysis, we consider a range of three values for each quantity: the depth z (m), the stress exponent n , the amplitude A (MPa ^{n} s ^{-1}), and the activation energy E (kJ mol ^{-1}). For convenience, we describe the configurations using the index values 1, 2, 3 for each of them as described in Table 2. For the activation energy, this table shows the energy factor E_F used in the calculation of $E = E_F \times E_0$, where $E_0 = 134$ (kJ mol ^{-1}) is a reference value (Carcione and Poletto, 2013). For example the ordered index values 1, 3, 2, 1 mean that we have used the values z_1 , n_3 , A_2 and E_1 .

Table 2: Index table.

Index:	1	2	3
z (km)	5	10	20
n	1	2	4
A (MPa ⁻ⁿ s ⁻¹)	10 ⁻⁶	10 ⁻²	10 ¹⁰
E_F	0.5	1	2

Figure 1 shows the effect of the activation energy by E_F on the shear velocity (V_S) versus temperature, while the other quantities are maintained constant as denoted by the indexes 3, 2, 2, $j=(1,..,3)$. The melting effect in the velocity is clear. This example shows the intuitive result that a lower temperature is required to melt with a lower activation energy. Similar curves are obtained for compressional P-waves, with the difference that for S waves the velocity after melting is zero (a liquid), while for P-waves the velocity is greater than zero.

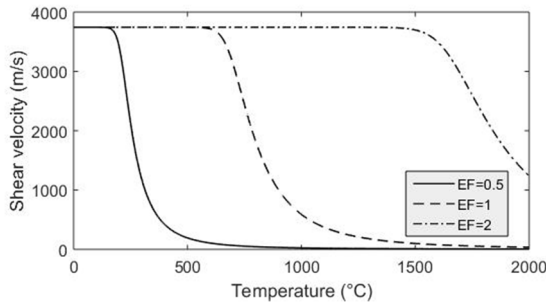
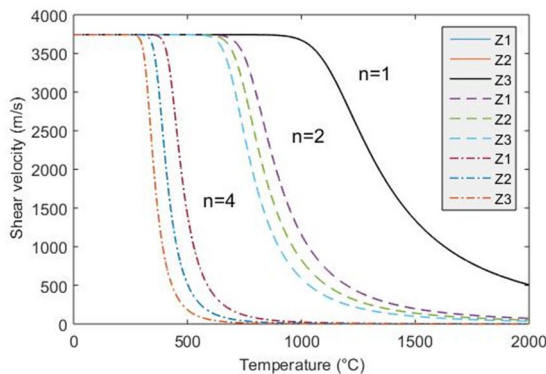
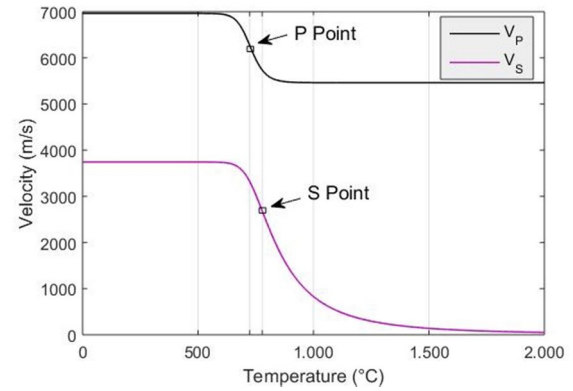
**Figure 1:** Shear velocity curves showing the melting effects of temperature with different activation energies. Case 3, 2, 2, $j=(1,..,3)$.

Figure 2 shows the behaviour of the S-wave velocity for different depths z and stress index n . The index values of A and E are set 2 and 2, respectively. The exponent index n governs the effects of confining pressure through the octahedral stress, and $n = 1$ means that there is no dependence on confining pressure, hence on depth. For this reason, all the curves with $n = 1$ are superimposed. For $n > 1$, the melting effects occur at lower temperatures for higher depths, hence at higher confining pressures.

**Figure 2:** Shear velocity curves showing the melting effects of temperature with different depths and exponent index n .

These results pose the problem to estimate the depth of melting under different conditions. We introduce two criteria based on seismic velocity as a function of temperature. Similar considerations can be made also for attenuation (e.g., Poletto et al., 2018), which is significantly affected because the Burgers viscosity decreases due to the thermally induced creep flow. However, it is in general more difficult to measure the Q factor than the seismic velocity. For this reason, we introduce two criteria to characterize the melting conditions, based on the behaviour of P- and S-waves. The P-wave and S-wave velocity curves are different not only in magnitude, but also because the P-wave velocity decreases from the velocity of a solid to that of a liquid (full melting). Conversely, the shear velocity in the melted rock fluid at high temperatures is zero. These effects can be observed in Figure 3, where we show the temperature-velocity profiles of the case identified by indexes 2, 2, 2, 2.

**Figure 3:** Characteristic melting-rate points for P and S waves at different temperatures (case 2, 2, 2, 2).

We see that the curve of the P wave has a sort of ‘symmetry’ around its flexing point, while the curve of the S wave is ‘asymmetric’ with a trend tending to zero for high temperatures. We keep as characteristic temperature point the inflexion point, i.e., the point where the derivative, i.e., the negative melting rate, is minimum (absolute maximum)

$$\frac{\partial V_{P,S}}{\partial T} = \min, \quad [6]$$

after an initial decrease and then an increase with increasing temperature. These points are indicated by arrows (Fig. 3), and correspond to 724 °C and 778 °C for P and S waves, respectively. We define these points where the melting effect has its maximum rate (negative rate for velocity) as the characteristic melting-rate points. In other words, we observe the ‘central’ melting point in the velocity curve, rather than an ‘initial’ one.

Figure 4 shows the temperature-depth curves of the melting-rate points for the P and S waves (case $z, n, 2, 2$) calculated with different values of the n Arrhenius stress exponent. Using an exponent $n > 1$, we obtain a decrease of the melting temperature with increasing

depth. In this example, the maximum confining pressure is 0.589 GPa at 20 km and the pressure increases by 0.0294 GPa/km.

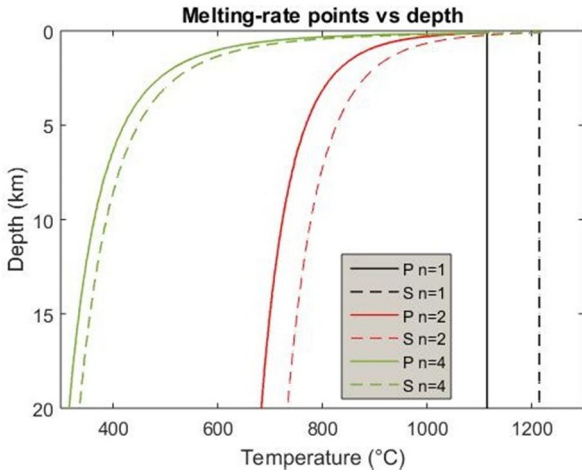


Figure 4: Characteristic melting-rate points of the P and S waves versus temperature and depth (case $z, n, 2, 2$).

In Figure 5, we compare the characteristic melting-rate curve calculated for P waves (case $z, 2, 2, 2$) with temperature curves obtained by different linear temperature gradients: $TG = 10 \text{ }^\circ\text{C/km}$ and $TG = 5 \text{ }^\circ\text{C/km}$. This figure gives an estimate of the melting depth for an assumed temperature profile, accordingly with our definition of melting-rate points (marked by small rectangles in the plot) defined as the inflexion point (maximum negative rate for the velocity) in the temperature-velocity profile.

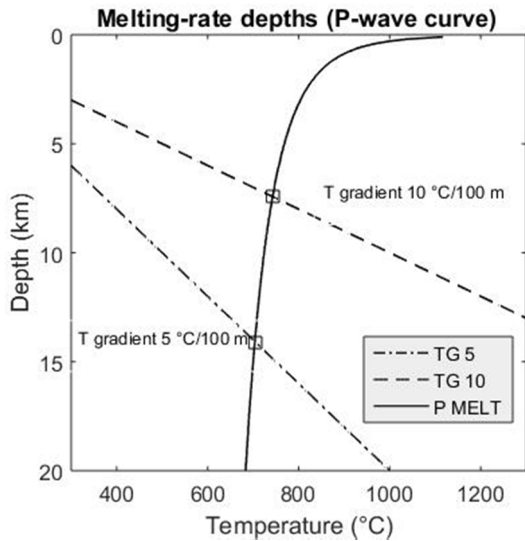


Figure 5: Estimation of melting points at depth according to the velocity-inflexion point definition (case $z, 2, 2, 2$).

The results in Figures 4 and 5 have trends versus depth similar to and consistent with those of the melting temperature-pressure curves obtained for crustal wet rocks (Schilling et al., 2006; Lambert and Wyllie, 1972), in our case characterized by the rock properties of Table 1.

In the next section, we extend the analysis to compute wavefield simulations with seismic properties in heterogeneous poro-viscoelastic geothermal media, including fluids and pressure.

4. SIMULATIONS

We calculate synthetic full waveforms focusing on the superhot geothermal field of Los Humeros, the largest active caldera located in the northernmost part of the eastern sector of the Trans-Mexican volcanic belt (Carrasco-Núñez et al., 2017). This is one of the two field sites studied by the joint European-Mexican GEMex project (funded from the European Union's Horizon 2020 research and innovation programme under grant agreement No. 727550).

In this context, we consider two geothermal scenarios in which the seismic response is sensitive to the high temperature and pressure conditions.

4.1 Proximity to melting formations

In the first scenario, we consider proximity to a magma chamber with melting formations. We use the geological and temperature model proposed by Verma et al. (1990), located along the profile shown in the map by the red line in Figure 6.

In this model, Verma et al. (1990) proposed the presence of a circular magma chamber under the caldera, with two cylindrical chimneys at the top, that they located according to geochemical and geological studies on some wells near and along the line.

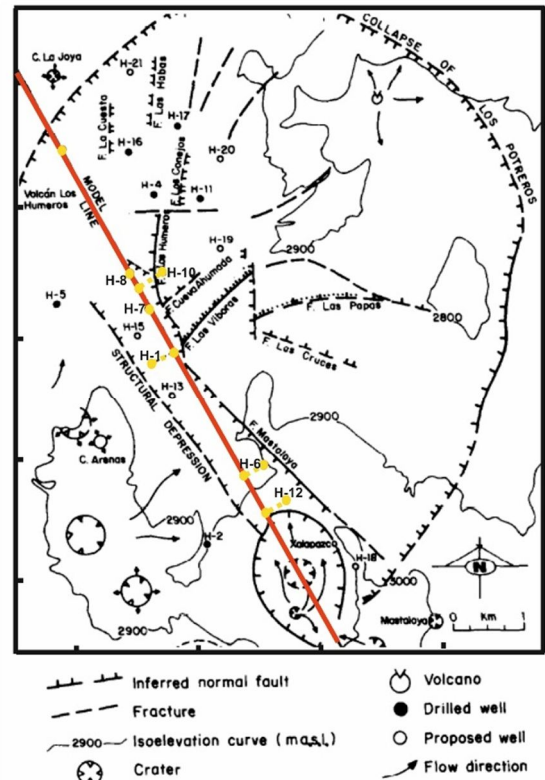


Figure 6: Location of the seismic line (red) with the position of drilled wells (modified after Verma et al., 1990).

A view of the chimney, with the corresponding lithological units of the line proposed by Verma et al. (1990), is shown in Figure 7, with the isotherms superimposed to the lithology section. In the first scenario, we neglect the presence of the hotter chimney, in a medium with temperature calculated assuming a linear gradient between the isotherms.

Assuming these lithological units and isotherms, we construct the geological model. Then we simulate the wave-fields by using the rock-frame and Arrhenius properties given in Table 3. For all the formations we assume $V_p/V_s = 2$, porosity 5 % and pure water as geothermal fluid, as an approximation. We simulate the non-melting and melting condition by changing only the Arrhenius parameters, denoted as A1 and A2, respectively, of the last two layers, and compare the results to analyse the sensitivity of the seismic response to the thermal properties. To evaluate the melting conditions we used the analysis of the case (2, 2, 2, 2) of the previous section. For this purpose, we extend the model to a depth of 9.9 km.

Figure 8 shows the geological model for a VSP synthetic experiment with the seismic source at depth (3.6 km), located at a lateral position with respect to the right chimney, to simulate a natural micro-crack, or passive SWD measurements from a source well (Poletto and Miranda, 2004). The VSP is extended from the surface to 8.5 km depth (Fig. 9), thus entering the zone of melting. Obviously this condition is not realistic because of the high recording depth in melting areas, but for limited hot-zone approaching by ICDP (International Continental Scientific Drilling) wells. For the numerical simulation we use the 2D Burgers-Gassmann full-waveform propagation code in poro-viscoelastic media with temperature of Carcione et al. (2017). The grid pixel size is $30 \text{ m} \times 30 \text{ m}$.

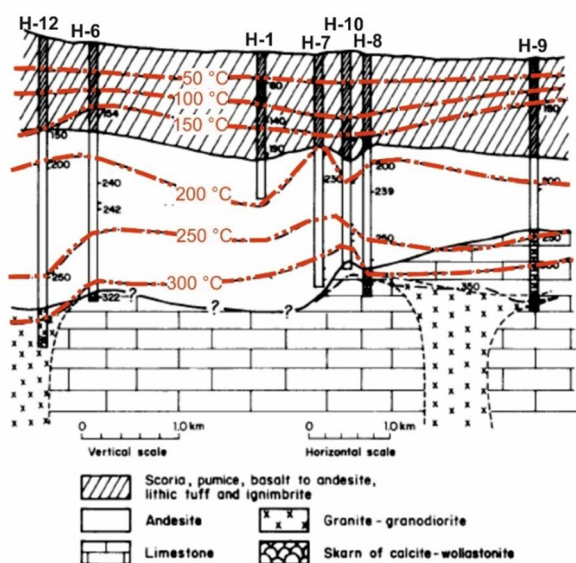


Figure 7: Geological model of the line in Figure 6 with superimposed isotherm (modified after Verma et al., 1990).

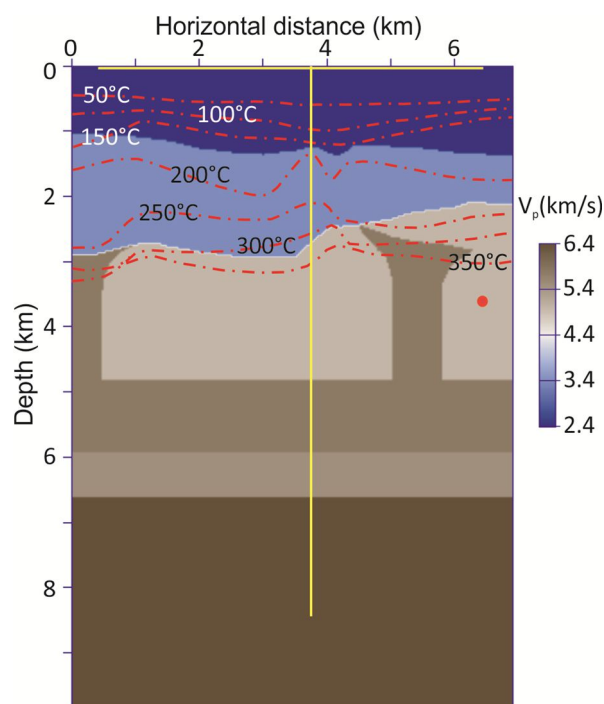


Figure 8: Input P-velocity model of the rock frame used for synthetic simulation. The yellow lines indicate the VSP and the surface profiles, the red star denotes source.

Figure 9 shows the temperature model used for the VSP experiment without and with melting in the presence of different Arrhenius values (A1) and (A2) in Table 3, respectively.

We can observe differences in the prediction signals, namely up-going wave-fields, which can be observed from shallower positions before reaching the melting zone.

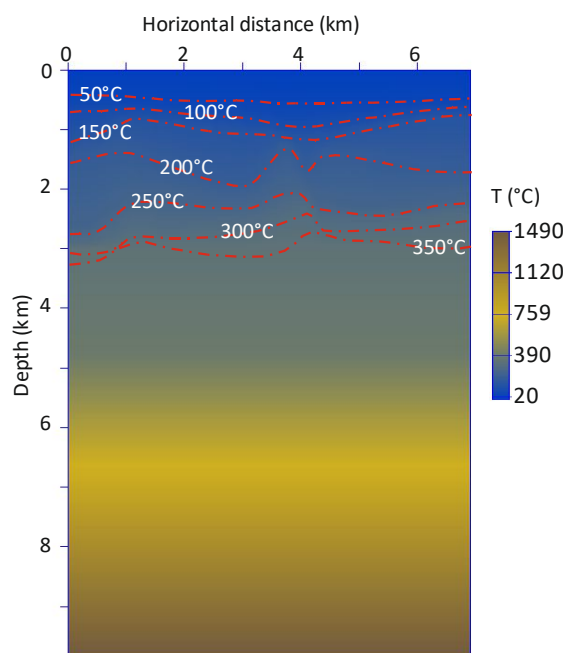


Figure 9: Temperature model used for synthetic simulation of the VSP experiment.

Table 3: Seismic and Arrhenius parameters used for the model of Los Humeros.

Rock Type	V_p (m/s)	ρ (g/cm^3)	References for Arrhenius parameters	A ($\text{MPa}^{-n} \text{s}^{-1}$)	n	E (kJ/mol)
Tuff, Pumice, Basalt, Andesite	2400	2.140	Fernández and Ranalli (1997)	10^{-2}	1.8	151
Hornblende Andesite	3400	2.474	Ranalli (1997)	3.2×10^{-1}	2.4	293
Granite	5800	2.667	Ranalli (1997)	2×10^{-4}	1.9	137
Limestone	5000	2.600	Fernández and Ranalli (1997)	3.3×10^{-6}	2.4	134
Vescicular Andesite	5500	2.570	A1) Ranalli (1997) A2) Carcione et al. (2014)	3.3×10^{-4} 10^2	3.2 2	238 134
Basalt	6400	2.772	A1) Violay et al. (2012) A2) Carcione et al. (2014)	6.1×10^8 10^2	3.6 2	456 134

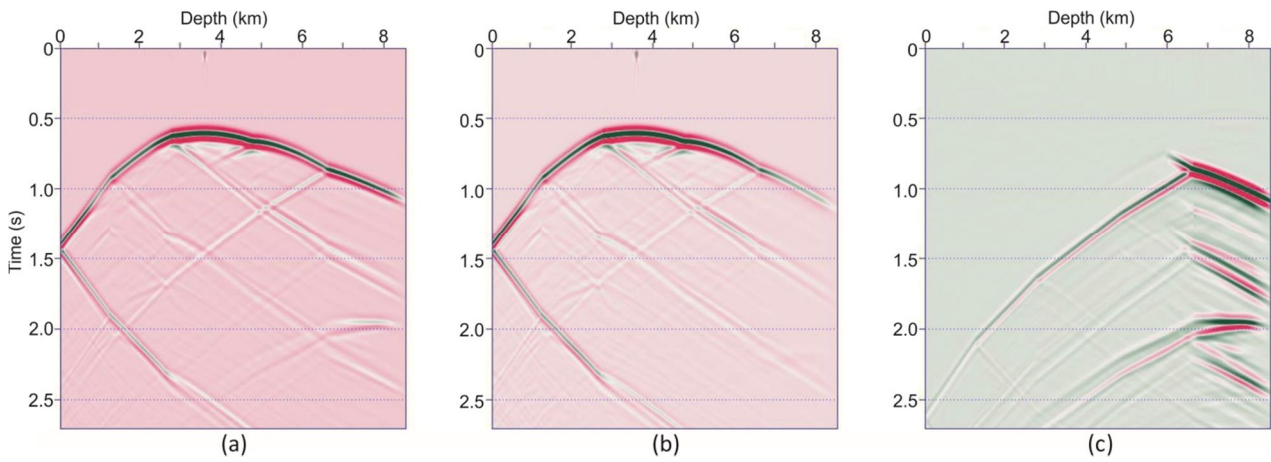


Figure 10: VSP acquired assuming a source at depth. a) In the absence of melting. b) with melting, and c) difference. We observe a clear variation of the synthetic signal in the melting zone. However also the reflection predicting the interface of the melting formation from shallower depths changes its magnitude, as shown by the upgoing events in panel (c).

Figure 10a shows the synthetic VSP, pressure waves, recorded under superhot conditions, but without reaching the limit of melting. Figure 10b is the result obtained with melting at depth, below 6 km, where there is attenuation of the direct P-wave arrivals, and also shear-wave conversion. The variation is clear in (c), obtained as the difference of (a) and (b), also at measurement depths shallower than 6 km for reflections.

4.2 Hot chimney detection

In the second scenario, we use the same geometry and model with and without the presence of the hot chimney (Fig. 11 and Fig. 9, respectively). In the first case, the temperature of the chimney is 400°C , higher than that of the superhot surrounding zone. In the second case (without chimney), its temperature is the same of the unperturbed formation (Figure 9). A simulation with the source at the same position of the previous example and receivers located at opposite sides of the chimney with respect to the source makes it possible to measure direct waves travelled through the chimney.

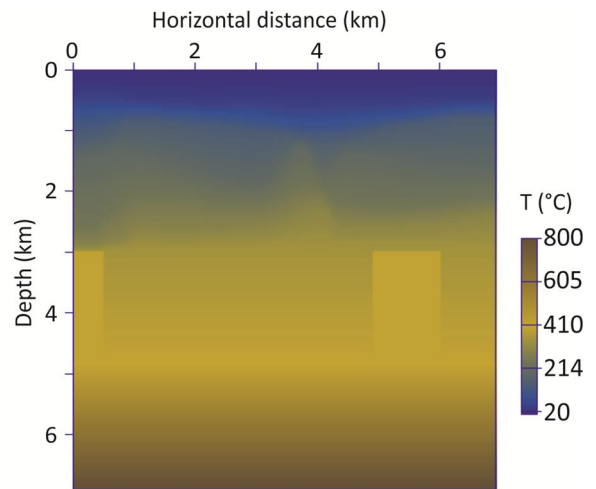


Figure 11: Temperature model with schematized superhot chimneys used for full waveform synthetic simulation and evaluation of effects on seismic wave-field propagation. To simulate the corresponding results in the model without chimneys, we used the model of Figure 9, where the temperatures are shown using different colour scales.

The difference between the two physical corresponds to different observable seismic results

Figure 12 shows the shots recorded with a line of geophones at the surface with and without the chimney. Figure 12a shows the result obtained with the superhot chimney, and Figure 12b shows the results obtained without the superhot chimney, whereas Figure 12c shows the difference. In this case, the variation is observable at the surface.

5. CONCLUSIONS

We have reviewed the physics to simulate seismic-wave properties and compute synthetic wave-fields in geothermal reservoirs as a function of temperature and confining pressure. The approach is based on heterogeneous poro-viscoelastic media.

In the application to hot and superhot systems, we introduce the concept of characteristic melting depth point, based on the melting rate observed in the seismic velocity, showing that this point is different

for P and S waves. The analysis is used for the estimation of melting as a function of depth, and hence with confining pressure, according to literature results in wet rocks. The analysis is then applied for full-waveform simulation in heterogeneous media, specifically in the Los Humeros superhot Mexican caldera and geothermal site.

The simulation provides an analysis tool and makes it possible to detect differences in the seismic wave-fields due to temperature effects, in surface and borehole measurements. Obviously, the repeatability conditions obtainable by synthetic data are not obtainable in nature, and the approach has to be adapted for full-waveform analysis of seismic data, with comparison and calibration of synthetic data and real measurements of deep structures.

Acknowledgements

This project has received funding from the European Union's Horizon 2020 research and innovation programme under grant agreement No. 727550.

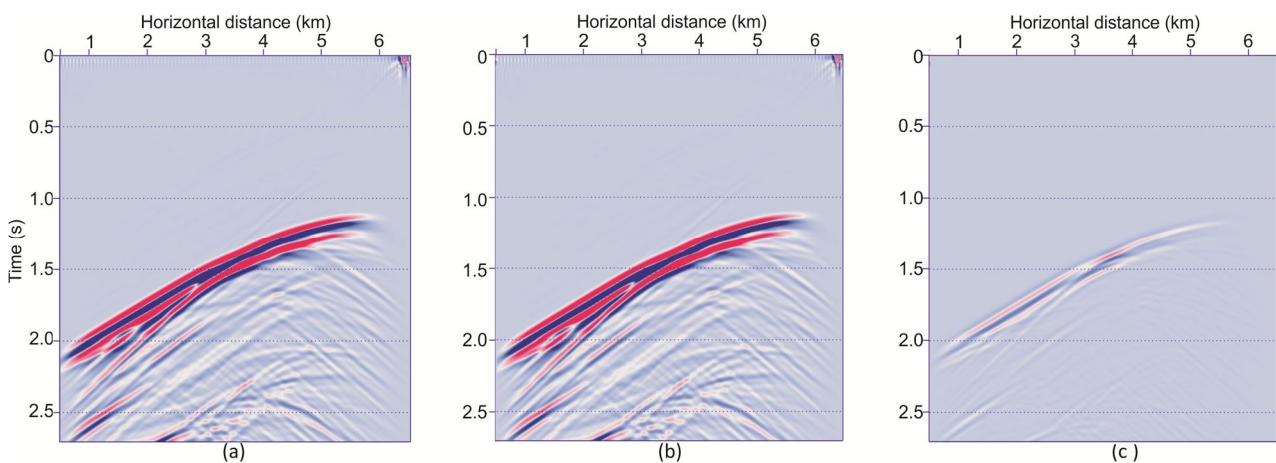


Figure 12: Signal of the surface seismic line acquired a) in the model with superhot chimney, b) in the model without superhot chimney, and c) difference of the results (a) and (b).

REFERENCES

- Carcione, J. M., and Poletto, F., 2013. Seismic rheological model and reflection coefficients of the brittle-ductile transition, *Pure and Applied Geophysics*, DOI 10.1007/s00024-013-0643-4.
- Carcione, J. M., Poletto, F., Farina, B. and Craglietto, A., 2014. Simulation of seismic waves at the Earth crust (brittle-ductile transition) based on the Burgers model, *Solid Earth*, 5, 1001-1010.
- Carcione, J. M., Poletto, F., Farina, B., and Craglietto, A., 2017. The Gassmann-Burgers model to simulate seismic waves at the Earth crust and mantle, *Pure and Applied Geophysics*, 174, 849-863. DOI: 10.1007/s00024-016-1437-2.
- Carrasco-Núñez G., López-Martínez M., Hernández J., and Vargas V., 2017. Subsurface stratigraphy and its correlation with the surficial geology at Los Humeros geothermal field, eastern Trans-Mexican volcanic belt. *Geothermics*, 67, 1-17.
- Farina, B., Poletto, F., Carcione, J., 2016. Seismic wave propagation in poro-viscoelastic hot rocks. In: *Proceedings, European Geothermal Congress 2016, Strasbourg, France*, p 7.
- Farina, B., Poletto, F., Mendrinós, D., Carcione, J. M., and Karytsas, C., 2019. Seismic properties in conductive and convective hot and super-hot geothermal systems. Paper submitted to *Geothermics*.
- Fernández, M., and Ranalli, R., 1997. The role of rheology in extensional basin formation modelling. *Tectonophysics*, 282, 129-145.
- Jaya, M. S., Shapiro, S. A., Kristinsdóttir, L. H., Bruhn, D., Milsch, H., Spangenberg, E., 2010. Temperature dependence of seismic properties in geothermal rocks at reservoir conditions. - *Geothermics*, 39, 1, pp. 115-123. DOI: <http://doi.org/10.1016/j.geothermics.2009.12.002>.
- Lambert, I. B. and Wyllie, P. J., 1972. Melting of gabbro (quartz eclogite) with excess water to 35 kilobar, with geological implications. *Journal of Geology*, v. 80, p 693-708
- Poletto, F., Farina, B., and Carcione, J. M., 2018. Sensitivity of seismic properties to temperature variations in a geothermal reservoir, *Geothermics*, 76, 149—163.
- Poletto and Miranda, 2004. *Seismic While Drilling. Fundamentals of Drill-bit Seismic for Exploration*. Elsevier, Vol. 35.
- Popp, T., and Kern, H., 1994. The influence of dry and water saturated cracks on seismic velocities of crustal rocks - A comparison of experimental data with theoretical model. *Surveys in Geophysics*, 15, 443-465.
- Ranalli, 1997. *Rheology of the lithosphere in space and time*. Geological Society, London, Special Publications 1997, V. 121, 19-37
- Schilling, F. R., Trumbull, R. B., Brasse, H., Haberland, C., Asch, G., Bruhn, D., Mai, K., Haak, V., Giese, P., Muñoz, M., Ramelow, J., Rietbrock, A., Ricaldi, E. and Vietor, T., 2006. Partial Melting in the Central Andean Crust: a Review of Geophysical, Petrophysical, and Petrologic Evidence. In book: *The Andes*. DOI: 10.1007/978-3-540-48684-8_22
- Verma M.P., Surendra, P. Verma, and Sanvincente H., 1990. Temperature field simulation with stratification model of magma chamber under Los Humeros caldera, Puebla, Mexico. *Geothermics*, 19 (2), 187-197.
- Violay, M., Gibert B., Mainprice D., Evans B., Dautria J. M., Azais P., and Pezard, P., 2012. An experimental study of the brittle-ductile transition of basalt at oceanic crust pressure and temperature conditions. *Journal of Geophysical Research*, 117.



Coordination Office, GEMex project

Helmholtz-Zentrum Potsdam
Deutsches GeoForschungsZentrum

Telegrafenberg, 14473 Potsdam

Germany